The University of Nottingham

UNITED KINGDOM · CHINA · MALAYSIA

Hybrid Substations for Low Voltage Distribution Networks

Amin Ganjavi, BEng, MSc.

Submitted to the University of Nottingham for the degree of Doctor of Philosophy

November 2018

Abstract

Voltage regulation has always been considered as the most important fundamental regulating functionalities in low voltage electrical power systems. The continuing trend toward heavier load and high penetration of distributed generation units in low voltage rural distribution feeders requires power electronic-based solution alternatives for voltage regulation purposes. The size of the power electronics is proportional to their power rating. The power rating of converters used for feeder voltage regulation is mainly based on substation voltage and feeder current which is influenced by load models.

This thesis presents a powerful analysis based on probabilistic structure in order to find the required optimised power rating of the power electronics. This thesis also introduces a power electronic solution, known as a hybrid substation for voltage regulation purposes. The hybrid substation comprises fractionally rated power electronic four-leg voltage source converters with a conventional low frequency distribution transformer. An approach to minimise the compensated injection voltage of the hybrid substation using symmetrical components estimation has been presented.

In this work, a comprehensive simulation study using MATLAB is carried out to analyse the optimum power rating of low voltage distribution power electronics based on statistics and probabilities. A simulation study using PLECS has been used to investigate the hybrid substation control performance. Furthermore, an experimental prototype has been built to validate the control algorithm.

Published Papers

The following papers have already been published from this work:

1. A. Ganjavi, E. Christopher, C. M. Johnson and J. Clare, "A study on probability of distribution loads based on expectation maximization algorithm," *2017 IEEE Power & Energy Society Innovative Smart Grid Technologies Conference (ISGT)*, Washington, DC, 2017, pp. 1-5.

2. A. Ganjavi, E. Christopher, C. M. Johnson and J. Clare, "A new analysis for finding the optimum power rating of low voltage distribution power electronics based on statistics and probabilities," *2017 19th European Conference on Power Electronics and Applications (EPE'17 ECCE Europe)*, Warsaw, 2017, pp. P.1-P.10

Acknowledgments

I would like to express my sincere gratitude to my supervisors Prof. Jon Clare, Prof. Mark Johnson and Dr. Edward Christopher for all their guidance, continuous support and patience over the duration of this research work. I would like to thank Dr. Alan Watson for sparing his time to examine me on this work. I would also like to thank Dr. Derrick Holliday from University of Strathclyde for his time and valuable comments on this thesis.

I would like to thank all the staff and technicians of the PEMC group at the University of Nottingham for their help and support. Thanks to all my friends and colleagues of the PEMC group, especially Dr. Alessandro Costabeber, Dr. Behzad Ahmadi and Petros Kounnos. I would also like to thank Dr. Laurence Shaw from School of Mathematical Sciences for his valuable suggestions.

I would like to express my deepest gratitude to my beloved parents for all their support and help over all this time far away from home, my sister Negin and my brother Armin for being supportive over the course of this work. And finally I would thank my beloved fiancée and future wife, Mehrnoosh for being supportive and believing in me.

Nottingham, 2018

Amin Ganjavi

List of Abbreviations and Symbols

Abbreviations

A/D………………………Analogue-to-Digital

CDF……………………...Cumulative Distribution Function

DG……………………….Distribution Generation

DSP………………………Digital Signal Processor

DSTATCOM…………….Distribution Static Compensator

DVR……………………..Dynamic Voltage Restorer

EM……………………….Expectation Maximisation

EMI……………………....Electromagnetic Interference

EMIF…………………….External Memory Interface

FACTS…………………..Flexible AC Transmission Systems

FC………………………..Feeder Compensator

FFT………………………Fast Fourier Transform

FIFO……………………..First in First Out

FPGA…………………….Field Programmable Gate Array

GMM…………………….Gaussian Mixture Model

HPI……………………….Host Port Interface

HT……………………….Hybrid Transformer

HV……………………….High Voltage

IEEE……………………..Institute of Electrical and Electronics Engineers

IGBT…………………….Insulated Gate Bipolar Transistor

IPFC……………………..Interline Power Flow Controller

KCL……………………..Kirchhoff's Current Law

KVL……………………..Kirchhoff's Voltage Law

LPF………………………Low-Pass Filter

LV……………………….Low Voltage

MFC……………………..Mid-Feeder Compensator

MV………………………Medium Voltage

NPC……………………...Neutral-Point Clamed

PCB……………………...Printed Circuit Board

PCC……………………...Point of Common Coupling

PD………………………..Phase Detector

PDF………………………Probability Density Function

PES………………………Power Electronic Substation

PFC………………………Power Factor Corrector

PLL………………………Phase-Locked Loop

POLC…………………….Point of Load Compensator

P.U……………………….Per Unit

PWM…………………….Pulse Width Modulation

QSG……………………..Quadrature Signal Generator

RMS……………………..Root Mean Square

SOGI…………………….Second Order Generalized Integrator

SST………………………Solid State Transformer

SSSC…………………… Static Synchronous Series Compensator

SVM……………………..Space Vector Modulation

THD…………………......Total Harmonic Distortion

UPFC……………………Unified Power Quality Conditioner

VCO……………………..Voltage Controlled Oscillator

VSC……………………...Voltage Source Converter

ZOH……………………...Zero Order Hold

ZPM………………………Zero-Pole Matching

Symbols

a........................Complex operator, $a = e^{j\frac{2\pi}{3}}$

a^{sh}.....................A parameter of resonant current controller for shunt VSC

a_{cc}^{se}...................A parameter of resonant current controller for series VSC

a_{vc}^{se}...................A parameter of resonant voltage controller for series VSC

b^{sh}.....................A parameter of resonant current controller for shunt VSC

b_{cc}^{se}...................A parameter of resonant current controller for series VSC

b_{vc}^{se}...................A parameter of resonant voltage controller for series VSC

C_{cap}......................Filtering capacitor

C_{dc}.......................DC-link capacitor

$d_{0,1,2,3}$..................Duty ratio of zero and non-zero switching vectors

$E_{X|y}[X]$................Refers as integral, $= \int xp(x|y)dx$

f_c.........................System frequency in Hz (50Hz)

F_s.........................Switching frequency

i...........................Represents phases of voltage or current, $i = a, b, c$

i_α.........................Real component of current in stationary frame

i_α^*.........................Real component of current reference in stationary frame

i_β.........................Imaginary component of current in stationary frame

i_β^*.........................Imaginary component of current reference in stationary frame

$i_{c,dc}$.....................Current flowing through the DC-link capacitor

i_{con}^i.....................Current flowing through the series VSC filtering inductor, $i = a, b, c$

i_d^*.........................Direct component of the current reference in synchronous frame

i_q^*.........................Quadrature component of the current reference in synchronous frame

i_{yi}........................Current flowing through the shunt VSC filtering inductor, $i = a, b, c$

I_f^i.........................Current flowing through the feeder, $i = a, b, c$

I_{ripple}^{pk}.................Peak value of the current ripple

j.........................Feeder number, $j = 1,2, \dots, \mathfrak{n}$

K_i^{PR}....................Integral gain of the resonant controller

$K_{i,cc}^{sh}$....................Integral gain of the resonant current controller for shunt VSC

$K_{i,vc}^{pi}$....................Integral gain of the DC-link voltage controller

K_p^{pll}....................Proportional gain of the PI controller for PLL

K_p^{PR}....................Proportional gain of the resonant controller

$K_{p,cc}^{se}$....................Proportional gain of the resonant current controller for series VSC

$K_{p,cc}^{sh}$....................Proportional gain of the resonant current controller for shunt VSC

$K_{p,vc}^{pi}$....................Proportional gain of the DC-link voltage controller

$K_{p,vc}^{se}$....................Proportional gain of the resonant voltage controller for series VSC

l_s.........................Line reactance

L_x......................Filtering inductance of series VSC

L_y......................Filtering inductance of shunt VSC

M_p.....................Overshoot

$\mathcal{n}$......................Independent distributed random variable

N_1.....................Primary winding of conventional transformer

$N_{2,3}$...................Secondary winding(s) of conventional transformer

N_{f1}....................Primary winding of injection transformer of feeder VSC

N_{f2}....................Secondary winding of injection transformer of feeder VSC

N_{s1}....................Primary winding of injection transformer of hybrid transformer

N_{s2}....................Secondary winding of injection transformer of hybrid transformer

$\mathcal{N}$......................Number of Gaussian components

P_D.....................Power dissipation

$P(\mathcal{X}|\mho_i)$............Probability density of $\mathcal{X}$ given $\mho_i$

$qv'_{\alpha\beta}$..................Quadrature signal for $\alpha\beta$ components used in QSG-SOGI

R_M.....................Burden resistor

R_s…………………Line resistance

R_{th}………………..Heat sink thermal resistance

R_y…………………Filtering resistance of shunt VSC

t_{set}………………..Settling time

T…………………..Threshold, considered as 0.001 in simulation

T_A…………………..Ambient temperature

$T^{\alpha\beta\gamma}$……………….Transformation matrix of Clarke's transformation

T_i…………………..Integral gain of PI controller for PLL

T_{jmax}………………Maximum allowable junction temperature

T_s…………………..One switching period

v_0……….................Instantons zero voltage

$v'_{\alpha\beta}$………………...Direct signal for $\alpha\beta$ components used in QSG-SOGI

v_a^*…………………Voltage demanded at the output of the converter

v_{cap}^i………………..Capacitor voltage of series VSC, $i = a, b, c$

v_{dis}………………...Voltage distortion

v_i^+…………………Instantaneous positive voltage, $i = a, b, c$

v_i^-…………………Instantaneous negative voltage, $i = a, b, c$

v_i…………………..Fundamental phase voltage, $i = a, b, c$

v_i^{max}………………..Maximum phase voltage, $i = a, b, c$

v_{li}…………………Load voltage, , $i = a, b, c$

v_{ref}^i……………….The reference injected voltage of hybrid substation, $i = a, b, c$

$\%v_{THD}$……………Total harmonic distortion in percent

$\%v_{unbalance}$……...Voltage unbalance in percent

$V^{+,-}$……………….Magnitude of Positive and negative sequence voltage

$\vec{V}_{\alpha\beta\gamma}^*$……………….Reference voltage for 3-dimensional space vector modulation

V_{DC}…………………DC-link voltage

V_{dc}^{*} ………………… DC-link voltage reference

$V_{dq}^{+,-}$ ………………. Positive and negative sequence voltage in synchronous frame

$V_{Feeder}^{+,-,0}$ ……………. Positive, negative and zero sequence voltage of feeder's VSC

$V_{HT}^{+,-,0}$ ……………... Positive, negative and zero sequence voltage of hybrid transformer

V_f^i ……………….... Output phase voltage of feeder for phase, $i = a, b, c$

V_{ht}^i ………………... Injection voltage of hybrid transformer, $i = a, b, c$

V_o^i ………………… Output phase voltage of hybrid transformer, $i = a, b, c$

$V_{o,optimum}^i$ ……….... Optimum output phase voltage of hybrid transformer, $i = a, b, c$

$\vec{V}_{ref}$ ……………….. Reference voltage for space vector modulation

V_{xi} ……………….... Voltage of secondary winding(N_2) of transformer for phase a, b, c

V_{yd} ………………... Direct supply voltage component in synchronous frame

V_{yi} ………………... Voltage of secondary winding(N_3) of transformer for phase a, b, c

V_{yq} ………………… Quadrature supply voltage component in synchronous frame

VSC$_f$ ……………… Feeder DC-AC VSC

w_i ………………… Weight (size) of i^{th} Gaussian component

x …………………... Phase variable

$x_{\alpha\beta}$ ………………... Variable x in stationary frame

$x_{\alpha\beta}^{+,-}$ ……………….. Positive and negative sequence components in stationary frame

$x_{a,b,c}^{+}$ ……………… Positive sequence of variable x for phase a, b, c

$x_{a,b,c}^{-}$ ……………… Negative sequence of variable x for phase a, b, c

$x_{a,b,c}^{0}$ ………………. Zero sequence of variable x for phase a, b, c

x_{dq} ………………... Variable x in synchronous frame

$x_{dq}^{+,-}$ ……………….. Positive and negative sequence components in synchronous frame

$\mathcal{X}$ …………………... Random variable

$\mathcal{X} \in R^d$ .... d-dimensional random variable

$X^{+,-,0}$.....................Magnitude of positive, negative and zero sequence component

$X_{BE}(Z)$................Backward Euler method in z-domain

$X_{FE}(Z)$.................Forward Euler method in z-domain

$X_{TU}(Z)$................Tustin method in z-domain

$X_{TUP}(Z)$...............Tustin with pre-warping method in z-domain

Z_f^i......................Line impedance, $i = a, b, c$

....

δ_i............................Standard deviation of i^{th} Gaussian component

δ_i^2.....................Variance of i^{th} Gaussian component

ΔV_d....................Voltage drop changes

λ.......................Controllable voltage range of hybrid transformer

ξ.......................Damping ratio

$\theta^{+,-,0}$...................Phase angle of positive, negative and zero sequence component

$\theta^{+,-}_{\mathrm{Feeder}}$................Positive and negative phase angle of feeder's VSC

$\theta^{+,-}_{\mathrm{HT}}$ ....Positive and negative phase angle of hybrid transformer

θ_{pll}....................PLL output angle

θ^*_{pll}.................... PLL output angle reference

μ_i....................... Mean of i^{th} Gaussian component

$\sum_i$.....................Covariance of i^{th} Gaussian component

τ.......................Controllable voltage range of feeder VSC

ω_c.....................Supply voltage frequency, 100π Rad/s

ω_n.....................Natural frequency

ω_{res}....................Resonant frequency of the LC-filter

ω_0.....................Resonant frequency in Rad/s

$\mho_i$...................... Parameters to be estimated of i^{th} Gaussian component

${\mho_i}^{(m)}$........................m^{th} estimate of $\mho_i$

Contents

List of Figures

List of Tables

CHAPTER 1: Introduction

1.1 Introduction

The first electric power station at Pearl Street Electric Power Station in New York City went into operation in 1882 [1]. The electric utility industry grew very quickly and generation, transmission and distribution networks have spread broadly across the entire globe in respect to the energy demand. The electric power systems are considered to be the largest and the most expensive man-made industry in the world [2]. The general structure of an electric power system can be divided into three main sectors: generation, transmission and distribution, as presented in Figure 1.1. The electrical energy produced by generating stations flows through the transmission lines and the transition from transmission to distribution happens in distribution substations.

Quality of the power delivered by the electric utilities to the end-user customers plays an important role in the modern power systems [3-5]. Electric power quality can be defined as ‘‘the goodness of the electric power quality supply in terms of its voltage wave shape, its current wave shape, its frequency, its voltage regulation, as well as level of impulses, noise and the absence of momentary outages’’ [1, 4, 5]. Any disturbance in power quality can have an economic influence on both the utility suppliers and the end-user customers. Furthermore, the common term for describing the power quality in most electrical books and references is equivalent to the voltage quality [3]. Thus, the aim in electric power quality matter is to keep the voltage at permitted levels for the end-user customers [3, 4].

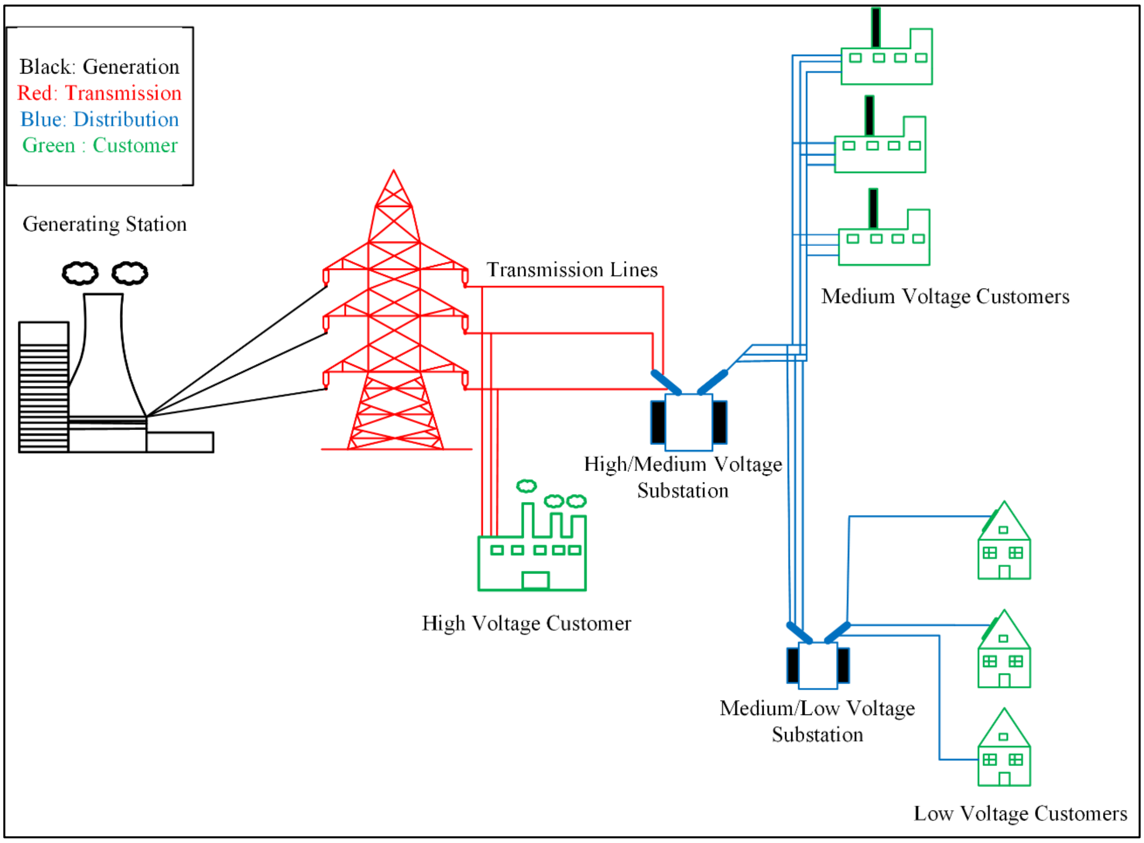

Figure 1.1: General structure of electric power system.

In the UK, the central network takes the electrical power from 132kV substations and distributes it to the customers by a network including 132kV, 66kV, 11kV, 6.6kV and 400/230V substations [6]. Distribution networks in the UK have no voltage regulation downstream of the 11kV primary substation [7]. The electric utility suppliers are required to supply the Low Voltage (LV) end-user customers within the voltage range defined in EN50160 [7, 8], which is 230V ±10% in the EU and 230V +10%, -6% in the UK.

The high influence of Distributed Generation (DG) units, increasing numbers of plug in electric vehicles and continuing trend toward heavier load in LV rural distribution feeders necessitate redefining the requirements of the design and control of the LV networks. Penetrations of DG, especially in the form of Photovoltaic (PV), causes network voltages to rise above the statutory limits by injecting power (inversion power) into the feeders and causing incorrect operation on the substation equipment. The inversion of power flow occurs when the base load is low and the amount of DG is at its greatest [9, 10]. However, voltage rise problems of DGs can be solved by implementing appropriate DGs reactive power controllers, setting a limit for maximum generator capacity and reducing substation voltage [11].

The quality of the voltage has the most impact on the power quality in AC distribution systems and any significant disturbances or changes in the voltage magnitude, frequency or purity can cause a serious power quality problem for the LV end-users customers [3]. The continued growth in electrical energy consumption in both AC and DC systems has affected the voltage profile in LV networks. Therefore, studies concerning performance of the distribution systems and the quality of the service in terms of power quality and satisfactory voltage level have gained more consideration.

In order to keep the distribution voltages within the permitted levels, several solutions for voltage quality problems have been seriously considered with the development of power electronic semiconductors since 1970 [12]. The advancement in integration of power electronic devices, such as Insulated Gate Bipolar (IGBT), Metal Oxide Semiconductor Field Effect Transistor (MOSFET), Diode, etc. [13], are now providing major enhancement in power reliability, voltage regulation, load balancing, efficiency and cost effectiveness of electrical systems [14, 15]. Design of an effective voltage control is essential. As a result, the focus has shifted to power electronic-based solution alternatives.

Due to the large range and unpredicted behaviour of the load data, selecting the right kVA power rating of the power electronics used in LV network is a challenging task. For an LV distribution substation, a higher power electronics capacity can be designed to compensate the power quality of the system. However, this solution brings some inherent disadvantages, such as a higher kVA rating leading to higher losses, larger equipment size, and an increase in the price of the whole system, turning it into an unpopular choice.

Distribution substations are designed based on the electrical load data gathered historically [1]. As a result, the effect and importance of load characteristics have a direct effect on their distribution. Load pattern is highly dependent upon the momentary activity profiles of consumers [16]. Therefore, a comprehensive study and analysis within a probability distribution of loads provided by a feeder/substation are required. By properly selecting a desired substation voltage based on statistics and probabilities, load voltages may be kept within permissible limits for end-users at most times and this reduces the power electronics kVA power rating, loss, cost and size.

In this thesis, a smart configuration, which is named hybrid substation is introduced. The main component of a hybrid substation is a Hybrid Transformer (HT) [17, 18], which comprises fractionally rated power electronic four-leg Voltage Source Converters (VSCs) with a conventional low frequency distribution transformer. The hybrid substation is designed for voltage regulation purposes and injects voltage by sequence analysis based controller. The output voltage of the prototype and the kVA rating of the proposed VSCs are based on an iterative optimisation algorithm. This configuration could be retrofitted to the existing LV substations. Figure 1.2 represents a hybrid substation connected to the LV networks.

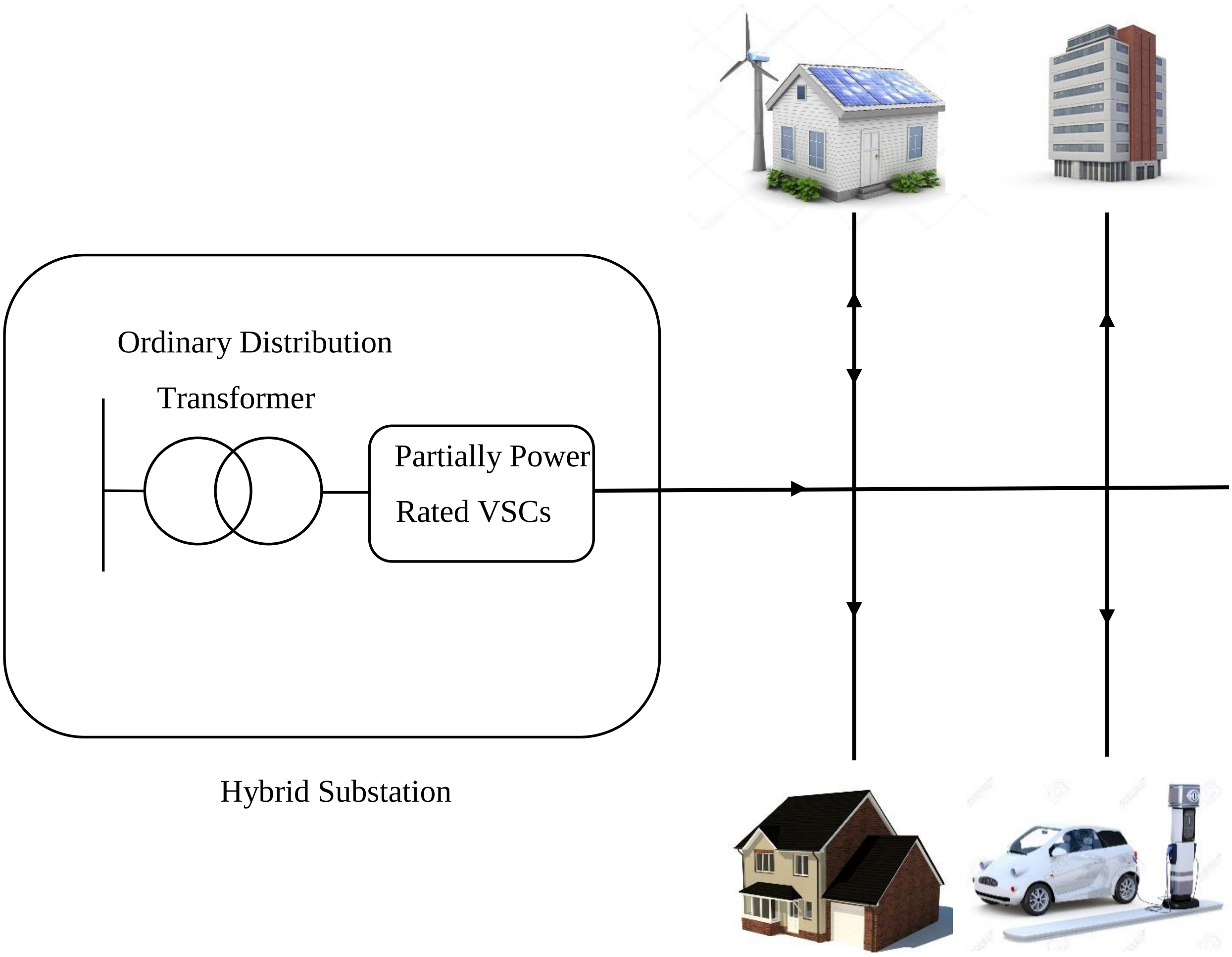

Figure 1.2: General configuration of hybrid substation connected to LV end-user customers.

1.2 Research Objectives

This PhD research project is aimed at investigating the power electronic-based solutions for voltage regulation purposes under the optimal conditions. The main objectives of the thesis are:

- Studying a meaningful set of probabilistic data concerning the time evolution of any type of load for any duration of time
- Optimising the substation voltage for any number of feeders based on the load probability
- Optimising the power rating of power electronics used in the LV distribution system for voltage regulation based on probability
- Research on power electronic-based solution for voltage regulation in LV distribution feeders and the substations
- Simulating the proposed hybrid substation for LV distribution network to investigate its voltage regulation performance
- Constructing the proposed power converter to validate the proposed voltage regulation approach

1.3 Thesis Outlines

The remainder of this thesis is divided into the following Chapters:

Chapter 2 provides a review to common electric power quality problems in LV distribution networks. Popular grid-connected power electronic voltage controllers are described in this chapter. This chapter also presents the hybrid substation.

Chapter 3 presents a powerful probabilistic analysis method to estimate probabilistic characterisation of the load pattern. A study has been carried out to estimate the optimised substation voltage. A new method has been introduced to find an optimal power rating of the proposed power electronic VSCs in order to minimise the injection voltage, cost and size of the system.

Chapter 4 gives a review of the state of the art, three-phase four-leg power electronic converters. This chapter presents a guideline for designing resonant controllers used in the grid-connected VSCs in addition to a detailed description of a 3-dimentional space vector modulation technique.

Chapter 5 presents an approach to calculate the required injection voltage of a hybrid substation based on the symmetrical components control algorithm. Simulation results of the effectiveness of the proposed controller for the hybrid substation are presented in this chapter.

Chapter 6 provides details for the power electronic converter design and its construction. A series-connected four-leg VSC is constructed to validate the voltage regulation capabilities of the power converter. The detailed structure of the control platform and its digital implementation are presented in this chapter.

Chapter 7 reports the results obtained from experimental power converter. The results are compared with simulation outcomes to verify the proposed control algorithm.

Chapter 8 presents the conclusion of the research and summarises the main contributions of the work followed by recommendations for future work in this field.

CHAPTER 2: Voltage Regulation in Low Voltage Distribution Systems

Summary: *This chapter provides a background to electric power quality problems in the distribution networks. It focuses on power electronic-based solution alternatives for voltage regulation purposes and introduces a power electronic solution, known as a hybrid substation.*

2.1 Introduction

Distribution systems performance and power quality are measured in terms of lack of restrictions from interruption, and maintenance of satisfactory voltage levels with a desired frequency, amplitude and phase at the customer's permitted voltage limits [12, 19]. The utilities' aim is to continuously provide their customer voltage within limits in distribution systems. In the UK, the utility suppliers are required to supply low voltage end-user customers within the voltage range which is 230V +10%, -6% [7]. However, due to power system variations under different load conditions and existence of unavoidable faults, utility suppliers do not guarantee to provide load voltage at an acceptable range.

The distribution voltages have to be within the restricted levels. Hence, since 1970 several alternative solutions for voltage quality issues have been considered [12]. There are numerous ways to keep distribution voltages within the desired levels. Some of the conventional possible solutions are [1]:

- Utilisation of generator voltage regulator
- Increasing the feeder conductor size
- Transferring loads to other substations and feeders
- Changing feeder sections from single phase to multi-phase
- Installing new substations, tap changers, autotransformers on primary feeders

The selection of a technique or techniques depend on the specific system requirements. However, the continued growth trend toward heavier load and high penetration of distribution generation units in low voltage rural distribution feeders may require power electronic-based solution alternatives, such as Voltage Source Converters (VSCs) for voltage regulation purposes. The advancements in integration of power electronics VSCs are now enabling major improvement in power reliability, compensation voltage range, load balancing, energy efficiency and cost effectiveness of electrical systems in distribution and generation networks [14, 15]. Some of the popular voltage regulation solutions based on power electronics for distribution substations are: Distribution Static Compensator (DSTATCOM) [20, 21], Dynamic Voltage Restorer (DVR) [22-24], Unified Power Quality Conditioner (UPFC) [25, 26], Interline Power Flow Controller (IPFC) [27], on-load tap changers [28] and the Solid State Transformer (SST) [29, 30].

This chapter presents a review of voltage control strategies for voltage regulation purposes in LV networks. The main focus of the chapter is on a novel power electronic solution called Hybrid Substation, which is based on a Hybrid Transformer (HT) [18, 31] used in multi-feeder LV systems.

2.2 Electric Power Quality

In general, there is no a standard definition for the term of 'electric power quality' that is acceptable by every electrical scholars. But referring to *Heydt* [5], electric power quality can be well-defined as ''the goodness of the electric power quality supply in terms of its voltage wave shape, its current wave shape, its frequency, its voltage regulation, as well as level of impulses, noise and the absence of momentary outages''. Power quality, like quality in other subjects and services, is difficult to evaluate. Nevertheless, end-user residential customers may define the power quality in terms of absence of any power quality disturbances, which may lead to unsatisfactory operation of end-user residential customers' equipment [1].

The power quality has a direct economic influence on consumers. Nowadays, automation systems and modern equipment used in industrial areas are much more sensitive to any disturbances or deviations in supply voltage. Thus, minor disturbances in the provided supply voltage can be costly for industrial customers. The electric power utilities are also concerned about power quality issues. It is important to exceed customer expectations and maintain the power quality at desired values. In recent years, the electric power utilities effort for providing good power quality is more important than ever; the loss of unhappy customers have a significant financial impact on utility companies.

In electrical engineering, power is the rate of energy transfer and depends on the voltage and current. In general, power suppliers can only control the voltage quality, and there is no control over the currents that particular loads might draw; thus for most power suppliers, the aim in the electric power quality area is to keep the voltage at permissible levels for end-user customers [3].

The common expression for defining the power quality in most electrical books and references is equivalent to voltage quality [3]. In the opinion of the author, the quality of the voltage has the most influence on power quality distribution systems and any significant disturbances or variations in voltage level, frequency or purity can cause a serious power quality problems for end-users customers. Therefore, it is necessary to have voltage controller for voltage regulation purposes. A brief description of possible common voltage disturbances in LV distribution systems will be described in the next section.

2.2.1 Voltage Sag

Referring to IEEE recommended practice for monitoring electric power quality [4], a voltage sag or dip can be considered as ‘‘a short-duration voltage variation category and is defined as a decrease between 0.1 to 0.9 per unit (p.u) in RMS voltage at the power frequency with a duration from 0.5 cycle to 1 minute”. Voltage sags or dips are usually related to system faults, but can also be caused by energization of heavy loads, starting large induction motors (which can draw six to ten times its full load current), and short-circuit faults in the distribution system [3]. Figure 2.1 (a) shows the simulation result of a 30% voltage sag; in this event the RMS voltage level decreases by 30% to 0.7 p.u.

2.2.2 Voltage Swell

A voltage swell is considered as a short-duration voltage variation category, and can be defined as ‘‘an increase of 1.1 to 1.8 p.u in RMS voltage at the power frequency for durations of 0.5 cycle to 1 minute” [4]. Similar to voltage sags, voltage swells usually arise because of system fault conditions, but they are not as common as voltage sags. Voltage swell can be caused by a temporary voltage rise on the un-faulted phases when a single line-to-ground fault occurs in one phase. Voltage swells can also be caused by switching off a large load, energising a large capacitor bank, unexpected load reduction insulation breakdown [3] or using heavy distribution generation sources in the distribution network. Figure 2.1 (b) illustrates the simulation result of a 30% voltage swell that might happen in LV distribution network.

The term short-duration overvoltage or momentary overvoltage as used by many researchers has the same meaning as the term voltage swell.

2.2.3 Voltage Interruptions

A voltage interruption occurs when the supply voltage decreases to less than 0.1 p.u and in the European standard EN 50160 [32] two definitions are used:

- Long interruptions: voltage interruptions longer than three minutes

- Short interruptions: voltage interruptions of up to three minutes

Voltage interruption can be classified into pre-arranged and unexpected (accidental) interruptions. Pre-arranged voltage interruptions happen in order to allow for the execution of scheduled work on the distribution system, when end-user customers are informed in advance. Unexpected or accidental interruption is caused by permanent (long interruption) or transient (short interruption) faults, mostly related to external events, equipment failures or interference [32]. Figure 2.1 (c) shows the simulation result of a short interruption at which the voltage drops to zero for 60ms.

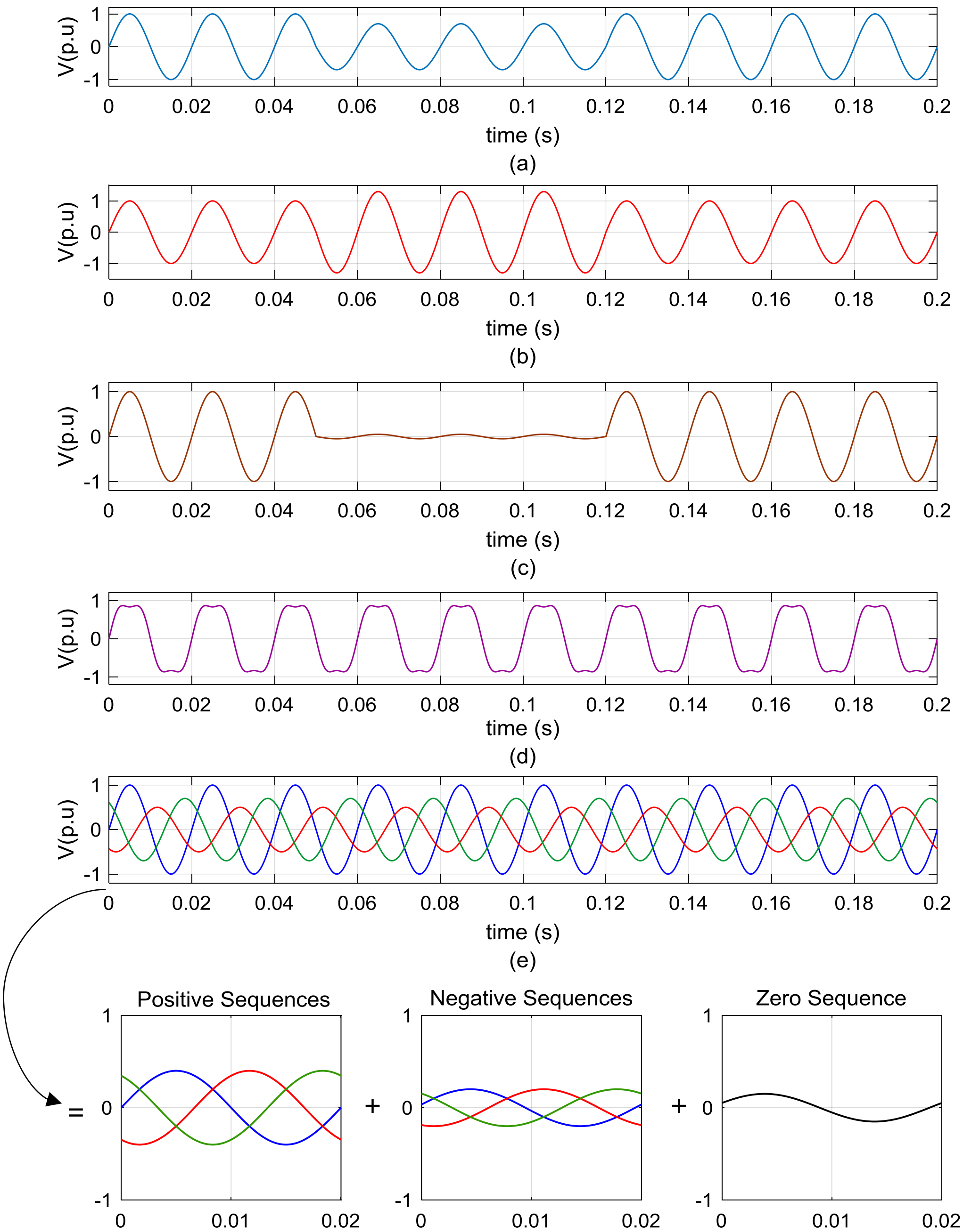

Figure 2.1: Simulation results of possible common voltage disturbances in LV networks, (a): voltage sag, (b): voltage swell, (c): voltage interruption, (d): voltage harmonics, (e): voltage unbalance.

2.2.4 Voltage Harmonics

Voltage harmonics are sinusoidal voltages having frequencies that are integer multiples of the fundamental frequency. Intermittently distorted signals can be decomposed into a sum of fundamental frequency and the harmonics. Voltage harmonic distortions usually come from non-linear characteristics of devices and loads in LV distribution systems [3]. Voltage distortion v_{dis} can be expressed by summation of the harmonic components v_h, according to:

$$v_{dis} = \sqrt{\sum_{h=2}^{\infty} v_h^2} \tag{2.1}$$

and for a fundamental phase voltage v_i for $i = a, b, c$, the total harmonic distortion (THD) in percent can be calculated by:

$$\%v_{THD} = \frac{v_{dis}}{v_i} \times 100 \tag{2.2}$$

Figure 2.1 (d) illustrates the simulation result of a distorted voltage waveform that might occur when non-linear load systems are presented in LV distribution network.

2.2.5 Voltage Unbalance

Voltage unbalance is a condition where the RMS value of the phase voltages or the phase angles between consecutive phases in three-phase system are not equal. This mostly happens when an unbalanced three-phase load is present in an LV distribution system. An unbalanced load can be caused by unevenly distributed single-phase loads or by a balanced three-phase load with a fault condition, such as a short-circuit fault. An unbalanced load might draw currents with positive, negative and zero sequences and this causes the undesired neutral current (zero sequence) to be circulated in the system. A solution to harness the neutral current will be explained in Chapter 4.

The voltage unbalance (sometimes called imbalance) can also be defined as the ratio of the magnitude of the negative sequence component to the magnitude of the positive sequence component, as shown below:

$$\%V_{unbalance} = \frac{|x_{neg}|}{|x_{pos}|} \times 100 \tag{2.3}$$

where for a phase group of variables in the abc frame x_a, x_b, x_c (voltage or current), the positive, negative and zero sequences can be expressed as [33]:

$$\begin{bmatrix} x_a^+ \\ x_b^+ \\ x_c^+ \end{bmatrix} = \frac{1}{3} \begin{bmatrix} 1 & a & a^2 \\ a^2 & 1 & a \\ a & a^2 & 1 \end{bmatrix} \begin{bmatrix} x_a \\ x_b \\ x_c \end{bmatrix} \tag{2.4}$$

$$\begin{bmatrix} x_a^- \\ x_b^- \\ x_c^- \end{bmatrix} = \frac{1}{3} \begin{bmatrix} 1 & a^2 & a \\ a & 1 & a^2 \\ a^2 & a & 1 \end{bmatrix} \begin{bmatrix} x_a \\ x_b \\ x_c \end{bmatrix} \tag{2.5}$$

$$\begin{bmatrix} x_a^0 \\ x_b^0 \\ x_c^0 \end{bmatrix} = \frac{1}{3} \begin{bmatrix} 1 & 1 & 1 \\ 1 & 1 & 1 \\ 1 & 1 & 1 \end{bmatrix} \begin{bmatrix} x_a \\ x_b \\ x_c \end{bmatrix} \tag{2.6}$$

where $a = e^{j\frac{2\pi}{3}}$ and $a^2 = e^{j\frac{4\pi}{3}}$. Typically the voltage unbalance of a three-phase service for 95% of the week is less than 3% , the current unbalance is usually higher especially when single phase loads are present in LV networks [32]. Figure 2.1 (e) shows the simulation result of a voltage unbalance situation where each phase voltage comprises positive, negative and zero sequences.

Although there are other voltage quality problems such as voltage spikes, noise, fluctuations, etc. [3], the mentioned short-duration voltage variations are the most common types of power quality problems in the LV distribution network.

2.3 Grid-Connected Voltage Controllers in LV Networks

Figure 2.2 shows a simple radial arrangement of a distribution network. Distribution substations deliver electric power from High Voltage (HV) to Medium Voltage (MV) primary substations and then from MV to LV secondary substations for LV customers. The voltage problems described previously might occur in distribution networks. These problems are the major concerns for both customers and utility power suppliers.

There are numerous types of voltage compensators that mitigate the undesired effects on both supplies and loads. As shown in Figure 2.3, there are two general groups of voltage compensators for LV networks. The most popular group of voltage compensators are electromagnetic devices based on a conventional transformer with mechanical or electronic tap changers. This method has been used for many years and voltage regulation typically depends on the action of the HV/MV primary substation tap changer transformer in addition to the appropriate transformer tap position of the MV/LV secondary substation [21]. Moreover, fixed tap positions are much more common in conventional LV distribution networks and to change the output voltage, the load should be disconnected from the network. Thus, this technique is not able to generate continuous output voltage and it has poor response to rapid voltage changes in LV networks [34, 35].

Another group of voltage compensators considered for improvement of voltage profile in LV feeders is based on power electronics and can be divided into four general categories: Mid-Feeder Compensator (MFC), Point of Load Compensator (POLC), Feeder Compensator (FC) and Power Electronic Substation (PES). Figure 2.4 shows the possible arrangements of power electronics used for voltage regulation in LV feeders. Figure 2.4 (a) can be used as a feeder regulator at the specific section of the feeder. POLC can regulate the voltage at affected customers independently as shown in Figure 2.4 (b). Fully electronic substation and FC can be illustrate in Figure 2.4 (c) and (d) respectively. Figure 2.4 (e) shows a feeder regulator in conjunction with a point of load compensator in order to regulate the voltage in both feeder and load. A more complete configuration of voltage regulator in LV networks can be found in Figure 2.4 (f) where a hybrid substation along with a POLC has been used. More details about hybrid substations will be explained in the following section of this chapter.

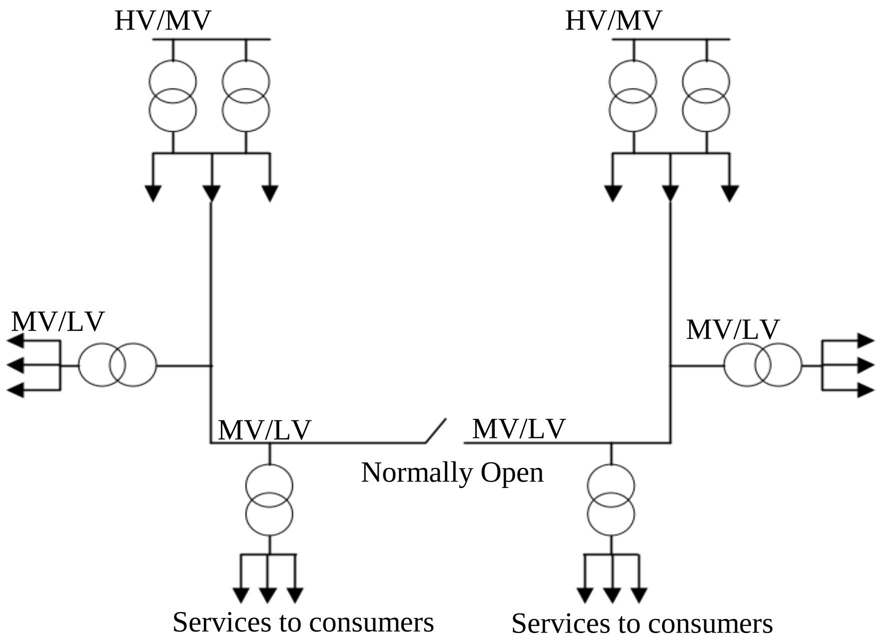

Figure 2.2: Simple arrangement of radial distribution network with normally open point for safety reasons.

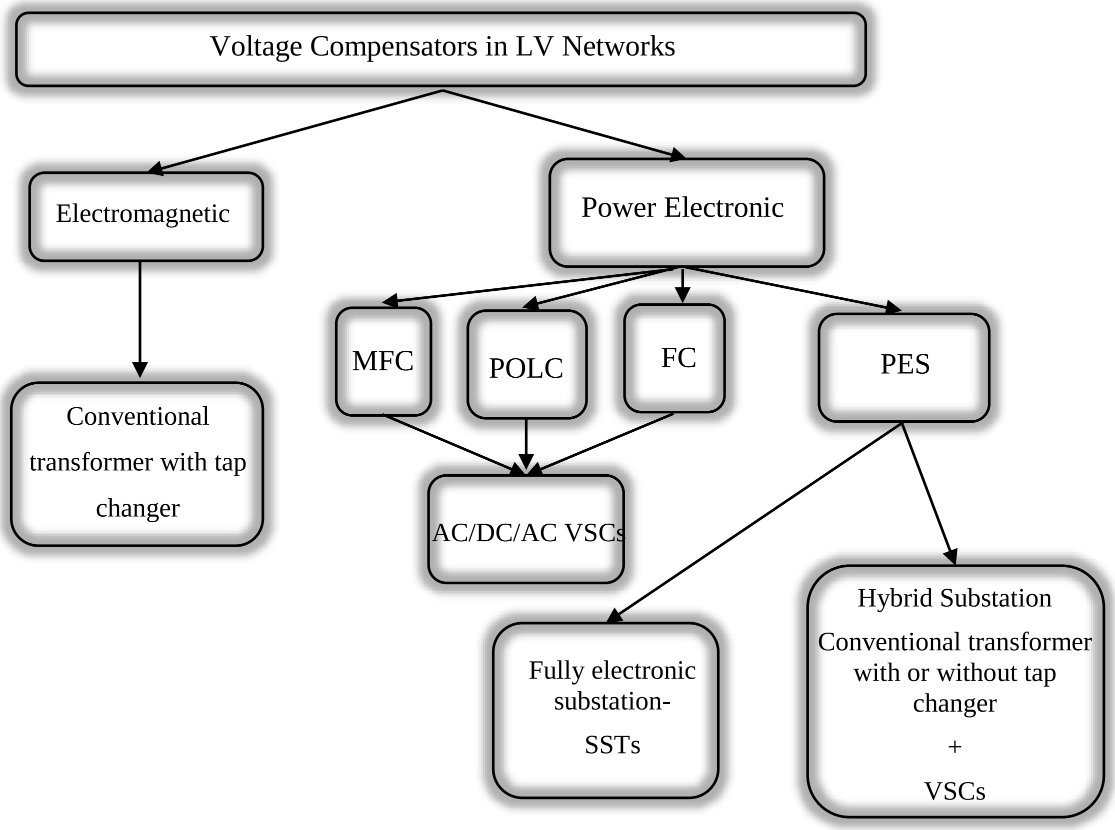

Figure 2.3: Various types of voltage compensators in LV networks.

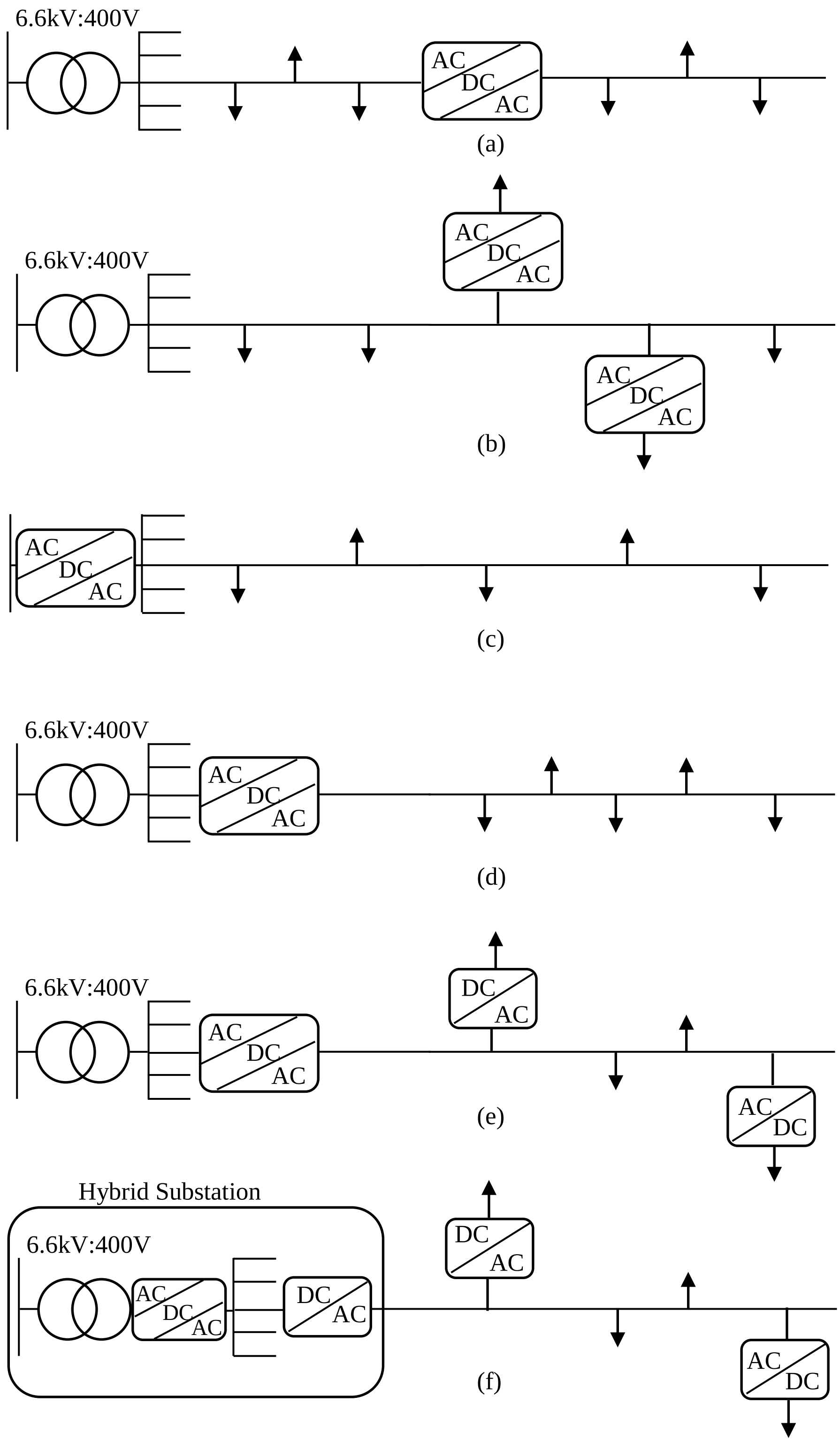

Figure 2.4: Power electronics voltage compensators in LV distribution networks, (a): mid-feeder compensator, (b): point of load compensator, (c): fully electronic substation, (d) feeder compensator, (e): feeder regulator with point of load compensator, (f): hybrid substation with point of load compensator.

The possible main elements of power electronic voltage controllers depicted in Figure 2.4 can be voltage source converters, which are the most common power electronic converters that are widely used for different applications, such as grid connected converters for voltage regulation purposes [7, 23-25], electric drives [26, 27], photovoltaic applications [28, 29], aerospace applications [30], matrix converters [30-32], etc. Figure 2.5 shows the standard two-level three-leg VSC which have been the subject of intensive research during the past decades. The basic operation and modulation strategies of the two-level three/four-leg VSCs will be explained in Chapter 4 of this thesis.

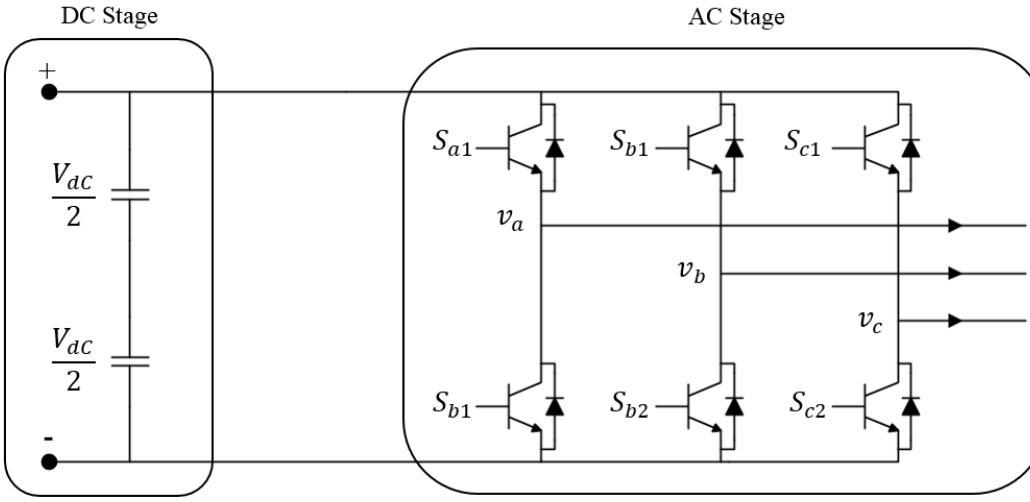

Figure 2.5: A standard two-level three-leg voltage source converter.

2.4 Power Electronic Voltage Compensators

Voltage regulation at distribution feeders can be effectively controlled by power electronic voltage controllers [34]. Power electronic based systems can enhance controllability and increase power transfer capability of the network [34, 36]. Flexible AC Transmission Systems (FACTS) [37] are based on power electronics and for voltage regulation purposes, this system can be classified into three independent sections: shunt-connected (Figure 2.6), series-connected (Figure 2.7) and shunt-series connected (Figure 2.8) voltage controllers.

2.4.1 Shunt Voltage Controllers

The concept of a shunt-connected VSC [12, 20, 21, 38-40] is to filter current harmonics, compensate reactive power and cancel small voltage fluctuations. A shunt-connected VSC can only compensate small voltage dips or swells, which can be controlled by injecting reactive power. In this case, the device has to inject current to the grid to change the voltage amplitude at the Point of Common Coupling (PCC). The ability to control the voltage depends on the impedance seen by the shunt-connected VSC and the power factor of the load [38]. If any high rating fault such as unsymmetrical faults occur, the impedance seen by VSC becomes very small and as the result of the device being in parallel with the system, a large current needs to be injected by the VSC to compensate the voltage [38]. This leads to having a high current rating device and a large energy storage. Therefore, this is not an ideal solution for a fully control voltage regulation purpose.

Distribution Static Compensators (DSTATCOMs) are the most common shunt-connected power electronics-based device that are used in distribution systems [41]. A DSTATCOM comprises a VSC, a DC energy storage device and a coupling transformer connected in shunt to the LV network. The basic configuration of DSTATCOM is shown in Figure 2.6.

However, not all shunt-connected voltage controllers are suitable for voltage regulation in LV feeders as the voltage drop changes over reactive power changes is proportional to line reactance $\left({}^{d\Delta V_d}/_{dQ} \propto L_s\right)$ [7]. For example, DSTATCOMs and reactive compensators are appropriate to use in high voltage networks where the ratio of ${}^{L_s}/_{R_s}$ is high (≥ 3). Nevertheless, this ratio is low in LV networks [7] and small changes in voltage can require a large reactive power, leading to an inefficient and expensive device in LV systems.

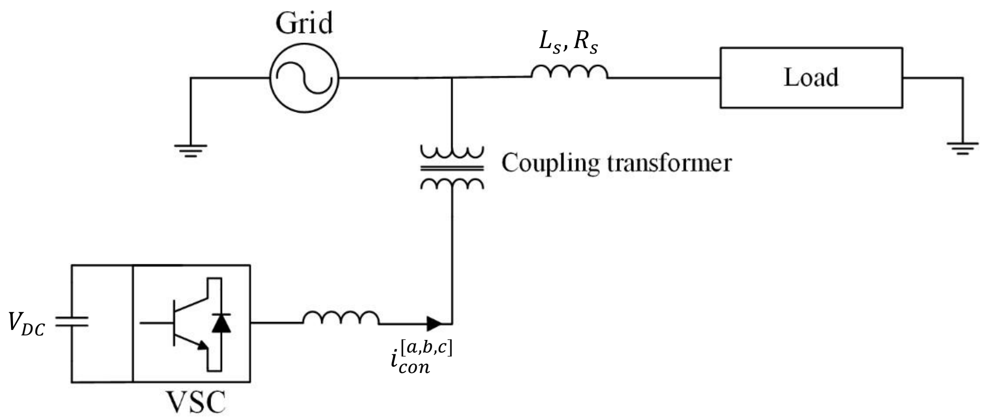

Figure 2.6: single-line diagram of DSTATCOM.

2.4.2 Series Voltage Controllers

A series-connected voltage controller [22, 23, 38, 42] consists of a VSC connected in series with distribution feeder by an injection transformer, as shown in Figure 2.7. The basic concept is to inject a voltage of desired amplitude, phase and frequency in order to regulate the load voltage. The most common series-connected VSCs are the Dynamic Voltage Restorer (DVR) [22-24] and the Static Synchronous Series Compensator (SSSC) [43, 44]. The main components of a series voltage controller are: a VSC, the filter, the injection transformer, and energy storage.

The device can inject desired voltage into the distribution feeder, therefore restoring the load voltage at the desired value v_{li} for $i = a, b, c$ during voltage disturbances. The series-connected VSC is connected to a DC energy storage element to convert DC voltage to controllable AC voltage. A voltage injection transformer is used to inject the voltage in addition to acting as a passive filter to improve harmonic voltage content generated by VSC. The voltage regulation capability of this device is based on the rating of the energy storage, the kVA rating of the VSC and injection transformer.

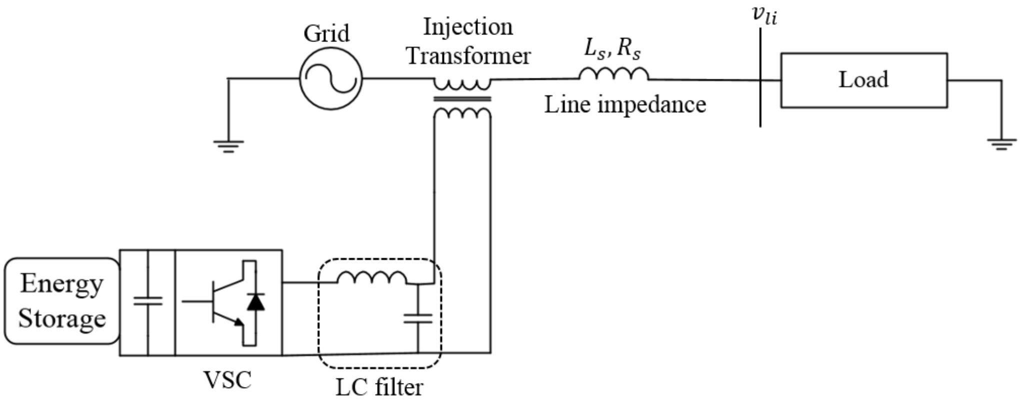

Figure 2.7: Single-line diagram of series-connected VSC (DVR).

2.4.3 Shunt-Series Voltage Controllers

A very flexible device can be obtained by combining the above-mentioned series and shunt-connected VSC controllers with a common DC link. UPS, UPFC and IPFC are the most popular shunt-series configurations [25, 26, 38, 45]. A shunt-series voltage controller, such as UPFC and IPFC is one of the most popular power electronic solutions that is used for mid feeder voltage regulation. The shunt-series VSC controller has the capability of regulating the voltage, as well as power factor correction and harmonic compensation in LV systems. Figure 2.8 illustrates the single-line diagram of shunt-series VSC controller.

The key features of this device are as follows:

- Two VSCs are connected with a common DC-link (energy storage), one connected in parallel and the other connected in series
- The main purpose of a shunt-connected VSC is to reduce harmonics by injecting current. The coupling isolation transformer is used to isolate the VSC from the network
- The main reason of having a series-connected VSC is to inject voltage to keep the load voltage, v_{li} for $i = a, b, c$ at the desired value
- A Low-Pass Filter (LPF) is used to eliminate high frequency ripples on the generated series-connected VSC output voltage

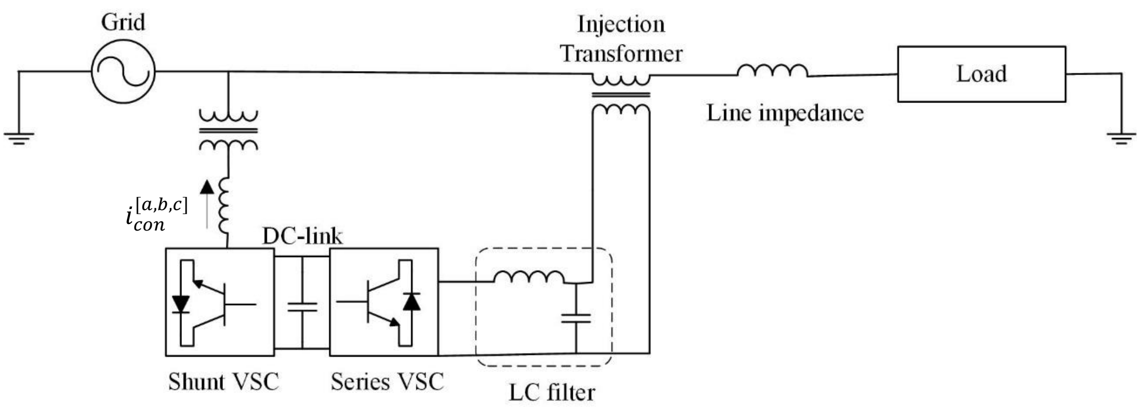

Figure 2.8: Single-line diagram of shunt-series connected VSC

2.5 Power Electronic Substation in LV Networks

The Power Electronic Substation (PES) for voltage regulation purposes has received a great attention globally in recent years [7, 18]. The main advantage of a PES is the ability to continually generate the desired output voltage for each feeder individually. The PES is appropriate for the LV distribution network and can be divided into two main categories:

- Fully electronic substations which are based on Solid State Transformer (SST)
- A combination of a line frequency transformer and a fractionally rated power electronic converter which together form a hybrid substation

The hybrid substation topology is the main subject of investigation for this thesis.

2.5.1 Fully Electronic Substation

Fully electronic substations and the electronic transformer for use in LV networks have received a great attention recently [7, 46, 47]. Figure 2.9 shows the general configuration. The key element of a fully electronic substation is the SST.

In recent years, the SST concept has generated a great deal of interest and has been investigated extensively for applications in power distribution systems. As shown in Figure 2.10, an SST comprises a high frequency transformer and provides with AC-AC conversion. Conversion between different systems is also possible, such as AC-DC, DC-DC, DC-AC and AC-AC with any appropriate frequency [46, 47].

The basic motivation of SST technology is to increase the voltage controllability in the network. This technology with three additional conversions can step the voltage down by a high frequency transformer and provide an acceptable performance and significantly decrease weight. The other main features are:

- Instantaneous voltage regulation for both AC and DC loads
- Maintaining unity power factor under reactive load condition
- Harmonic filtering
- Protection against unbalanced load
- Galvanic isolation
- Bidirectional power flow

However, the SST has some inherent drawbacks which has prevented the market penetration of this technology. Firstly, it is too costly in comparison to other technologies, thus it is a suitable option for specific fields and it is not a good solution to re-modify the technology of existing substations. Secondly, the total kVA rating of the power electronic switches is significantly high (fully rated power electronic converter), which leads to more losses in the system. Thirdly, usage of silicon devices and DC capacitors reduces reliability and life expectancy of such devices, making them an undesired option for some applications [18, 48, 49]. Finally, if an SST ceases functioning for any reason, it causes the serious problem of power transmission loss from the substation to the feeders.

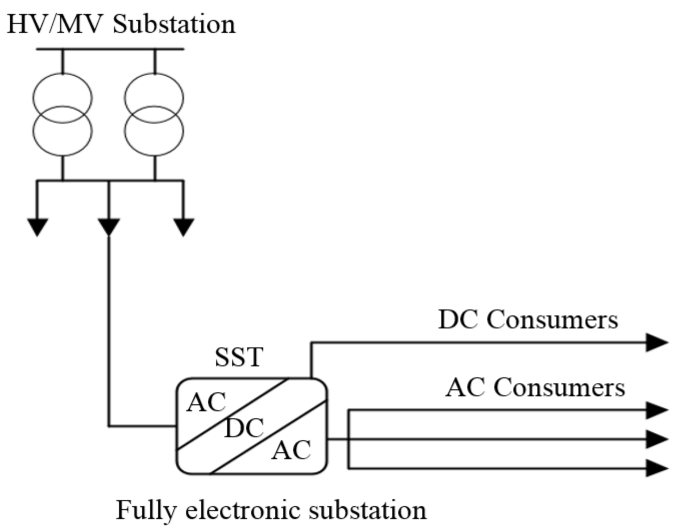

Figure 2.9: General configuration of fully electronic substation.

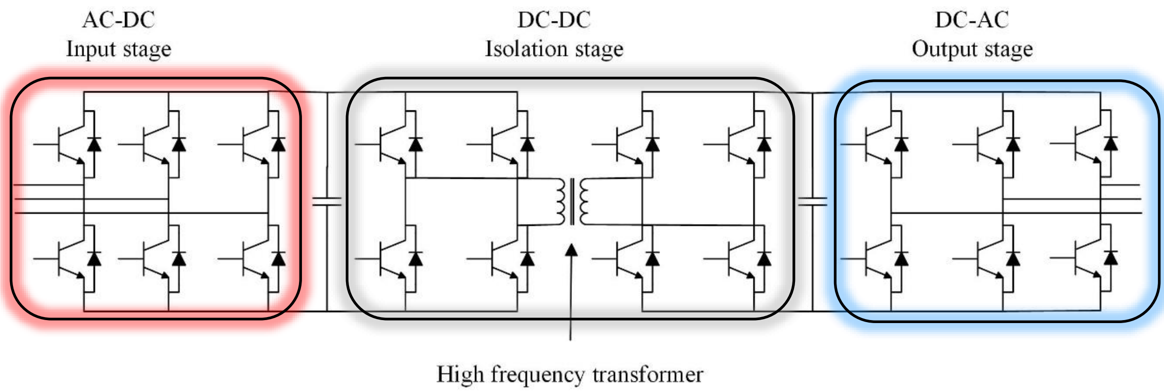

Figure 2.10: Circuit diagram of solid state transformer (SST) [18].

2.5.2 Hybrid Substation in LV Networks

The main component of a hybrid substation is a Hybrid Transformer [17, 18] which comprises fractionally rated power electronic VSCs with a conventional low frequency distribution transformer. The next section discusses possible arrangements for the hybrid transformer and its use in a hybrid substation.

2.5.2.1 Hybrid Transformer

The main concept of the distribution hybrid transformer was introduced by *Aeloiza et.al* [17] in 2003 and several alternative configurations have been presented by *Bala et.al* in [18]. The hybrid transformer is formed by augmenting a regular transformer with a fractionally rated power electronic VSC giving additional voltage control capabilities. The hybrid distribution transformer is able to continue functioning without the power electronic element and this configuration can be used for voltage regulation purposes in LV networks. In contrast, expensive SSTs are fully electronic and any failure in the silicon devices or gate drives, for example, can stop power transferring from the substation to the feeders and reduce the reliability of the system.

The fractionally rated power electronic converter allows the hybrid transformer to have various control capabilities depending on the configuration and operational requirements as shown in Figure 2.11. Selecting the ideal size of the fractionally rated power electronic VSC is based on the system requirements and load models. An optimised algorithm for finding the optimal power rating of the VSC [50, 51] will be described in Chapter 3 of this thesis.

As shown in Figure 2.11, similar to FACTS devices, the power electronic VSC can be connected in shunt, series and shunt-series with a conventional transformer. Not only can this smart configuration reduce the cost and overall size of the system, but it can also enhance the voltage regulation that can be retrofitted to existing LV substations. A key feature of the hybrid transformer is that the fractionally rated power electronic VSC can be completely bypassed in case of failure within the converter. In this case the transformer acts like an ordinary distribution transformer.

Each configuration of Figure 2.11 has its own merits. In configurations (A) and (B) a current can be injected into the HV or LV side of the transformer by using a shunt-connected VSC. As a result, these topologies have the ability to filter the unwanted harmonics and operate as a Power Factor Corrector (PFC). Configuration (A) also has an isolated DC-link which can be used as an energy store for DC loads. Alternatively, a voltage can be altered on the HV or LV side of the transformer with a series-connected VSC using configurations (C) and (D). Based on system requirement, the series injection transformer can adjust the power rating needed of the VSC (configuration (D)). For example, as the power losses in the IGBTs can be defined as a function of current [52, 53], adding a series injection transformer would contribute to reducing the total current rating of the VSC, as a result, the converter has lower power losses. The drawback of configurations (A), (B), (C) and (D) is that an extra energy storage is required.

By combining both shunt and series-connected VSC (configurations (E), (F), (G) and (H)), the above-mentioned advantages with extra phase shifting and voltage regulation controllability can be achieved. The shunt and series VSC are connected back-to-back to the same DC-link and the VSC can be energised by the secondary winding of the conventional transformer. As can be seen, configurations (E) and (F) have no injection transformer, therefore these two topologies deal with higher losses in comparison to configurations (G) and (H). In addition, configuration (F) might deal with higher current and voltage in comparison to configurations (E) as it is connected directly to the main output of the transformer (winding N_2).

It seems configurations (G) and (H) are the most promising options in terms of voltage regulation capabilities and total kVA rating. Configuration (H) has an advantage over (G) as the VSC of arrangement (H) is supplied from a separate winding N_3 of the conventional transformer, leading to a VSC based on the required voltage range capabilities, limits and kVA rating. Moreover, if the secondary winding N_3 of configuration (H) is protected separately from the conventional transformer, the VSC is isolated from the main output of the conventional transformer and if the converter stops working for any reason, it will not affect the main output voltage. A detailed description to find the optimum kVA rating of this configuration will be discussed in Chapter 3 of this thesis. The main notable features of arrangement (H) are summarised as follows:

- It has the most voltage regulation capabilities as it has a back-to-back VSC to generate instantaneous voltage with desired amplitude, frequency and phase for AC loads
- It has the ability to supply DC voltage from the DC-link for LV DC end-user customers especially for new and trending plug in electric vehicles by using the common DC-link
- It is supplied from a separate power source, secondary winding of the conventional transformer. If the secondary winding is separately protected, the VSC is isolated from the main output of the transformer
- This configuration has a series injection transformer to adjust the semiconductor ratings
- It has the ability to filter harmonics and operate as a power factor corrector
- It can operate properly for balanced, unbalanced, linear and non-linear load conditions if a suitable VSC such as a 4-leg VSCs are used

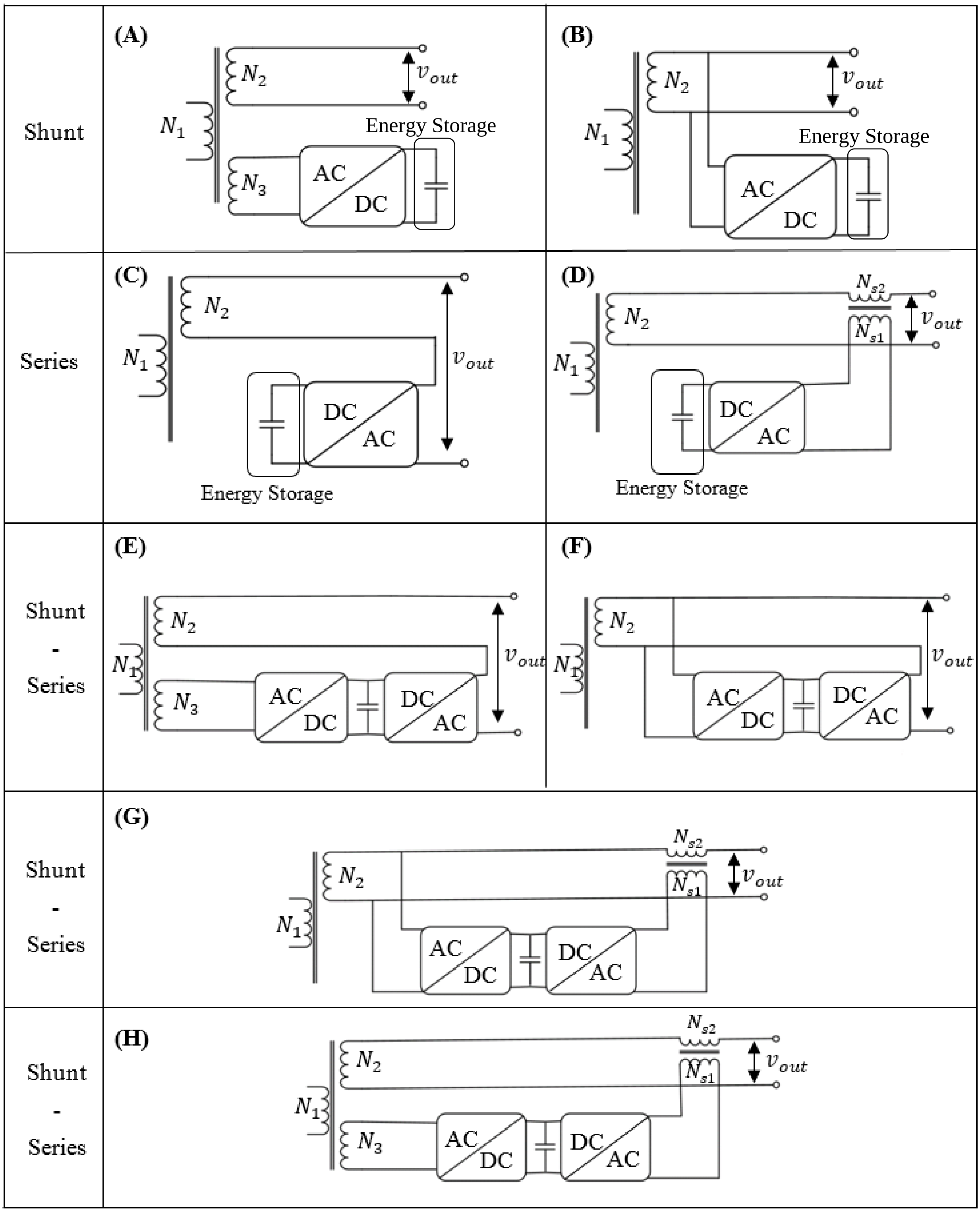

Figure 2.11: Different configuration of hybrid transformer.

2.5.3 Hybrid Substation

Figure 2.12 shows the general configuration of a hybrid substation. The principal component of the hybrid substation is the hybrid transformer (Figure 2.11 (H)). The hybrid transformer is connected to a multi-feeder network and each feeder at the substation-end (feeder starting point) comprises a DC-AC power converter (VSC_{fj}, j is the number of feeder, $j = 1, 2, \dots, \mathrm{n}$) in series with the feeder in order to compensate the voltage for any voltage disturbances in LV the network.

The hybrid transformer has a primary side (high voltage side) to receive input line-to-line voltage from a source $V_{l,i}$ for $i = a, b, c$ and a secondary side providing output voltage for LV distribution networks. The secondary side of the proposed transformer has two separate windings. The primary winding is the main source of the feeders V_{xi} for $i = a, b, c$ and the secondary winding is the source of the AC-DC VSC V_{yi} for $i = a, b, c$ of the hybrid transformer. A DC bus is created by an AC-DC converter and connected in parallel with all other VSCs attached to the feeders.

The proposed VSC for the hybrid transformer and feeders is a two-level four-leg converter (Figure 4.1 (b)). A four-leg VSC can effectively provide an extra connection (by fourth leg) and the neutral current in a three-phase system if the feeder is connected to unbalanced or non-linear load. The concept of the four-leg VSC and a complete review of its most important features such as modulation schemes and arrangement of switching patterns will be discussed on in Chapter 4 of this thesis.

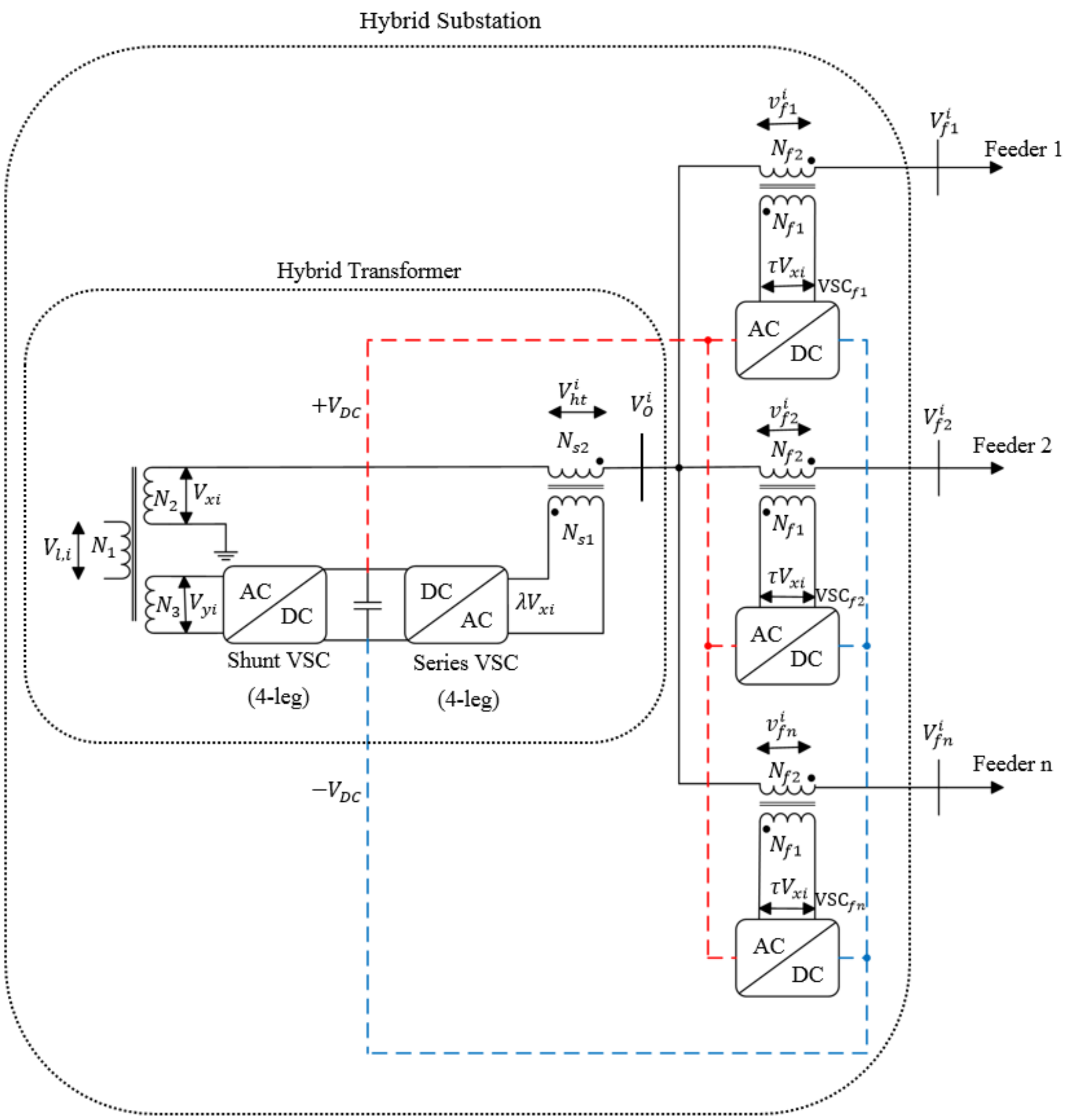

Figure 2.12: Configuration of multi-feeder hybrid substation.

From Figure 2.12 the phase voltages of the secondary winding of the conventional transformer can be expressed as:

$$V_{xi} = \frac{V_{l,i} N_2}{\sqrt{3} N_1} \tag{2.7}$$

$$V_{yi} = \frac{V_{l,i} N_3}{\sqrt{3} N_1} \tag{2.8}$$

where N_1, N_2 and N_3 are the turn ratio for primary and two separate secondary windings of the conventional transformer, respectively. The AC-DC VSC of the hybrid transformer is energised from V_{yi} and the output voltage of the DC-AC converter can be given by

λV_{xi}, where λ is a controllable voltage range. For simlpicity it is assumed that λ and V_{xi} are in phase and both represent the magnituude, $\lambda = |\lambda|e^{0j}$and $V_{xi} = |V_{xi}|e^{0j}$.

The injection voltage of the hybrid transfomer can be written as:

$$V_{ht}^{i} = \pm\lambda \frac{V_{xi} N_{s2}}{N_{s1}} \tag{2.9}$$

where N_{s1} and N_{s2} are the turns ratio of the injection transformer used in hybrid transformer. Now the output phase voltage of the hybrid transformer can be given by:

$$V_{o}^{i} = V_{xi} \pm V_{ht}^{i} = V_{xi}\left(1 \pm \lambda \frac{N_{s2}}{N_{s1}}\right) \tag{2.10}$$

From Figure 2.12, the output phase voltage of feeder 1 can be expressed as:

$$V_{f1}^{i} = V_{o}^{i} \pm v_{f1}^{i} = V_{xi}\left(1 \pm \lambda \frac{N_{s1}}{N_{s2}} \pm \tau \frac{N_{f2}}{N_{f1}}\right) \tag{2.11}$$

where N_{f1} and N_{f2} are the turns ratio of injection transfomer used in feeders and τ is a controllable votage range and it is in phase with λ . If $N_{s1} = N_{s2}$ and $N_{f1} = N_{f2}$

the total voltage controllability $V_{control}$ capability of the proposed system can be stated as:

$$\begin{cases} V_{control} = V_{xi}(1 \pm \lambda) & \text{Hybrid transformer} \\ V_{control} = V_{xi}(1 \pm \tau) & \text{Feeders' VSCs} \\ V_{control} = V_{xi}(1 \pm \lambda \pm \tau) & \text{Hybrid substaion} \end{cases} \tag{2.12}$$

As both back-to-back AC-AC converter and feeder DC-AC VSC$_{fj}$ for $j = 1,2,\dots,\text{π}$ are connected together, they have the ability to inject voltage at the same time ($V_{xi}(1 \pm \lambda \pm \tau)$). The way that the converters interact with each other, in addition to the amount of voltage required to be injected is totally dependant on a specific scenario which will be discussed in the next chapter. A powerful approach to minimising the injection voltage based on symmetrical components will be introduced in Chapter 5.

Choosing a suitable value of λ and τ is proportional to the size, cost and total kVA rating of the VSCs used in a hybrid substaion. Selecting appropriate values of λ and τ is quite a complex and difficult task as the design of VSCs is based on load models with no certain pattern or predicted behaviour. The next chapter of this thesis will introduce a novel iterative optimisation algorithm to identify a powerful probability model in order to find an optimum kVA rating of proposed VSCs in hybrid substation (optimum value of λ and τ).

2.6 Conclusion

Any voltage disturbances may lead to unacceptable operation and can be costly for both end-user customer and electrical utility in LV distribution systems. Therefore, it is necessary to maintain the voltage at satisfactory levels. In order to keep distribution load voltages within permissible levels, power electronic-based solution alternatives such as power electronic substations have gained attention for voltage regulation purposes.

The hybrid distribution transformer has the potential to be retrofitted to existing LV substations and so can be upgraded to meet the demand of the future electrical distribution grid. Each possible configuration of hybrid transformer (Figure 2.11) has its own merits, but using shunt-series connected VSC (Figure 2.11 (H)) could provide the greatest flexibility and robustness to faults. An important feature of the hybrid transformer is that the fractionally rated power electronic VSC can be completely bypassed in case of a fault within the converter; in this case the transformer acts like an ordinary distribution transformer. The hybrid transformer can be connected to a multi-feeder network where each feeder has a VSC with a common DC-link with hybrid transformer. This smart configuration which is named ‘hybrid substation’, can increase instantaneous voltage injection controllability and at the same time can reduce the switching losses and overall cost of the power electronic substation in comparison with fully electronic substations (SST).

CHAPTER 3: Power Rating of Power Converters Based on Load Probability in LV Networks

Summary: *This Chapter presents a powerful analysis method based on probabilistic statistics to evaluate the probabilistic load data concerning the time-evolution of any type of distribution load for any duration of time. In addition, a detailed description to find the required distribution power rating of power electronics under optimal conditions is provided.*

3.1 Introduction

Distribution system planning is essential to assure that the growing demand for electricity can be satisfied in an optimum way by using additional distribution substations. Distribution substations are designed based on the electrical utility data gathered historically [1]. As a result, the effect and importance of load characteristics have a direct influence on their distribution. The characterisation of load models is the main aspect in the distribution planning [1]. In recent years, the progress of load models has shifted the focus of electricity usage to the importance of evaluating the time-evolution of electricity utilisation [54]. The time-evolution estimation of different loads is a challenging task because the pattern is highly dependent upon the momentary activity profiles of consumers [55].

The size and cost of power electronics is proportional to their power rating. The power rating of converters used for the feeder voltage regulation is mainly based on the substation voltage and the feeder current which is influenced by the load models. The load models have no certain pattern or predicted behaviour due to the large range of data and changes in the energy consumption. The simplistic approach of summing up all potential loads would result in a massive over-sizing of the system. Therefore, in order to find the required distribution kVA rating of power electronics under optimal conditions, a powerful load analysis based on a probabilistic structure is required.

Several researches have been carried out to model the loads through different probability distributions. *Walker et al.* [56] have used the bottom-up method which is based on psychological considerations, electrical demographic and technical changes. The bottom-up method uses probabilistic procedures to combine the load profile of customers, for example, for each residence the load on an appliance is calculated during a specific period and the loads for all appliances are added together at the end. However, the data are selected for one day and it is not an appropriate method for the small/medium scale investigations because a successful social data analysis is mostly based on a larger scale of population.

In [16] the time-evolution of the aggregated residential load for a different number of customers is compared by various probability distributions. It is concluded that Gamma, Log-Normal and the Gaussian distributions are the most suitable methods for load modelling although the study was based on the data selected for one day only.

The Monte Carlo simulation is used in [55] and a detailed statistical study has been performed. The results show that the aggregated load data can be modelled by using a Gamma distribution with the best goodness-of-fit. However, one specific hour of a day is selected for this specific study. [57] introduces a method to estimate the customer load confidence intervals. The method was verified with the hourly load measurement data from the Finnish Load Research project and the author uses the Log-Normal distribution.

Singh et al. [58] concluded that there is no unique probability distribution technique to model the load. However, the Gaussian distribution seems to be a powerful method for modelling due to its simplicity as can be described by two parameters, mean and variance.

Other studies have been made to model the loads through various probability distributions [59-61].

Due to the complexity of the load profile, most electric distribution system planners used one specific day or hour of the year (in winter or summer) to obtain a comprehensive estimate of the load patterns for the aggregations of different types of loads. It seems the Gaussian distribution is useful for load modelling, but the single Gaussian distribution is not an effective method to model all type of loads due to its inherent limitations, such as its inaccurately and uncertainty for a larger data [58]. Different types of data distributions can be properly and accurately represented as a convex combination of several single Gaussian distributions with respective means and variances by the Gaussian Mixture Model (GMM) [58, 62-66]. In the opinion of the author, for a tested load profile, GMM can be used for the load modelling due to its powerful and accurate modelling.

The unknown mixture components such as weight, mean and variance of GMM can be estimated by a distribution parameter estimation algorithm, known as Expectation Maximisation (EM) [50, 65, 67]. This chapter introduces a new method to evaluate the probabilistic data concerning the time-evolution of any duration and comprises the following three main sections. The first section focuses on the mathematical procedures of estimating the parameters of GMM by applying the EM algorithm using an example of the EM algorithm for GMM fitting. In the second section, an overall load probability distribution curve for a generated load data over a year is simulated based on the mathematical methodology described in the first section. Third section introduces a new method to find an optimal hybrid substation voltage for a distribution system based on load statistics and probabilities in order to minimise the kVA power rating of the power electronics used for voltage regulation purposes in the LV distribution network.

3.2 Load Data

In the past, collecting the load data needed to evaluate the load pattern was a challenging task. Nowadays, due to the smart real-time metering, the real load patterns are available and all the data can be gathered for comparative assessments [3]. Utility companies supply electricity to a large number of consumers. These companies need to have an accurate prediction of electricity demand. Therefore, the load patterns of different type of consumers can be obtained from load measurements and this information can be used for distribution planning processes

For the purpose of this chapter, the yearly set of data based on CREST load model [68] for residential houses is used. Figure 3.1 provides an overview of the load data for 100 residential houses for the duration of one year. Each dot represents the total load demand for all 100 houses per minute. As can be seen, there is a large spread in values at each minute. This is due to changes in energy load consumption of the customers. The resolution of time scale of Figure 3.1 is in minute thus for one year, 525,600 dense data exist for the tested load profile.

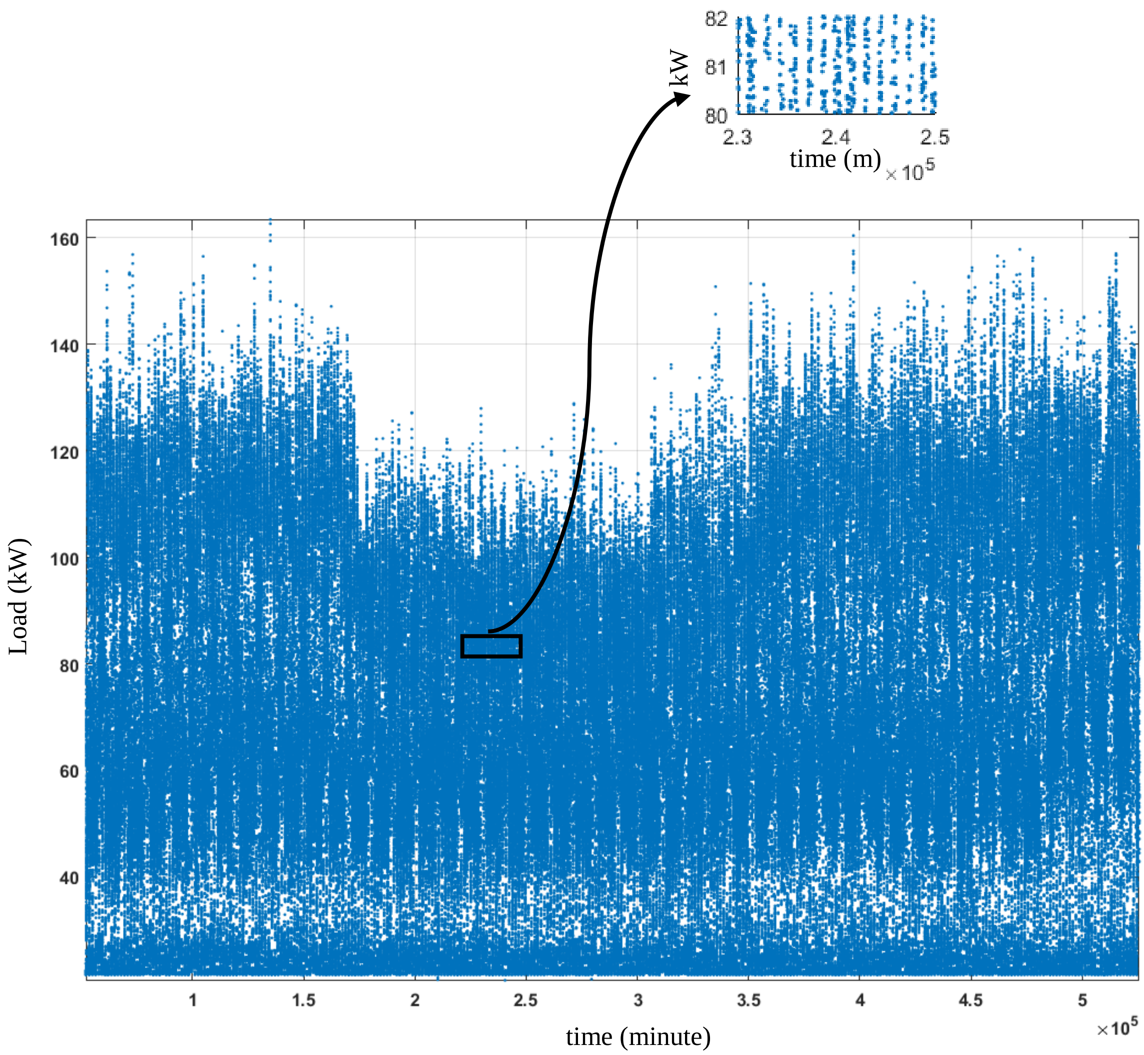

Figure 3.1: Yearly load profile of 100 residential houses (525,600 minutes).

3.3 Analysis Methodology

This section presents a powerful approach to the iterative computation of maximum-likelihood estimates when the observations can be noticed as a large set of data. Table 3.1 represents the key notation summary of the parameters used in the proposed algorithm.

Table 3.1: Notation summary.

Symbol	Description
$\mathcal{X}$	Random variable
$P(\mathcal{X}\|\mho_i)$	Probability density of $\mathcal{X}$ given $\mho_i$
$\mho_i$	Parameters to be estimated of i^{th} Gaussian component
$\mathcal{X} \in R^d$	d-dimensional random variable
T	Threshold, considered as 0.001 in simulation
${\mho_i}^{(m)}$	m^{th} estimate of $\mho_i$
δ_i	Standard deviation of i^{th} Gaussian component
$\sum_i$	Covariance of i^{th} Gaussian component
μ_i	Mean of i^{th} Gaussian component
w_i	Weight (size) of i^{th} Gaussian component
δ_i^2	Variance of i^{th} Gaussian component

3.3.1 Gaussian Mixture Model

GMM is one of the most powerful probability models and has been widely used in the fields of pattern recognition, information processing, tracking objects, image processing data mining, error correction codes, etc. [69]. GMM has the functionality to show a model representing one or several clusters, with each cluster being different from each other. The data points within the same cluster can be fitted properly by a Gaussian distribution [70, 71]. GMM is a beneficial technique that allows different types of load distributions to be presented as a combination of several Gaussian distributions with respective means and variances.

If samples $\mathcal{X}_1, \mathcal{X}_2, \ldots, \mathcal{X}_j \in R^d$ and random variable $\mathcal{X}$ is Gaussian, the i^{th} Gaussian probability function can be defined as follows:

$$P_i(\mathcal{X}|\mho_i) = \frac{w_i}{(2\pi)^{d/2}|\sum_i|^{1/2}} e^{\left(-\frac{1}{2}(\mathcal{X}-\mu_i)^T(\sum_i)^{-1}(\mathcal{X}-\mu_i)\right)} \tag{3.1}$$

For a GMM with $\mathcal{N}$ mixture components, the Gaussian probability function can be defined by making each of the i^{th} component a Gaussian density with mean μ_i and covariance $\sum_i$, as expressed by equation (3.2):

$$P(\mathcal{X}|\mho_i) = \sum_{i=1}^{\mathcal{N}} w_i P(\mathcal{X}|\,\mu_i, \textstyle\sum_i) \tag{3.2}$$

where $\mho_i = \{(w_i, \sum_i, \mu_i)\}_{i=1}^{\mathcal{N}}$ and w_i is the weight (size) of the i^{th} Gaussian component and ranges from 0 to 1, and their sum is equal to 1, 0≤ $w_i \leq 1$, $\sum_{i=1}^{\mathcal{N}} w_i = 1$.

It is worth noting that, covariance refers to the measure of how two random variables change and is used to calculate the correlation between variables, while variance refers to the spread of the data in relation to the mean. If a single continuous probability curve consisting of multiple Gaussian is the main concern, covariance is considered exactly the same as variance and d should be set to 1 in equation (3.1). By referring to equations (3.1) and (3.2), the one-dimensional Probability Density Function (PDF) for a single and $\mathcal{N}$ Gaussian components in respect to variance, mean and weight can be given by (3.3) and (3.4) respectively:

PDF for a single Gaussian:

$$P(\mathcal{X}|\delta^2,\mu) = \frac{1}{\sqrt{2\pi\delta^2}} e^{-\frac{(\mathcal{X}-\mu)^2}{2\delta^2}} \tag{3.3}$$

PDF for $\mathcal{N}$ Gaussian:

$$P(\mathcal{X}|\delta_i^2,\mu_i,w_i) = \sum_{i=1}^{\mathcal{N}} \frac{w_i}{\sqrt{2\pi\delta_i^2}} e^{-\frac{(\mathcal{X}-\mu_i)^2}{2\delta_i{}^2}} \tag{3.4}$$

However, the probability parameters such as weight, mean and variance (covariance) of GMM are unknown and difficult to find for a large spread of data. The next section will introduce an iterative method to find the maximum likelihood estimates of parameters in GMMs.

3.3.2 Expectation Maximisation Algorithm

The problem of estimating the parameters, such as mean μ and variance δ^2 for a set of random data like load that determines a mixture density, has been the subject of research for many years [67]. The Expectation Maximisation (EM) algorithm is one of the most complex and powerful methods of finding the maximum-likelihood estimate of the parameters of an underlying distribution from a given data set when the data is incomplete or has missing values [65, 72]. The EM algorithm has been widely used in genetics [67, 73] where the observed data is a function of the unknown gene pattern, econometric [74], signal processing [75] and sociological studies [76] in which unknown factors affect the outcomes. A complete list can be found in [67].

The EM algorithm consists of two major steps: an expectation step, followed by a maximisation step. The expectation step is with regard to the unknown parameters, using the current estimate of the parameters. The maximisation step is responsible for a new estimate of the parameters to update the model. More details about the EM algorithm can be found in [67, 72, 77, 78].

Estimating parameters for the Gaussian mixture model by using the EM algorithm can be summarised in 4 main steps as follows [65]:

Step 1: Initialization

The algorithm starts from some initial estimates of ${\mho_i}^{(m)}$ (e.g. random) where m^{th} iteration happens at the i^{th} Gaussian component. For example, the initial estimates of $w_i^{(0)}, \mu_i^{(0)}, \sum_i^{(0)}$ are chosen and for j^{th}sample fitted to i^{th} Gaussian component, the initial log-likelihood can be calculated by using equation (3.5):

$$\ell^{(0)} = \frac{1}{n}\sum_{j=1}^{n} \log(\sum_{i=1}^{\mathcal{N}} w_i^{(0)} P\left(\mathcal{X}_i \middle| \mu_i^{(0)}, \Sigma_i^{(0)}\right) \qquad (3.5)$$

Step 2: E-step

Computing $\gamma_{ij}^{(m)}$ which is the guess at the m^{th} iteration of the probability that the j^{th} sample belongs to the i^{th} Gaussian component. $\gamma_{ij}^{(m)}$ is the probability that belongs to the cluster i for all data points $\mathcal{X}_j$, $1 < j < n$ and all mixture components $1 < i < \mathcal{N}$:

$$\gamma_{ij}^{(m)} = \frac{w_i^{(m)} P\left(x_j \middle| \mu_i^{(m)}, \Sigma_i^{(m)}\right)}{\sum_{l=1}^{\mathcal{N}} w_l^{(m)} P\left(x_j \middle| \mu_l^{(m)}, \Sigma_l^{(m)}\right)} \qquad (3.6)$$

Step 3: M-step

For each cluster i, the mixture parameters are updated by using an estimate of the probabilities $\gamma_{ij}^{(m)}$(E step). Let us assume that the $n_i^{(m)}$ is the total number of guesses of cluster i at the m^{th} iteration:

$$n_i^{(m)} = \sum_{j=1}^{n} \gamma_{j\,i}^{(m)} \tag{3.7}$$

Now the weight (size) of the average data can be expressed by (3.8) as follows:

$$w_i^{(m+1)} = \frac{n_i^{(m)}}{n}\ , \quad i = 1, \dots, \mathcal{N} \tag{3.8}$$

Equation (3.8) is the new weight data point probabilities that is assigned to cluster i. The weighted mean which is the average of the data can be expressed by:

$$\mu_i^{(m+1)} = \frac{1}{n_i^{(m)}} \sum_{j=1}^{n} \gamma_{j\,i}^{(m)}\, \mathcal{X}_j\ , \qquad i = 1, \dots, \mathcal{N} \tag{3.9}$$

The new weighted covariance that is assigned to cluster i can be given by:

$$\Sigma_i^{(m+1)} = \frac{1}{n_i^{(m)}} \sum_{j=1}^{n} \gamma_{j\,i}^{(m)} \left(\mathcal{X}_j - \mu_i{}^{(m+1)}\right)^T \left(\mathcal{X}_j - \mu_i{}^{(m+1)}\right), \qquad i = 1, \dots, \mathcal{N} \tag{3.10}$$

where $w_i^{(m+1)}$, $\mu_i^{(m+1)}$ and $\Sigma_i^{(m+1)}$ are the weight (size), mean and covariance of i^{th} Gaussian component at the $(m+1)$ iteration, respectively.

Step 4: Convergence Check

By referring to equation (3.5) the new log-likelihood can be given by:

$$L^{(m+1)} = \frac{1}{n} \sum_{j=1}^{n} \log\left(\sum_{i=1}^{\mathcal{N}} w_i^{(m+1)} P\left(\mathcal{X}_i \middle| \mu_i^{(m+1)}, \Sigma_i^{(m+1)}\right)\right) \tag{3.11}$$

And then if $\left|L^{(m+1)}\right| > \left|L^{(m)}\right|$, the procedures return to step 2 otherwise the algorithm ends.

Figure 3.2 represents the general flowchart diagram of the described EM algorithm. By using EM algorithm, the unknown parameters of GMM for a real load data can be identified. More details about mathematics calculations and derivations of EM steps can be found in Appendix A.

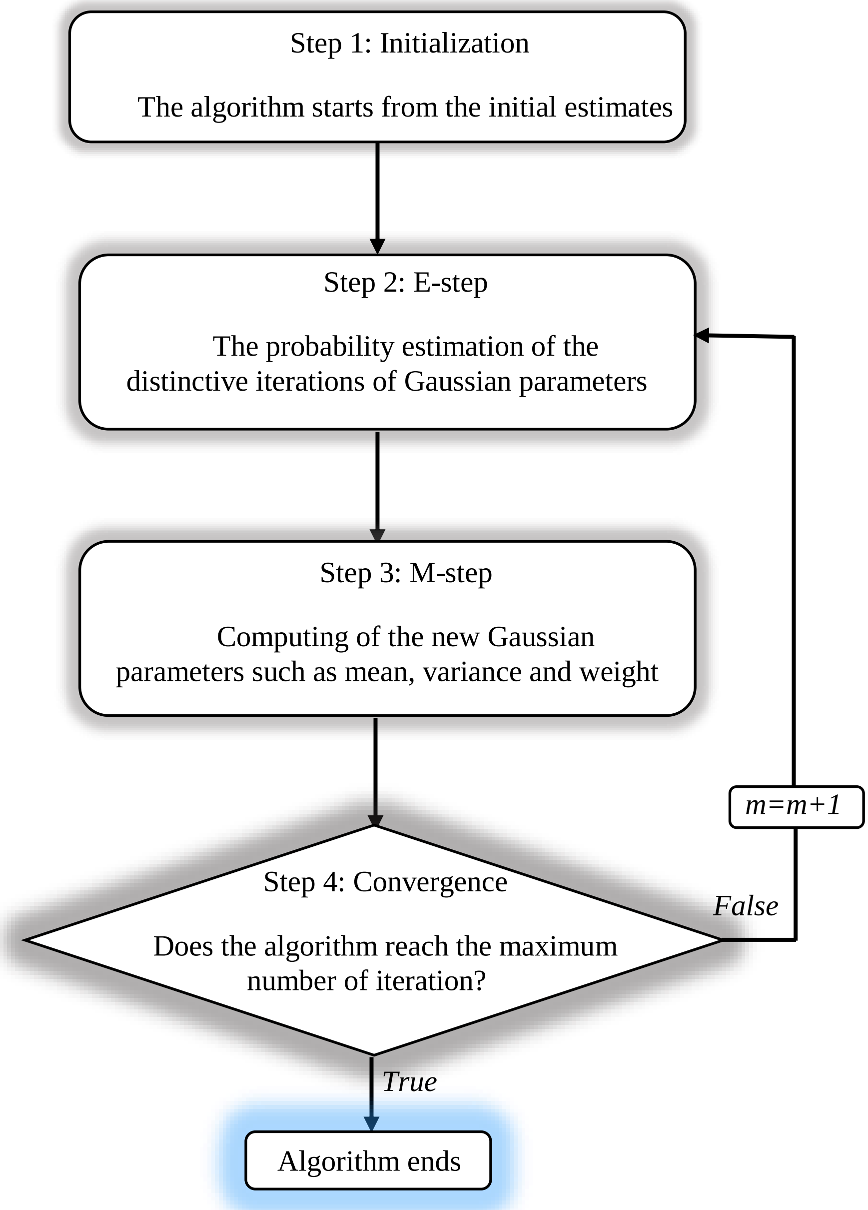

Figure 3.2: Flowchart diagram of EM algorithm steps.

3.4 EM Algorithm Estimating GMM Parameters

3.4.1 Simulation Study on Probability of Distribution Loads

To gain a better understanding of the EM algorithm for estimating the GMM parameters, a randomly synthetic dataset has been generated as shown in Figure 3.3 (a). This example shows how to create GMM from a mixture data set by using the EM algorithm. As discussed above, EM algorithm gets the parameters of the Gaussian distribution by creating sampling from the given set of data. Figure 3.3 (b) shows the estimated probability density contours obtained from EM steps. As can be seen, there are four general clusters (Gaussian distributions) A, B, C, D and each cluster represents a single Gaussian distribution containing several contours. As can be observed, the biggest cluster consists of two merged clusters, B and C due to the adjacent spread of the data. The centre of the smallest contour is the corresponding mixture component μ_i (peak of the Gaussian distribution curve), and the length of the largest contour of each cluster is approximately equal to $6\delta_i$ where δ_i is the standard deviation. EM algorithm can identify the clusters and calculate w_i, δ_i and μ_i of each cluster and create PDFs of individual Gaussian and GMM by using EM steps and then referring to equations (3.1)-(3.4), as stated before.

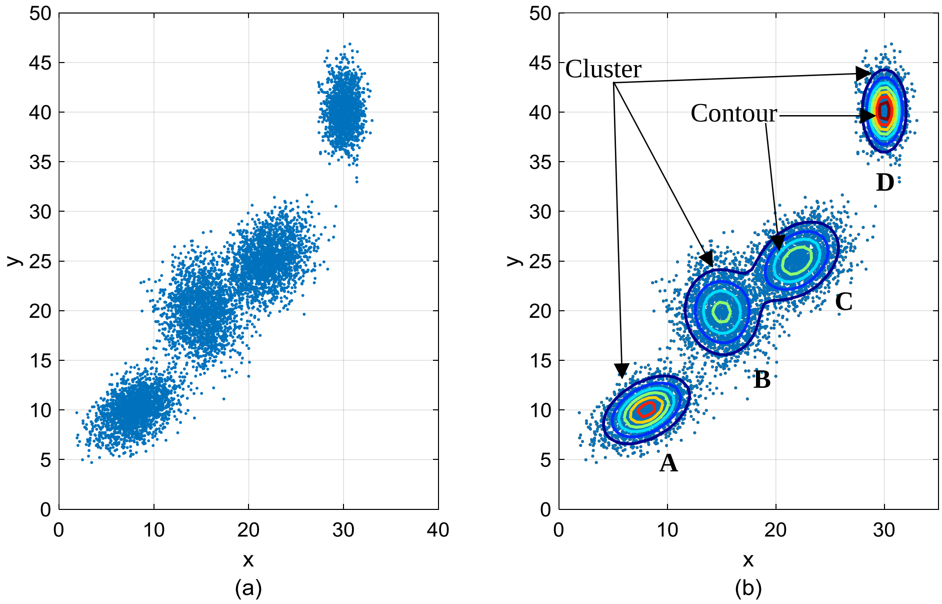

Figure 3.3: Synthetic dataset in which data are grouped in four clusters, a) synthetic dataset, b) estimated probability density contours.

Once the mixture components of the random data points are identified, the corresponded PDF of data can be obtained. In this case Figure 3.4 gives an overview of PDFs of individual and mixture Gaussians (GMM) of the data points obtained from previous steps shown in Figure 3.3. The one-dimensional density function curves of x-axis variable $P(\mathrm{x}|\mho_i)$ and y-axis variable $P(\mathrm{y}|\mho_i)$ are shown in Figure 3.4 (a) and (b), respectively. Figure 3.4 (c) shows the two-dimensional density function of the proposed data set.

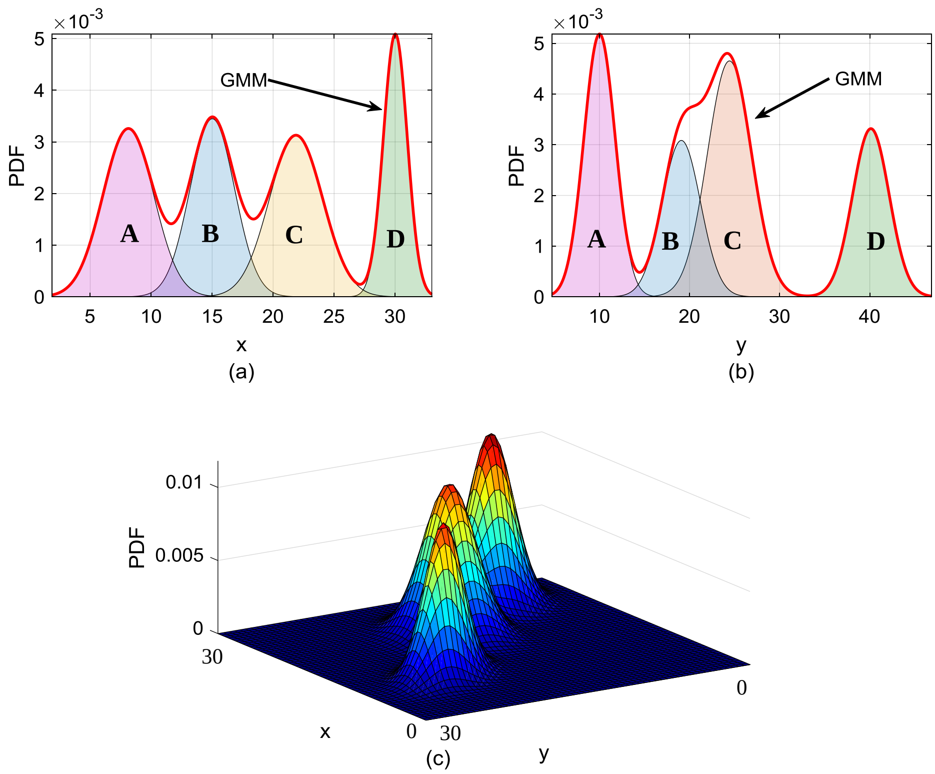

Figure 3.4: PDFs of individual and mixture Gaussian of the generated data.

Now let us refer to the yearly load profile of 100 residential houses (Figure 3.1). This section applies the same methodology described in previous sections but in a larger data spread. The study is carried out in two main stages: first the data points per minute of the load are extracted (Figure 3.1). In the second stage, the data extracted is then used in fitting GMM by the EM algorithm as described in subsection 3.3.2, to achieve the results shown in Figure 3.5. Figure 3.5 shows the estimated probability density clusters of the demand load over a year. Simulations use 200 clusters, which are extracted from the EM steps. Each cluster shown in Figure 3.5 contains several contours (similar to Figure 3.3

(b)) based on the density and propagation of the load data, which indicates the corresponding mixture components' mean μ_i, variance ${\delta_i}^2$ and weight w_i ($i = 1, \ldots, 200$). Now by having distribution parameters of each Gaussian component and referring to equations (3.1)-(3.4), the total load PDFs of the individual Gaussian and mixture Gaussian can be acquired and the result can be seen in Figure 3.6. and Figure 3.7.

Figure 3.6 shows the total GMM PDF of 100 residential houses over a year. The result presented is beneficial for showing a realistic set of probabilistic data, including time-evolution of load profile of one year. For example, load range of 20-27 kW has the highest weight and a small standard deviation. The small standard deviation means that the data points tend to be close to the mean. This means that the load demand is mostly happening around 23kW, which might represent the load demand from midnight to early morning at a specific time of the year for instance at autumn and winter. Figure 3.7 is the two-dimensional form of Figure 3.6. This Figure illustrates the probability distribution of various mixture components for the tested load data. Each surface is an overall density component comprises several component densities (200 Gaussian distributions in total).

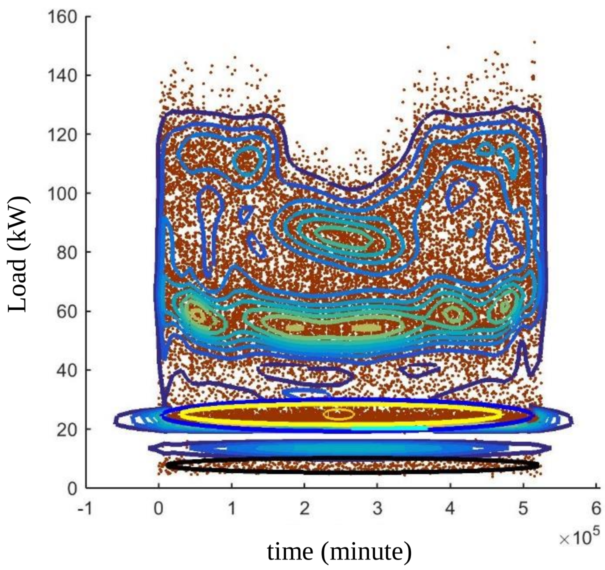

Figure 3.5: Estimated probability density clusters (200 clusters) of the load for 100 residential houses for one year

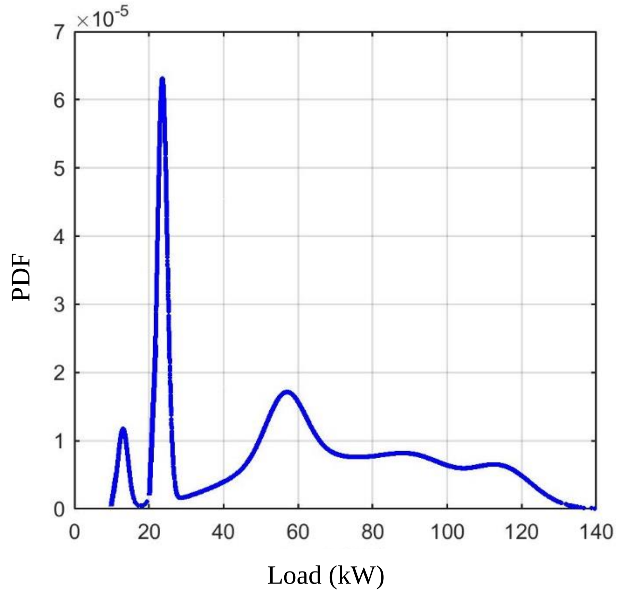

Figure 3.6: GMM PDFs of 100 residential houses yearly load demand by 200 single Gaussian distribution.

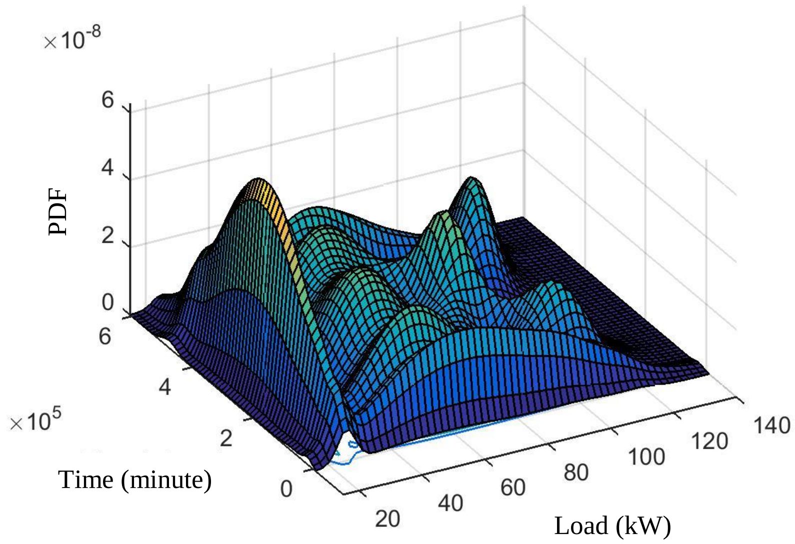

Figure 3.7: Two-dimensional GMM PDFs of 100 residential houses yearly load demand by 200 single Gaussian distribution.

3.4.2 Optimum Hybrid Substation Voltage Based on the Yearly Load Profile

As mentioned before, the size of the power electronics is mainly proportional to their power rating. The power rating of converters used for the feeder voltage regulation is mainly based on substation voltage and feeder current which is influenced by load models. The described method for load probabilities can be applied for estimating the optimum power rating of the VSCs used in the hybrid substations.

Figure 3.8 shows the basic configuration of the tested system. The hybrid substation is connected to 100 residential houses by feeder 1 through a 300m long and 300mm^2 cable. It is worth noting that the DC-AC VSC of the feeder has a common DC-link with the back-to-back AC-AC VSC of the hybrid transformer. The aim of using power electronics is to keep the load phase voltage $v_{L1,i}$ at the desired value, 230V, by injecting the lowest possible compensating voltage in series with the supply and feeder to regulate the load terminal voltage during voltage disturbances, such as sag and swell.

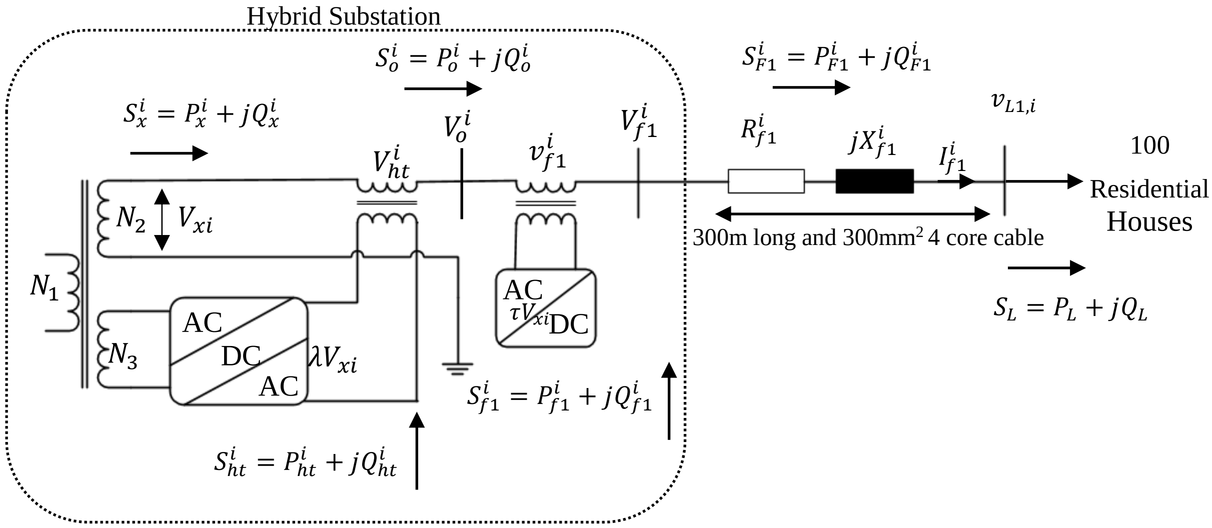

Figure 3.8: Schematic diagram of distribution hybrid substation connected to 100 residential houses.

By referring to Figure 3.8 and knowing that $V_o^i = |V_o^i| e^{j\theta_o^i}$, $V_{f1}^i = |V_{f1}^i| e^{j\theta_{f1}^i}$, $V_{ht}^i = |V_{ht}^i| e^{j\theta_{ht}^i}$ $v_{L1,i} = |V_{L1,i}| e^{j\theta_{L1,i}}$ and $S = VI^*$ the power flow calculations of the hybrid transformer can be given by (substation impedance is neglected):

$$S_{ht}^i = S_o^i - S_x^i$$
$$= V_o^i . \left(\frac{V_o^i - v_{L1}^i}{R_{f1}^i + jX_{f1}^i} \right)^* - V_{xi} . \left(\frac{V_{xi} - v_{L1}^i}{R_{f1}^i + jX_{f1}^i} \right)^* \tag{3.12}$$

And the power flow of the series VSC of the feeder can be expressed as:

$$S_{f1}^i = S_{F1}^i - S_o^i$$
$$= V_{f1}^i . \left(\frac{V_{f1}^i - v_{L1,i}}{R_{f1}^i + jX_{f1}^i} \right)^* - V_o^i . \left(\frac{V_o^i - v_{L1}^i}{R_{f1}^i + jX_{f1}^i} \right)^* \tag{3.13}$$

It is preferred to have a power converter to be switched off most of the time to minimise the power rating, losses and size of the power electronics. In order to approach this, the hybrid transformer voltage V_o^i should be kept at the optimum value. As a result, it is assumed that the feeder VSC is bypassed and $V_o^i = V_{f1}^i$. Thus, by referring to equation (3.12), the hybrid substation power flow and the voltage of feeder 1 can be written by (3.14) and (3.16), respectively:

$$S_o^i = S_L + \left(R_{f1}^i + jX_{f1}^i\right) . (I_{f1}^i)^2 \tag{3.14}$$

and

$$V_o^i = v_{L1,i} + \left(R_{f1}^i + jX_{f1}^i\right) . I_{f1}^i \tag{3.15}$$

where $I_{f1}^i = \frac{(S_{L1}^i)^*}{v_{L1,i}}$, the hybrid substation voltage can be re-written as:

$$V_o^i = v_{L1,i} + \left(R_{f1}^i + jX_{f1}^i\right) \frac{(S_{L1}^i)^*}{v_{L1,i}} \tag{3.16}$$

For carrying out the simulation, the yearly 100 residential load data mentioned on previous subsection is used, and the feeder reactance is neglected (reactance is neglected to reduce the complexity of calculations). The resolution of time scale is in minutes thus, for one year the tested load profile consists of 525,600 data points. It is assumed that for this load profile, the hybrid substation phase voltage (V_o^i) could have a range 230V< $V_{o,\mathcal{K}}^i$ < 270V with $\mathcal{K}$=1,…, 525600. Subsequently, for every minute of load demand in a whole year, one value of $V_{o,\mathcal{K}}^i$ is applied and the voltages at the load side of the feeder 1, $v_{L1,i}^{\mathcal{K}}$ are calculated using equation (3.16). The results can be seen in Table 3.2. Table 3.2 has 525,600×525,600 total set of data of which each column represents the load voltage values of a specific substation phase voltage at $V_{o,\mathcal{K}}^i$. As can be seen in Table 3.2, load voltage for each substation voltage varies every minute without any certain pattern. This can be due to a consumer dependant load type, their lifestyle, their family composition, number/type of electrical appliances, etc.

Table 3.2: Results of load phase voltages for every minute of load demand per different substation phase voltage (525,600×525,600).

$V_{o,i}^k$ / $V_{L1,i}^k$	$V_{o,1}^i$ 230(V)	. . .	$V_{o,150000}^i$ 239 (V)	. . .	$V_{o,300000}^i$ 252 (V)	. . .	$V_{o,525600}^i$ 270 (V)
$v_{L1,i}^1$	226	. . .	221.5	. . .	222.8	. . .	216.6
⋮	⋮	⋮	⋮	⋮	⋮	⋮	⋮
$v_{L1,i}^{150000}$	216	. . .	227.5	. . .	231.6	. . .	228.7
⋮	⋮	⋮	⋮	⋮	⋮	⋮	⋮
$v_{L1,i}^{300000}$	222	. . .	232.8	. . .	246.3	. . .	240.8
⋮	⋮	⋮	⋮	⋮	⋮	⋮	⋮
$v_{L1,i}^{525600}$	216	. . .	230	. . .	241	. . .	238.8

525,600 data

525,600 data

To gain a better understating of the EM algorithm for estimating GMM parameters, one random $V_{o,\mathcal{K}}^{i}$ at 239V ($V_{o,150000}^{i}$) has been used. The unknown GMM parameters of load voltages of the 150,000th column in Table 3.2 are obtained by using the EM algorithm. As discussed above, the EM algorithm receives the parameters of the Gaussian distribution by creating sampling from the given set of data. Figure 3.9 shows the estimated probability density cluster obtained from the EM steps when the substation phase voltage is selected to be 239V.

The scattered data points of Figure 3.9 represent the load phase voltage for every minute when substation voltage is selected at 239V. As can be seen, there is a set of load voltage data (scatter data) per cluster and each cluster represents a single Gaussian distribution containing several contours. The centre of the smallest contour of each cluster is the corresponding mixture component μ_i (peak of the Gaussian distribution curve), and the length of the largest contour of each cluster is approximately equal to $6\delta_i$.

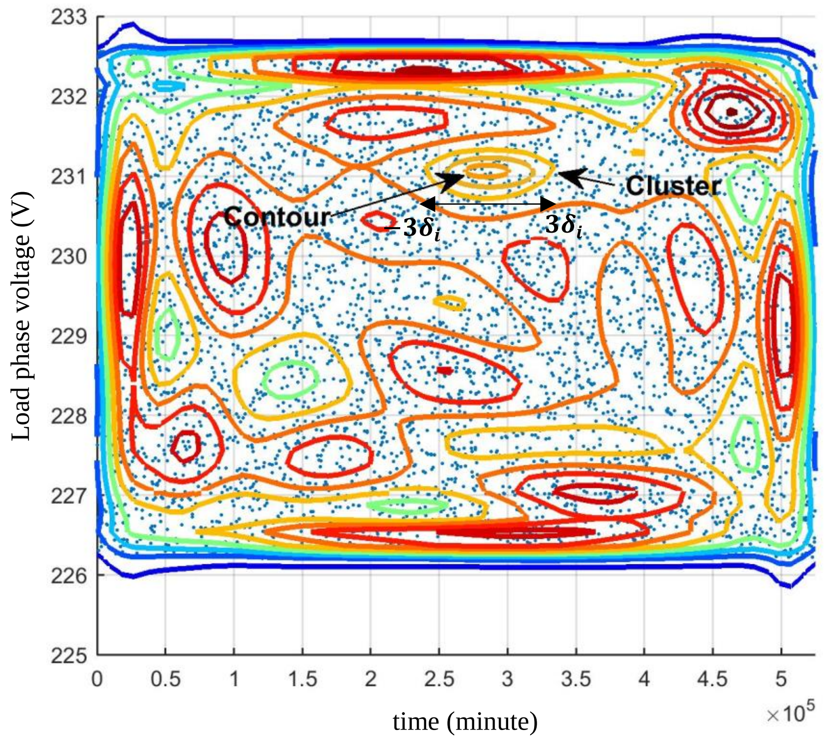

Figure 3.9: Estimated probability density clusters of yearly load voltages for $V_o^i = 239\ V$.

Now by having distribution parameters of each Gaussian component and referring to equations (3.1)-(3.4), the 2-dimentional and 1-dimensional load voltage PDFs of individual Gaussians and mixture Gaussians of the substation at 239V for the whole year can be acquired, and the result can be seen in Figure 3.10.

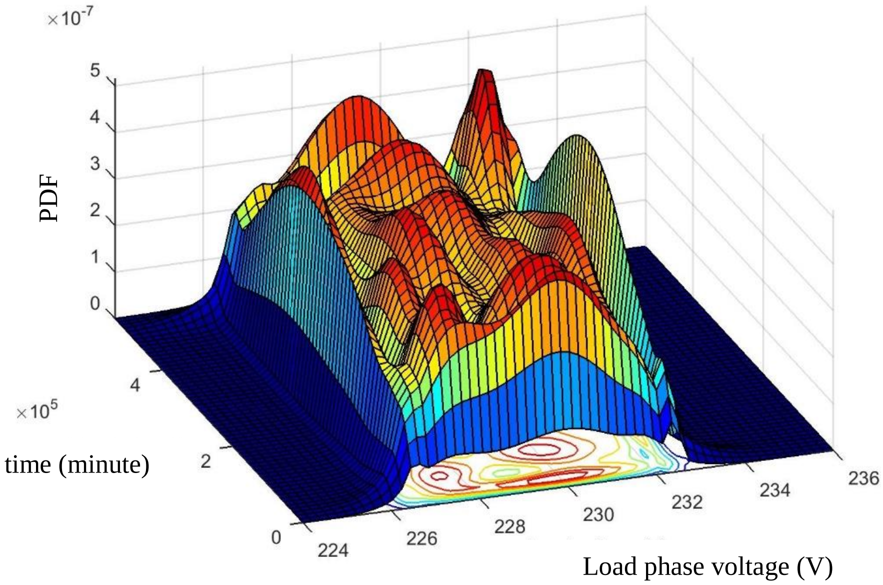

(a)

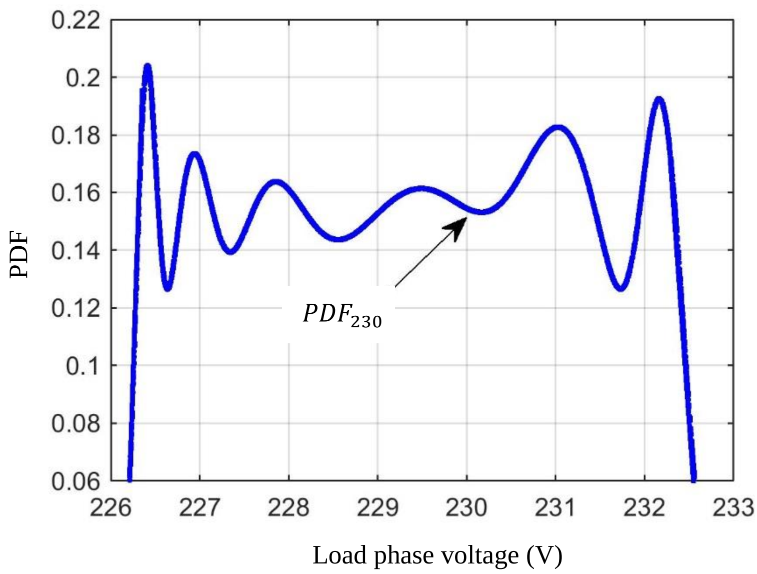

(b)

Figure 3.10: GMM PDFs of yearly load phase voltages for $V_o^i = 239\ V$. a) 2-dimensional GMM PDFs, b) 1-dimensional GMM PDFs.

Each surface of Figure 3.10 (a) represents an overall density component consisting of several component densities (200 Gaussian distributions in total). In addition, at each selected substation voltage ($V_{o,\mathcal{K}}^{i}$), for the duration of the whole year, the load voltage might have a PDF value at 230V, which in this thesis is referred to as PDF_{230} (230V is the desired load voltage). For example, as shown in Figure 3.10 (b), when the substation voltage is selected at 239V, the overall GMM of load voltages has a PDF value at 230 V.

Now by creating the PDF graphs of each individual Gaussian and GMM of each column of Table 3.2, 525,600 GMM PDFs (similar to Figure 3.10) for all hybrid substation voltages ($V_{o,\mathcal{K}}^{i}$) can be made. This leads to finding the PDF_{230} value of every column of Table 3.2 (if available). The final result of all PDF_{230} values per corresponding available $V_{o,\mathcal{K}}^{i}$ figures can be seen in Figure 3.11. The most probable range for PDF_{230} for this type of load is $232\text{V} < V_{o,\mathcal{K}}^{i} < 257\text{V}$ with the most optimum point being at 242.5V. Outside of this range, there is no probability for the load voltage to be at 230V. This finding leads to the conclusion that for a feeder attached to 100 residential houses with a 300m and 300 mm^2 cable, if the substation voltage is selected to be $V_{o,optimum}^{i} = 242.5\,V$ ($V_{o,164000}^{i}$), the load phase voltage will be kept at the optimum voltage of 230V most of the time. In this case, it is assumed that the substation is connected to one feeder only (feeder 1), hence $V_{o,optimum}^{i} = V_{f1}^{i}$. This leads lower kVA power rating of the power converters used for the voltage regulation in LV networks, which is explained in the next section of this chapter.

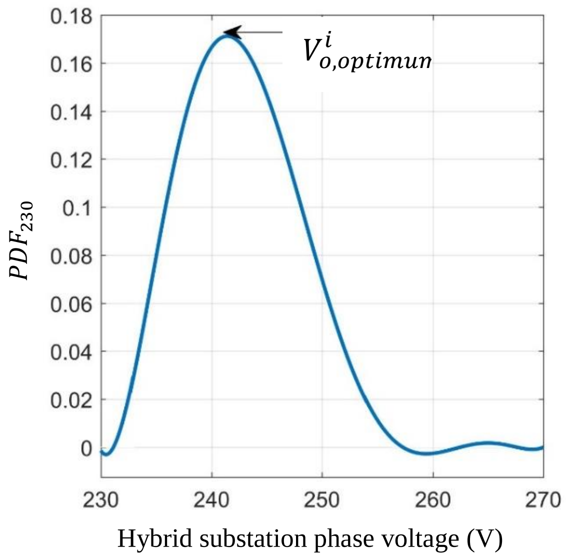

Figure 3.11: Calculated PDF_{230} for different substation phase voltages, $V_{o,optimum}^{i} = 242.5V$.

3.4.3 The Optimum Voltage Source Converter Power Rating for One Feeder

In order to assess the feasibility of the previous section, the chosen $V_{o,optimum}^{i}$ (242.5V) is used for the system to determine the probability density of the converter power rating based on the tested load. The maximum power rating of the power electronic converters is given as the maximum active power demand of the series power converter, [79, 80], therefore $S_{ht}^{i} = \max\left|P_{ht}^{i}\right|$. By referring to equation (3.12) and with the assumption that the feeder and the converter current is equal and no power is injected by the feeder VSC, the power injected by the series-connected power converter of the hybrid transformer into the system per substation voltage, can be expressed as:

$$\begin{aligned} P_{ht,\mathcal{K}}^{i} &= P_{F1,\mathcal{K}}^{i} - P_{x,\mathcal{K}}^{i} \\ &= \mathrm{Re}\left(V_{f1,\mathcal{K}}^{i}.I_{f1,\mathcal{K}}^{i}\right) - \mathrm{Re}\left(V_{o,\mathcal{K}}^{i}.I_{f1,\mathcal{K}}^{i}\right) \end{aligned} \tag{3.17}$$

where $P_{ht,\mathcal{K}}^{i}$ is the required injected power for every minute ($\mathcal{K} = 1, 2, \dots, 525600$) to keep each individual feeder phase of $i = a, b, c$ load voltage at 230V.

The total injected power of the converter for the whole year of the tested feeder can be written as:

$$P_{ht}^{i}(total) = \sum_{\mathcal{K}=1}^{525600} P_{ht,\mathcal{K}}^{i} \tag{3.18}$$

By using equation (3.18), the results of the power converter injection for 10 random substation voltages including the optimum voltage ($V_{o,optimum}^{i}$) can be given in Table 3.3. Table 3.3 shows that the selected optimum hybrid substation voltage ($V_{o,optimum}^{i} = 242.5\ V$) has the lowest amount of total injected power for the whole year. Consequently, for the tested 100 residential houses, choosing V_{o}^{i} at 242.5V allows the converter to operate at its lowest average power rating at which it produces the most efficient power electronic design with lower losses and size.

Table 3.3: Total power injection of hybrid transformer VSC per different $V^{i}_{o,\mathcal{K}}$ for the whole year

$V^{k}_{o,i}$ / $P^{\mathrm{M}}_{ht,i}$	$V^{i}_{o,1}$ 230 (V)	$V^{i}_{o,50000}$ 233.7 (V)	$V^{i}_{o,100000}$ 237.6 (V)	$V^{i}_{o,164000}$ 242.5 (V)	$V^{i}_{o,200000}$ 245.2 (V)	$V^{i}_{o,250000}$ 249.1 (V)	$V^{i}_{o,300000}$ 252.8 (V)	$V^{i}_{o,350000}$ 256.6 (V)	$V^{i}_{o,400000}$ 260.4 (V)	$V^{i}_{o,525600}$ 270 (V)
$P^{i}_{ht,1}$(kVA)	0.1	0.25	0.35	0.67	0.88	1.2	1.47	1.6	1.9	2.6
⋮	⋮	⋮	⋮	⋮	⋮	⋮	⋮	⋮	⋮	⋮
$P^{i}_{ht,250000}$(kVA)	6.1	4.6	3	1.2	1.4	1.7	3.2	4	5	6
⋮	⋮	⋮	⋮	⋮	⋮	⋮	⋮	⋮	⋮	⋮
$P^{i}_{ht,525600}$(kVA)	3.1	2	0.9	0.3	1.2	2.6	3.5	4.3	5.5	8.3
$\boldsymbol{P^{i}_{ht}(total)}$**(MVA)**	**18**	**13**	**8.6**	**5.9**	**6.2**	**9.1**	**14**	**19**	**24**	**38**

The PDF and Cumulative Distribution Function (CDF) of the power converter with respect to the optimum substation voltage for 100 residential houses with 300 m, 300 mm^2 cable over a year can be found and the results are plotted Figure 3.12. As can be observed in Figure 3.12 (a), the mode of the converter's power rating is around 1kVA (peak value of the PDF plot). In the statistical concept, the mode of set of data values is the value that happens most often. As a result, 1kVA is the value that the power converter is operating for the most of the year. It is worth noting that 1kVA is not the average power rating of the converter, and for this specific example the average kVA rating for the whole year is around 2.5kVA. Furthermore, as can be seen in Figure 3.12 (b), a power converter with 4.6kVA power rating can satisfy the load voltage to be kept at 230V at 90% of the time in a year, and a power converter with 6.5kVA power rating can guarantee the load voltage satisfaction for 99% of the time.

It is worth noting that the calculations are based on the assumption that the load voltage is kept exactly at 230V. However, as discussed earlier, in the UK, the regulatory voltage levels are 230V, +10%-6%. Therefore, even a lower kVA rating can be chosen for the converter. Furthermore, some variables such as population growth, geographical factors, community development plans and substation fault, might affect the total power rating of the converters. As a result, the power network planner should take the mentioned variable factors into account by increasing the total kVA rating of the power converters by considering a suitable safety factor.

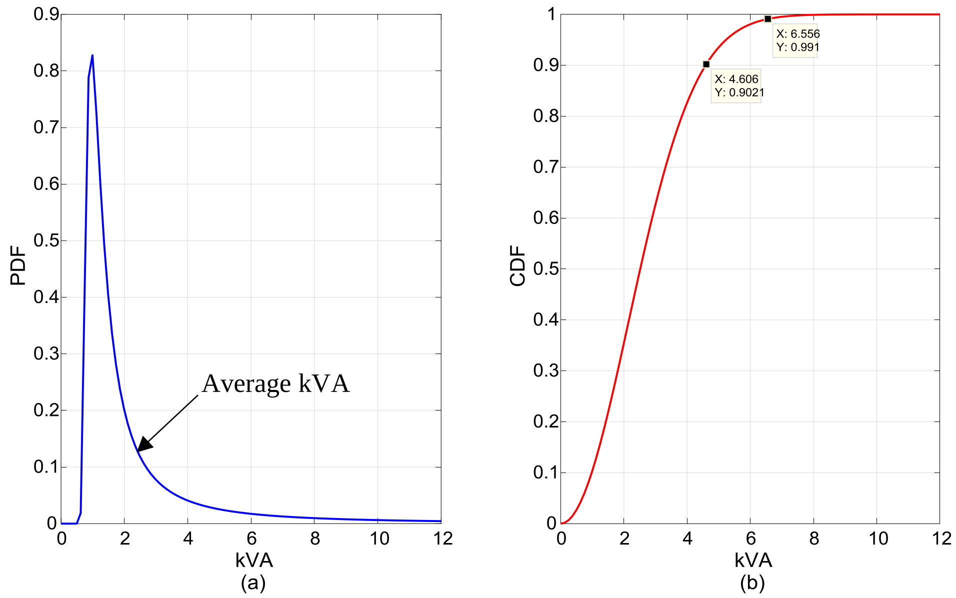

Figure 3.12: PDF and CDF of converter kVA rating at $V^{i}_{o,optimum} = 242.5V$ for 100 residential houses.

3.4.4 The Optimum Voltage Source Converter Power Rating for Multi-Feeder Network

In this section, more complex test scenarios will be investigated. It is assumed that the hybrid substation is connected to three, three-phase feeders with a different demand, as shown in Figure 3.13. Similar to the previous section, a yearly load profile has been used for each feeder. The tested feeders for simulation is chosen to be a 300m and 300 mm^2 cable with 100 residential houses for feeder 1, 500m and 185 mm^2 cable with 30 residential houses for feeder 2, and 600 m and 300 mm^2 cable with 120 residential houses for feeder 3.

The previously described analysis methodology has been used and the final results of all PDF_{230} values per different hybrid substation voltage $V_{o,i}^{k}$ for all three feeders can be seen in Figure 3.14. In general, the overall optimum substation voltage $V_{o,optimum}^{i}$ for *j*-feeder network can be given by:

$$V_{o,optimum}^{i} = \frac{\sum\left(PDF_{230}^{j} \times V_{o,optimum}^{i,j}\right)}{\sum PDF_{230}^{j}} \tag{3.19}$$

where PDF_{230}^{j} is the load voltage PDF value of feeder *j* at 230V and $V_{o,optimum}^{i,j}$ is the optimum substation voltage for feeder *j*. For the proposed 3-feeder system the overall optimum substation voltage should be kept at 244 V.

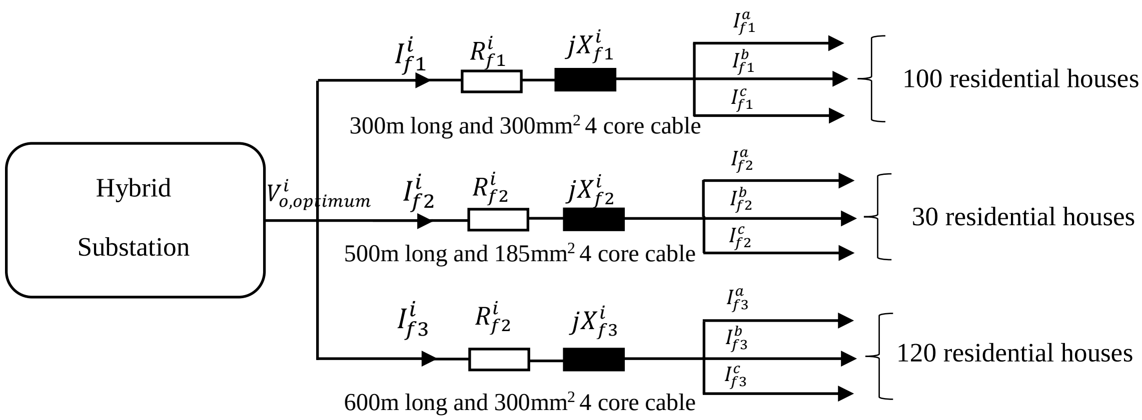

Figure 3.13: Schematic diagram of distribution hybrid substation connected to 3 different feeders

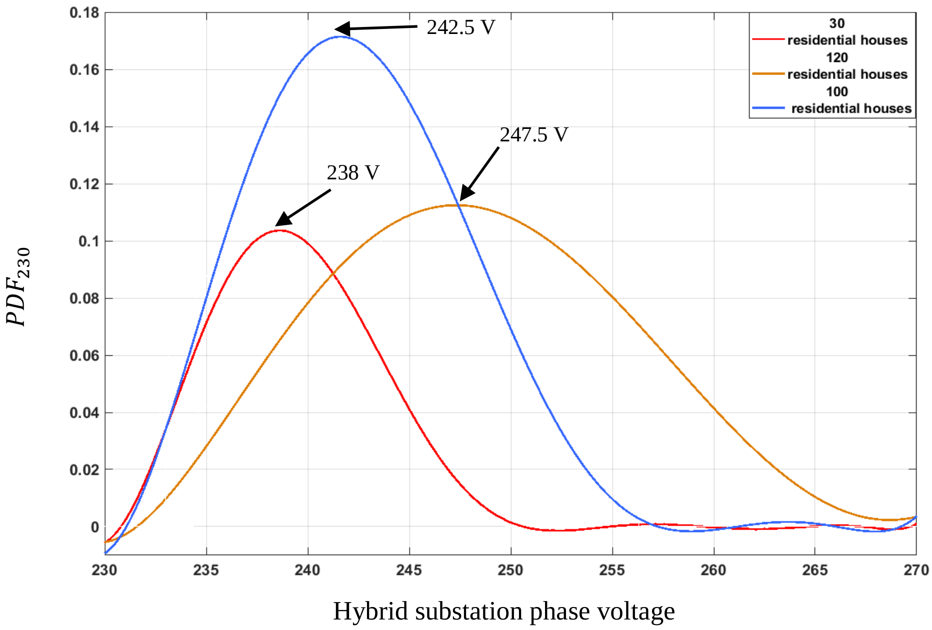

Figure 3.14: Calculated PDF_{230} for different substation phase voltages for 3 feeders with different load demand.

The overview flow chart of the whole process discussed in this chapter is shown in Figure 3.15. In the proposed case study, choosing $V^{i}_{o,optimum}$ for the hybrid substation can result to obtain the maximum injection voltage at 25V. As a result, the value of the controllable voltage range of λ and τ can be set to $\pm 10\%$. In addition to the amount of voltage injection, there are three possible scenarios for the hybrid substation's power converters to interact with each other as follows:

Back-to-back VSC of hybrid transformer operates only

This is a suitable option if the substation is connected to a multi-feeder network with a similar load diversity factor. Load diversity factor is the ratio of the sum of the individual maximum demands to the coincident maximum demand [1]. A good example can be given by Figure 3.13, where the feeders are connected to residential houses and the maximum demand of loads occur at the same interval time. In this case, λV_{xi} is injected to the system to keep the output voltage at $V^{i}_{o,optimum}$ and the total voltage controllability is $V_{xi}(1 \pm \lambda)$ for $\lambda = \pm 10\%$.

DC-AC VSCs of feeders operate only

This is an appropriate solution if the substation is connected to a multi-feeder network with different load diversity factors. For example, one feeder is connected to a heavy load with significant voltage drop and the other feeder is attached to a heavy DG load with voltage rise. Alternatively, one feeder is supplying residential houses while the other is connected to industrial applications. In this case, each phase of the VSCs can compensate the feeder voltage and the total voltage controllability is $V_{xi}(1 \pm \tau)$ for $\tau = \pm 10\%$.

Back-to-back VSC and feeders VSCs operate together

A more complete configuration can be given by combining the AC-AC VSC of hybrid transformers and DC-AC VSCs of the feeders. This configuration can satisfy all scenarios. For instance, if the substation is connected to a multi-feeder network with a similar load diversity factor, only the AC-AC VSC will be operating and if any unexpected voltage demand is required, the corresponding DC-AC VSC of the affected feeder will compensate the voltage along with the hybrid transformer. In addition, if the substation is connected to a multi-feeder network with different load diversity factors, the back-to-back hybrid transformer VSC keeps the output voltage at the optimum value $V_{o,optimum}^{i}$ and if needed, the DC-AC VSC will inject the required voltage. Moreover, if any fault happens at the low or high voltage side of the conventional transformer, the AC-AC VSC will compensate it and the feeders' VSCs will operate normally. In this case, the total voltage controllability is $V_{xi}(1 \pm \lambda \pm \tau)$ for $\tau = \lambda = \pm 10\%$.

The kVA value of the VSCs are found from the optimum substation output voltage, but it is important to note that for long-term planning, a great number of variables such as the optimum substation location, the optimum substation transformer sizes, ideal feeder routes and sizes, population growth, geographical factors, community development plans, etc. are involved. Therefore, there can be a number of feasible alternative plans along with optimum substation voltage variations.

Finding the most efficient and cost-effective plan for a distribution system with several variables can be a challenging undertaking for the power distribution planning engineers. However, estimation of the optimum kVA rating of the power electronics used in LV networks that are based on load demand forecasting and probabilities can be a great achievement and have an influence on such decisions in the remaining variables. In addition to the optimum power converter kVA rating selection, a powerful approach to minimise the converter injection voltage will be introduced in Chapter 5 of this thesis.

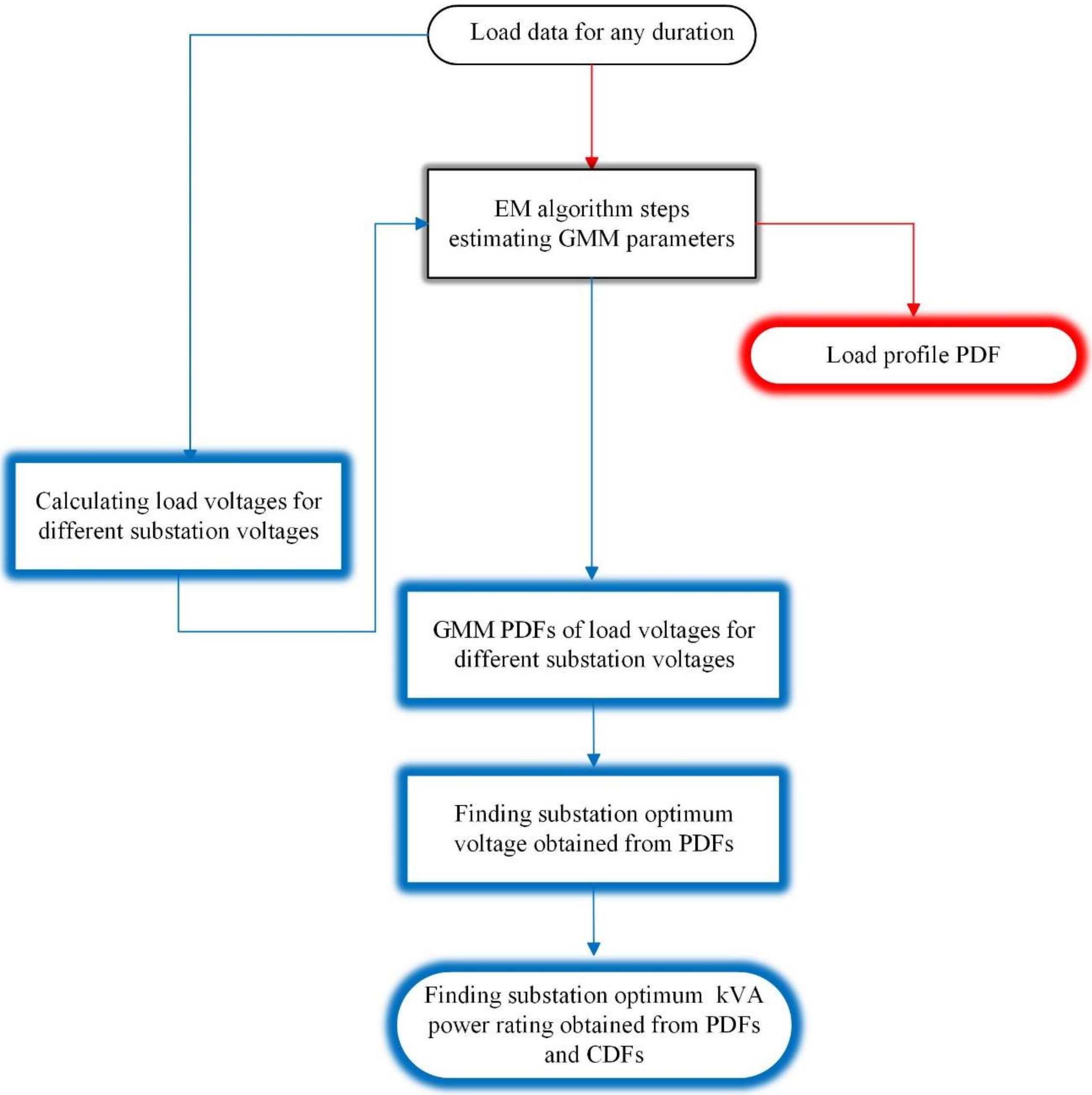

Figure 3.15: overview flow chart of the whole process.

3.5 Conclusion

In real life, load model does not have any certain pattern or a predicted behaviour. Thus, most studies use a specific day or hour of the year to estimate load patterns and probabilities. For this Chapter a comprehensive novel study has been carried out to evaluate probabilistic load data, concerning the time-evolution of any type of load for any time duration.

GMM is a powerful probability model that has been widely used in many scientific fields. It is a beneficial technique that utilises EM algorithms and as a result, allows different types of load distributions to be presented as a combination of several Gaussian distributions with respective means and variances.

Substation voltage optimisation plays an essential role in the power system in terms of load voltage quality, network losses, power system safety, etc. A new method has been introduced to find an optimal substation voltage for the distribution system based on statistics and probabilities. This finding points to the conclusion that for a system with a series set up of power converter (for voltage regulation purposes), choosing $V_{o,optimum}^{i}$ leads to the lowest amount of total injected power, power rating of the power electronics. The explained method can be used in any probabilistic-based power system analysis for any time duration, including distribution planning, probabilistic load flow, load forecasting, load management, distribution automation, etc.

CHAPTER 4 : Control of Grid-Connected Four-Leg Voltage Source Converter

Summary: *This Chapter provides a review of four-wire power converters. It presents the general control strategies for the shunt and series VSCs. This chapter also provides a guideline for designing resonant current and voltage controllers used in grid-connected four-leg power converters. In addition, a detailed description of the Space Vector Modulation (SVM) technique implemented in two-level four-leg converters is given.*

4.1 Introduction

As explained earlier in Chapter 2, a hybrid substation comprising both shunt-connected and series-connected four-leg VSCs with a common DC-link, can be used to increase the voltage regulating capabilities in LV distribution feeders. Three-phase four-wire Voltage Source Converters (VSCs) have been used extensively in a wide range of industrial and information technology applications [81]. The four-wire VSC was introduced early in [82] to support commutation for a current-fed thyristor inverter by adding an extra neutral load wire in the late 1970s. They become more popular for voltage regulation purposes, motor-driven applications and harmonic distortion mitigation in the presence of unbalanced and non-linear loads in the late 1980s and throughout 1990s [45, 83-85].

In several low voltage applications, unbalanced or non-linear loads might draw currents with positive, negative and zero sequences, which cause a neutral current to be circulated in the system; therefore a four-wire VSC is required to handle the neutral current using an extra wire or leg [86]. There are two common ways to provide the neutral connection: a three-leg converter structure with split DC-link capacitors to provide the fourth wire or a three-leg converter with an additional leg acting as a fourth leg. Figure 4.1 shows the two main topologies of four-wire converters known as the two-level three-leg four-wire converter and the two-level four-leg converter.

By referring to Figure 4.1, the main advantages of four-leg converters over three-leg four-wire converters can be expressed as follows:

- Three-leg four-wire converters operate well when the level of non-linear or unbalance load is low. As loads become more non-linear or unbalanced then the neutral current can become large. Since the load is connected to the mid-point of the DC-link, the capacitors must usually be very large in order to handle the high current ripple [87]
- The split capacitors of Figure 4.1(a) create a serious problem when the voltages are not equally distributed among the capacitors, and this may affect the performance of the VSC as the peak-to-peak amplitude of the VSC output voltage is shifted from the central position
- The maximum phase voltage (voltage between each phase and DC-link mid-point) of Figure 4.1(a) is limited $V_{dc}/2$. Therefore, the three-leg four-wire converter only uses half of DC-link voltage. However a four-leg converter utilises the full DC-link voltage for modulation. Moreover, by implementing an appropriate modulation method, the output phase voltage increases providing an approximate 15% advantage in DC voltage utilisation [88, 89]
- A three-phase four-leg converter provides three different phase voltage levels $\mathrm{V_{dc}}$, 0 and -$\mathrm{V_{dc}}$, but a three-phase four-wire converter only has two voltage levels $+V_{dc}/2$ and -$V_{dc}/2$ [90]. Therefore, the output voltage of a three-phase four-wire converter has higher harmonic content in comparison to a four-leg converter

Four-leg converters are considered to be the best candidate to provide neutral connection to single phase or three-phase balanced, unbalanced, linear and non-linear loads. The four-leg converter is a promising solution for most low voltage applications such as: Dynamic Voltage Restorers (DVRs) [42, 91, 92], grid connected converters [93-95], uninterruptible power supplies (UPSs) [45, 96] , four-leg matrix and multilevel converters for different applications [86, 97-99], active power filtering [100-102], etc. Due to the benefits of four-leg converters, a four-leg power converter is proposed as the main conversion element in this thesis.

As discussed earlier in Chapter 2, the main purpose of the shunt-connected VSC is to generate a common DC-link voltage from the secondary winding of the conventional transformer to feed all series-connected VSCs. Moreover, the shunt-connected VSC can act as an active power filter and inject the required current to compensate the grid current harmonic components generated by non-linear loads. However, as discussed in Chapter 3, the series converter injection range is typically $\pm 10\%$ of the rated voltage, it is evident that the shunt converter will be similarly partially rated with respect to the feeder current. As a result, the shunt-connected VSC of the hybrid substation could compensate only a limited range of grid current harmonics. The series-connected VSCs of the hybrid substation can control the magnitude, frequency and phase of the injected voltage. The control structures for both the shunt and series VSCs of the hybrid substation are provided in this chapter.

A four-leg VSC, in comparison with a three-phase three-wire VSC, needs a more complex control algorithm for the modulation of the output voltages to control the neutral current circulation. The control of four-leg converters can be implemented using several methods [103-109], the most common modulation schemes for four-leg VSCs being: carrier-based Pulse Width Modulation (PWM) [107, 109-111] and three-dimensional Space Vector Modulation (SVM) in abc and $\alpha\beta\gamma$ coordinate frames [108, 109, 112-114]. The three-dimensional SVM in $\alpha\beta\gamma$ coordinate frames is recognised to have benefits such as lower output phase voltage harmonic distortion, less switching and conduction losses and more output phase voltage levels in comparison to other modulation strategies [108], hence this method is used in the work reported in this thesis.

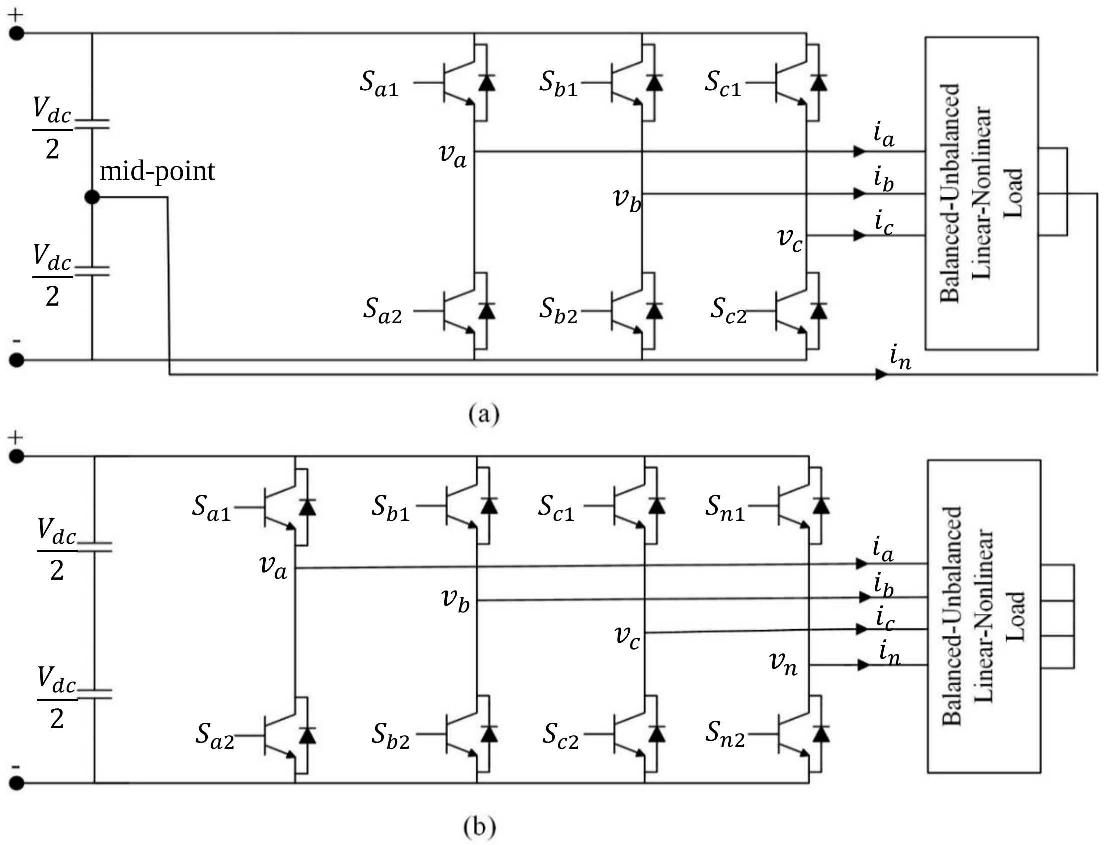

Figure 4.1: Schematic diagram of (a) two-level four-wire converter (b) two-level four-leg converter.

4.2 Control of Grid-Connected Four-Leg VSC

Figure 4.2 shows the three-phase schematic diagram of a hybrid substation connected to a three-phase feeder(s) (extended schematic diagram of Figure 2.12). As can be observed from Figure 4.2 (a) and (b), the power electronic topology used the in the hybrid substation connected to a three-phase feeder and two three-phase feeders are a 12-leg and a 16-leg VSC, respectively. In general, the converter topology of the hybrid substation has $4(2 + \mathrm{n})$ legs, where n is the number of feeders of the system.

The shunt-connected VSC creates a common DC-link for the system and may inject a limited current to do grid current harmonic compensation. The series VSCs inject voltage with appropriate magnitude and phase angle to keep the load voltages or hybrid transformer output voltages balanced at a predetermined value. The fourth-leg of the series VSC controls the zero sequence when the load or supply is unbalanced. The series-connected VSC has an LC-filter at its output to remove switching related harmonics. The design of the LC-filter will be explained in Chapter 6. Series injection transformers are used for isolation and to match the voltage/current to values appropriate for the IGBT converter. The power rating of these transformers is determined by the current flowing in the feeders and by the maximum voltage to be injected.

There are several control structures for grid-connected VSCs [33]. The most common control strategies are: Synchronous Reference Frame (SRF) control or dq control, stationary reference frame control or $\alpha\beta$ control, and abc frame control. The dq control structure is normally associated with Proportional Integral (PI) controllers as they have a satisfactory behaviour when regulating DC variables. However, the compensation capabilities of PI controllers for low-order harmonics is poor leading to a major drawback in grid-connected VSCs systems [115].

Proportional Resonant (PR) controllers [116-118] have gained attention in the last decade due to their capability to eliminate the steady-state error when tracking sinusoidal signals, unlike PI controllers which are not capable of compensating low-order harmonics and cannot remove steady-state error when tracking sinusoidal signals [119]. The proportional resonant controller is accordingly considered for this thesis. The general form of a PR controller can be expressed as:

$$G_{PR}(s) = K_p^{PR} + \frac{2K_i^{PR}s}{s^2 + \omega_0^2} \tag{4.1}$$

where K_p^{PR} and K_i^{PR} are proportional and integral gains, respectively and ω_0 is the resonance frequency.

Blaabjerg et.al. [115], *Teodorescu et.al.* [33] and [119] have evaluated different types of control structures for grid-connected VSCs and concluded that each control structure has its own merits. However, in LV distribution systems, the stationary frame control ($\alpha\beta$ control structure) associated with PR controllers and abc frame control with PR or deadbeat controllers [33, 120] have superior results in dynamic performance for grid-connected VSCs. As a result, in this thesis, an $\alpha\beta$ control structure with a PR controller is implemented to control the shunt-connected VSC and an abc frame control structure with a PR controller is applied to control the series-connected VSCs.

a)

b)

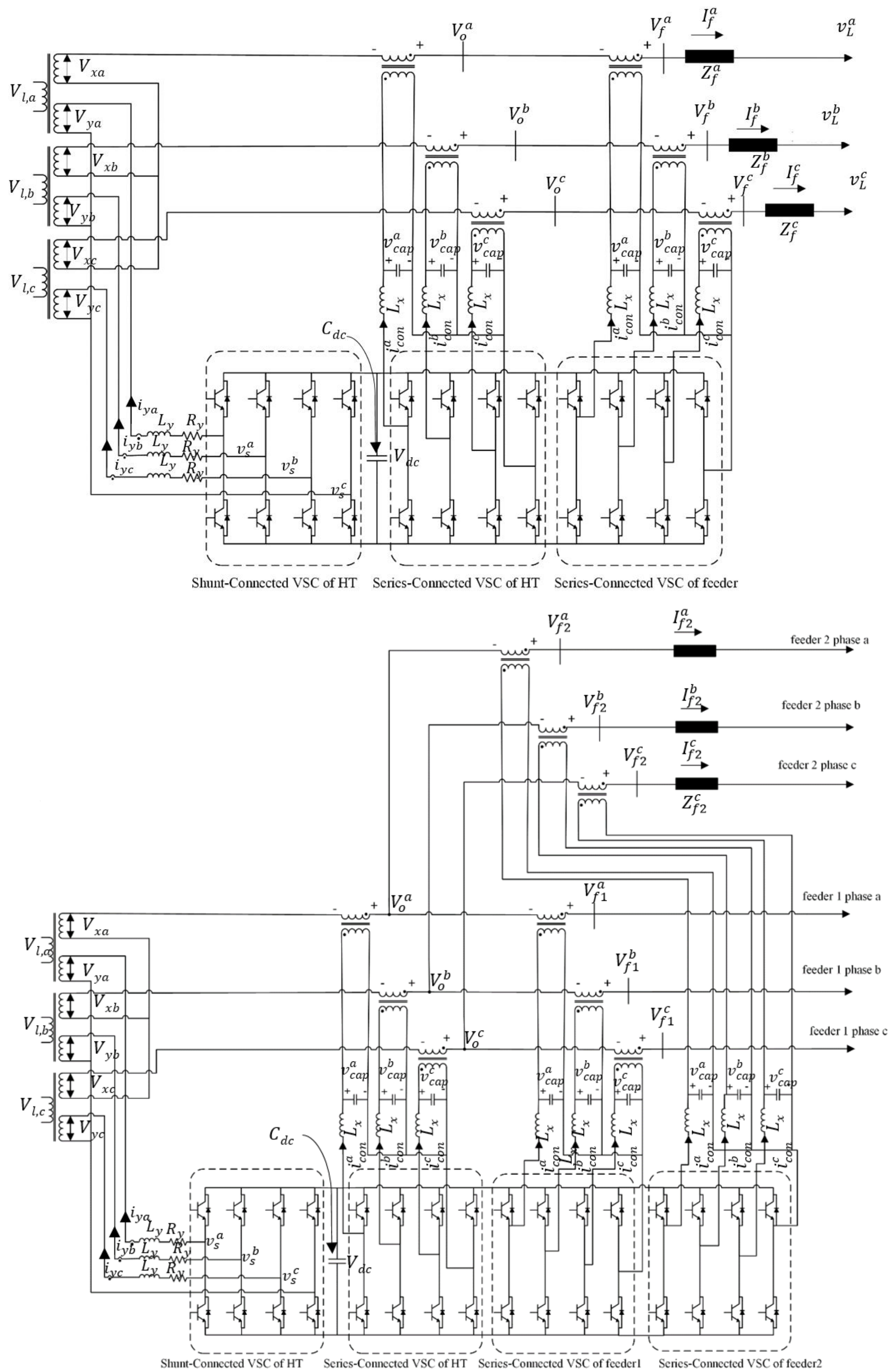

Figure 4.2: Three-phase schematic diagram of a hybrid substation, a) one-feeder system, b) two-feeder system.

4.3 Control of Shunt-Connected VSC

The proposed control structure for stationary reference frame control of a three-phase, four-leg shunt-connected VSC with RL-filter is shown in Figure 4.3. The voltage across the common DC-link capacitor can be kept at constant value by controlling the power flow on AC side of the secondary winding of the conventional transformer.

As can be seen, the shunt VSC has two controller loops: an outer DC voltage loop and a fast internal current loop. The outer DC voltage loop is based on a PI controller to achieve the optimum regulation and stability for balancing the power flow and controlling DC-link voltage. The fast internal current loop is based on a PR controller. A Phase-Locked Loop (PLL) algorithm has been used to synchronise with the grid voltages and currents. In addition, a 3-dimensional SVPWM algorithm is used to synthesise the voltages demanded by the control loops at the output of the power converter.

4.3.1 Phase-Locked Loop

A phased-locked loop [119, 121-123] is a closed-loop system which enables an output signal to be synchronised with a reference input signal in frequency and phase. The PLL technique has been broadly used in the fields of communications, computers, modern electronics, etc. In grid-connected VSC applications, the PLL provides information on phase, frequency and the RMS value of the grid voltage and also the current for the main control loops. The PLL is based on a PI controller and regulates the quadrature supply voltage component V_{yq}, to zero in order to synchronise the d-axis of the synchronous reference frame (direct component) to the supply voltage. Figure 4.4 shows the typical block diagram of a three-phase PLL for grid monitoring. The PLL has three main blocks, as follows:

- The Phase Detector (PD) block generates an output signal proportional to the phase difference between the input signal and the signal generated by PLL
- A Loop Filter (LF), which is based on a first order low-pass filter or a PI controller
- The Voltage-Controlled Oscillator (VCO) generates the output AC signal with a shifted frequency with respect to ω_c

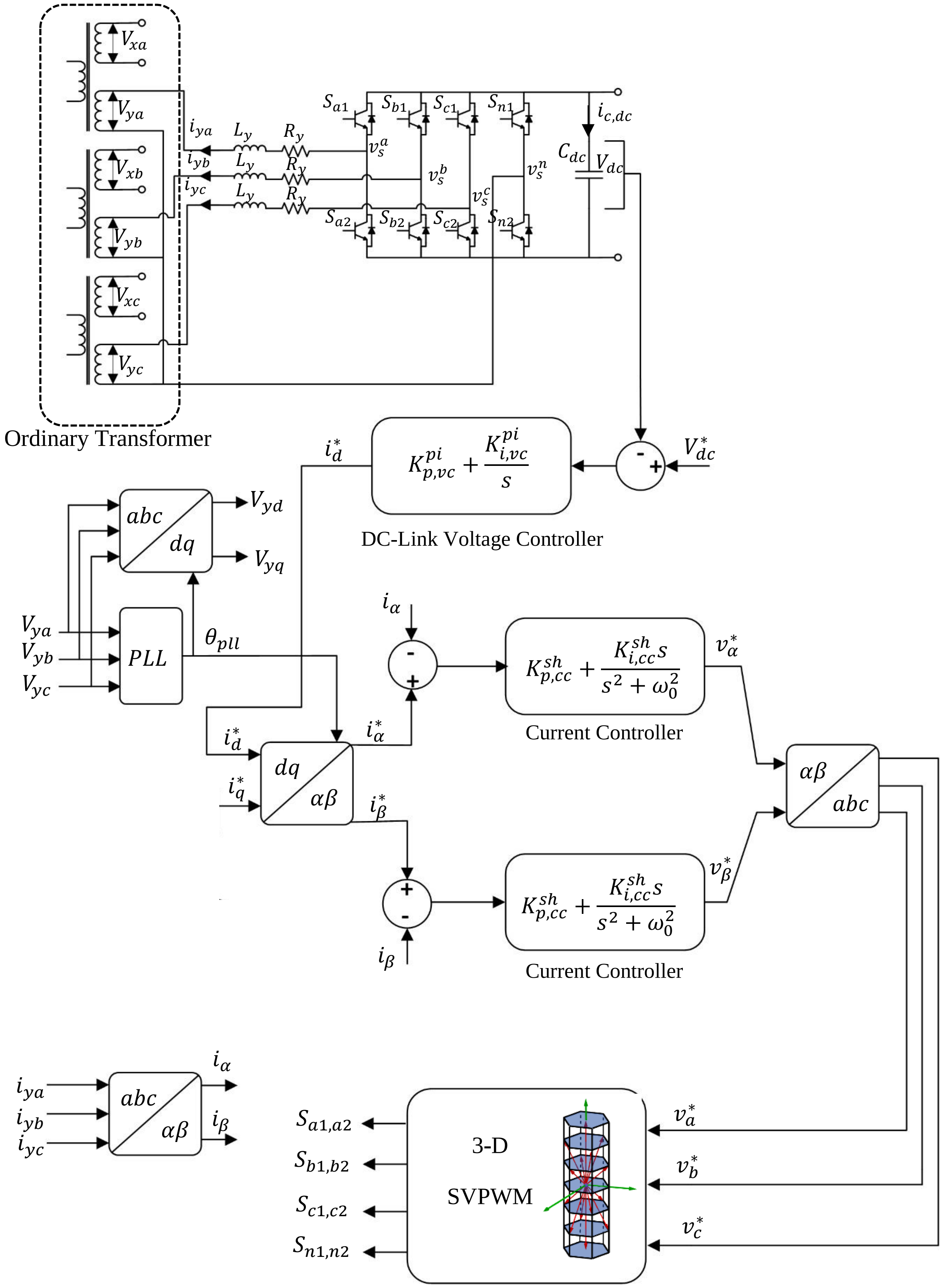

Figure 4.3: Proposed control structure for stationary reference frame of a shunt-connected VSC.

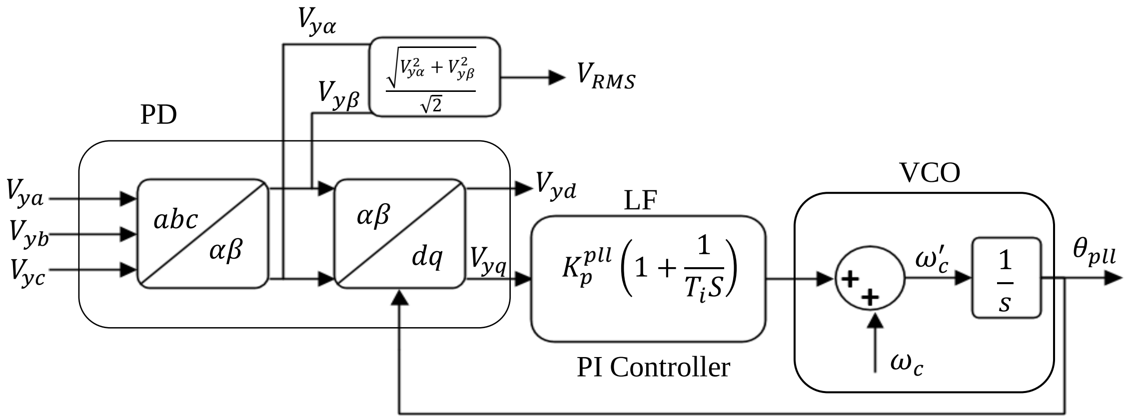

Figure 4.4: Block diagram of a three-phase PLL used for shunt-connected VSC for grid monitoring.

4.3.2 Current Controller of Shunt-Connected VSC

By referring to Figure 4.3 and applying Kirchhoff's law, the following differential equations for the three-phase shunt-connected VSC can be obtained [124]:

$$v_s^i(t) - V_{yi}(t) - R_y i_{yi}(t) - L_y \frac{d}{dt} i_{yi}(t) = 0 \tag{4.2}$$

where $i \in (a, b, c)$.

Variables in an abc frame can be transformed into $\alpha\beta$ coordinates by using Clarke transformation (see subsection 4.5.1.1), the equation (4.2) can be re-written as:

$$v_s^{(\alpha\beta)}(t) - V_y^{(\alpha\beta)}(t) - R_y i_y^{(\alpha\beta)}(t) - L_y \frac{d}{dt} i_y^{(\alpha\beta)}(t) = 0 \tag{4.3}$$

Taking Laplace transforms of the equation (4.3) and neglecting the feed forward terms $V_y^{(\alpha\beta)}(t)$, the transfer function of the plant for the current controller is given by (4.4):

$$G_{cc}^{sh}(s) = \frac{i_y^{(\alpha\beta)}(s)}{v_s^{(\alpha\beta)}(s)} = \frac{1}{sL_y + R_y} \tag{4.4}$$

The schematic diagram of current controller loop is shown in Figure 4.5.

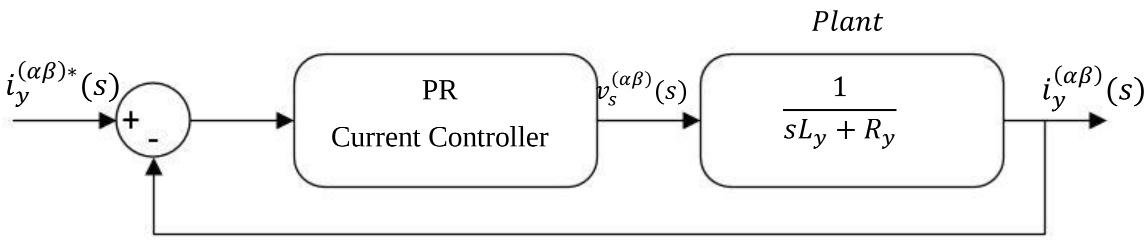

Figure 4.5: Schematic diagram of current controller loop for shunt-connected VSC.

Resonant controller of (4.1) can be adjusted by three degrees of freedom, as follows [86, 125]:

$$G_{PR}^{sh}(s) = K_{p,cc}^{sh}\frac{s^2 + a^{sh}s + b^{sh}}{s^2 + \omega_0^2} \tag{4.5}$$

where $K_{p,cc}^{sh}$, a^{sh} and b^{sh} are the resonant current controller parameters that need to be designed. To obtain a good closed-loop response and achieve the unrestricted allocation of the zeros of the resonant controller, equation (4.5) has been used. Hence, the equivalent closed-loop transfer function of the proposed current controller (Figure 4.5) can be expressed as:

$$\frac{i_y^{(\alpha\beta)}(s)}{i_y^{(\alpha\beta)*}(s)} = \frac{\frac{K_{p,cc}^{sh}}{L_y}(s^2 + a^{sh}s + b^{sh})}{s(s^2 + \omega_0^2) + \frac{R_y}{L_y}(s^2 + \omega_0^2) + \frac{K_{p,cc}^{sh}}{L_y}(s^2 + a^{sh}s + b^{sh})} \tag{4.6}$$

The values of the current resonant controller are obtained through root locus analysis, as shown Figure 4.6 (a). The closed-loop poles have been placed to get an optimum damping ratio of $= 0.707$. As can be seen from Figure 4.6 (b), a fast and stable system with overshoot of $M_p = 4.3\%$ and settling time of $t_s = 4.5$ms has been obtained. The resonance frequency is set to $\omega_0 = 100\pi\ Rad/s$ with RL-filter of $R_y = 1\Omega$, $L_y = 2$mH. The filtering parameters estimation for grid-connected shunt VSC can be found in [126].

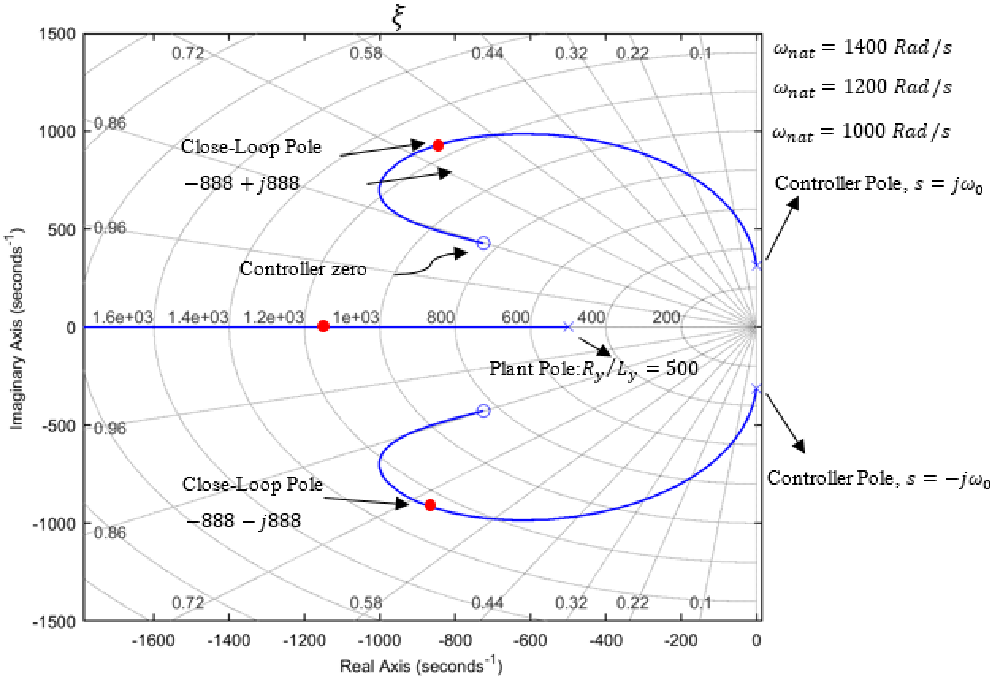

(a)

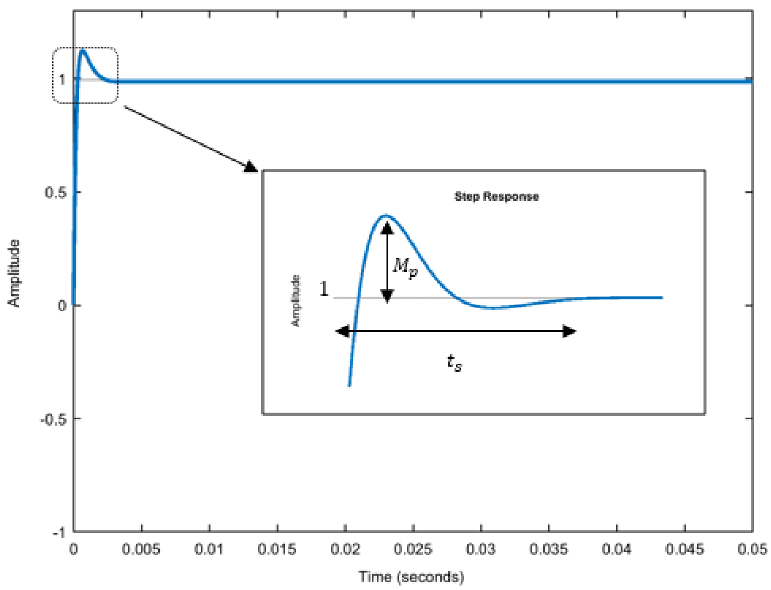

(b)

Figure 4.6: Plots of : a) root-locus of the resonant current controller, b): time domain step response of the resonant current controller for shunt VSC, $K_{p,cc}^{sh} = 4.6$, $a^{sh} = 1450$, $b^{sh} = 708000$.

Figure 4.7 (a) shows the frequency response of the proposed resonant current controller which has very high gain at the resonant frequency $\omega_0 = 100\pi\ Rad/s$. Figure 4.7 (b) presents the closed-loop frequency response of the system. As can be seen, excellent reference tracking at the fundamental frequency $f_c = 50\ Hz\ (314\ Rad/s)$ can be achieved. The resonant closed-loop controller has $0.001\ dB$ gain and -0.002° phase shift at the supply frequency ω_0 and this allows the resonant controller to track the signal excellently.

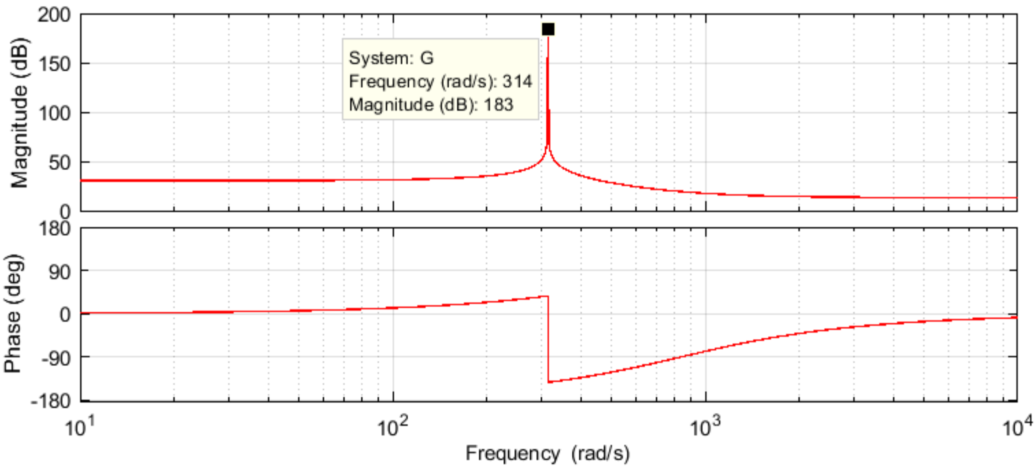

a)

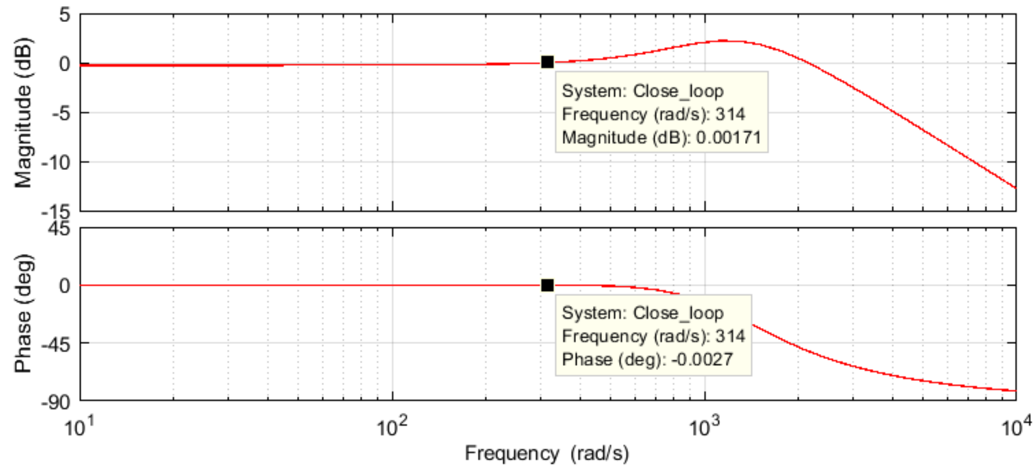

b)

Figure 4.7: Bode plots of: a) resonant current controller, b): closed-loop response of the current controller for shunt VSC.

4.3.3 Voltage Controller of Shunt-Connected VSC

The voltage control loop is responsible for generating the reference signal, i_d^* for the current controller (i_q^* =0 for unity displacement factor). DC-link voltage control is normally associated with a simple PI controller due to its satisfactory behaviour for tracking DC quantities [33, 120]. A standard transfer function of the DC-link plant can be written as [120]:

$$G_{PI}^{dc}(s) = \frac{V_{dc}}{i_d^*} = \frac{1}{sC_{dc}} \tag{4.7}$$

The schematic diagram of the DC-link voltage controller loop is shown in Figure 4.8. The transfer function of the closed-loop system can be calculated as:

$$\frac{G_{PI}G_{PI}^{dc}}{1 + G_{PI}G_{PI}^{dc}} = \frac{s\dfrac{K_{p,vc}^{pi}}{C_{dc}} + \dfrac{K_{i,vc}^{pi}}{C_{dc}}}{s^2 + s\dfrac{K_{p,vc}^{pi}}{C_{dc}} + \dfrac{K_{i,vc}^{pi}}{C_{dc}}} \tag{4.8}$$

The transfer function of equation (4.8) can be presented in characteristic polynomial form as:$s^2 + 2\xi\omega_{nat}s + \omega_{nat}^2$. Thus, the tuning parameters of the DC-link voltage controller can be given by:

$$K_{p,vc}^{pi} = 2C_{dc}\,\xi\omega_{nat} \tag{4.9}$$

$$K_{i,vc}^{pi} = C_{dc}\,\omega_{nat}^2 \tag{4.10}$$

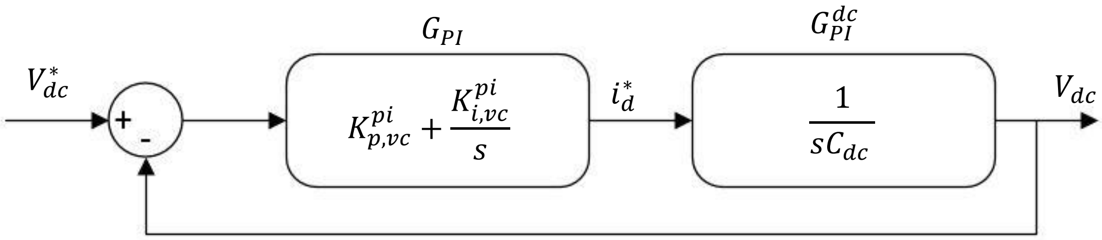

Figure 4.8: Schematic diagram of DC-link voltage controller loop for shunt-connected VSC.

The tuning of DC-link controller parameters can be done assuming that the outer loop DC-link voltage controller is slower than the inner loop resonant current controller [125]. The natural frequency of the voltage controller of the shunt VSC should be at least 3 times less than the natural frequency of the current controller [124]. The closed-loop poles of the DC-link voltage controller have been located to get a damping ratio of $\xi = 0.707$ with natural frequency of $\omega_{nat} = 20$ Hz, the root-locus plot can be given in Figure 4.9. DC-link capacitor C_{dc} value is chosen to be 1mF and the method to choose the required DC-link capacitor C_{dc} value will be explained in Chapter 6.

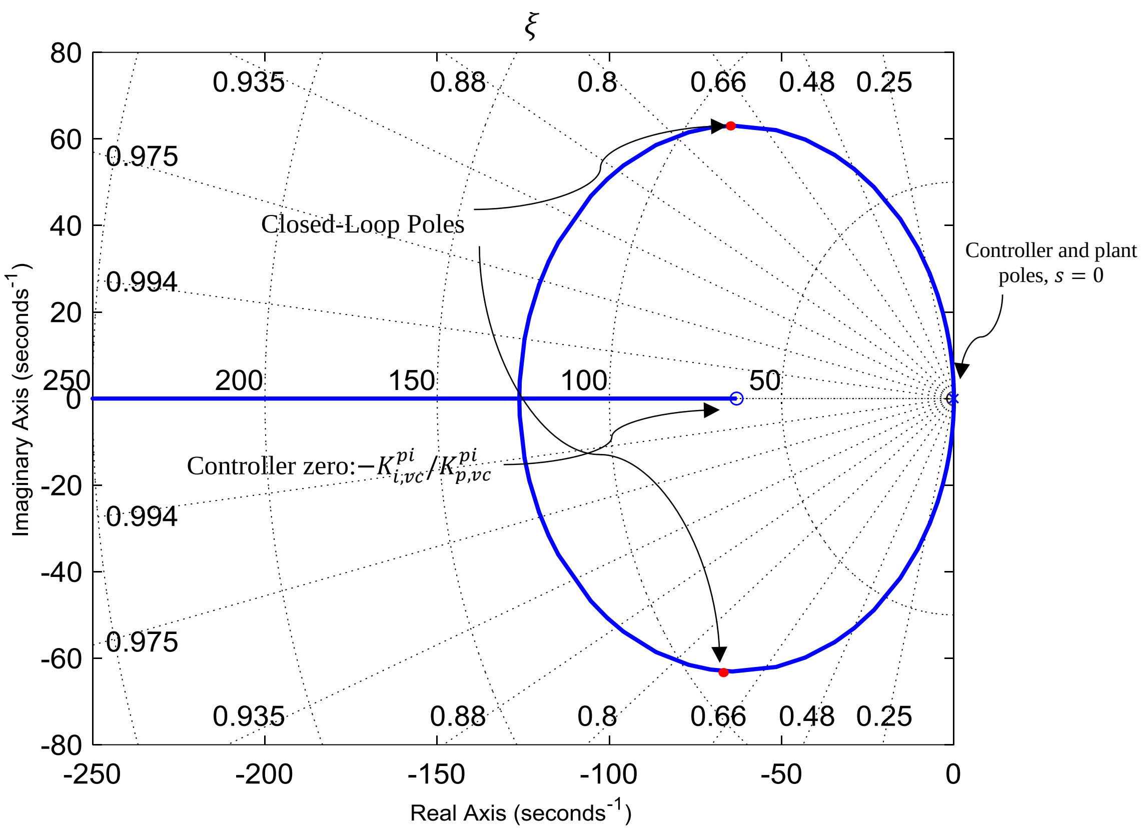

Figure 4.9: Root-locus plot of a PI voltage controller, $K_{p,vc}^{pi} = 0.25, K_{i,vc}^{pi} = 15.77$

4.4 Control of Series-Connected VSC

As mentioned earlier, the control structure in the abc frame is one of the most popular structures used for grid-connected VSCs applications. This control structure is implemented in series-connected VSC of the hybrid transformer and feeders' VSCs of the hybrid substation. Figure 4.10 shows the general control structure in abc frame of the series-connected VSC, where the DC-link voltage is created and controlled by the shunt-connected VSC described in previous section. Each phase of the system is controlled individually by a multi-loop PR controller with an inner current loop and an outer voltage loop to generate the injected voltages (Figure 4.15). The reference injected voltages v_{ref}^{a}, v_{ref}^{b} and v_{ref}^{c} are determined by a symmetrical sequence components method for controlling the VSCs of the hybrid substation which will be presented in Chapter 5. A 3-dimensional SVPWM algorithm is used to synthesise the voltages demanded by the control loops at the output of the power converter.

4.4.1 Current Controller of Series-Connected VSC

For the derivation of current controller of series VSC, KVL is applied to the LC filter in Figure 4.10, and the following differential equation for each phase can be obtained:

$$v_{se}^{i}(t) - v_{cap}^{i}(t) - L_x \frac{d}{dt} i_{con}^{i}(t) = 0 \tag{4.11}$$

where $i \in (a, b, c)$.

It is assumed that the inductor's resistance has a small value and so is neglected. Similar to current controller of shunt VSC, taking Laplace transforms of (4.11) and neglecting feed forward terms, the transfer function of the plant for current controller is given by [124]:

$$G_{cc}^{se}(s) = \frac{i_{con}^{i}(s)}{v_{se}^{i}(s)} = \frac{1}{sL_x} \tag{4.12}$$

The schematic diagram of current controller of series VSC can be shown in Figure 4.11.

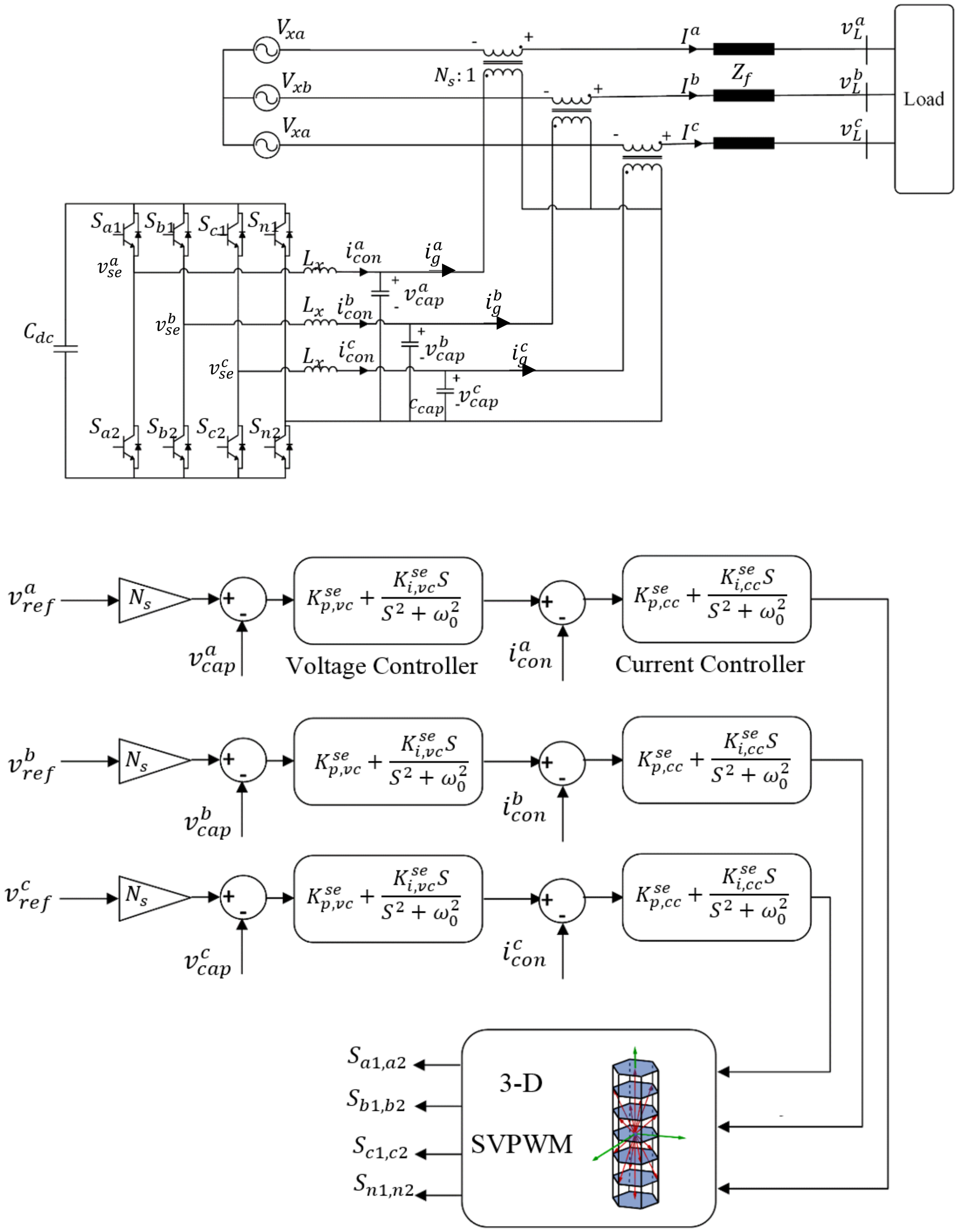

Figure 4.10: Proposed general control structure of the series-connected VSCs.

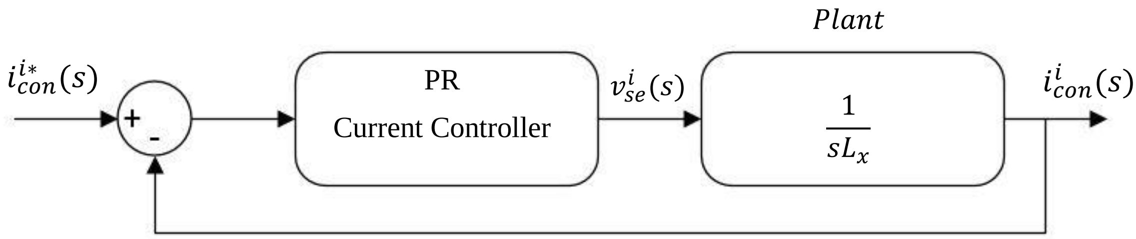

Figure 4.11: Schematic diagram of current controller loop for series-connected VSC.

Similar to current controller of shunt-connected VSC, the inner current controller needs to be tuned first. The control design of the current controller is similar to the shunt-connected VSC explained in the previous section. The resonant current controller of the series-connected VSC can be adjusted by three parameters, as follows:

$$G_{PR,cc}^{se}(s) = K_{p,cc}^{se} \frac{s^2 + a_{cc}^{se} s + b_{cc}^{se}}{s^2 + \omega_0^2} \tag{4.13}$$

where $K_{p,cc}^{se}$, a_{cc}^{se} and b_{cc}^{se} are the resonant controller gain parameters of the current controller and needs to be designed. The series VSC has an inductor of $L_x = 10$mH, and this value has been used for both simulation and experimental work. The method to choose the rating value of the inductor will be explained in Chapter 6. The values of the current controller parameters $K_{p,cc}^{se}$, a_{cc}^{se} and b_{cc}^{se} are obtained through root-locus analysis in order to have a fast and stable system. Figure 4.13 shows the closed-loop frequency response of the system with $0.004\,dB$ gain and -0.01° phase shift of the resonant controller at the main frequency, ω_0, which results in a reasonable signal tracking.

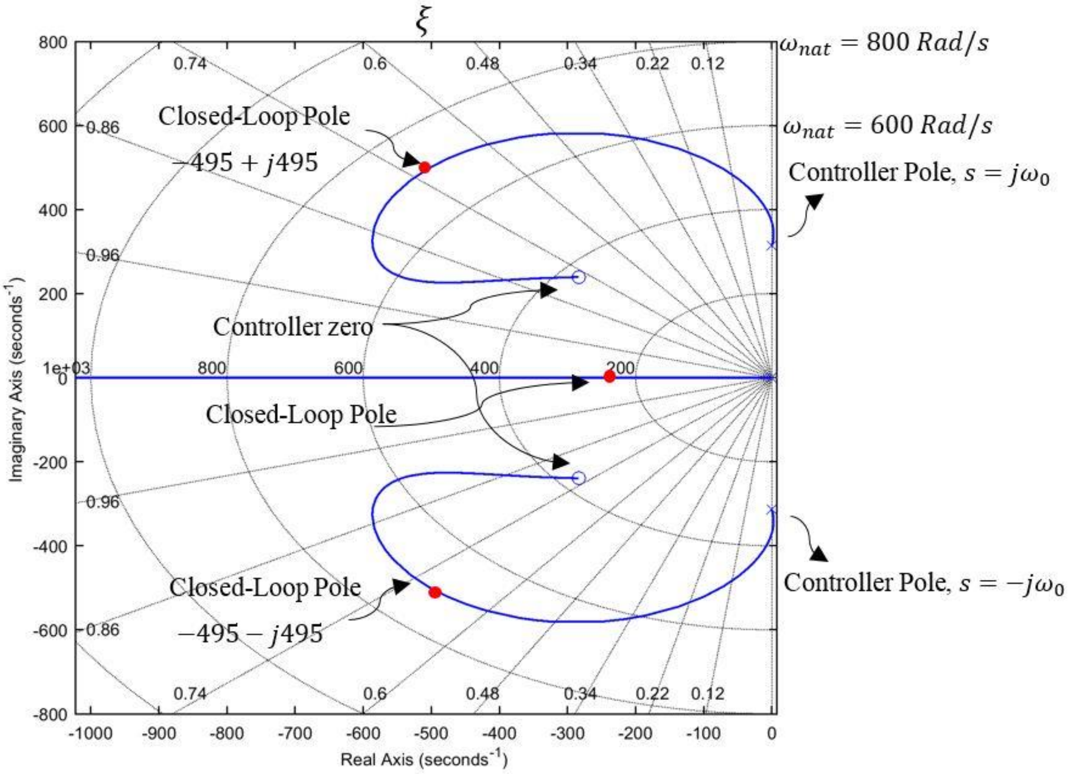

Figure 4.12: Root-locus plot of resonant current controller of series-connected VSC, $K_{p,cc}^{se} = 13.7, a_{cc}^{se} = 566, b_{cc}^{se} = 137000$

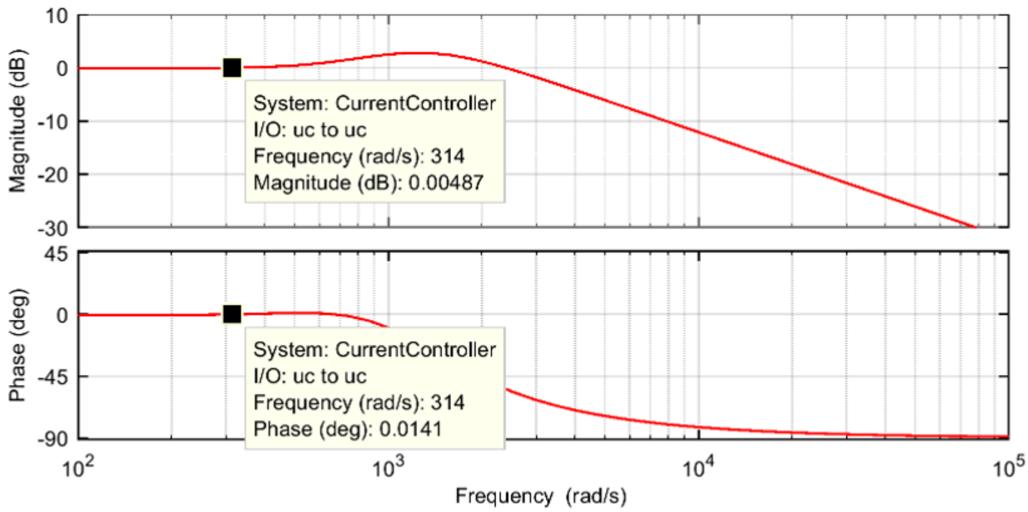

Figure 4.13: Closed-loop bode diagrams of current controller for series-connected VSC.

4.4.2 Voltage Controller of Series-Connected VSC

By referring to Figure (4.10) and applying Kirchhoff's Current Law (KCL) to the LC-filter of the series-connected VSC, the following equation can be obtained [124]:

$$i_{con}^{i}(t) = C_{cap}\frac{d}{dt}v_{cap}^{i}(t) + i_{g}^{i}(t) \tag{4.14}$$

By neglecting the feed forward terms and taking Laplace transformation, the transfer function of the plant for voltage controller can be given in (4.15):

$$\frac{d}{dt}v_{cap}^{i}(t) - \frac{1}{C_{cap}}i_{con}^{i}(t) = 0$$

$$= G_{vc}^{se}(s) = \frac{v_{cap}^{i}(s)}{i_{con}^{i}(s)} = \frac{1}{sC_{cap}} \tag{4.15}$$

The schematic diagram of voltage controller of series-connected VSC is shown in 4.14.

Similar to previous section, the resonant voltage controller of the series-connected VSC can be adjusted by three parameters as follows:

$$G_{PR,vc}^{se}(s) = K_{p,vc}^{se}\frac{s^{2} + a_{vc}^{se}s + b_{vc}^{se}}{s^{2} + \omega_{0}^{2}} \tag{4.16}$$

where $K_{p,vc}^{se}$, a_{vc}^{se} and b_{vc}^{se} are the resonant controller gain parameters of the resonant voltage controller for series VSC.

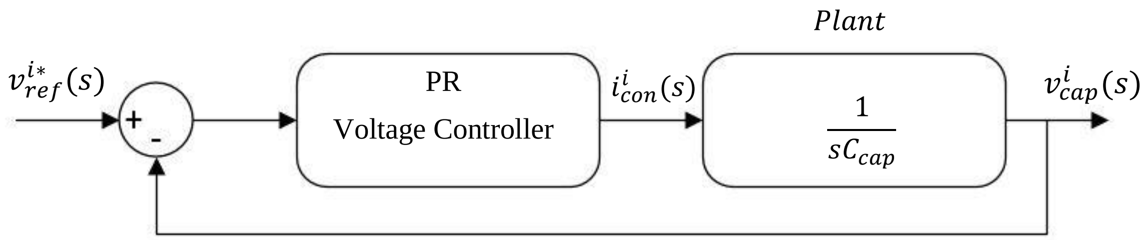

Figure 4.14: Schematic diagram of voltage controller loop for series-connected VSC.

The voltage controller is designed with the inner current loop closed. The block diagram of multi-loop PR controllers for series VSC is shown in Figure 4.15. Figure 4.16 shows the closed-loop root-locus plot of the multi-loop PR controllers of Figure 4.15 for the series-connected VSC. As shown in Figure 4.16, the closed-loop transfer function of the current controller has three poles (two complex poles, one real pole) and two complex zeros. As mentioned before, the closed-loop poles of current controller are placed to obtain a damping ratio of $\xi = 0.707$. The complex imaginary poles of voltage controller can cause oscillatory response in closed-loop transfer function of Figure 4.15, but placing the unrestricted allocation of the zeros of the resonant voltage controller in correct locations can cancel the oscillatory response of the complex poles. To achieve this, the equation (4.16) can be re-written as [86]:

$$G_{PR,vc}^{se}(s) = K_{p,vc}^{se} \frac{s^2 + 2\xi\omega_{nat}s + \omega_{nat}^2}{s^2 + \omega_0^2} \tag{4.17}$$

where $K_{p,vc}^{se}$ is the gain parameter of the resonant controller and ω_{nat} is the natural frequency and it is much slower than the resonant current controller. As closed-loop transfer function of Figure 4.15 has 6th order, it is impossible to obtain an optimum damping ratio of $\xi = 0.707$ for all closed-loop poles of the proposed multi-loop PR controllers. If $\xi = 0.707$ is selected for voltage controller, the zeros of voltage controller are far from its complex poles and they are close to the zeros of the current controller, and may lead to an increase in the oscillation of transient response and instability for the entire system. For the voltage controller of 4.17, choosing $\xi = 0.58$ and $K_{p,vc}^{se} = 0.0025$ can give a very good dynamic response with desired signal tracing for the multi-loop PR controllers. Figure 4.17 shows the closed-loop frequency response of the multi-loop PR controllers proposed in series-connected VSC. As can be seen, the response has a gain at $\approx 0\ dB$ and $\approx 0^{\circ}$ phase shift resulting into an excellent signal tracking for the multi-loop PR controllers.

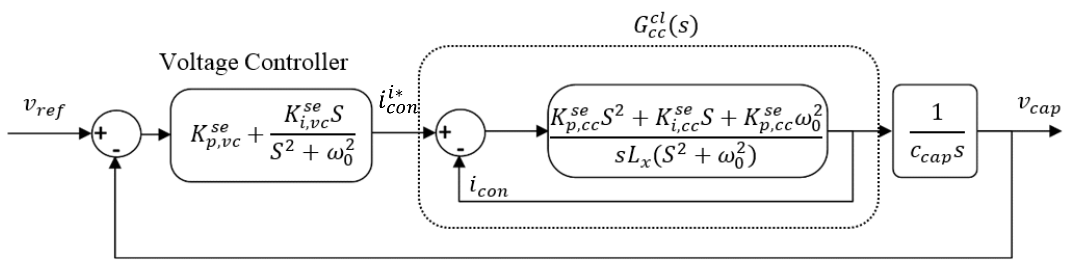

Figure 4.15: The block diagram of multi-loop PR controllers for series-connected VSC.

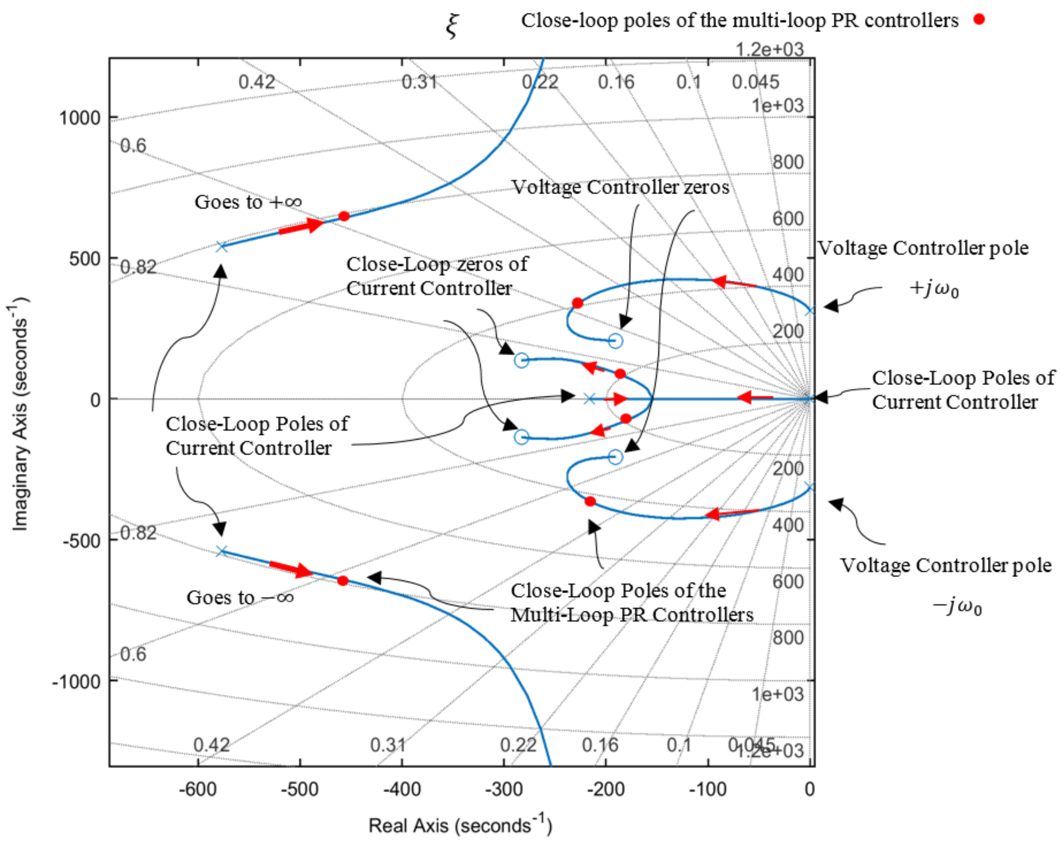

Figure 4.16: Root-locus of multi-loop PR controllers of series-connected VSC.

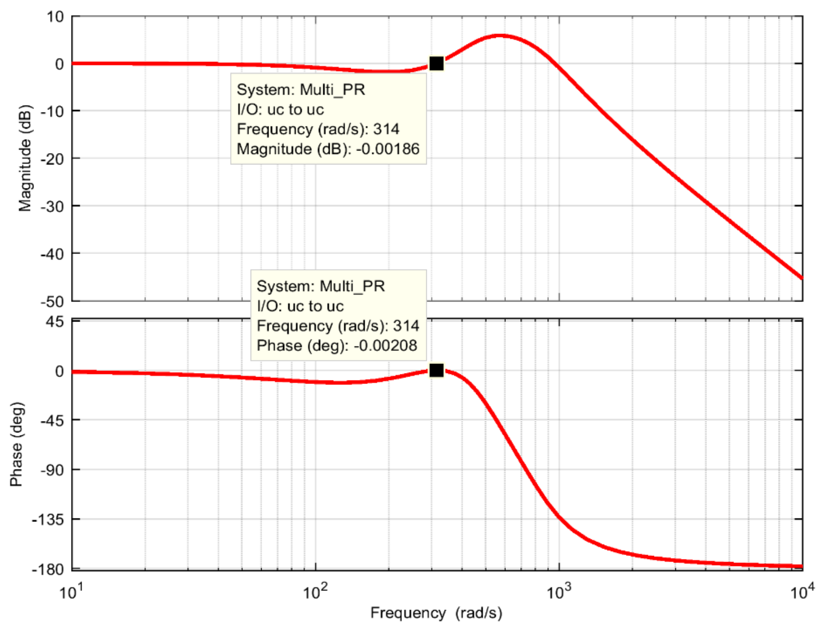

Figure 4.17: Closed-loop bode diagram of multi-loop PR controllers of series-connected VSC.

4.5 Space Vector Modulation

This section presents a 3-dimensional Space Vector Pulse Width modulation (3-D SVPWM) technique for the four-leg VSCs. In order to gain a better understating of modulation technique for the four-leg converters, the basic concept of space vector modulation of two-level three-leg VSC is explained first. Figure 2.5 or Figure 4.1 (a) without the extra neutral wire can be considered as a standard two-level three-leg VSC.

4.5.1 Two-Dimensional Space Vector Modulation

With improvement of digital microprocessors, space vector modulation has become one of the most important PWM methods for three-phase power electronic converters [127, 128]. This technique has several advantages over the carrier-based PWM [110, 129] methods such as: inherent injection of "common mode components" or "triple harmonic components", implementing both in transient and steady-state operating condition, less output current and voltage ripple, computation of the zero sequence voltage, applying different switching sequence patterns, less switching harmonic spectrum, and less switching losses [90, 128, 130].

There are four main steps to implement SVM as follow:

- The reference signal of each phase should be transformed to $\alpha\beta$ coordinate
- The non-zero and zero switching vectors are selected to synthesise the reference vector $\vec{V}_{ref}$ for one switching cycle
- The time durations of all selected switching vectors are calculated
- The switching vectors are sequenced and sent to VSC

Since the switching scheme is implemented in two-dimensional $\alpha\beta$ coordinate, this method is known as two-dimensional (2-D) space vector PWM.

4.5.1.1 Clarke Transformation

The sum of any balanced three-phase group of variables in abc frame x_a, x_b, x_c should be equal to zero ($x_a + \ x_b, +x_c = 0$). To simplify the analysis of three-phase variables, the set of variables in abc frame can be transformed into $\alpha\beta$ coordinate by a mathematical transformation known as Clarke transformation:

$$[x_\alpha \; x_\beta] = T^{\alpha\beta}.[x_a \; x_b \; x_c \,] \tag{4.18}$$

where $T^{\alpha\beta}$ is the transformation matrix and can be expressed as:

$$T^{\alpha\beta} = \frac{2}{3}\begin{bmatrix} 1 & -\frac{1}{2} & -\frac{1}{2} \\ 0 & \frac{\sqrt{3}}{2} & -\frac{\sqrt{3}}{2} \end{bmatrix} \tag{4.19}$$

Three-phase (abc) frame and two-phase stationary frame ($\alpha\beta$ frame) is shown in Figure 4.18.

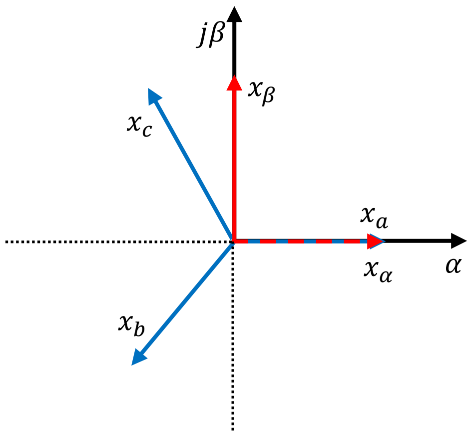

Figure 4.18: Three-phase abc and $\alpha\beta$ frames.

4.5.1.2 Space Vectors

The space vector modulation is quite a different method compared to carrier-based PWM techniques. As shown in Figure 4.19, the switching scheme for two-level three-leg VSC is based on a total of eight possible switching states, where for each leg, 'p' denotes that the upper switch is closed, and 'n' represents that the lower switch is closed. Table 4.1 shows the line-to-neutral voltage v_i , for $i = a, b, c$ for all eight switching combinations in abc frame. By applying equation (4.18) to $[v_a\ v_b\ v_c\ ]$, listed in Table 4.1, the line-to-neutral voltages of two-level three-leg VSC in $\alpha\beta$ orthogonal coordinate can be generated. The results are shown in Table 4.2.

Transforming switching states from abc frame to $\alpha\beta$ coordinate can create six non-zero switching vectors $\overrightarrow{V_1} - \overrightarrow{V_6}$ on the corners of hexagon and two zero switching vectors $\overrightarrow{V_0}$ and $\overrightarrow{V_7}$ on the origin of hexagon as shown in Figure 4.20. The six non-zero vectors $\overrightarrow{V_1} - \overrightarrow{V_6}$ are also known as active vectors, and are located symmetrically every 60^0, producing voltage in the four different quadrant of $\alpha\beta$ plane dividing the hexagon into six different sectors.

Table 4.1: Switching combinations and line-to-neutral voltage in abc frame.

	nnn	pnn	ppn	npn	npp	nnp	pnp	ppp
V_c	$-\frac{1}{2}V_{dc}$	$\frac{1}{2}V_{dc}$	$\frac{1}{2}V_{dc}$	$-\frac{1}{2}V_{dc}$	$-\frac{1}{2}V_{dc}$	$-\frac{1}{2}V_{dc}$	$\frac{1}{2}V_{dc}$	$\frac{1}{2}V_{dc}$
V_b	$-\frac{1}{2}V_{dc}$	$-\frac{1}{2}V_{dc}$	$\frac{1}{2}V_{dc}$	$\frac{1}{2}V_{dc}$	$\frac{1}{2}V_{dc}$	$-\frac{1}{2}V_{dc}$	$-\frac{1}{2}V_{dc}$	$\frac{1}{2}V_{dc}$
V_a	$-\frac{1}{2}V_{dc}$	$-\frac{1}{2}V_{dc}$	$-\frac{1}{2}V_{dc}$	$-\frac{1}{2}V_{dc}$	$\frac{1}{2}V_{dc}$	$\frac{1}{2}V_{dc}$	$\frac{1}{2}V_{dc}$	$\frac{1}{2}V_{dc}$

Table 4.2: Switching combinations and line-to-neutral voltage in αβ frame

	nnn	pnn	ppn	npn	npp	nnp	pnp	ppp
V_α	0	$\frac{2}{3}V_{dc}$	$\frac{1}{3}V_{dc}$	$-\frac{1}{3}V_{dc}$	$-\frac{2}{3}V_{dc}$	$-\frac{1}{3}V_{dc}$	$\frac{1}{3}V_{dc}$	0
V_β	0	0	$\frac{1}{\sqrt{3}}V_{dc}$	$\frac{1}{\sqrt{3}}V_{dc}$	0	$-\frac{1}{\sqrt{3}}V_{dc}$	$-\frac{1}{\sqrt{3}}V_{dc}$	0

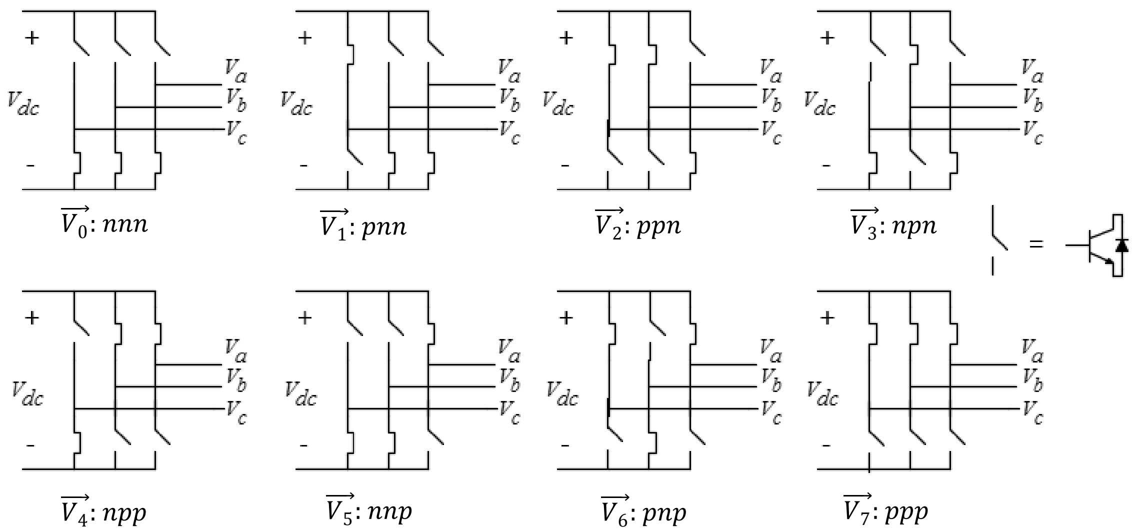

Figure 4.19: Switching states of two-level three-leg VSC.

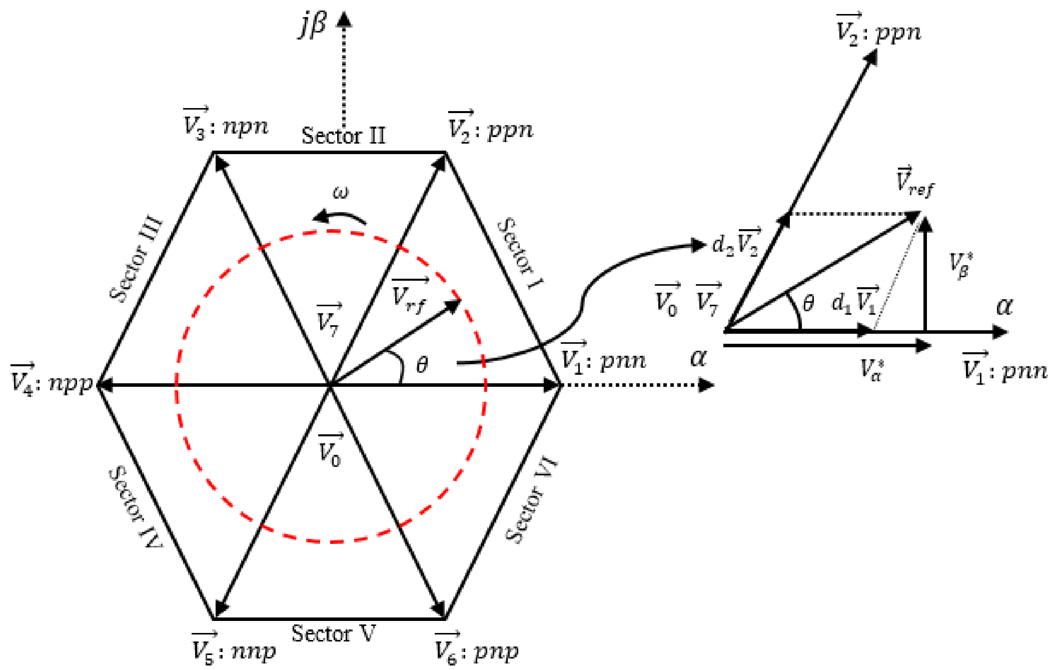

Figure 4.20: The two-dimensional space vector representation.

The objective of the SVM technique is to synthesise the reference vector $\vec{V}_{ref}$ using the available switching vectors [13]. $\vec{V}_{ref}$ can be obtained by transforming three-phase references in abc frame to $\alpha\beta$ plane as shown in Figure 4.20. $\vec{V}_{ref}$ is laying between two adjacent active vectors $\vec{V}_k$ and $\vec{V}_{k+1}$, and rotates around a circle at the frequency of ω. The reference voltage vector is given by:

$$\vec{V}_{ref} = v_\alpha^* + jv_\beta^* \tag{4.20}$$

$$\measuredangle\vec{V}_{ref} = \theta = \omega t = atan\left(v_\beta^*/v_\alpha^*\right) \tag{4.21}$$

4.5.1.3 Time Duration of Switching Vectors

The reference vector $\vec{V}_{ref}$ is determined by time averaging of the available switching vectors. The reference vector is sampled over a cycle and the interval of each sample is defined as T_s ($T_s = {}^1/_{F_s}$, F_s is switching frequency). By referring to Figure 4.20, for sector I, equation (4.20) this can be re-written as:

$$\vec{V}_{ref} = \frac{d_1.\vec{V_1} + d_2.\vec{V_2} + d_0.\vec{V_0}}{T_s} \tag{4.22}$$

where d_0 is the duty ratio of zero switching vector and d_1,d_2 are duty ratios of non-zero switching vectors.). The time duration of each vector of sector I can be expressed as:

$$d_1 = \frac{T_s\sqrt{3}\left|\vec{V}_{ref}\right|}{V_{DC}}\sin\left(\frac{\pi}{3} - \theta\right) \tag{4.23}$$

$$d_2 = \frac{T_s\sqrt{3}\left|\vec{V}_{ref}\right|}{V_{DC}}\sin(\theta) \tag{4.24}$$

$$d_0 = T_s - d_1 - d_2 \tag{4.25}$$

4.5.1.4 Switching Sequence Schemes of Two-Dimensional Space Vector Modulation

After selecting the reference vector, switching vectors and their respective time durations, a well-defined sequence needs to be set for these vectors. However, the switching sequence is not unique and there are several ways to sequence the switching vectors. [112] has proved that symmetrically aligned switching scheme using two zero vectors has the lowest harmonic distortion and switching loss in comparison to other switching sequencing schemes. The symmetrically aligned switching sequence scheme is shown in Figure 4.21. More details about switching sequence schemes of space vector modulation can be found in [112, 127, 131, 132].

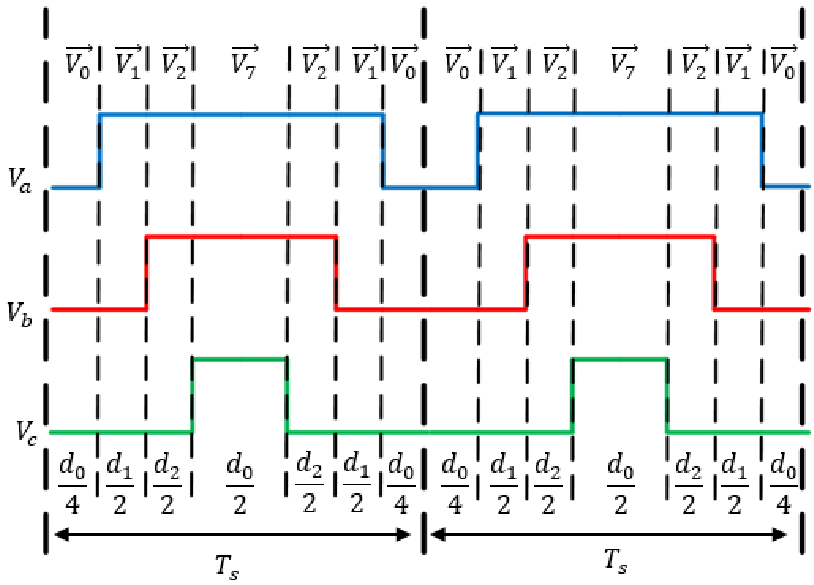

Figure 4.21: Symmetrically aligned switching sequencing scheme using two zero vectors for 2-D SVPWM.

4.5.2 Three-Dimensional Space Vector Modulation

Now consider an unbalanced three-phase group of variables in abc frame x_a, x_b, x_c. The sum of these unbalanced three-phase variables is not equal to zero anymore:

$$x_a + \ x_b, + x_c \neq 0 \tag{4.26}$$

These three variables can be voltage or current and they are independent of each other and two-dimensional SVM does not have enough degrees of freedom to be able to describe them fully. Therefore, for an unbalanced system, the explained two-dimensional space vector modulation is not valid. As a result, in this case the neutral current is equal to the sum of three-phase currents as given by:

$$i_a + \ i_b + i_c = i_n \neq 0 \tag{4.27}$$

The presence of the fourth leg for the four-leg VSC requires a more complex control algorithm for the modulation of the output voltages in comparison to the two-level three-leg VSC leading to a three-dimensional SVM to be introduced.

The concept of three- dimensional SVM in $\alpha\beta\gamma$ coordinates frame was introduced by *Zhang et. al.* in 1997 [108, 112]. This method is the extension of two-dimensional SVM technique which was explained in section 4.5.1. Next section of this chapter will present the three-dimensional SVM in $\alpha\beta\gamma$ coordinates frame in more detail. The three-dimensional space vector in $\alpha\beta\gamma$ reference frame is the most promising modulation strategy for the four-leg applications [112]; as a result, it will be used as the main modulation technique in this thesis.

4.5.2.1 Space Vectors of SVM in $\alpha\beta\gamma$ Frame

In three-dimensional SVM in $\alpha\beta\gamma$ coordinate frames method, the zero sequence of the converter is represented by a third coordinate known as γ. Therefore, for a set of unbalanced variables x_a, x_b, x_c in the abc frame, equations (4.18) and (4.19) can be extended to:

$$\left[x_\alpha \; x_\beta \; x_\gamma\right] = T^{\alpha\beta\gamma}.\left[x_a \; x_b \; x_c\,\right] \tag{4.28}$$

where $T^{\alpha\beta\gamma}$ is the transformation matrix and can be expressed as:

$$T^{\alpha\beta\gamma} = \frac{2}{3}\begin{bmatrix} 1 & -\frac{1}{2} & -\frac{1}{2} \\ 0 & \frac{\sqrt{3}}{2} & -\frac{\sqrt{3}}{2} \\ \frac{1}{2} & \frac{1}{2} & \frac{1}{2} \end{bmatrix} \tag{4.29}$$

As mentioned before, a standard two-level three-leg VSC has eight (2^3) possible switching arrangements. By adding a fourth neutral leg the total number of switching combinations increases to sixteen (2^4) as shown in Figure 4.22. For each leg of this four-leg VSC, 'p' indicates that the upper switch is closed and 'n' represents that the lower switch is closed.

Table 4.3 shows the line-to-neutral voltage v_i, for $i = a, b, c$ in abc frame, and also the corresponding line-to-neutral voltages in $\alpha\beta\gamma$ orthogonal coordinate frames for all sixteen switching combinations. It should be noted that v_γ is the zero sequence component and is associated to neutral current. There are four main steps to implement SVM:

- The reference signal of each phase should be transformed to $\alpha\beta\gamma$ coordinate
- Prisms and corresponded tetrahedrons need to be identified and then non-zero and zero switching vectors are selected to synthesise reference vector $\vec{V}^*_{\alpha\beta\gamma}$ for one switching cycle

- The time durations of all selected switching vectors are calculated
- The switching vectors are sequenced and sent to VSC

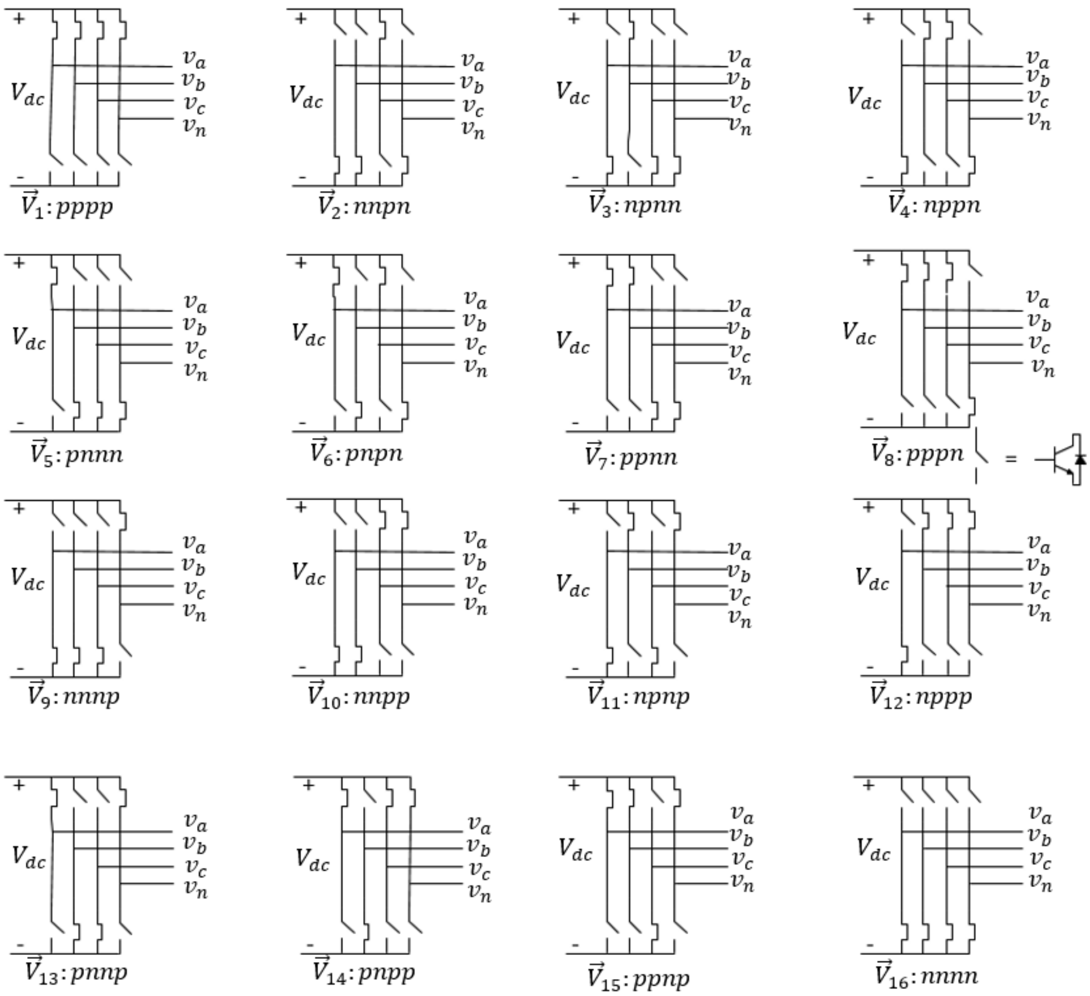

Figure 4.22: Switching states of two-level four-leg VSC.

Table 4.3: Switching vectors and corresponded line-to- neutral voltages of four-leg VSC in $\alpha\beta\gamma$ coordinates frame.

Vectors	$S_a\, S_b\, S_c\, S_n$	v_a	v_b	v_c	v_γ	v_α	v_β
$\vec{V}_9$	$n\ n\ n\ p$	$-V_{dc}$	$-V_{dc}$	$-V_{dc}$	$-V_{dc}$	0	0
$\vec{V}_{10}$	$n\ n\ p\ p$	$-V_{dc}$	$-V_{dc}$	0		$-\frac{1}{3}V_{dc}$	$-\frac{1}{\sqrt{3}}V_{dc}$
$\vec{V}_{11}$	$n\ p\ n\ p$	$-V_{dc}$	0	$-V_{dc}$	$-\frac{2}{3}V_{dc}$	$-\frac{1}{3}V_{dc}$	$+\frac{1}{\sqrt{3}}V_{dc}$
$\vec{V}_{13}$	$p\ n\ n\ p$	0	$-V_{dc}$	$-V_{dc}$		$+\frac{2}{3}V_{dc}$	0
$\vec{V}_{12}$	$n\ p\ p\ p$	$-V_{dc}$	0	0		$-\frac{2}{3}V_{dc}$	0
$\vec{V}_{14}$	$p\ n\ p\ p$	0	$-V_{dc}$	0	$-\frac{1}{3}V_{dc}$	$+\frac{1}{3}V_{dc}$	$-\frac{1}{\sqrt{3}}V_{dc}$
$\vec{V}_{15}$	$p\ p\ n\ p$	0	0	$-V_{dc}$		$+\frac{1}{3}V_{dc}$	$+\frac{1}{\sqrt{3}}V_{dc}$
$\vec{V}_{16}$	$n\ n\ n\ n$	0	0	0	0	0	0
$\vec{V}_1$	$p\ p\ p\ p$	0	0	0	0	0	0
$\vec{V}_2$	$n\ n\ p\ n$	0	0	$+V_{dc}$		$-\frac{1}{3}V_{dc}$	$-\frac{1}{\sqrt{3}}V_{dc}$
$\vec{V}_3$	$n\ p\ n\ n$	0	$+V_{dc}$	0	$+\frac{1}{3}V_{dc}$	$-\frac{1}{3}V_{dc}$	$+\frac{1}{\sqrt{3}}V_{dc}$
$\vec{V}_5$	$p\ n\ n\ n$	$+V_{dc}$	0	0		$+\frac{2}{3}V_{dc}$	0
$\vec{V}_4$	$n\ p\ p\ n$	0	$+V_{dc}$	$+V_{dc}$		$-\frac{2}{3}V_{dc}$	0
$\vec{V}_6$	$p\ n\ p\ n$	$+V_{dc}$	0	$+V_{dc}$	$+\frac{2}{3}V_{dc}$	$+\frac{1}{3}V_{dc}$	$-\frac{1}{\sqrt{3}}V_{dc}$
$\vec{V}_7$	$p\ p\ n\ n$	$+V_{dc}$	$+V_{dc}$	0		$+\frac{1}{3}V_{dc}$	$+\frac{1}{\sqrt{3}}V_{dc}$
$\vec{V}_8$	$p\ p\ p\ n$	$+V_{dc}$	$+V_{dc}$	$+V_{dc}$	$+V_{dc}$	0	0

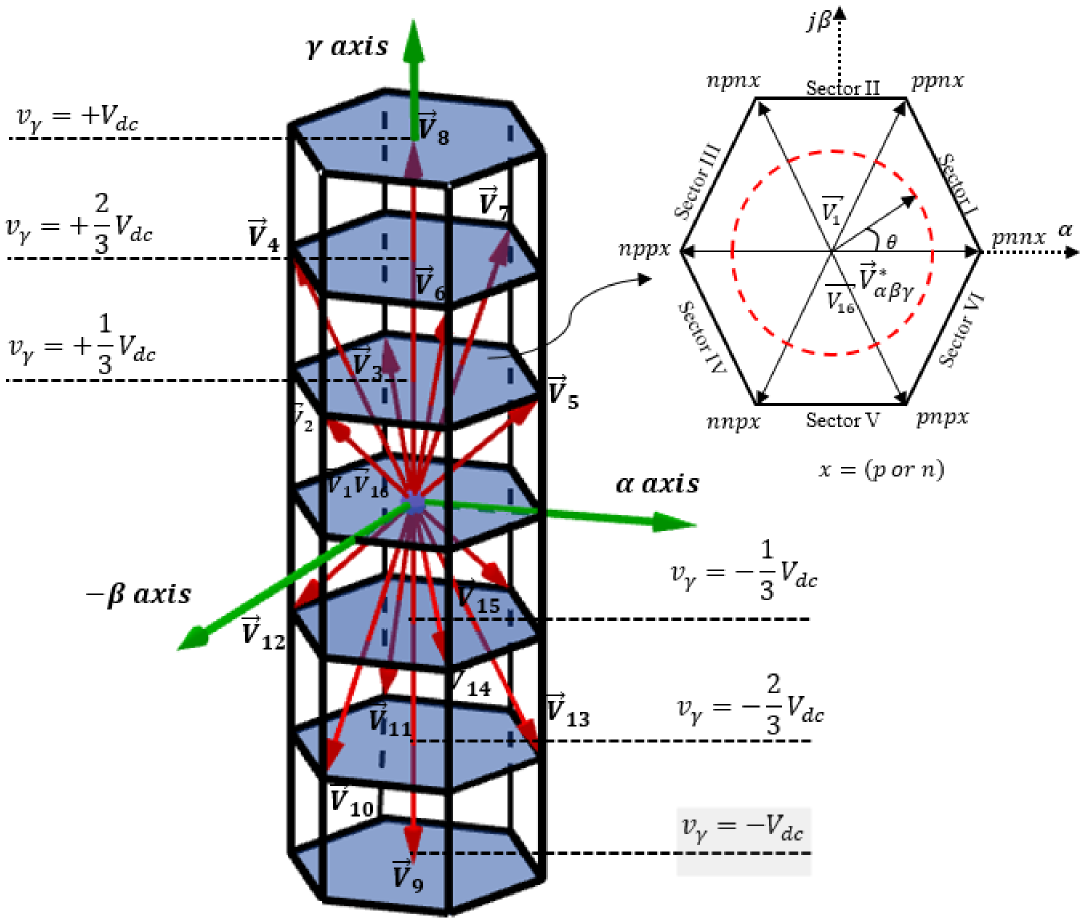

Figure 4.23: Control region of hexagonal prism with switching vectors for four-leg VSC in $\alpha\beta\gamma$ coordinate frames.

Figure 4.23 shows the space of vectors for all possible sixteen switching vectors $\vec{V}_1 - \vec{V}_{16}$ in three-dimensional space. These vectors create a hexagonal prism with fourteen non-zero or active vectors $\vec{V}_2 - \vec{V}_{15}$ spread in allowable space in addition to two zero vectors $\vec{V}_1$ and $\vec{V}_{16}$, which are placed at the origin of $\alpha\beta\gamma$ coordinate frame. The hexagonal prism is divided into seven different layers, where each layer v_γ (zero sequence) has a voltage level of $\left[-1, -\frac{2}{3}, -\frac{1}{3}, 0, +\frac{1}{3} + \frac{2}{3}, +1\right].V_{dc}$ as presented in Table 4.3. Furthermore, each layer is a hexagon in the $\alpha\beta$ plane which is divided into six sectors where each sector can be stretched in γ axis creating a triangular prism in space. There are six sectors in a hexagon resulting into six prisms in total with each prism rotating 60° from the previous prism. Each prism can be subdivided into four tetrahedrons in $\alpha\beta\gamma$ space. The prisms corresponding to each sector and four tetrahedrons of prism I are shown in Figure 4.24 and Figure 4.25, respectively. Each tetrahedron has three active voltage vectors and two zero voltage vectors. In three-dimensional SVM, the reference voltage vector $\vec{V}^*_{\alpha\beta\gamma}$ is formed from three adjacent active voltage vectors and the two zero voltage vectors. The reference voltage in $\alpha\beta\gamma$ frame can be obtained from equation (4.28) and the adjacent vectors can be identified by two steps: prism identification followed by determining the corresponding tetrahedron.

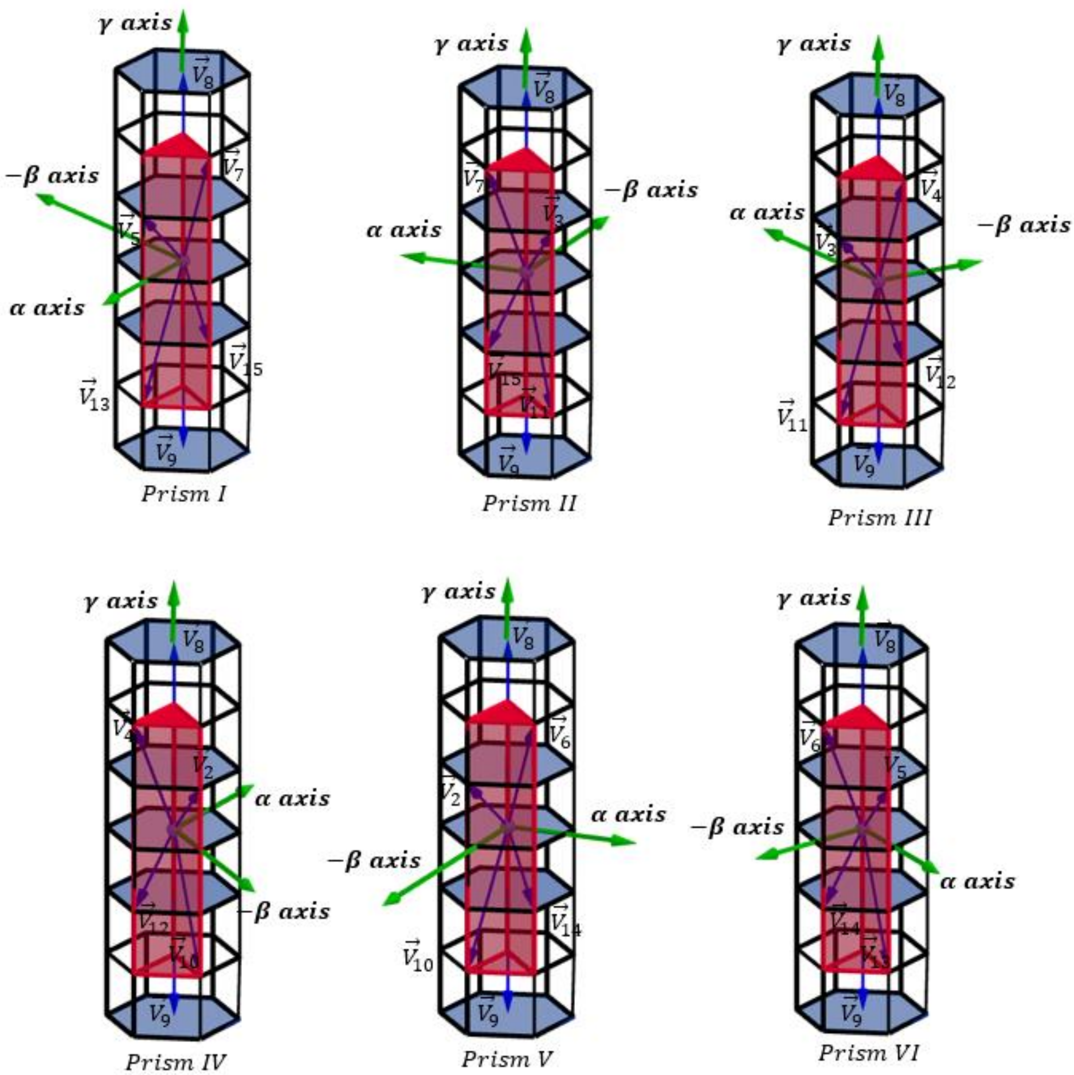

Figure 4.24: Triangular prisms of four-leg VSC in $\alpha\beta\gamma$ coordinate frames.

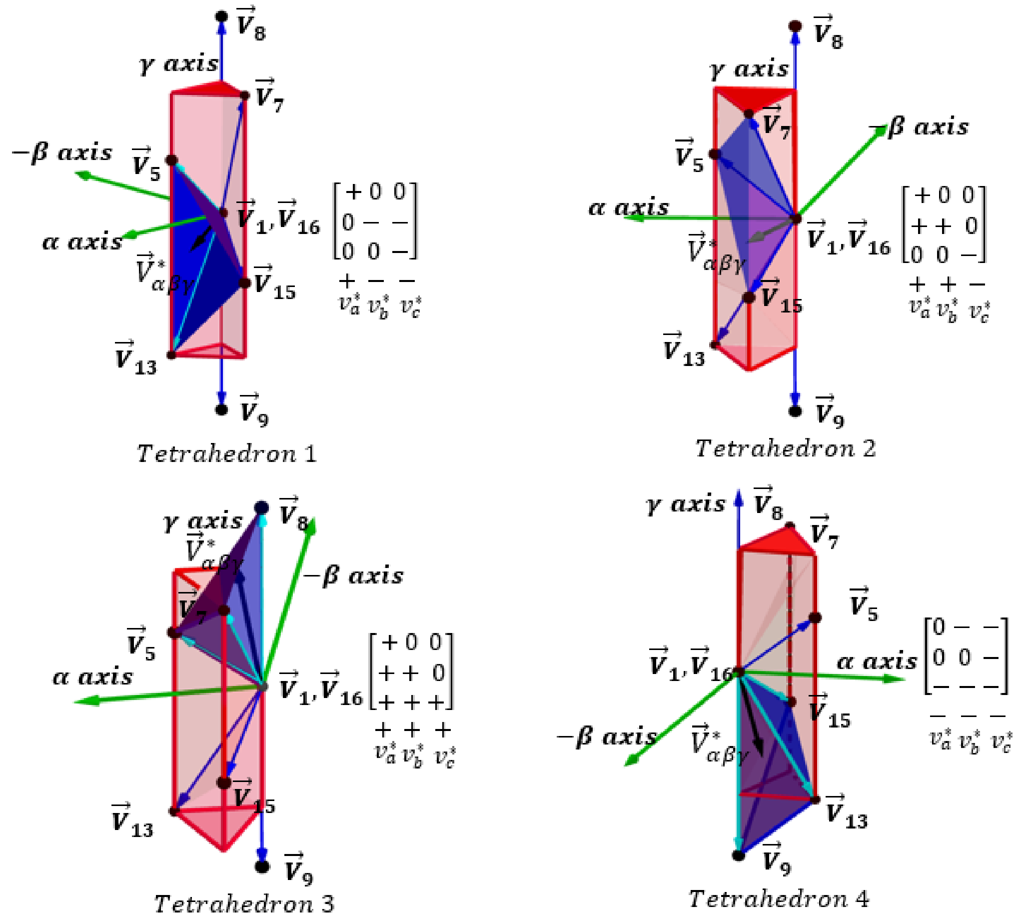

Figure 4.25: Presentations of tetrahedrons for triangular prism I in $\alpha\beta\gamma$ coordinate frames.

4.5.2.2 Prism and Tetrahedron Identification

Using the projection of the reference vector in the $\alpha\beta$ plane, prism identification is straightforward and is similar to 2-D SVM with tetrahedron identification being the main complexity of three-dimensional SVM in the $\alpha\beta\gamma$ frame. The prism can be determined by several methods with one method being similar to subsection 4.5.1.2 where the sectors of the reference vectors $v_{\alpha\beta}^{*}$ can be obtained based on angle of the reference vector θ (equation (4.21)):

$$\begin{cases} Prism\ I: 0 \leq \theta < \dfrac{\pi}{3}\,, & Prism\ II: \dfrac{\pi}{3} \leq \theta < \dfrac{2\pi}{3} \\ Prism\ III: \dfrac{2\pi}{3} \leq \theta < \pi\,, & Prism\ IV: \pi \leq \theta < \dfrac{4\pi}{3} \\ Prism\ V: \dfrac{4\pi}{3} \leq \theta < \dfrac{5\pi}{3}\,, & Prism\ IV: \dfrac{5\pi}{3} \leq \theta < 0 \end{cases} \tag{4.30}$$

The other method for prism identification is the algorithm presented in Figure 4.26. The reference voltages in abc frame v_i^* for $i = a, b, c$ are transformed to $\alpha\beta$ coordinate by applying equation (4.18) without considering the γ axis.

Once the prisms have been identified, the corresponded tetrahedrons for each prism are required to be determined. As mentioned before, each prism has four tetrahedrons. As a result, there are twenty four possible tetrahedrons in the overall hexagonal prism. To avoid complex tetrahedron determination in three-dimensional space, a simple comparison look-up table as shown in Table 4.4 has been used. When the prisms are identified, the polarity of the reference voltages v_i^* for $i = a, b, c$ in the abc frame are compared. This allows the corresponded tetrahedrons of each prism to be found easily. For instance, let us consider that the reference vector is located in prism I and the polarities of reference voltages in abc frame are $[+, +, -]$, from Figure 4.25, only tetrahedron 2 with active vectors $\vec{V}_5, \vec{V}_7$ and $\vec{V}_{15}$ can satisfy the demanded voltages. Table 4.4 presents the corresponded active vectors and polarity of the reference voltages for all twenty four possible tetrahedrons.

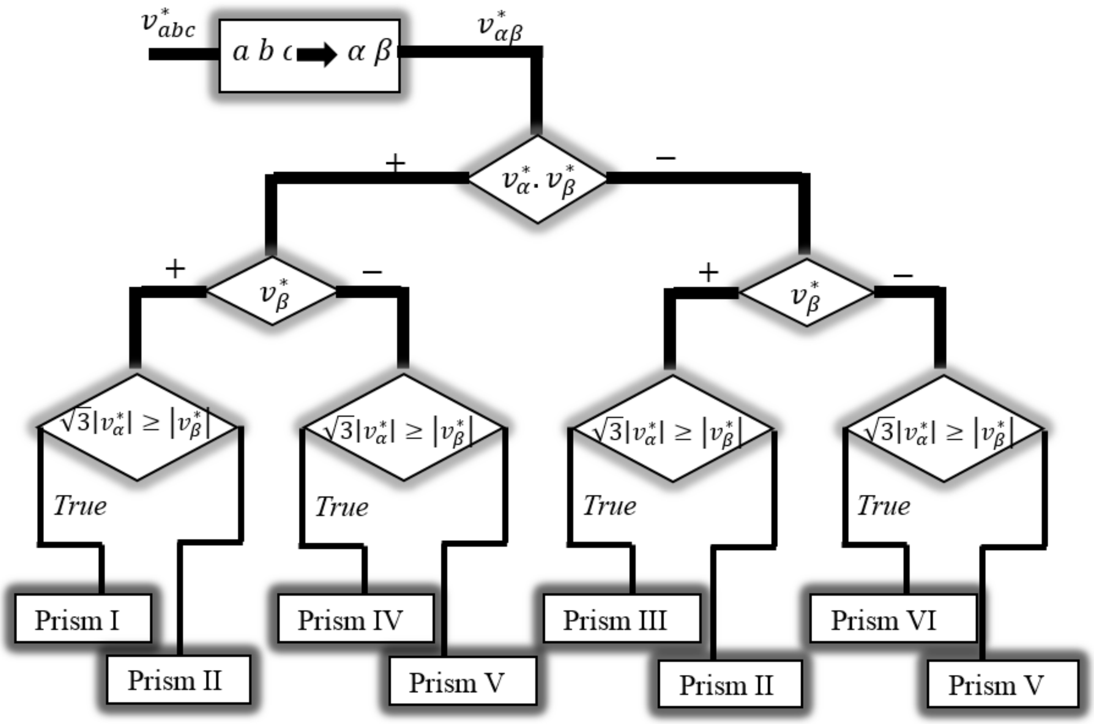

Figure 4.26: Flowchart diagram for prism identification, three-dimensional SVM in $\alpha\beta\gamma$ coordinate frames.

Table 4.4: Tetrahedron and active vectors look-up table for 3-D SVM in αβγ frame.

Prism	**Tetrahedron**	**Active Vectors**	$\boldsymbol{v_a^*}\ \boldsymbol{v_b^*}\ \boldsymbol{v_c^*}$
Prism I	1	$\vec{V}_5 - \vec{V}_{13} - \vec{V}_{15}$	$+\ -\ -$
	2	$\vec{V}_5 - \vec{V}_7 - \vec{V}_{15}$	$+\ +\ -$
	3	$\vec{V}_5 - \vec{V}_7 - \vec{V}_8$	$+\ +\ +$
	4	$\vec{V}_{13} - \vec{V}_{15} - \vec{V}_9$	$-\ -\ -$
Prism II	1	$\vec{V}_7 - \vec{V}_{15} - \vec{V}_3$	$+\ +\ -$
	2	$\vec{V}_{15} - \vec{V}_3 - \vec{V}_{11}$	$-\ +\ -$
	3	$\vec{V}_7 - \vec{V}_3 - \vec{V}_8$	$+\ +\ +$
	4	$\vec{V}_{15} - \vec{V}_{11} - \vec{V}_9$	$-\ -\ -$
Prism III	1	$\vec{V}_3 - \vec{V}_{11} - \vec{V}_{12}$	$-\ +\ -$
	2	$\vec{V}_3 - \vec{V}_4 - \vec{V}_{12}$	$-\ +\ +$
	3	$\vec{V}_3 - \vec{V}_4 - \vec{V}_8$	$+\ +\ +$
	4	$\vec{V}_{11} - \vec{V}_{12} - \vec{V}_9$	$-\ -\ -$
Prism IV	1	$\vec{V}_4 - \vec{V}_{12} - \vec{V}_2$	$-\ +\ +$
	2	$\vec{V}_{12} - \vec{V}_2 - \vec{V}_{10}$	$-\ -\ +$
	3	$\vec{V}_4 - \vec{V}_2 - \vec{V}_8$	$+\ +\ +$
	4	$\vec{V}_{12} - \vec{V}_{10} - \vec{V}_9$	$-\ -\ -$
Prism V	1	$\vec{V}_2 - \vec{V}_{10} - \vec{V}_{14}$	$-\ -\ +$
	2	$\vec{V}_2 - \vec{V}_6 - \vec{V}_{14}$	$+\ -\ +$
	3	$\vec{V}_2 - \vec{V}_6 - \vec{V}_8$	$+\ +\ +$
	4	$\vec{V}_{10} - \vec{V}_{14} - \vec{V}_9$	$-\ -\ -$
Prism VI	1	$\vec{V}_{14} - \vec{V}_5 - \vec{V}_{13}$	$+\ -\ -$
	2	$\vec{V}_6 - \vec{V}_{14} - \vec{V}_5$	$+\ -\ +$
	3	$\vec{V}_6 - \vec{V}_5 - \vec{V}_8$	$+\ +\ +$
	4	$\vec{V}_{14} - \vec{V}_{13} - \vec{V}_9$	$-\ -\ -$

4.5.2.3 Time Durations of Switching Vectors

Once the active vectors of each tetrahedron are obtained, the related time durations of each applied switching vector are required to be calculated. The reference vector $\vec{V}^*_{\alpha\beta\gamma}$ is obtained by time averaging of available active switching vectors over a cycle with interval of T_s ($T_s = {}^{1}/_{F_s}$, F_s is switching frequency). The time duration of each selected switching vector can be calculated by projecting the reference vector on the switching vectors for corresponding tetrahedron and prism [112]. For instance, let us assume that vector $\vec{V}^*_{\alpha\beta\gamma}$ is located in Prism I tetrahedron 2; the $\vec{V}^*_{\alpha\beta\gamma}$ can be expressed as:

$$\vec{V}^*_{\alpha\beta\gamma}.T_s = d_1\vec{V}_5 + d_2\vec{V}_7 + d_3\vec{V}_{15} \tag{4.31}$$

Time duration calculations of the selected switching vectors can be given by [112]:

$$\begin{bmatrix} d_1 \\ \\ d_2 \\ \\ d_3 \end{bmatrix} = \frac{T_s}{V_{dc}}[G]\begin{bmatrix} v^*_\alpha \\ \\ v^*_\beta \\ \\ v^*_\gamma \end{bmatrix} \tag{4.32}$$

$$d_0 = T_s - d_1 - d_2 - d_3 \tag{4.33}$$

where d_0 and $d_1 - d_3$ are time durations for zero vectors and non-zero vectors, respectively and G is the matrix needed to compute the duty ration. A complete look-up table of matrix G for all possible 24 tetrahedrons is summarised in Appendix B.

4.5.2.4 Switching Sequence Schemes of Three-Dimensional SVM in $\alpha\beta\gamma$ frame

The switching sequence scheme is similar to two-dimensional SVM explained in subsection 4.5.1.3, but instead of having two active (none-zero) vectors, three active vectors have been used. From several possible switching sequence schemes, symmetrically sequence pattern with two zero vectors is a suitable option to minimise harmonic distortion and switching losses [112]. Figure 4.27 shows the proposed symmetrically aligned sequence schemes with two zero vectors for prism I and tetrahedron 1 used in this thesis. The switching scheme initiates with zero vector $\vec{V}_{16}(nnnn)$ and nine sequences at each sampling time T_s. More details about switching sequence schemes of 3-D SVPWM can be found in [112].

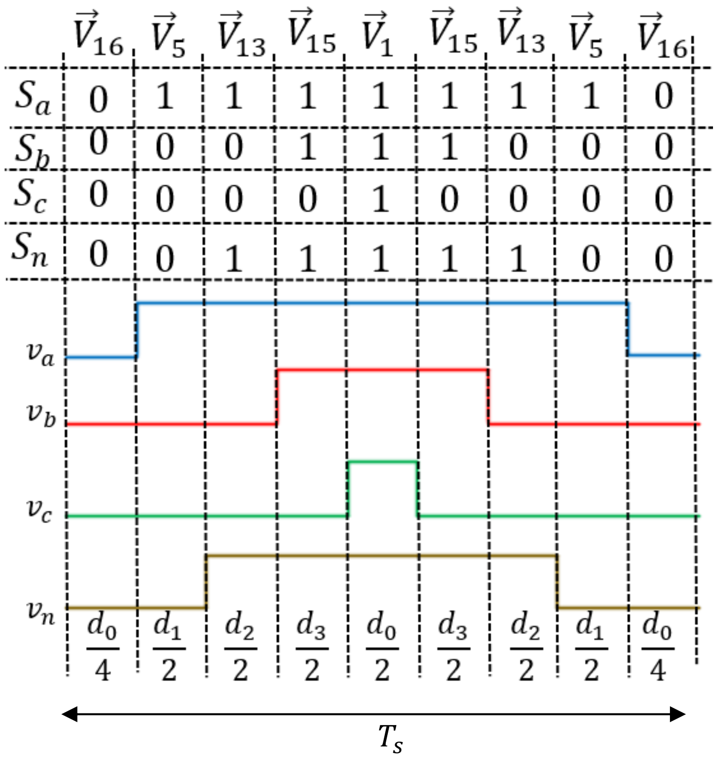

Figure 4.27: Symmetrically aligned switching sequence scheme for four-leg VSCs.

4.6 Conclusion

The control structure of the grid-connected VSCs is important as it defines the voltage controllability and dynamic response. The advantages of PR controller is the possibility of tuning the desired resonant frequency for precise fundamental reference tracking of the voltage/current for grid-connected VSCs.

A four-leg VSC is a distinctive topology because of the existence of the fourth leg when compared to a three-phase three-wire VSC. Consequently, it needs a more complex control algorithm for the modulation of the output voltages in order to control the neutral current circulation. Three-dimensional SVM methods in the $\alpha\beta\gamma$ frame is the most flexible modulation technique that satisfies all the features of four-leg VSC. The advantages of the three-dimensional SVM method in the $\alpha\beta\gamma$ frame can be summarised as follows:

- The modulation region of four-leg VSC in the $\alpha\beta\gamma$ frame is an extension of the standard two-dimensional SVM in three-dimensional space. This allows having several switching sequence schemes and selective harmonic elimination for different applications requirements
- The complex calculations can be calculated only once and presented as pre-set look-up tables for ease of referral
- This method is feasible for converters with several switches, such as a multilevel converters

Due to advantages of three-dimensional SVM in the $\alpha\beta\gamma$ coordinate frame, this modulation technique will be used for the proposed four-leg VSC in this thesis.

CHAPTER 5: Control of Hybrid Substation

Summary: *This Chapter introduces a robust control algorithm to control the compensated injection voltage of the hybrid substation using symmetrical components estimation. In addition, this chapter presents the performance of the hybrid substation under different case studies. Simulation studies carried out by PLECS software and results show the robustness and fast response of the proposed hybrid substation. The presented controller works effectively for all test cases considered, such as voltage sags, swells and unbalanced.*

5.1 Introduction

The main objective of the hybrid substation is to balance and regulate the load voltages at the reference value. This can be achieved by maintaining the positive sequence components at a pre-determined value (reference value), in addition to reducing both the negative and zero sequences (disturbance signals), at the time when the substation is connected to an unbalanced system. Figure 5.1 shows the general configuration of the hybrid substation connected to a two-feeder network (the simplified version of Figure 4.2).

Compensation for grid voltage disturbances can be achieved in various ways. The most popular approach is to use PLL in order to synchronise the injected voltages with the grid voltages [133, 134]. In this method, PLL computes the phase angle and the magnitude of the grid voltage to generate the required injection voltage when a fault occurs. However, this technique is suitable for symmetric voltage sag and swell and it has an unsatisfactory performance under asymmetric voltage disturbances as undesired negative and zero sequence components are created [135-137]. The lack of negative and zero sequence detection by this method can create phase oscillation when there is an unbalanced fault. The negative sequence components can create 2nd, 5th , 8th and 11th harmonic contents and zero sequence components can produce 3rd ,6th and 9th harmonics [138]. The harmonics can create difficulty in voltage disturbance detection, leading to an increase in the required injection voltage and the size of DC-link [137]. Therefore, a robust technique is needed to extract instantaneous positive, negative and zero sequence components (symmetrical components) in order to minimise the amount of the injection voltage under various grid voltage disturbances. It is vital to extract symmetrical components not only for controlling the hybrid substation, but also for detecting and assessing the instantaneous power quality of the system.

This chapter introduces an approach for controlling the hybrid substation based on symmetrical components estimation. This chapter also presents the simulation results that validate the effectiveness of the proposed control algorithm for the control of hybrid substation. Simulation have been carried out using the PLECS simulation program. The proposed method has been implemented in the experimental work (Chapter 7) of this thesis.

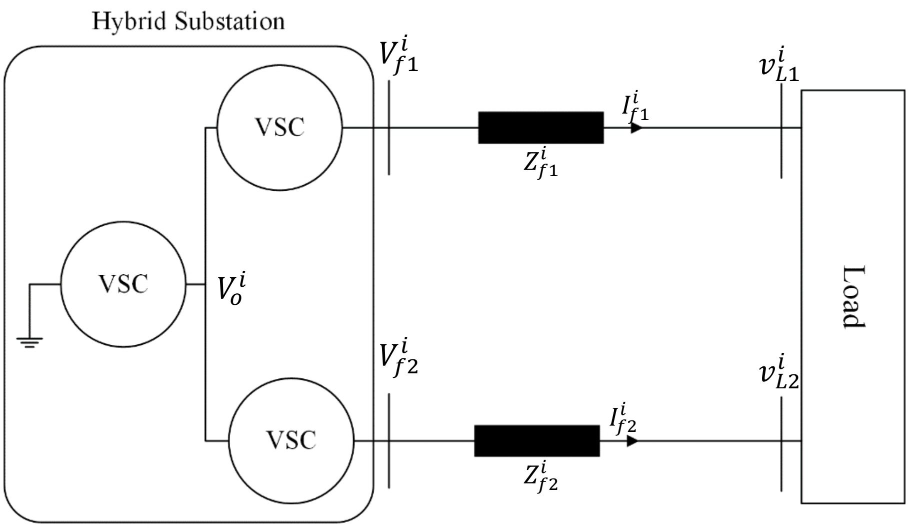

Figure 5.1: General configuration of the hybrid substation connected to a two-feeder system.

5.2 Hybrid Substation Control Strategy

Let us refer to 5.1 (or Figure 4.2 (a)), during normal operation, the output voltage of the hybrid transformer is set to the optimum value, $V_o^i = V_{o,optimum}^i$ for $i = a, b, c$. If any fault occurs and changes the pre-defined optimum voltage value, the hybrid transformer injects the required voltage to keep its output voltage at a pre-determined value which is $V_{o,optimum}^i$. The proposed hybrid substation can instantaneously receive the flowing currents of the feeder ($I_{fj}^a, I_{fj}^b, I_{fj}^c$) and substation-end voltages ($V_{fj}^a, V_{fj}^b, V_{fj}^c$). The hybrid substation has the information on feeder impedances for each phase ($Z_{fj}^a, Z_{fj}^b, Z_{fj}^c$) and as a result, the voltage at the load terminals can be estimated by hybrid substation as follows:

$$v_{Lj}^i = V_{fj}^i \ - Z_{fj}^i I_{fj}^i \tag{5.1}$$

where $i = a, b, c$ and $j = 1, \dots, \mathfrak{n}$.

As discussed in Chapter 3, while the hybrid transformer keeps its output voltage at the optimum value ($V_{o,optimum}^i$), if any feeder voltage disturbances occur, the feeders' VSCs of hybrid substation compensates the feeder and keeps the load balanced at the reference value.

To calculate the required injection voltage, the positive and negative sequences should be extracted. Let us refer to equations (2.4), (2.5) and (4.18), the positive and negative sequence components of x_{abc} can be expressed in the $\alpha\beta$ reference frame by using Clarke's transformation as follows:

$$\begin{cases} x_{\alpha\beta}^+ = \left[T^{\alpha\beta}\right].\, x_{abc}^+ \\ x_{\alpha\beta}^- = \left[T^{\alpha\beta}\right].\, x_{abc}^- \end{cases} \tag{5.2}$$

where $T^{\alpha\beta}$ is the Clarke transformation matrix and expressed in (4.18). Using (2.4) and (2.5), the positive and negative sequence components can be given by:

$$\begin{cases} x_{\alpha\beta}^+ = \left[T^{\alpha\beta}\right].\, [T^+].\, x_{abc} \\ x_{\alpha\beta}^- = \left[T^{\alpha\beta}\right].\, [T^-].\, x_{abc} \end{cases} \tag{5.3}$$

where T^{+} and T^{-} are the transformation matrices of (2.4) and (2.5) respectively. Now by applying inverse transformation, the equation (5.3) can be re-written as:

$$\begin{cases} x_{\alpha\beta}^{+} = \left[T^{\alpha\beta}\right].\left[T^{+}\right].\left[T^{\alpha\beta}\right]^{-1}.x_{\alpha\beta} \\ x_{\alpha\beta}^{-} = \left[T^{\alpha\beta}\right].\left[T^{-}\right].\left[T^{\alpha\beta}\right]^{-1}.x_{\alpha\beta} \end{cases} \tag{5.4}$$

Consequently, three-phase group of variables x_a, x_b, x_c in abc frame, can be expressed in positive and negative $\alpha\beta$ reference frame as follows [33]:

$$x_{\alpha\beta}^{+} = \frac{1}{2}\begin{bmatrix} 1 & -e^{-j\frac{\pi}{2}} \\ e^{-j\frac{\pi}{2}} & 1 \end{bmatrix}.\begin{bmatrix} x_{\alpha} \\ x_{\beta} \end{bmatrix} \tag{5.5}$$

$$x_{\alpha\beta}^{-} = \frac{1}{2}\begin{bmatrix} 1 & e^{-j\frac{\pi}{2}} \\ -e^{-j\frac{\pi}{2}} & 1 \end{bmatrix}.\begin{bmatrix} x_{\alpha} \\ x_{\beta} \end{bmatrix} \tag{5.6}$$

where $e^{-j\frac{\pi}{2}}$ is a 90° lagging phase-shifting operator applied on the time domain to obtain a quadrature version of the input signals. The overview of the symmetrical component model and its associated comparison with the conventional injection method (PLL) can be found in Appendix C.

The hybrid substation can balance and regulate load voltage by keeping the positive sequence component at the reference value in addition to considering both the negative and zero sequence components. To achieve that, the magnitude and phase angle of the positive and negative sequence voltage in synchronous reference frame should be calculated [139]. The magnitude and the angle of the positive sequence voltage can be expressed by:

$$\begin{cases} |V^{+}| = \sqrt{(V_d^{+})^2 + (V_q^{+})^2} \\ \theta^{+} = \tan^{-1}\left(\frac{V_q^{+}}{V_d^{+}}\right) \end{cases} \tag{5.7}$$

and the negative sequence voltage can be presented as:

$$\begin{cases} |V^-| = \sqrt{(V_d^-)^2 + (V_q^-)^2} \\ \theta^- = \tan^{-1}\left(\frac{V_q^-}{V_d^-}\right) \end{cases} \tag{5.8}$$

Figure 5.2 shows the proposed control algorithm for both the hybrid transformer (Figure 5.2 (a)) and feeders' VSCs (Figure 5.2 (b)). As can be seen from Figure (5.2), the magnitude of positive sequence voltage $|V^+|$ and its corresponding angle θ^+ is compared to the desired reference voltage ($V_{o,optimum}$ for the hybrid transformer voltage and $v_{L,ref}$ for the load voltage) and the result, $V_e\angle\theta^+$ is converted to instantaneous positive values in abc framev_a^+, v_b^+, v_c^+. Furthermore, the reference injection voltages, $v_{ref}^a, v_{ref}^b, v_{ref}^c$, can be generated by subtracting the zero sequence (equation (2.6)) and the instantaneous negative sequence component in abc frame v_a^-, v_b^-, v_c^- from the positive sequence regulating component of each phase. Consequently, the reference injection voltages can be created and sent to the multi-loop PR controllers of the four-leg VSCs as follows:

$$v_{ref}^i = v_i^+\angle\theta^+ - v_i^-\angle\theta^- - v_0 \tag{5.9}$$

where $i = a, b, c$. The proposed control algorithm determines the maximum possible positive sequence injection to achieve balanced voltage conditions at the load terminals. The advantage of this method (sequence component based controller) is that under unbalanced/balanced voltage sag or swell, the series-connected VSC is able to inject voltage as minimum as possible to compensate for both the substation voltage and the voltage at load terminals.

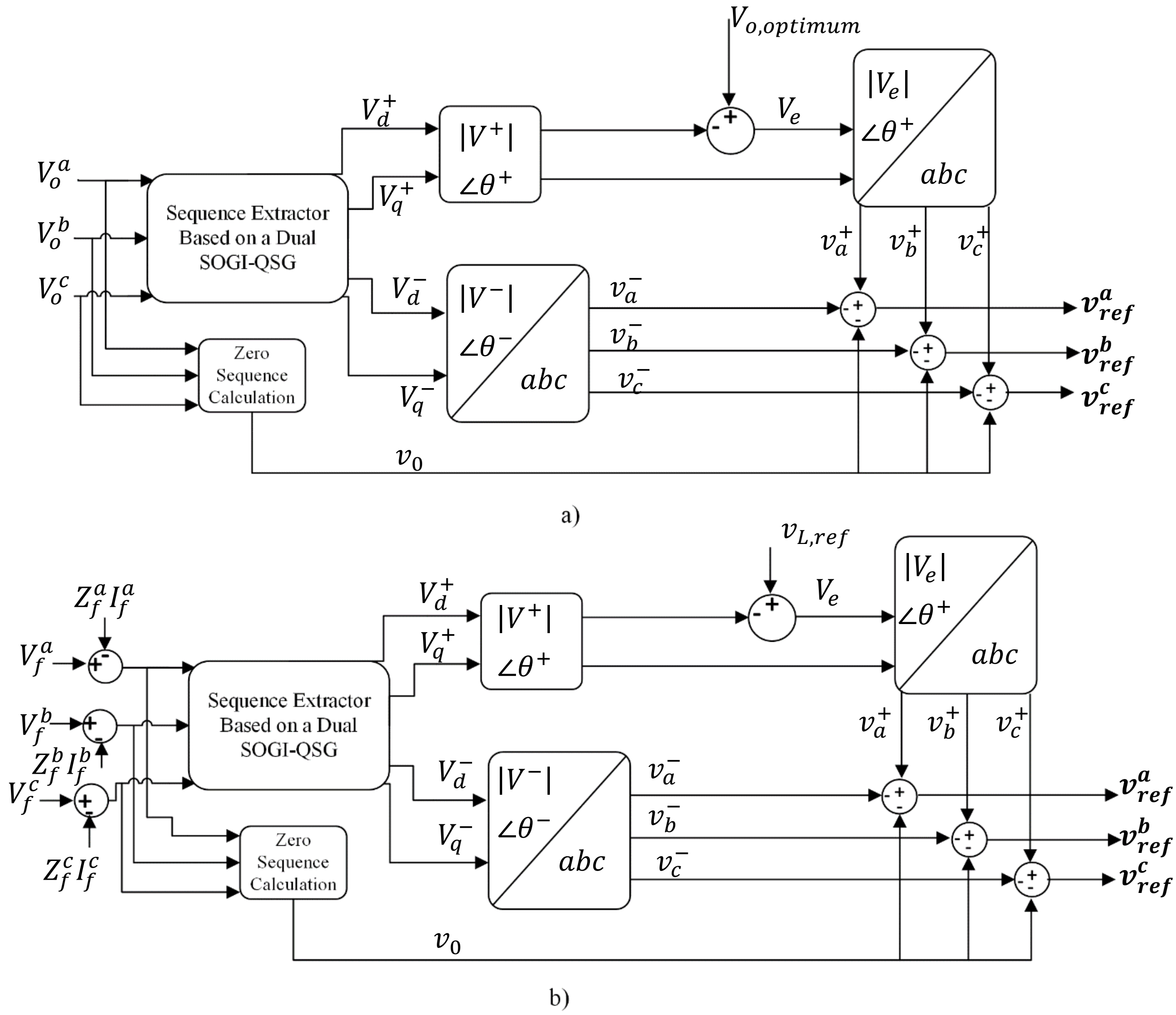

Figure 5.2: Control algorithm for hybrid substation, a) control algorithm for hybrid transformer, b) control algorithm for feeders' VSCs.

The structure of the proposed sequence detection can be shown in Figure 5.3 where a Quadrature Signal Generator (QSG) based on dual Second Order Generalized Integrator (SOGI) [33] provides the input signals on the $\alpha\beta$ reference frame in positive and negative sequences. As can be seen, two SOGI-QSGs are in charge of generating the direct and quadrature signals for $\alpha\beta$ components, v'_α, v'_β, qv'_α and qv'_β. These signals are delivered as inputs to a positive and negative sequence calculations. Moreover, the positive and negative sequences are transformed in synchronous reference frame to compute the signals in dq frame where x_d^+ and x_q^+ are the positive sequences, and x_d^- and x_q^- are the negative sequences in the SRF. The positive and negative sequence components in dq frame ($x_{dq}^{+,-}$) are extracted with the help from moving average filter. It is worth noting that variables x_a, x_b, x_c can be a voltage or current of the system.

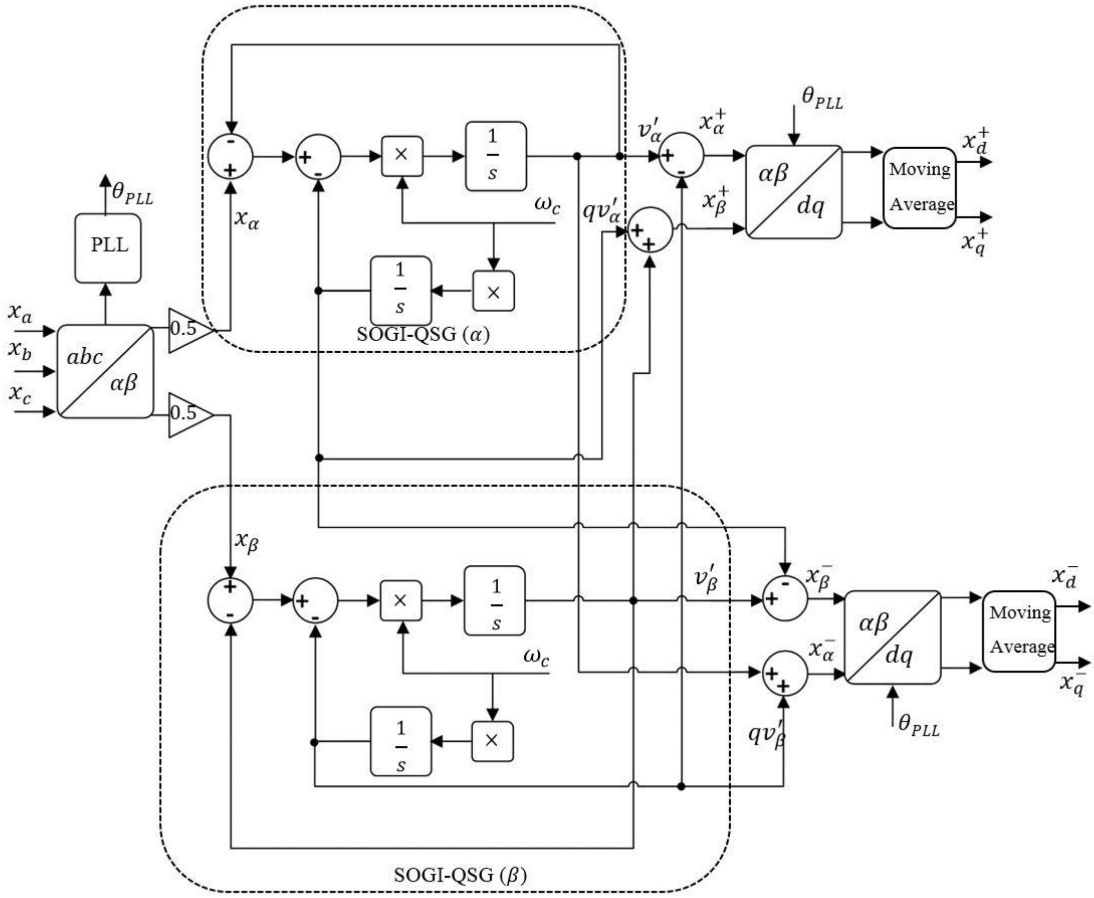

Figure 5.3: Positive and negative sequence calculation based on SOGI-QSG.

5.3 Hybrid Substation Simulation Results

To show the versatility of the proposed hybrid substation performance, the system is tested for the following case studies:

- **Case 1:** Voltage sag and swell mitigation for a three-phase feeder connected to an unbalanced three-phase load (Figure 4.2 (a))
- **Case 2:** Voltage sag and swell mitigation when grid voltages are phase unbalanced. The substation is connected to an unbalanced three-phase linear load (Figure 4.2 (a))
- **Case 3:** Voltage sag and swell mitigation for two three-phase feeders connected to an unbalanced and balanced loads (Figure 4.2 (b))

Figure 5.4 shows the general configuration of the hybrid substation considered in the simulation. The simulation parameters are shown in Table 5.1. In the simulation, it is assumed that the hybrid transformer VSC is identical to the feeders' VSCs. In addition, as discussed earlier, the back-to-back VSC of the hybrid transformer keeps V_o^i at the optimum value $V_{o,optimum}^i$, and if any unexpected voltage demand is required, the corresponded DC-AC series-connected VSC of the affected feeder will compensate the voltage along with hybrid transformer with the total voltage controllability range of $V_{xi}(1 \pm \lambda \pm \tau)$; $\lambda = \tau = \pm 10\%$. The simulation have been carried out using the PLECS simulation program.

Unbalanced loads are considered in this simulation. A symmetrically aligned switching sequence scheme with two zero vectors (subsection 4.5.2.4) is used for the proposed four-leg VSCs of the hybrid substation. The line-to-line voltage of the primary winding of the conventional transformer $V_{l,i}$ (see Figure 2.12) is set to 5kV. In addition, the shunt-connected VSC of HT generates a constant 300 V DC voltage to supply other series-connected VSCs. Figure 5.5 shows the DC-link voltage response in stand-alone mode using the PI controller explained in subsection 4.3.3.

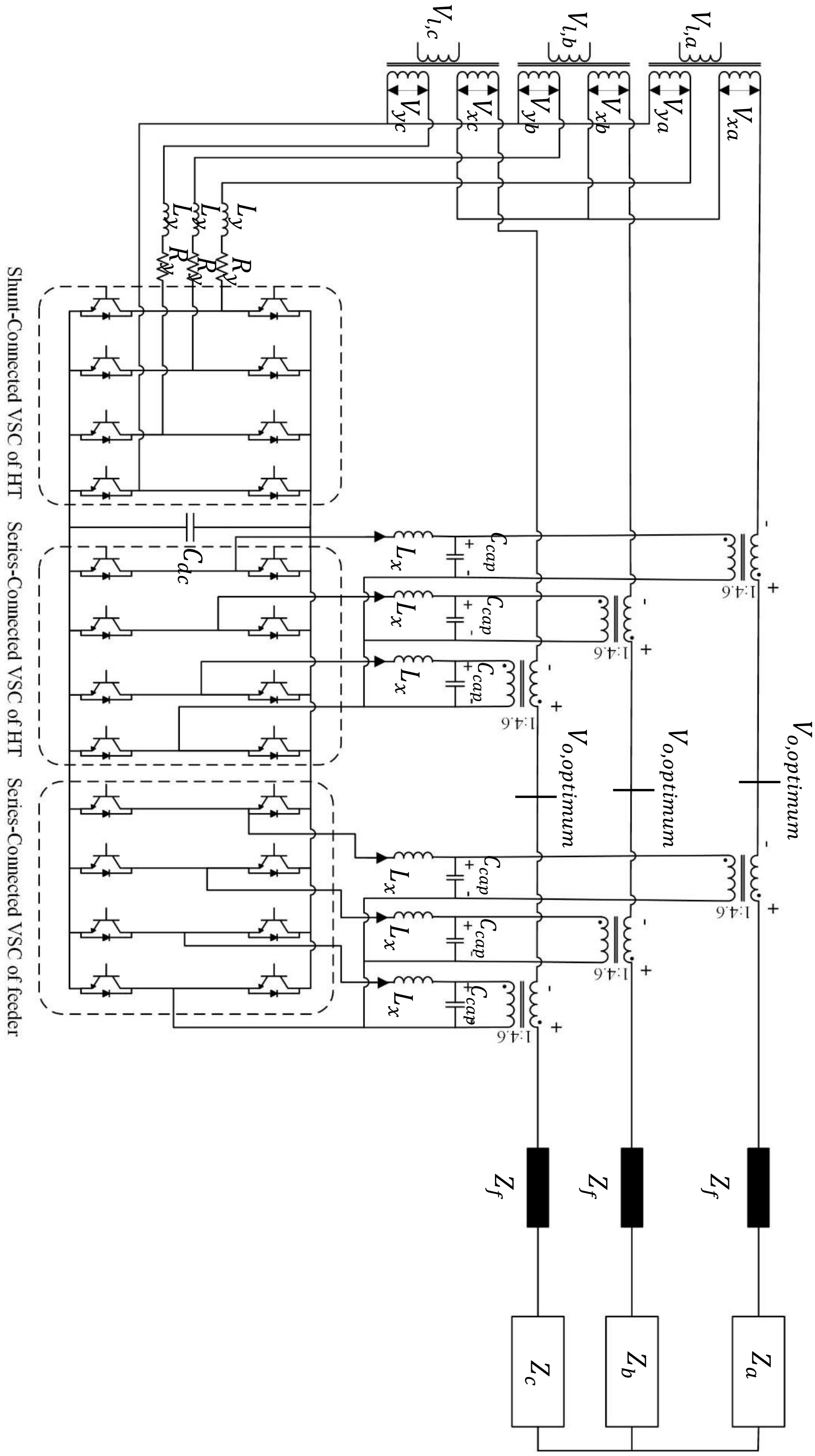

Figure 5.4: General configuration of hybrid substation used in in the simulation.

Table 5.1: Parameters of simulated hybrid substation.

System	
Supply Voltage (Phase Voltage)	$V_{xi} = 300\,V, V_{yi} = 120\,V\ (i = a, b, c)$ $V_{o,optimum} = 245\,V$
Line Impedance	$Z_f = (1\ + j0)\Omega$
Load Parameters	$Z_a = (18 + j0.3)\Omega, Z_b = (15 + j0.6)\Omega,$ $Z_c = (12 + j0.9)\Omega$
Switching Frequency	$10\ kHz$
System Fundamental Frequency	$50Hz$
Shunt-Connected VSC	
Filtering parameters	$R_y = 1\,\Omega \quad L_y = 2\,mH$
Series-Connected VSCs	
Maximum Voltage injection	$0.1V_{xi} \approx 30\,V$
Filtering Parameters	$C_{cap} = 5\,\mu F, L_x = 10\,mH$
Injection transformer turns ratio	1:4.6
DC-Link	
Capacitor	$C_{dc} = 1000\,\mu F$
Voltage	$300\,V$

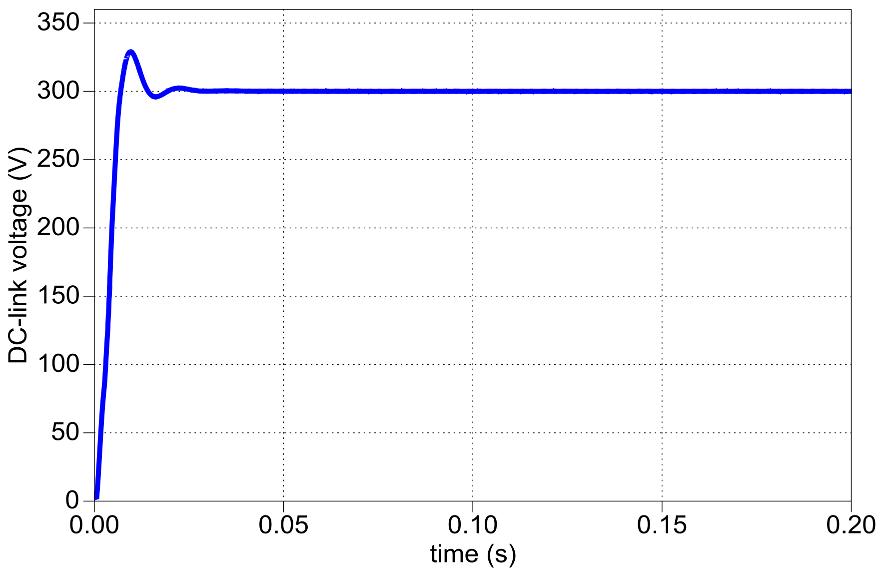

Figure 5.5: DC-link voltage response of the shunt-connected VSC.

5.3.1 Case 1: Asymmetric Voltage Dip and Swell

In this case, an unbalanced three-phase linear load has been considered. A linear load can be defined as a linear relationship between voltage across and current through the load. The supply line-to-neutral voltages V_{xi} for $i = a, b, c$ can be expressed as follows:

$$\begin{cases} V_{xa} = 300\sin(100\pi t) \\ V_{xb} = 300\sin\left(100\pi t - \frac{2\pi}{3}\right) \\ V_{xc} = 300\sin\left(100\pi t + \frac{2\pi}{3}\right) \end{cases} \tag{5.10}$$

In the simulation, phase a, phase b and phase c voltages/currents are presented in green, red and blue colours, respectively. As shown in Figure 5.6 (a), the supply voltages V_{xi} are balanced and kept at the desired magnitude and frequency up to $t = 0.15$s. As the hybrid substation output voltage is set to the optimum value, during normal conditions, VSC of hybrid transformer (HT) inject no voltage or low voltage to the system. At $t = 0.15$s, a fault occurs on supply voltages for phase a and phase b.

As can be seen from Figure 5.6 (a), supply voltage of phase a drops by 10% and supply voltage of phase b increases to 10%, while supply voltage of phase c remains constant at the previous value. The VSC of HT detects the voltage drop and swell immediately and inject the required voltages to keep the output voltage of HT at the predetermined value $V_{o,optimum}^{i} = 245\ V$. In addition, an unbalanced voltage dip and swell occurs once more at $t = 0.30\ s$ for all three supply voltages. The series-connected VSC of HT compensates the voltages and keeps its output voltage at the optimum value. The results are shown in Figure 5.6 (b) and (c).

Meanwhile, the VSC of HT is operating to clear the fault, the series-connected VSC of the feeder injects the required voltages regardless of any disturbance happening at the supply side (Figure 5.6 (d)). This happens in order to keep the load voltages balanced at the reference 230V, the results are shown in Figure 5.6 (e). Moreover, at $t = 0.45$s, the phases a and c of the three-phase unbalanced load require new demands and this causes voltage dropping in the feeder. As soon as the feeder's series-connected VSC detects the voltage drop by using symmetrical components' control algorithm, it injects the accurate magnitude and phase angle to keep the voltages balanced at a predetermined value at load terminals.

Figure 5.7 shows the positive, negative, zero sequence voltages and their corresponded phase angles for both series-connected VSCs of the hybrid substation. As can be seen from Figure 5.7 (a) and (b), the proposed control algorithm detects the voltage drop/swell quickly and compensates the positive and negative sequence voltages with appropriate phase angle less than 20ms. Moreover, as the supply voltages are balanced up to $t = 0.15\text{s}$, the hybrid transformer negative sequence voltage V_{HT}^{-} ($|V^{-}|$ of Figure 5.2 (a)) and zero sequence voltage V_{HT}^{0} (v_0 of Figure 5.2 (a)) have zero values. In Contrast, as an unbalanced load has been used, the feeder's VSC negative sequence voltage V_{Feeder}^{-} ($|V^{-}|$ of Figure 5.2 (b)) and zero sequence voltage V_{Feeder}^{0} (v_0 of Figure 5.2 (b)) have non-zero values all the time.

Positive and negative phase angles of hybrid substation VSC and feeder's VSC are shown in Figure 5.7 (d) and (e). As can be observed, the phase angles changes every 100ms and that is due to the length of the averaging period of the moving average filter. The moving average filter [140], averages a continuous input signal over a specific averaging time (100ms for this case). The proposed averaging method is suitable for the control algorithm as it smooths the signals with fast calculations.

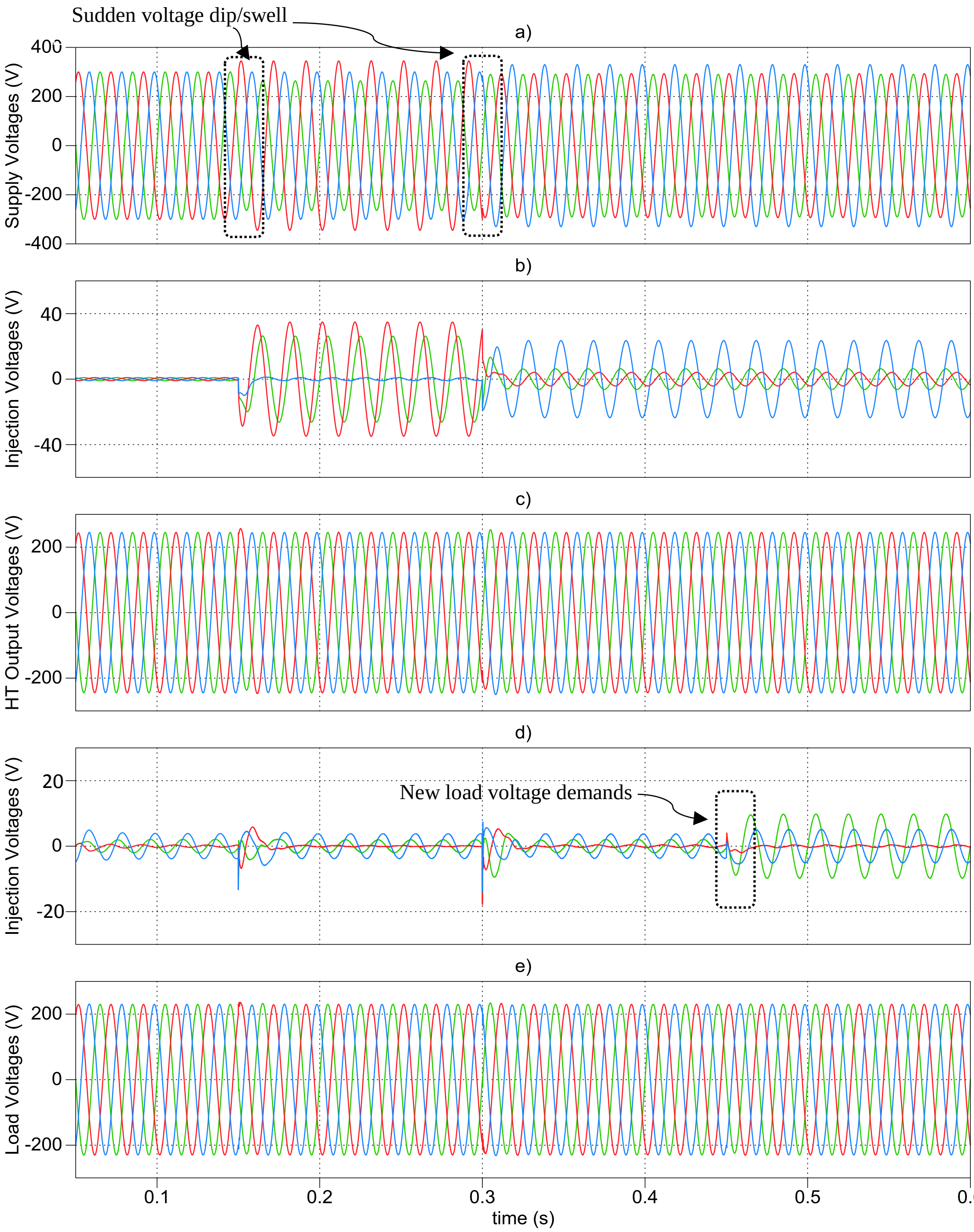

Figure 5.6: Simulation results for Case 1: a) supply voltage V_{xi}, b) injection voltages of HT c) HT output voltages, $V^{i}_{o,optimum}$, d) injection voltages of feeder's VSC, e) load voltages.

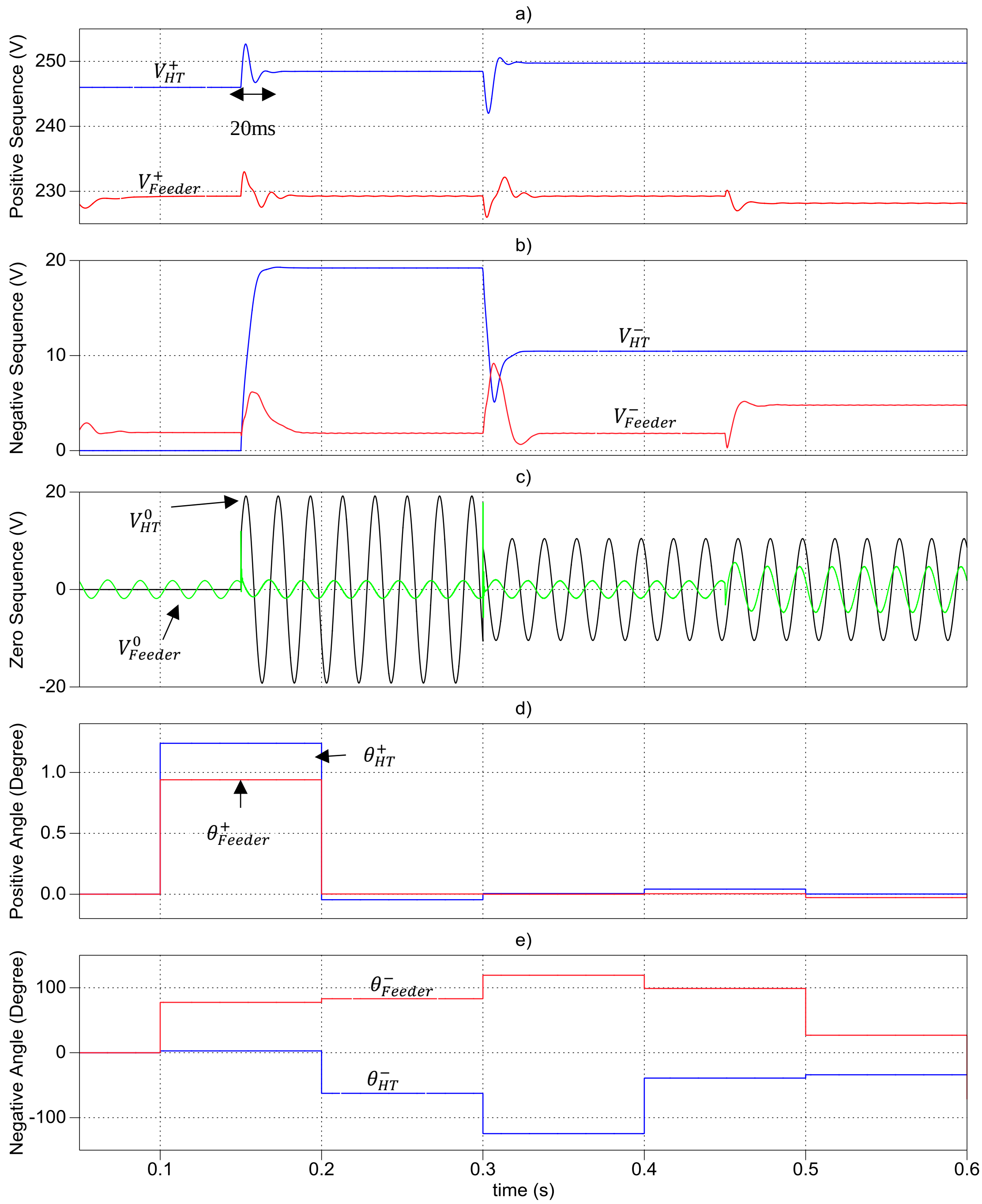

Figure 5.7: Simulation results for Case 1: a) positive sequence voltages, b) negative sequence voltages, c) zero sequence voltages, d) positive phase angles, e) negative phase angles of HT and feeder's VSC.

5.3.2 Case 2: Phase Unbalanced Grid Voltage for Unbalanced loads

Phase unbalanced grid voltage is normally caused by faults on the bulk power transmission systems with a large block of load being disconnected, or a large source of generation going off line [4]. Consequently, when the supply voltages are not 120° phase shifted from each other, the feeder's current and voltage, as well as the voltages at load, are not 120° phase shifted leading to harmonics in the system.

This case can be defined as voltage unbalanced (or imbalanced). For this case study, the grid supply voltages are not identical with 120° phase shifted between them. The supply voltages are presented as follows:

$$\begin{cases} V_{xa} = 280\sin(100\pi t) \\ V_{xb} = 300\sin\left(100\pi t - \dfrac{2\pi}{3}\right) \\ V_{xc} = 320\sin\left(100\pi t + \dfrac{2\pi}{3}\right) \end{cases} \qquad 0 < t < 0.15 \qquad (5.11)$$

and:

$$\begin{cases} V_{xa} = 300\sin\left(100\pi t + \dfrac{\pi}{18}\right) \\ V_{xb} = 290\sin\left(100\pi t - \dfrac{\pi}{2}\right) \\ V_{xc} = 320\sin\left(100\pi t + \dfrac{5\pi}{9}\right) \end{cases} \qquad 0.15 < t < 0.5 \qquad (5.12)$$

In this case, while the supply voltage is unbalanced, and phase shifted, there is a new load demand for phase a, b, c at $t = 0.25$s, $t = 0.35$s and $t = 0.4s$, respectively. Grid voltages (equations (5.11) and (5.12)) can be seen in Figure 5.8 (a). As can be observed from 5.7 (b), the HT series-connected VSC injects the required voltage to keep the HT output voltage balanced at the optimum value of 245 V (Figure 5.8 (c)). As can be seen from Figure 5.8 (d), the load currents change as the load demands change. While the output of the HT is balanced at the reference value, the VSC of the feeder can deal with loads by injecting the lowest voltage value to maintain the voltages at load terminal at 230 V. The results are shown in Figure 5.8 (e) and (f). The estimated sequence components of the proposed controller is shown in Figure 5.9. As can be observed, for each individual fault, the positive, negative and zero sequences change accordingly.

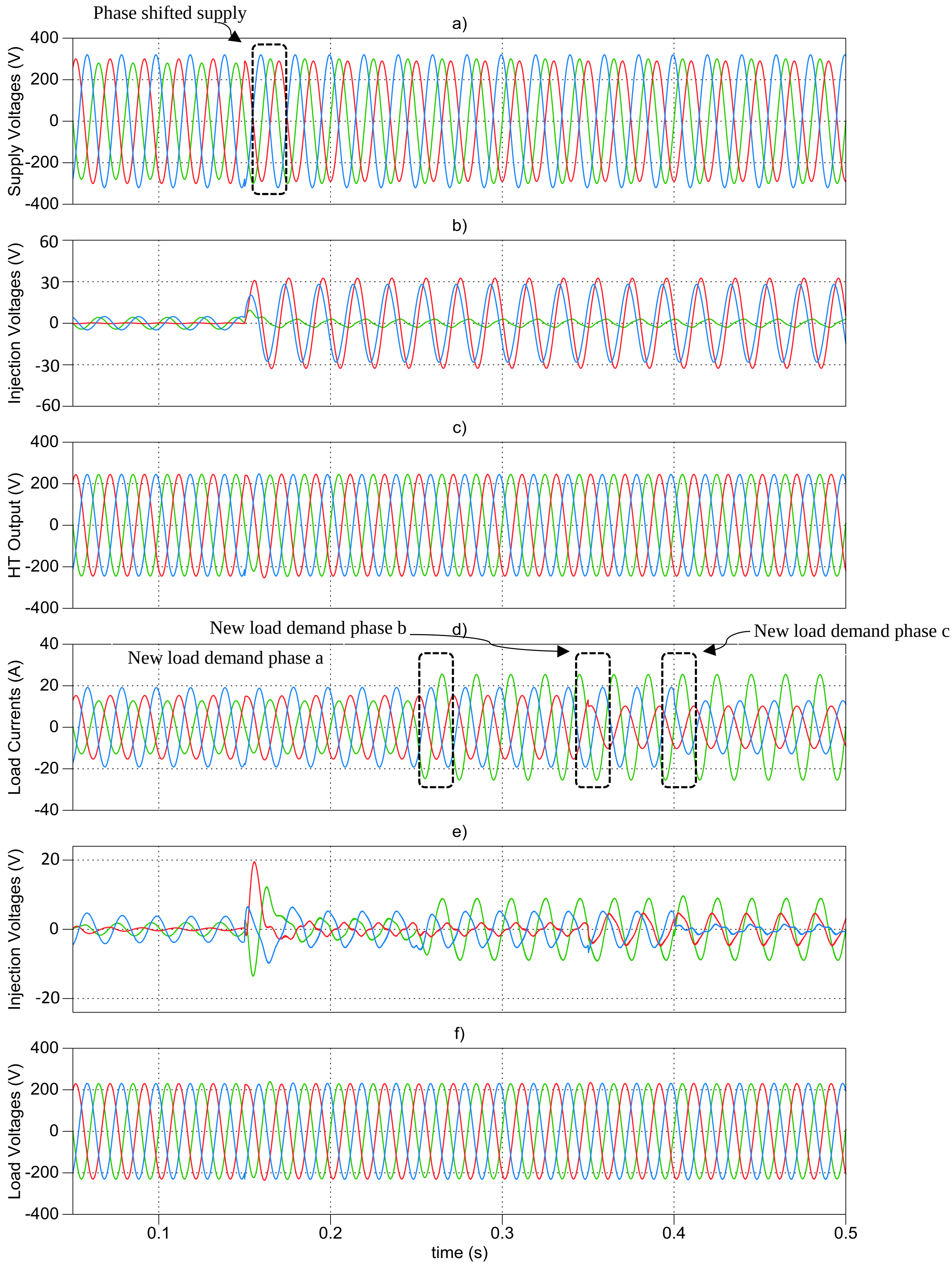

Figure 5.8: Simulation results for Case 2: a) supply voltage V_{xi}, b) injection voltages of HT c) HT output voltages $V^{i}_{o,optimum}$, d) load currents, e) injection voltages of feeder's VSC, f) load voltages.

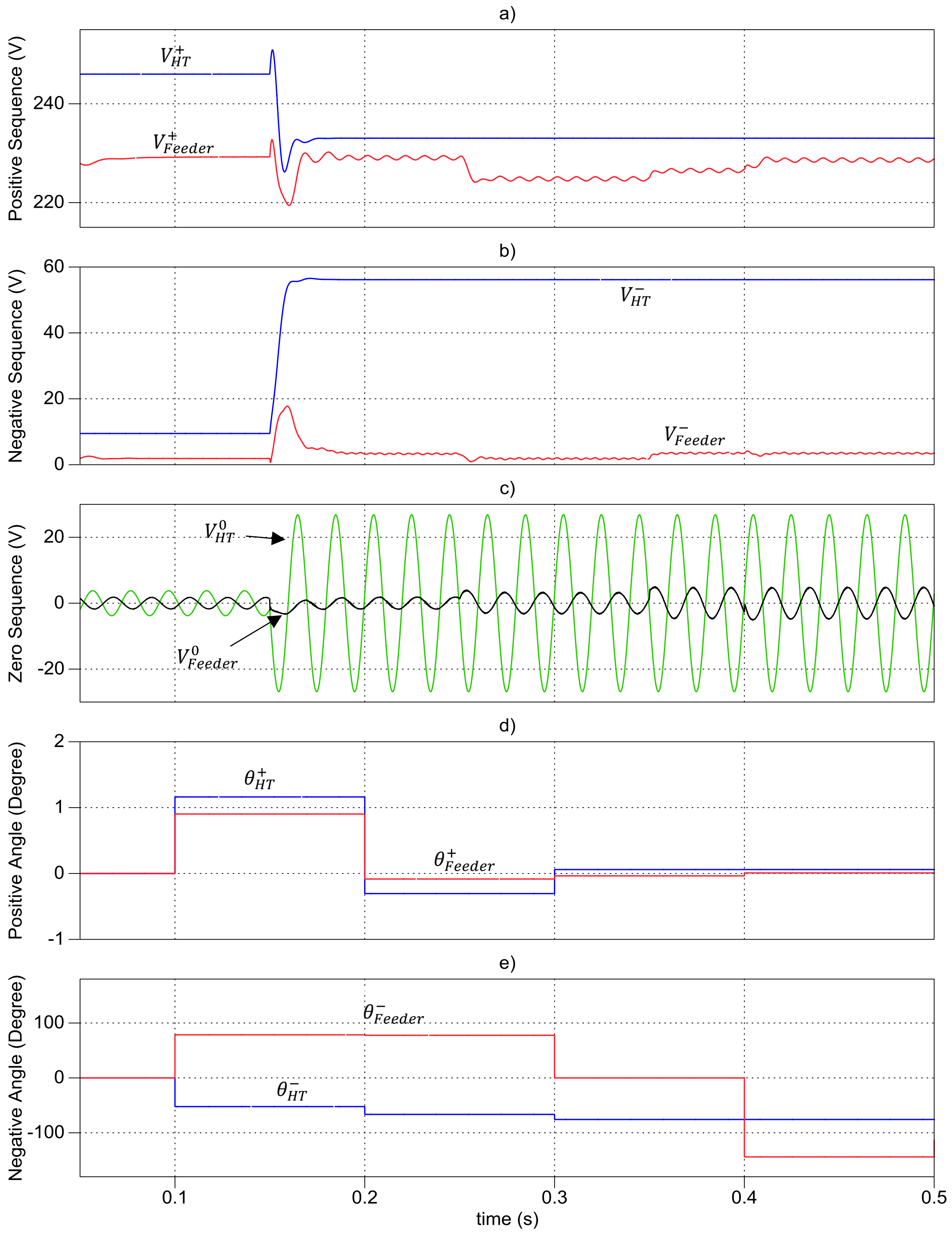

Figure 5.9: Simulation results for Case 2: a) positive sequence voltages, b) negative sequence voltages, c) zero sequence voltages, d) positive phase angles, e) negative phase angles of HT and feeder's VSC.

5.3.3 Case 3: Voltage Sag and Swell for Multi-Feeder System

The general configuration of this case study is shown in Figure 5.10 (similar to Figure 4.2 (b)). In this case, the hybrid substation is connected to two feeders with different load demands. Feeder 1 is connected to a balanced three-phase linear load, and feeder 2 is connected to an unbalanced three-phase linear load. Table 5.2 presents the simulation specifications for this case study. This is the worst-case scenario at which the unbalanced and phase shifted supply voltages are occurring along with different load demands.

Three different faults that occur are as follows: first fault is related to the supply grid and it happens at $t = 0.15$s; second and third faults are associated with change of load demands of the two feeders which occur at $t = 0.25$s and $t = 0.4$s. Figure 5.11 presents the system performance when the hybrid substation is not operating. As can be seen, the load voltages of feeder 1 and 2 are unbalanced and phase shifted after the fault, leading to have an undesired system. Figure 5.12 shows the simulation results for Case 3 when the hybrid substation is operating. As can be observed from Figure 5.12 (b), the VSC of HT is in the standby mode operation during normal conditions. As soon as fault occurs, and grid voltages become unbalanced in phase and magnitude ($t = 0.15s$), the VSC of HT injects the required voltage in order to keep the output voltage of HT balanced at the optimum value. The series-connected VSCs of both feeder 1 and 2 operate individually and based on load demands, they inject the desired voltage to keep their load voltages balanced at the reference value.

Figure 5.13 shows the sequence values obtained from the proposed control algorithm to generate the required injection voltage. As can be seen, the positive, negative and zero sequence voltages along with their corresponding phase angle respond to the fault quickly to generate the required voltage. The oscillations of positive and negative sequences are due to the severe unbalanced condition and moving average filter’s performance.

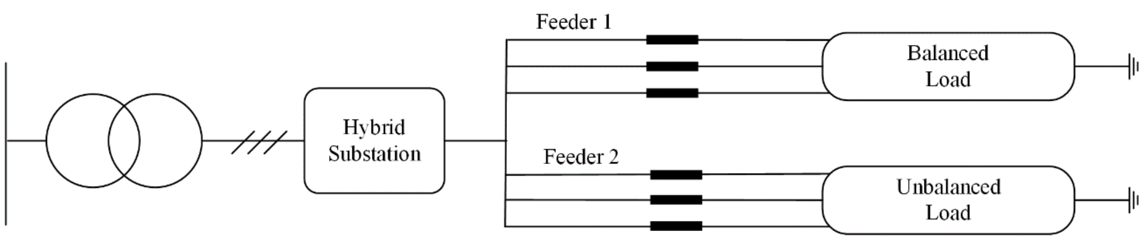

Figure 5.10: General configuration for case 3.

Table 5.2: Simulation parameters for Case 3.

	Phase a	Phase b	Phase c	time
Supply Voltage	$300\sin(100\pi t)$	$300\sin\left(100\pi t - \frac{2\pi}{3}\right)$	$300\sin\left(100\pi t + \frac{2\pi}{3}\right)$	$0 < t < 0.15$
	$300\sin\left(100\pi t + \frac{\pi}{18}\right)$	$290\sin\left(100\pi t - \frac{\pi}{2}\right)$	$320\sin\left(100\pi t + \frac{5\pi}{9}\right)$	$0.15 < t < 0.55$
Load Feeder1	$(18 + j0.3)\Omega$	$(18 + j0.3)\Omega$	$(18 + j0.3)\Omega$	$0 < t < 0.25$
	$(12 + j0.3)\Omega$	$(12 + j0.3)\Omega$	$(12 + j0.3)\Omega$	$0.25 < t < 0.55$
Load Feeder2	$(18 + j0.3)\Omega$	$(15 + j0.6)\Omega$	$(12 + j0.9)\Omega$	$0 < t < 0.4$
	$(9 + j0.3)\Omega$	$(30 + j0.6)\Omega$	$(24 + j0.9)\Omega$	$0.4 < t < 0.55$

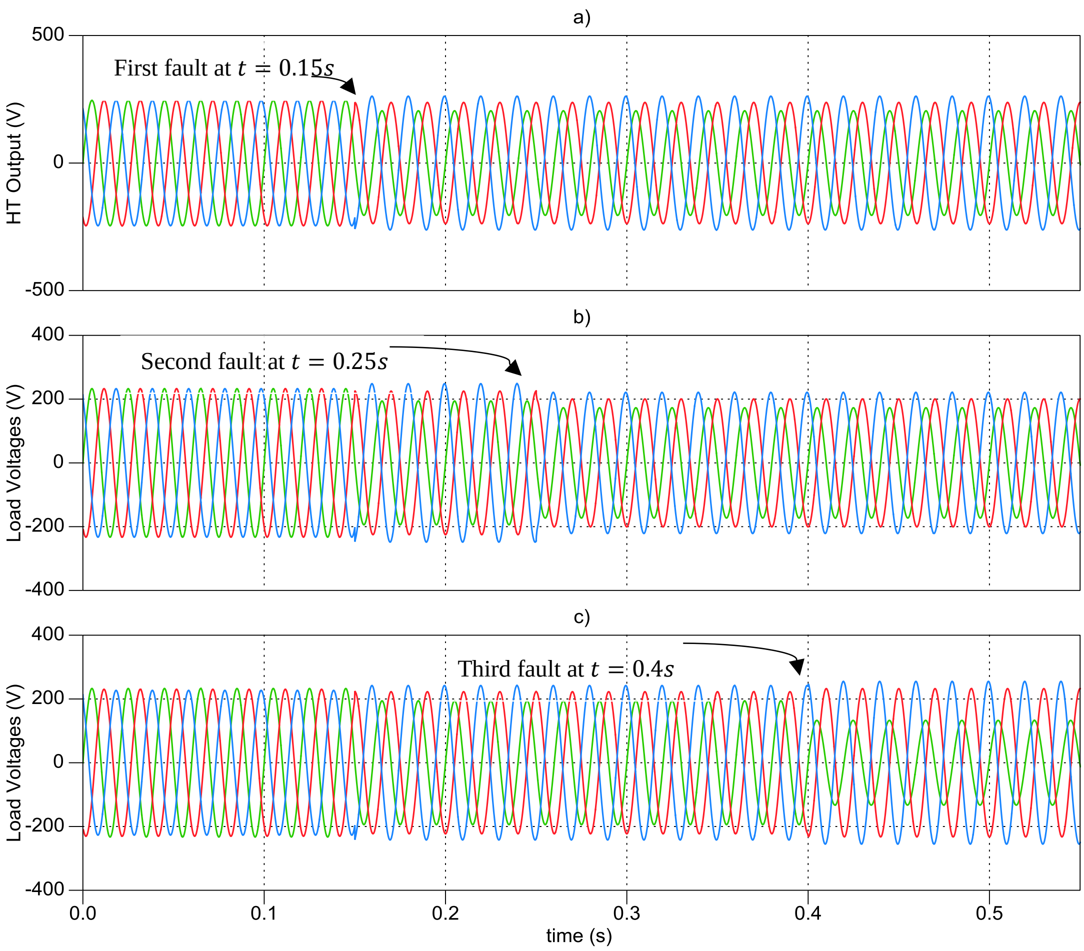

Figure 5.11: Simulation results for Case 3: a) HT output voltage, b) load voltages of feeder 1, c) load voltages of feeder 2 when hybrid substation is not operating.

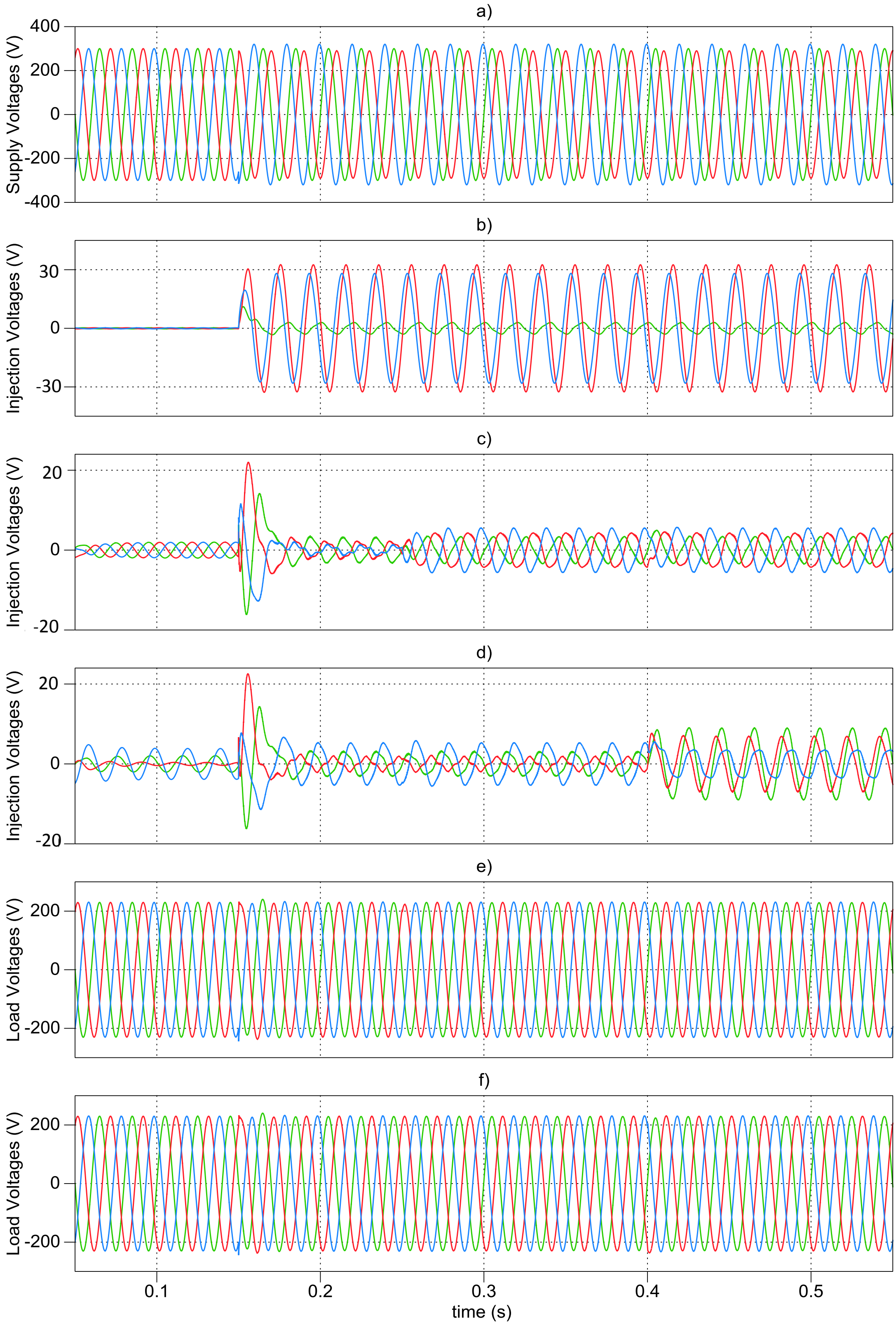

Figure 5.12: Simulation results for Case 3: a) supply voltage V_{xi}, b) injection voltages of HT c) injection voltages of feeder 1 VSC, d) injection voltages of feeder 2 VSC, e) load voltages of feeder 1, f) load voltages of feeder 2.

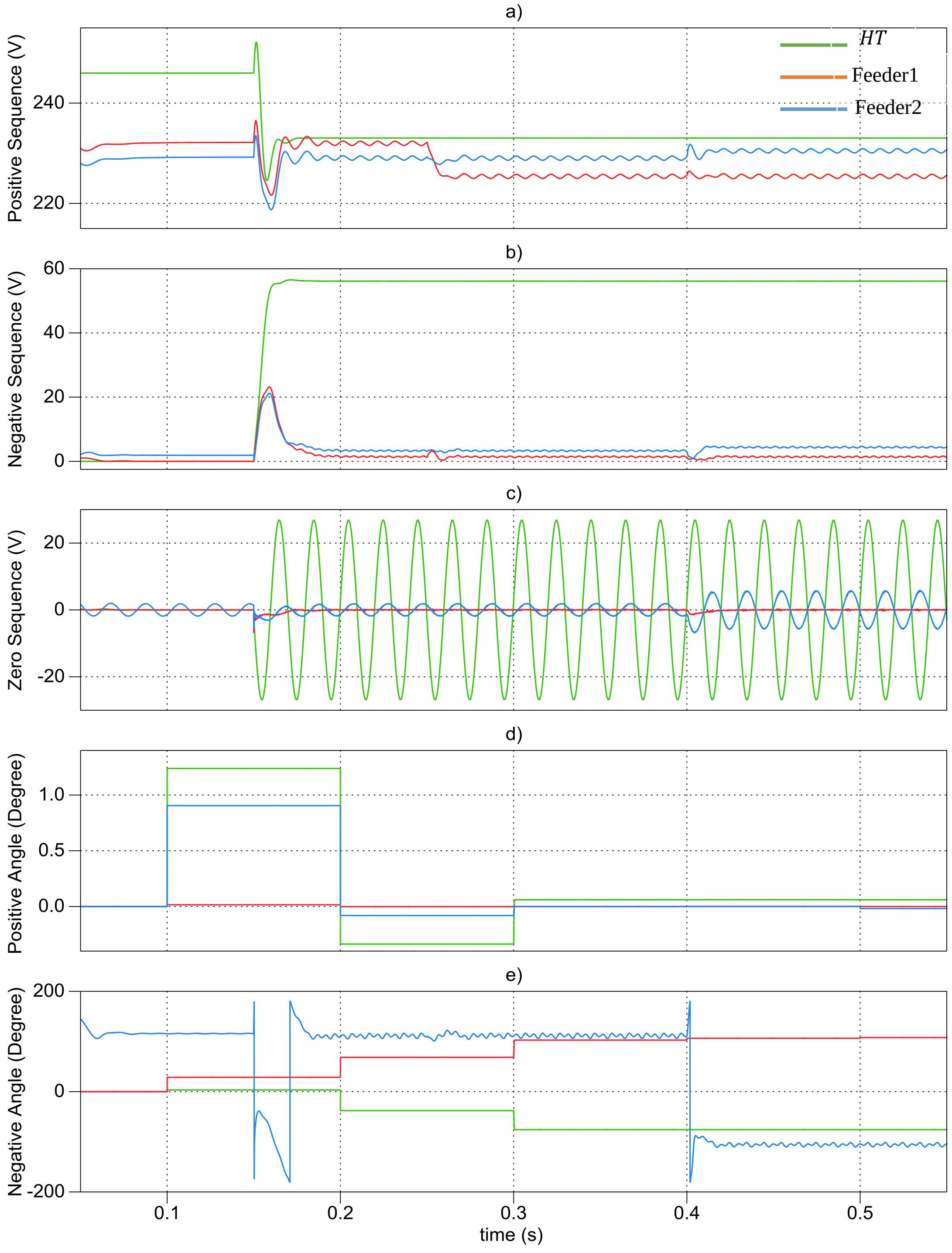

Figure 5.13: Simulation results for Case 3: a) positive sequence voltages, b) negative sequence voltages, c) zero sequence voltages, d) positive phase angles, e) negative phase angles of HT and VSCs of feeder1 and2.

5.4 Conclusion

A robust control algorithm based on sequence component for the hybrid substation has been presented. It is important to extract symmetrical components not only for controlling the hybrid substation, but also for observing and evaluating the instantaneous power quality of the system. The simulation results are presented to show the performance of the hybrid substation under different case studies. The hybrid substation uses a robust algorithm based on positive, negative and zero sequences to inject the required voltage to the system and to keep the voltage balanced at a reference value. The simulation results show a fast response, accurate tracking and robustness of the proposed control system.

It is worth noting that the power quality problems, such as interruption and fundamental frequency variations can be compensated by a hybrid substation. However, as discussed in Chapter 3, the voltage range controllability is set to $\pm 10\%$ of the rated voltage, thus in this case the system requires a higher voltage range controllability and a larger DC-link to inject the required voltage into the system.

CHAPTER 6: Experimental Rig

Summary: *This Chapter describes the design and construction of the series-connected four-leg VSC to be used in experimental work. Firstly, this chapter focuses on the power converter structure which is then followed by description of the digital control implementation. In addition, 3-dimensional SVPWM and resonant controllers have been implemented to verify the power converter's performance.*

6.1 Introduction

After evaluating the control performance of the hybrid substation discussed in Chapter 5, it is important to experimentally validate the simulation results and the proposed controllers. The overall block diagram of the entire rig and a photograph of the experimental prototype are shown in Figure 6.1 and 6.2, respectively. The control platform comprises a Digital Signal Processor (DSP) board and a Field Programmable Gate Array (FPGA) board. The DSP is the central processing unit that executes all control functions and modulation calculations and is programmed by C language. The FPGA is programmed with an interface between the DSP and the power converter and would be able to receive data from voltage/current transducers in order to perform Analogue-to-Digital (A/D) conversion. Subsequently, the FPGA produces the switching signals for the gate drives in respect to the modulation scheme from DSP. A Host Port Interface (HPI) daughter card provides a bi-directional data transfer between the host PC and the DSP without interrupting the central processor unit. More details about the digital control platform will be discussed in this chapter.

This chapter comprises four main sections. The first section focuses on the details of the construction of the four-leg VSC and its various circuits and components, including gate drives in addition to current and voltage transducers. This section is followed by detailed design of a protection circuit (for safety and protection of the experimental rig) and an input filter. In the second section, the control platform and digital control of the proposed four-leg VSC are described. The implementation of resonant controllers and SOGI-QSG in the digital system are described in the third section. Finally, the fourth section investigates the performance of 3-dimensional SVPWM and resonant controllers to ensure the proper operation of the power converter.

6.2 Series-Connected VSC Implementation

For this experimental test, a two layer 1.6mm Printed Circuit Board (PCB) of the four-leg VSC has been designed, as shown in Figure 6.3. A two layer PCB was designed to obtain a compact circuit board and separate the positive DC voltage (top layer) and negative DC voltage (bottom layer). The PCB board of the power converter has four main segments, as follows: switching devices known as IGBTs, gate drives, measurement circuits (current and voltage transducers) and DC-link capacitors. The PCB layout of a four-leg VSC can be found in Appendix D.

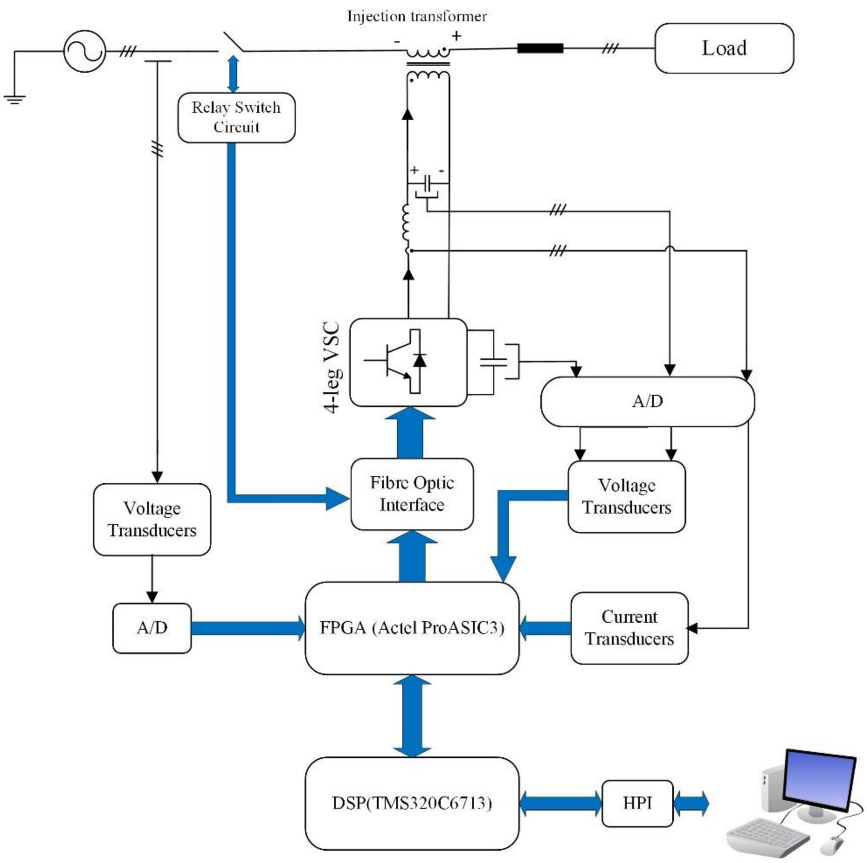

Figure 6.1: Overall block diagram of the entire rig and digital control unit.

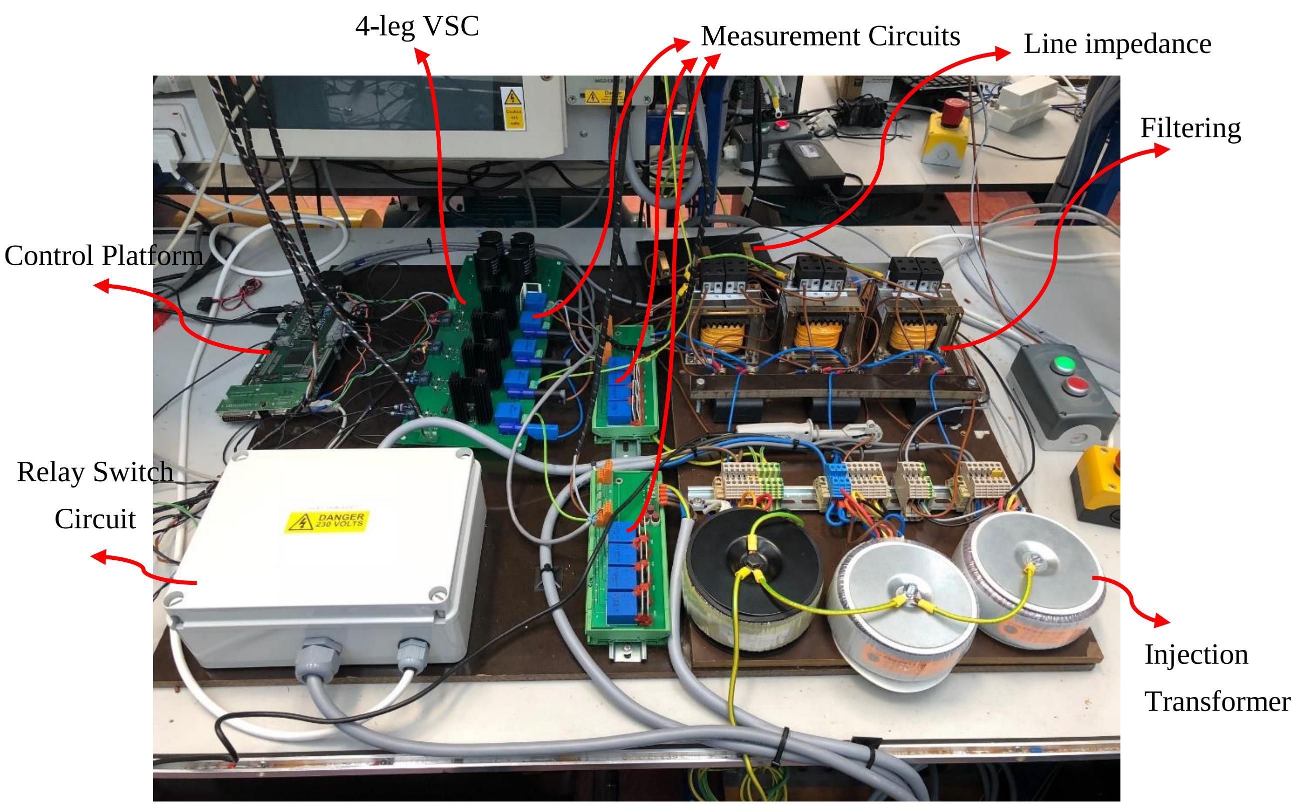

Figure 6.2: A photograph of the experimental system.

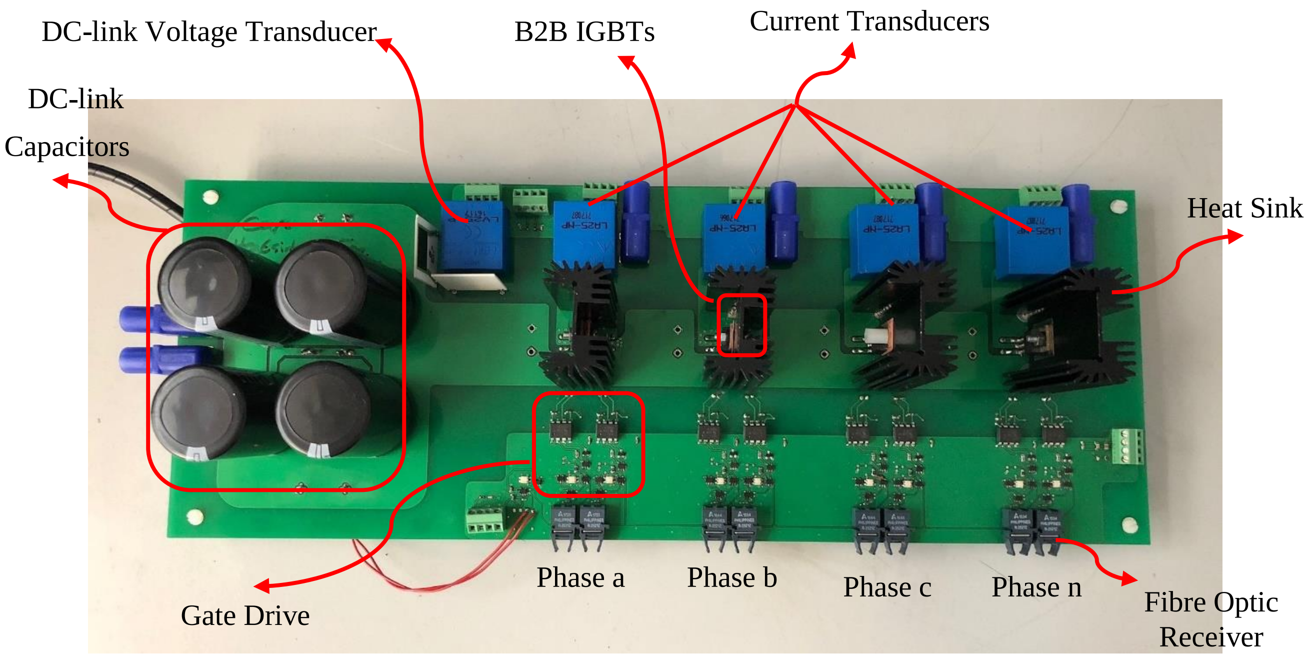

Figure 6.3: Proposed four-leg VSC implemented in practical work.

6.2.1 Switching Devices

Each leg of the four-leg VSC has a 1200V, 12A, back-to-back IGBT switch (8 IGBTs in total) from Infineon IRGB5B120KDPBF (Figure 6.4). Each IGBT is associated with an anti-parallel diode in order to obtain a fast reverse recovery and reduce leakage current. The recommended switching frequency of these devices is from 8 kHz to 30 kHz. Switching frequency of f_s=10 kHz with 1μs dead time is chosen. Switching frequency of 10 kHz is chosen to ensure that the time taken to execute the interrupt routine is less than sampling period $(1/f_s)$. Dead time is needed to avoid risk of damage from short circuit across the DC-link, thus the upper and lower switches of each leg must not be turned on simultaneously. The back-to-back IGBTs of each leg are directly mounted onto the PCB, attaching to a high power extruded heat sink (6400BG TO220) to disperse heat away from the switching devices.

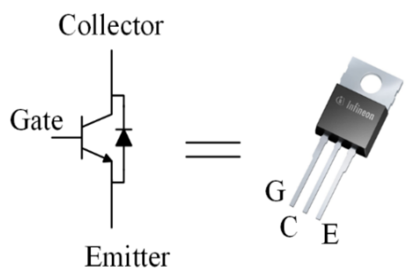

Figure 6.4: IGBT with anti-parallel recovery diode.

6.2.2 Thermal Design

A heat sink is a heat exchanger which is used to move away the heat generated by the switching devices. The heat sink is used to ensure that the temperature of the semiconductor device is kept within its defined temperature limits. The maximum allowable junction temperature is T_{jmax} and is defined by the manufacturer. Table 6.1 shows the thermal resistance specifications of the proposed IGBT switching devices (IRGB5B120KDPBF).

Table 6.1: Thermal resistance parameters of IRGB5B120KDPBF.

	Description	value	Unit
$R_{th(j-c)}^{IGBT}$	Junction to case IGBT	1.4	℃/W
$R_{th(j-c)}^{Diode}$	Junction to case diode	2.8	
$R_{th(c-s)}$	Case to sink	0.5	

A typical equation used for calculation of heat sink thermal resistance R_{th} can be given in (6.1) as follows [141]:

$$R_{th} = \frac{T_{jmax} - T_A}{P_D} - \left(R_{th(j-c)}^{IGBT} + R_{th(j-c)}^{Diode} + R_{th(c-s)}\right) \quad (6.1)$$

where T_A and P_D are the ambient temperature (25℃) and power dissipation, respectively. P_D can be obtained from the power dissipation graph of IGBT datasheet. The calculated heat sink thermal resistance R_{th} is 9.8 ℃/W and as each leg has two IGBTs connecting back-to-back to a heat sink, R_{th} is considered as 4.9 ℃/W.

A heat sink with a thermal resistance of 2.7 ℃/W 6400BG TO220 (see Figure 6.3) is used for this work.

6.2.3 Gate Drive Circuit

The main function of the gate drive is to convert the low power FPGA signal (5V) to the voltage and current necessary for the IGBTs to be turned on/off besides providing galvanic isolation between control circuit and power circuit. The schematic diagram of the gate drive circuits is shown in Figure 6.5. The logic switching signals generated by FPGA are sent by fibre optic transmitters (HFBR-1521Z) and received by the fibre optic receivers (HFBR-2521Z) of the four-leg VSC.

The fibre optic receiver inverts the FPGA signal and a single Schmitt inverter U_1 (SN74LVC1G14DBVR) is added to the circuit to invert the signal, and supply the required current for the opto-coupler as well as reducing the input signal noise. The output of the inverting logic gate U_1 is used to drive the gate drive opto-coupler (HCPL 3120). The opto-coupler provides a galvanic isolation between the main power circuit and the emitter of the IGBT in addition to the DSP/controller platform. Each opto-coupler is supplied by an isolated ± 15V power supply provided by a 12V to ± 15V DC-DC converter (MGJ2D121509SC). Moreover, on the other side of the opto-coupler, a gate resistor of $R_G = 15\Omega$ (recommended by the manufacturer) is used to limit the maximum current of the opt-coupler and the internal gate resistor of the IGBT. The pull-down resistor, $R_{GE} = 5k\Omega$, is connected between the gate-emitter connections to prevent the IGBT from being damaged by discharging the gate capacitance if the opto-coupler fails in operation.

6.2.4 Measurement Circuits

Voltage and current measurement circuits are necessary for controllers. The output currents and the DC-link voltage of the four-leg VSC are measured for the feedback of current controller and 3- dimensional SVPWM algorithm, respectively. These transducers are directly mounted on the PCB circuit of the four-leg VSC (see Figure 6.3). In addition, the converter filtering capacitor voltages (voltage controller feedback), and grid voltages are measured on separate measurement circuits (see Figure 6.2). There are four LEM LA 25-NP current transducers and seven LEM LV 25-P voltage transducers. These transducers are Hall effect closed-loop types with high accuracy, good linearity, wide frequency bandwidth and an optimised response time [142, 143]

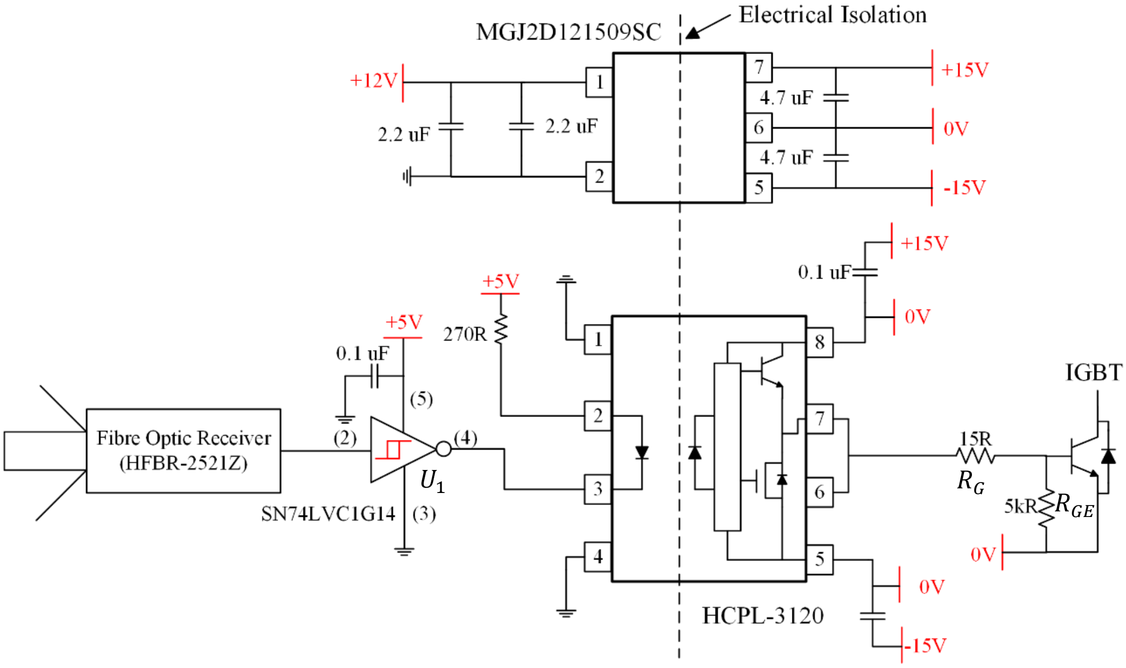

Figure 6.5: Schematic diagram of gate drive circuit.

6.2.4.1 Current Transducer

The schematic diagram of current transducer LEM LA 25-NP is shown in Figure 6.6. The output of the proposed current transducer is in form of current to be sent to the FPGA A/D control unit. To have a good accuracy, the current transducer needs to operate around the nominal operation condition. As a result, R_M which is known as the burden resistor is needed to generate a voltage signal, as each A/D channel of the FPGA has an input signal within the range of ± 5V.

The primary and secondary side nominal RMS current of LEM LA 25-NP is $I_{PN} = 25$A and $I_{SN} = 25mA$, respectively. However, the converter operating currents range from -5A to 5A. Hence, by referring to LA 25-NP datasheet, a suitable connection configuration (see Figure 6.6) has been implemented on the PCB board. The conversion ratio of the proposed connection is 3:1000, thus the secondary current can be written as:

$$I_S = \frac{3I_P}{1000} \tag{6.2}$$

To prevent the saturation of the A/D conversion step, the voltage across the burden resistor, R_M , should be less than the voltage of the A/D conversion circuit board, which is 5V. As a result, the burden resistor can be expressed as:

$$R_M < \frac{5}{I_S} = \frac{5}{3 \times 5mA} = 333\Omega \tag{6.3}$$

A 320Ω burden resistor has been used for current transducers.

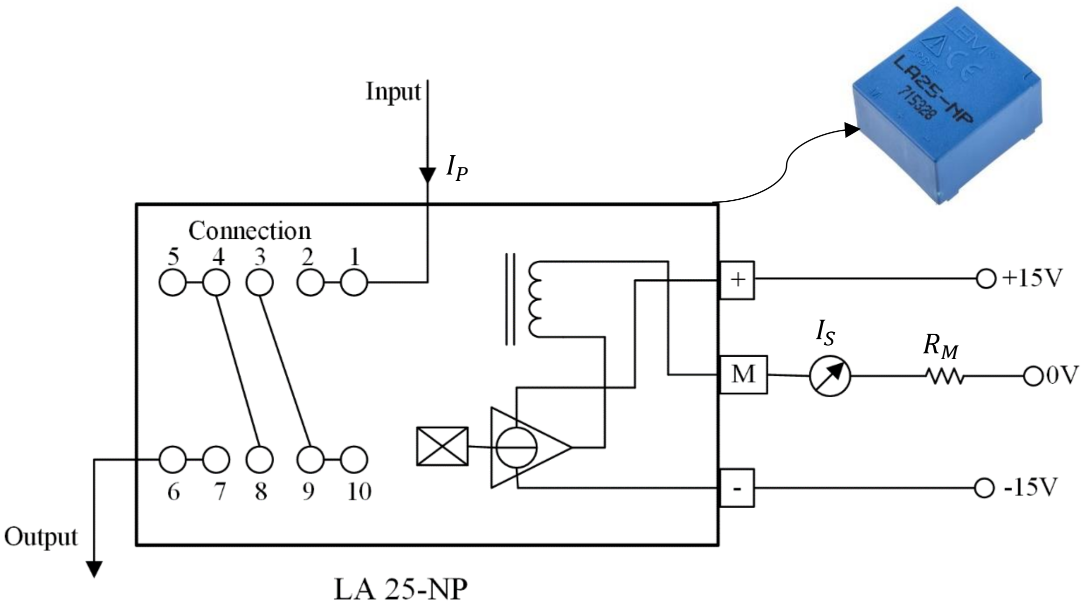

Figure 6.6: Connection diagram of current transducer LA 25-NP.

6.2.4.2 Voltage Transducer

The schematic diagram of the voltage measurement circuit is shown in Figure 6.7. Voltage transducer LEM LV 25-P is based on the same principle as the current LEM LA 25-NP. V_M is the voltage to be measured, which in doing so, a primary resistor, R_P is required to generate the primary current, I_P.

By referring to voltage transducer data sheet [143], the measuring range of the primary current I_P is from $-14\ mA$ to $14\ mA$. Thus, R_P is selected to ensure the primary current I_P to be within the range as expressed below:

$$I_p > \frac{V_{M(\max)}}{R_P}$$

$$= R_p > \frac{V_{M(\max)}}{I_P} \tag{6.4}$$

where $V_{M(\max)}$ is the maximum possible value of V_M, and I_P is equal to14 mA. In this work, the maximum value of the DC-link voltage and grid voltage are 300V and 240V, respectively. As a result, 25kΩ and 20kΩ primary thick film resistors, R_P have been selected for the DC-link voltage and the grid voltage transducers accordingly. The thick film resistors have high power density and low inductive behaviour.

Similar to LEM LA 25-NP current transducer, the burden resistor is selected that the voltage across the R_M should be less than the voltage of the A/D conversion circuit board (FPGA board). In addition, the primary and secondary side nominal RMS currents of LEM LV 25-P are $I_{PN} = 10mA$ and $I_{SN} = 25mA$, respectively. Therefore, since $I_S = 2.5I_P$, the burden resistor of the voltage transducer can be expressed as:

$$5V > \frac{2.5 \times V_{M(\max)}}{R_P} R_M \tag{6.5}$$

An R_M of 160Ω is chosen for this work. The measurement burden resistors are soldered on the FPGA board.

.

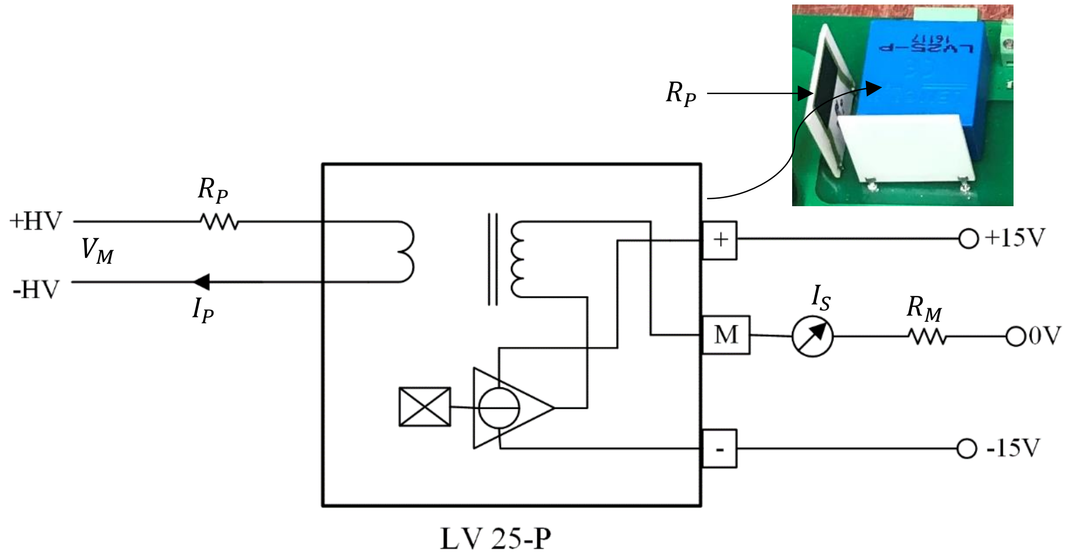

Figure 6.7: Schematic diagram of voltage transducer LV 25-P.

6.2.5 DC-Link Voltage and Capacitors

The maximum voltage injection capability of the four-leg VSC is 25V. As the turn ratio of the injection transformer is 1:4.6, the maximum line-to-neutral voltage v_{max}^{i} on the converter's side is 115V. The required DC-link voltage can be given by [138]:

$$V_{DC} = v_{max}^{i}.\sqrt{2}.\sqrt{3} = 280V \tag{6.6}$$

Under an unbalanced system, the negative sequence current requires a higher negative sequence voltage control [138]. As a result, the VSC needs a higher DC-link voltage, thus 300V is used as the DC-link voltage. In addition, the negative sequence current has a significant impact on the ripple of the DC-link capacitors [138]. Therefore, to design the minimum DC-link capacitors, 100% negative sequence unbalanced factor of equation (2.3) is considered. In this case, it is assumed that the load current of one phase has the maximum value, while the other two phases have zero current values. As a result, the minimum DC-link capacitance value needed to handle the 100% negative sequence unbalanced load current, can be expressed by (6.7) [138]:

$$C_{DC-min} = \frac{3.\, v_{max}^{i}.\, I_{n}^{max}}{4.\, V_{DC}.\, \omega_{c}.\, \Delta V_{DC}} \tag{6.7}$$

where I_{n}^{max}, ω_c and ΔV_{DC} are peak of the maximum negative sequence current, system frequency (100π) and capacitor voltage ripple (2% of the rated DC-link voltage), respectively. Referring to equation (6.6) results into having a minimum $650\mu F$ DC-link capacitor. However a larger value of $1000\mu F$ is chosen to make sure that it satisfies the system requirements for higher current applications.

In this work, EPCOS $1000\mu F$, 400V electrolytic snap in the capacitor has been chosen. As shown in Figure 6.3, four EPCOS capacitors are selected, two in series and two in parallel, with total equivalent of $1000\mu F$ and 800V DC bus in an effort to make the VSC usable for higher voltage/current applications.

6.2.6 Relay Switch Protection Circuit

As the four-leg VSC is connected in series with the grid, if the VSC stops working for any reason, the voltage across each injection transformer is equal to the grid voltage. In this case, the filtering capacitor voltage increases to grid voltage×transfomer turn ratio and the converter acts as a rectifier (only anti-parallel diodes are active) where the DC-link capacitors and the DC power supply behave like a load. This increases the voltage on the DC side which can lead to damaging the entire system.

A 9kW, 4 pole, 230V ABB contactor has been implemented to disconnect the grid from the rig if any fault happens. This contactor is energised by a relay switch circuit, as shown in Figure 6.8. An ordinary transistor switch can drive the relay coil by providing fast on/off (1/0 signal) switching control, which comes from the FPGA.

The proposed circuit takes the output from a fibre optic receiver and sends it to the transistor in order to drive the coil of a 5V relay (PE014005). When the input signal is high (or 1), the transistor is on and a current flow through the relay coil leading to drive the coil. When the input signal is low (or 0), the current flowing through the relay coil drops and relay coil is disconnected.

A flywheel diode has been used to prevent damaging the transistor while the relay coil is disconnected as the coil inductor has some stored energy. The advantage of using the relay is that it takes only a small amount of power to operate the relay coil and can be connected to the same 5V power circuit of the VSC. Consequently, the 5V relay coil can be connected/disconnect from the coil of the 4 pole 230V contactor. As a result, if any unwanted fault happens and the VSC stops operating, the FPGA sends a fast low signal (or 0) to the fibre optic receiver to cut off the contactor coil (by 5V relay coil) which leads to the grid getting disconnected from the experimental rig.

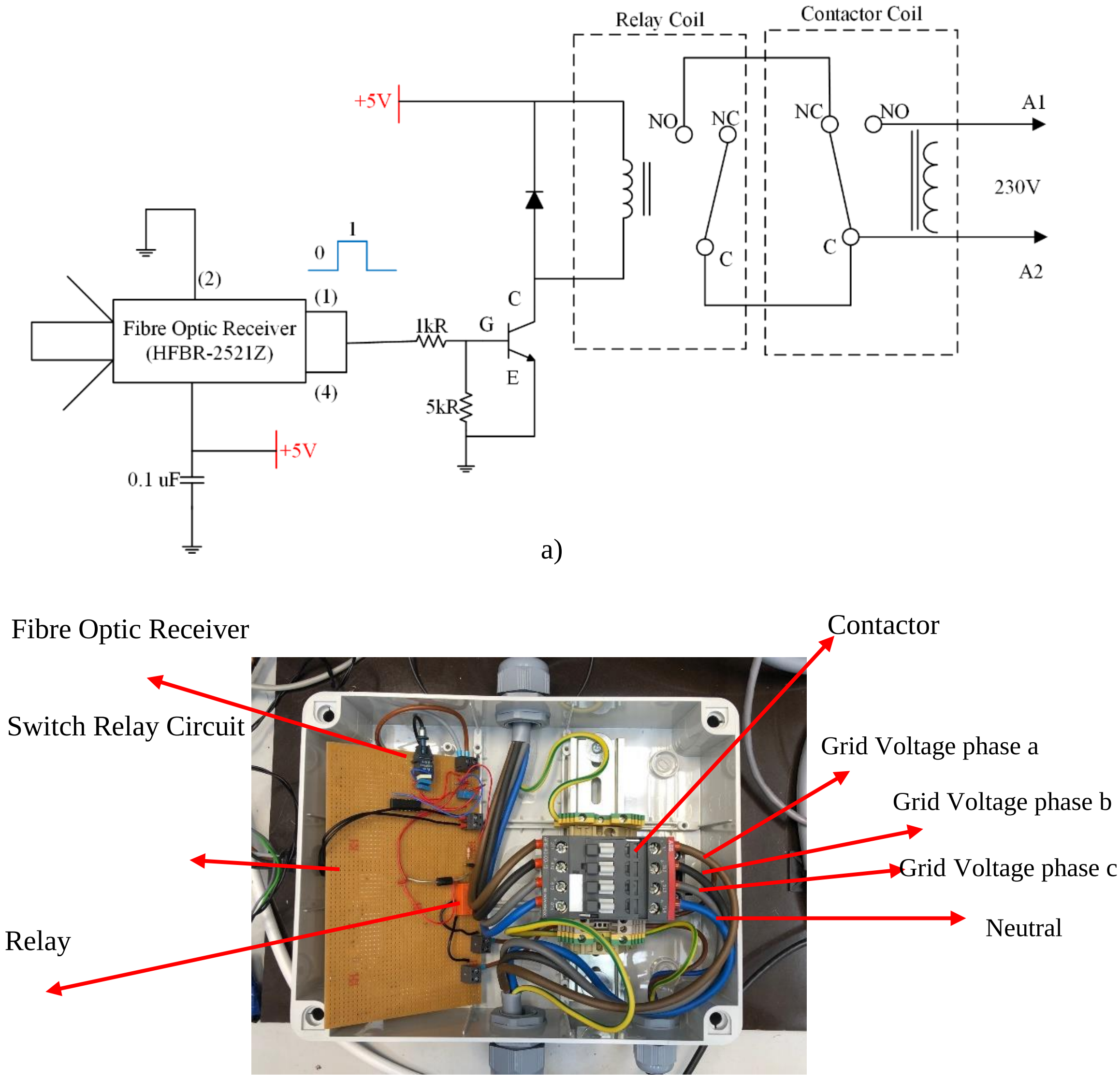

b)

Figure 6.8: Switch relay circuit, a) schematic diagram, b) implemented circuit board. NC=Normally Close, NO=Normally Open, C=Common.

6.2.7 Output Filter

As stated earlier, the four-leg VSC has an LC-filter at the output of the converter to reduce the ripple harmonics of both current and voltage generated by SVPWM and produce sinusoidal output signals. The mathematical model and design of the LC-filter can be found in several books and papers [144-147]. The inductor ripple of the current generated by modulation and the switching frequency, are the main parameters to be considered for inductor value. Typically, the ripple current can be chosen as 15%-25% of the rated current [145]. In this work, the inductor of the series-connected VSC (L_x) is chosen to have a ripple current of 20% of the rated current, the inductor value is given by:

$$L_x = \frac{V_{DC}}{I_{ripple}^{pk}.f_{sw}}|D|.(1-|D|) \tag{6.8}$$

where I_{ripple}^{pk} and f_{sw} are the peak value of the current ripple and switching frequency (10kHz), respectively. D is the duty ratio and can be expressed as [138]:

$$D = \frac{v_{max}^{i}}{V_{DC}}\sin(\omega t) \tag{6.9}$$

where v_{max}^{i} is the peak value of the line-to-neutral voltage. In this study, an output filtering inductor of $10mH$ is selected. The inductors used in the experimental rig are manufactured by JMS Transformers [148]. A photograph of three-phase inductors is shown in Figure 6.9.

Figure 6.9: Photograph of three-phase inductors.

In LC-filter structures, it is important to determine the resonant frequency ω_{res}. Resonance happens when in LC circuit, the inductive and capacitive reactances are equal in magnitude. The resonant frequency can be given by:

$$\omega_{res} = \frac{1}{2\pi\sqrt{L_x C_{cap}}} \tag{6.10}$$

The resonant frequency ω_{res} of the LC-filter is chosen to be smaller than half of the switching frequency f_{sw} , and adequately higher than the fundamental frequency f_c [149]. The resonant frequency, ω_{res} , is selected to be 700Hz and the filter capacitor value can then be easily calculated according to the equation (6.10). Therefore, three Vishay 5μF capacitors (MKP386M) are chosen, as shown in Figure 6.10.

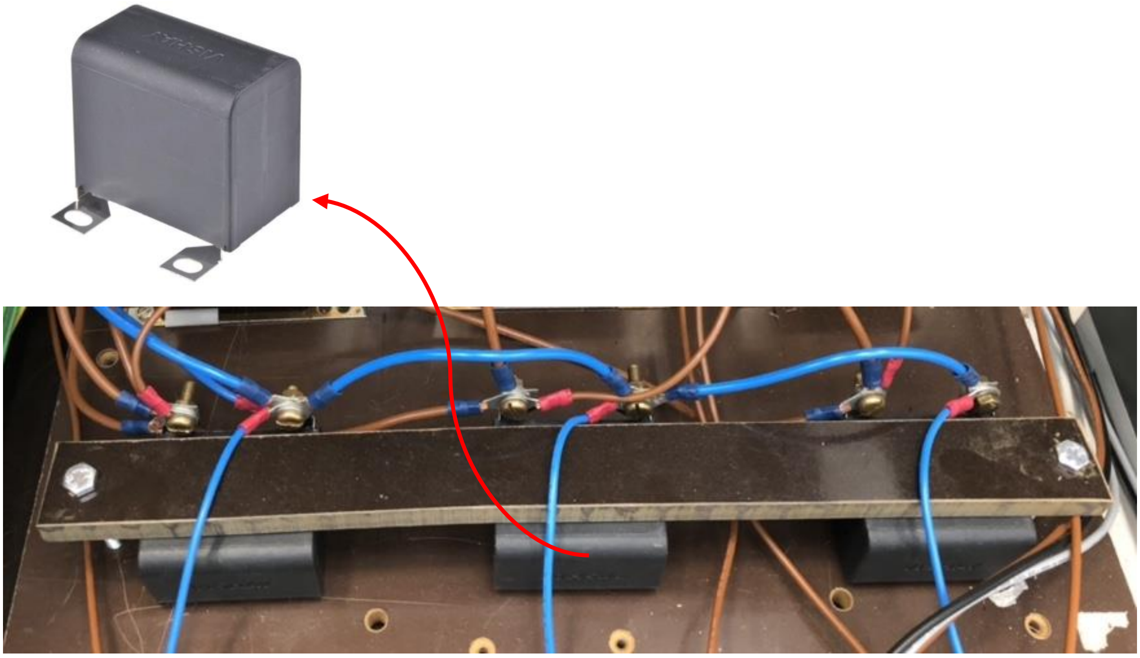

Figure 6.10: Photograph of three-phase capacitors.

6.2.8 Injection Transformer

As discussed earlier in Chapter 2, the main purpose of injection transformers is to provide a galvanic isolation between the four-leg VSC and the main feeder and inject the desired voltage into the system. In addition, as the power losses in the IGBTs is defined as a function of current [52], adding a series injection transformer would contribute to reducing the total rating of the VSC current resulting into the converter having lower power losses.

Several types of transformer can be used for the proposed system. In this work the 500VA toroidal transformer is used as the main injection component. The core of the toroidal transformer looks like a circular ring and due to its symmetry shape, it has a lower leakage flux, less Electromagnetic Interference (EMI), smaller size/weight and higher efficiency in comparison to the other low frequency 500VA transformers [150]. The proposed injection transformer is shown in Figure 6.11.

The transformer has two secondary windings and can be connected in series or parallel. In this study, the secondary winding is connected in series with a turn ratio of 1:4.6. The high voltage, low current (primary side) are connected to the converter side and the low voltage, high current (secondary side) are attached to the feeder side. As mentioned before, the maximum voltage injection range is ±25V. Therefore, this is the maximum allowable injection voltage at the secondary side of the transformer. Moreover, ±115V is the maximum limit of the voltage at the primary side (converter side).

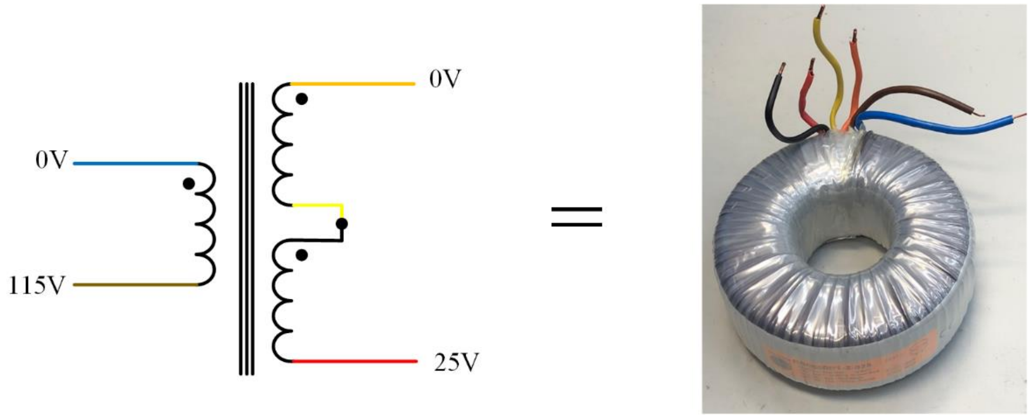

Figure 6.11: Toroidal injection transformer.

6.3 Control Platform

As shown in Figure 6.12, the control platform consists of three main parts: a DSP board, an FPGA custom designed board and an HPI daughter card board. Due to the complexity of the mathematical calculations of 3-dimensional SVPWM and symmetrical component algorithm/controller, a fast processor is required. For this experimental work, the TMS320C6713 (C6713) DSP operating at 225MHz is used. This DSP is widely used within the University of Nottingham PEMC research group.

The C6713 is a high speed 32-bit External Memory Interface (EMIF) floating point processor and can be programmed in C language, using the Code Composer Studio from Texas Instruments. The C6713 has three main tasks, as follows:

- Initialisation and peripheral setup to initialise the main variables and FPGA set-up
- Execute the main controller, including resonant controllers and the symmetrical components estimation algorithm
- Perform all the calculations for the 3-dimensional SVPWM

Due to complexity of the switching sequences of 3- dimensional SVPWM algorithm, and short timing of each switching sequence, an FPGA is required to connect the DSP to the gate drive circuits. The FPGA board was originally developed by the PEMC group at the University of Nottingham [151]. The FPGA is attached to the memory map of the DSP and communicates with the DSP board by EMIF. The FPGA chip used is ACTEL ProASIC3 A3P400 with ten 12 bit A/D channels. The main functions of the FPGA can be summarised, as follows:

- A/D conversion: The A/D channels receive the analogue data from the voltage/current transducers and convert them into digital data and pass the information to the DSP board for processing
- A FIFO (First in First Out) memory register: This memory register holds the PWM vector information for each interrupt cycle. The FPGA creates an interrupt in respect to the switching frequency. The process is implemented every interrupt cycle of $100\mu s$, which works in respect to the switching frequency of 10 kHz
- Generate modulation: The FPGA performs the timing of each vector and send the 3-dimensional SVPWM switching signals to the gate drive by the fibre optic transmitters in respect to the demands from DSP
- Fault trip: The FPGA uses comparators for over-current or overvoltage protection. For instance, if currents or voltages rise above a certain value, all the switches are turned off and the VSC stops working
- Watchdog timer: A trip is generated in the event of a communications failure between FPGA and DSP. For example, if the DSP program crashes or does not execute appropriately the power converter is turned off. This signal is sent at the beginning of every interrupt routine

The interrupt routine is driven by an interrupt signal generated by FPGA and executes the A/D channels reading, space vector modulation and control algorithm. The entire control program should run within an interrupt cycle of $100\mu s$ $(1/f_{sw})$. During the testing, it has been observed that the interrupt routine takes $80\mu s$ to complete, which is within the sampling period of $100\mu s$. Furthermore, the FPGA board has a 50 MHz clock, leading to a clock period of $0.02\mu s$. Therefore, all the switching time generated need to be multiples of this clock period. The block diagram of DSP and FPGA structure is shown in Figure 6.13.

The HPI daughter card is needed to provide a bi-directional data transfer between the host PC and the DSP without interrupting the central processor unit. The 16 bit HPI board is mapped on the DSP board and allows the control program to be loaded into DSP and to download sample variables. The HPI board is connected to the PC by a USB connection.

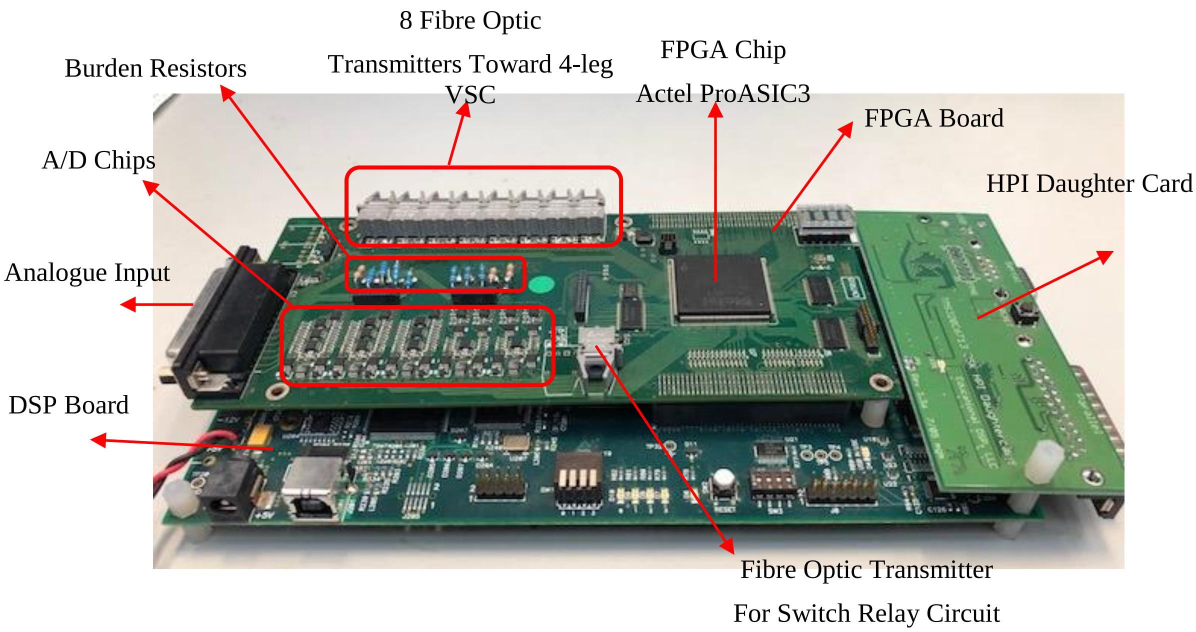

Figure 6.12: Control platform used for the experimental prototype.

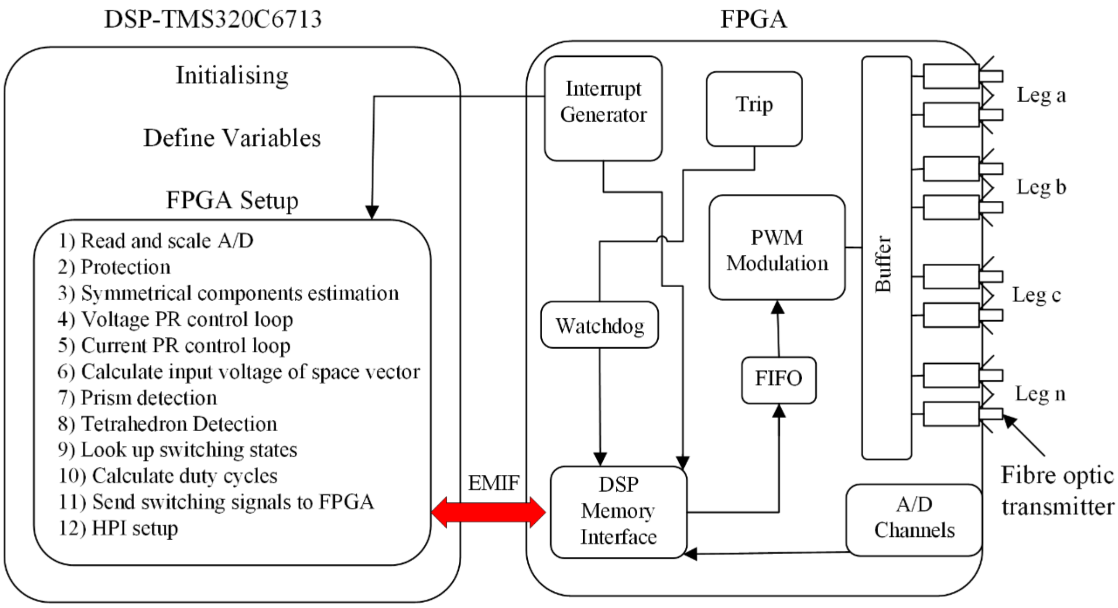

Figure 6.13: The block diagram of DSP and FPGA structure.

6.4 Implementation of Controllers in Digital Systems

6.4.1 Discretisation of Resonant Controllers

Resonant controllers have a narrow bandwidth and an infinite gain at resonant frequency, ω_0 [152]. A slight movement of the resonant poles causes a significant loss of performance. As a result, an appropriate discretisation method with satisfactory results needs to be used. Several discretisation methods [152-154] can be used for transforming the continuous-time domain $X(s)$ into an equivalent discrete-time domain $X(z)$. The most popular z-domain methods used in digital control can be summarised, as follows:

- Forward Euler and Backward Euler methods: These two methods are not appropriate for discretising the resonant controllers, as they have a potential stability issue [153]. In these two methods, the poles of the resonant controller are mapped out of the unitary circumference (stability region of the discrete-time domain) as shown in Figure 6.14. The discrete transfer functions of PR controller (equation (4.1)) obtained from Forward Euler and Backward Euler methods are given in (6.11) and (6.12), respectively:

$$X_{FE}(Z) = X(s)|_{s=\frac{z-1}{T_s}} = T_s.\frac{z^{-1} - z^{-2}}{1 - 2z^{-1} - z^{-2}(\omega_0^2 T_S^2 + 1)} \tag{6.11}$$

$$X_{BE}(Z) = X(s)|_{s=\frac{z-1}{zT_s}} = T_s.\frac{1 - z^{-1}}{(\omega_0^2 T_S^2 + 1) - 2z^{-1} + z^{-2}} \tag{6.12}$$

- Tustin method: Unlike Forward Euler and Backward Euler methods, the resonant controller poles in Tustin approximation are mapped into the stability region of discrete-time domain (unitary circumference). However, this method is not recommended for applications at which high frequency should be tracked as the steady-state error increases with sampling period and harmonic orders, [153] as shown in Figure 6.14. It is worth to note that, this method is acceptable for this study as the resonant frequency of the system is set to $\omega_0 = 100\pi\ Rad/s$. The resonant controller discrete transfer function of Tustin method can be given by:

$$X_{TU}(Z) = X(s)|_{s=\frac{2(z-1)}{T_s(z+1)}} = 2T_s.\frac{1 - z^{-2}}{(\omega_0^2 T_S^2 + 4) + z^{-1}(2\omega_0^2 T_S^2 - 8) + z^{-2}(\omega_0^2 T_S^2 + 4)} \tag{6.13}$$

- Zero Order Hold (ZOH), [153, 154], impulse invariant, Zero-Pole Matching (ZPM) [153] and Tustin with Pre-warping [153, 155] methods: These methods provide an accurate location of the resonant peaks, even for high frequencies and low sampling time [153] as shown in Figure 6.14. A complete list of z-domain transfer functions for resonant controllers can be found in [154]

Figure 6.14 shows the open-loop poles location of different discretisation methods used for resonant controllers. To achieve an infinite gain (zero damping ratio), the poles should be located on the unitary circumference in z-plane mapping [156]. This factor is not true for Forward Euler and Backward Euler methods, as the poles are out of the stability region of the z-plane mapping. In other words, these two methods map on the right-hand side (unstable region) of s-plane (continuous-time domain). In addition, as can be seen, high order frequencies cannot be tracked properly in Tustin method, while ZOH, impulse invariant, ZPM and Tustin with Pre-warping can provide an accurate location of the resonant peaks for high order frequencies [153].

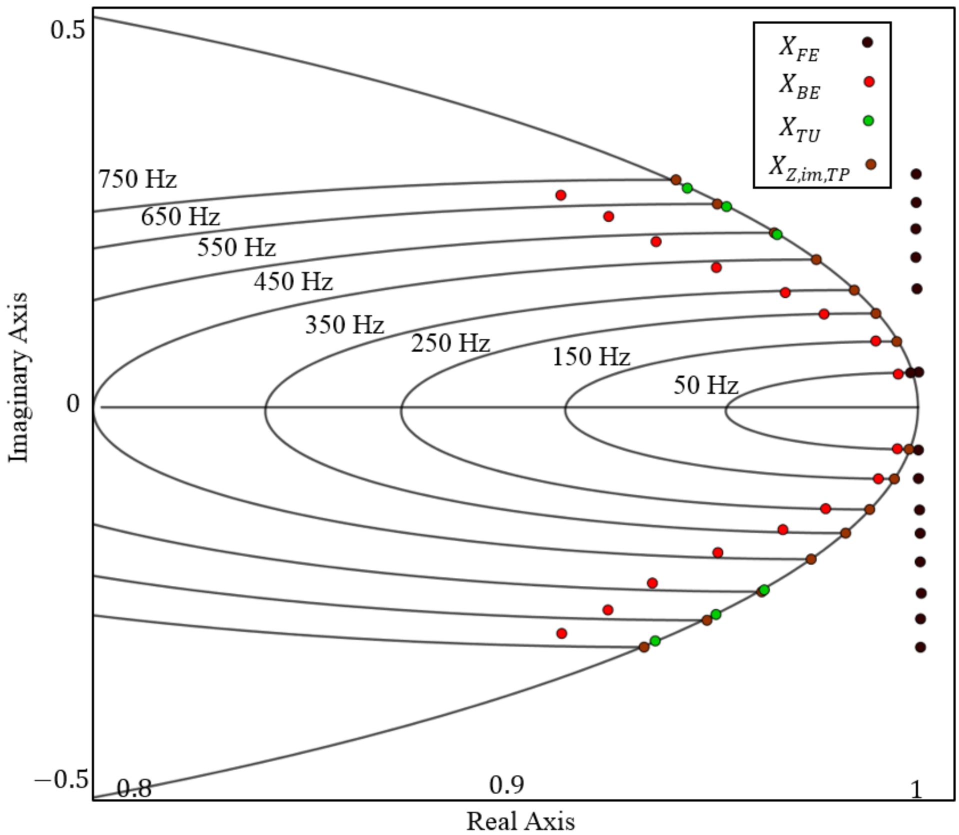

Figure 6.14: Poles location of the discretised resonant controller at $f_s = 10$ kHz. X_{FE}=Forward Euler, X_{BE}=Backward Euler, X_{TU}=Tustin, $X_{Z,im,TP}$=ZOH, ZPM, impulse variant and Tustin with pre-warping.

Tustin with Pre-warping is an extended method of Tustin approximation. This method centred the approximation on the pre-warp frequency ω_0 to ensure that the continuous-time domain and discrete-time domain act approximately similar on this frequency. Due to the simplicity and high performance of the Tustin with Pre-warping approximation, this method has been used in this work. The discrete transfer functions of PR controller of equation (4.1) can be expressed by:

$$X_{TUP}(Z) = X(s)|_{s=\frac{\omega_0}{\tan(\frac{\omega_0 T_s}{2})}\frac{z-1}{z+1}} = \frac{\sin(\omega_0 T_s)}{2\omega_0}.\frac{1-z^{-2}}{1-2z^{-1}\cos(\omega_0 T_s)+z^{-2}} \quad (6.14)$$

The design of the resonant controllers discussed in Chapter 4 is made directly in z-domain in order to obtain an expression that can be implemented in DSP. Using Tustin pre-warping method and with the assumption that $u(k)$ and $e(k)$ are the output and error signals, respectively, the resonant controller of (4.1) in z-domain can be written as:

$$\frac{u(k)}{e(k)} = \frac{a_0 + a_1 z^{-1} + a_2 z^{-2}}{b_0 + b_1 z^{-1} + b_2 z^{-2}} \quad (6.15)$$

where:

$$K_T = \frac{\omega_0}{\tan(\frac{\omega_0 T_s}{2})}$$

$$a_0 = {K_T}^2 K_p^{PR} + \omega_0^2 K_p^{PR} + 2K_i^{PR} K_T$$

$$a_1 = 2\omega_0^2 K_p^{PR} - 2{K_T}^2 K_p^{PR}$$

$$a_2 = {K_T}^2 K_p^{PR} + \omega_0^2 K_p^{PR} - 2K_i^{PR} K_T$$

$$b_0 = {K_T}^2 + \omega_0^2$$

$$b_1 = 2\omega_0^2 - 2{K_T}^2$$

$$b_2 = {K_T}^2 + \omega_0^2$$

Therefore, the differential equation implemented in DSP can be given by:

$$u(k) = \frac{1}{b_0}\big(a_0 e(k) + a_1 e(k-1) + a_2 e(k-2) - b_1 u(k-1) - b_2 u(k-2)\big) \quad (6.16)$$

6.4.2 Discretisation of SOGI-QSG

As discussed in Chapter 5, a SOGI-QSG is needed to provide the input signals on $\alpha\beta$ reference frame in positive and negative sequences. By referring to Figure 5.3, the general structure of SOGI can be presented in continuous-time domain, as follows [157]:

$$G_{SOGI}(s) = \frac{\omega_c s}{s^2 + \omega_c^2} \tag{6.17}$$

The closed-loop transfer functions of the SOGI-QSG (α) structure depicted in Figure 5.3 can be expressed by:

$$C_{cl-a}(s) = \frac{v'_\alpha}{x_\alpha} = \frac{\omega_c s}{s^2 + \omega_c s + \omega_c^2} \tag{6.18}$$

$$C_{cl-q}(s) = \frac{qv'_\alpha}{x_\alpha} = \frac{\omega_c^2}{s^2 + \omega_c s + \omega_c^2} \tag{6.19}$$

The discrete implementation of the SOGI is based on Tustin method. For this method, s is replaced by $2(z-1)/T_s(z+1)$, thus equation (6.18) can be written as:

$$C_{cl-a}(z) = \frac{2\omega_c T_s z^2 - 2\omega_c T_s}{4(z-1)^2 + 2\omega_c T_s(z^2-1) + (\omega_c T_s)^2(z+1)^2} \tag{6.20}$$

Now let us consider $A = 2\omega_c T_s$ and $B = (\omega_c T_s)^2$, equation (6.20) can be re-written as:

$$C_{cl-a}(z) = \frac{\left(\frac{A}{A+B+4}\right) + \left(\frac{-A}{A+B+4}\right) z^{-2}}{1 - \left(\frac{2(4-B)}{A+B+4}\right) z^{-1} - \left(\frac{A-B-4}{A+B+4}\right) z^{-2}} \tag{6.21}$$

Consequently, the discrete form of SOGI_QSG v'_α signal can be represented, as follows:

$$C_{cl-a}(z) = \frac{a_0(1 - z^{-2})}{1 - b_1 z^{-1} - b_2 z^{-2}} \tag{6.22}$$

where:

$$a_0 = \frac{A}{A+B+4}$$

$$b_1 = \frac{2(4-B)}{A+B+4}$$

$$b_2 = \frac{A-B-4}{A+B+4}$$

Therefore, the differential equation of the v'_α signal implemented in DSP can be given by:

$$u(k) = a_0 e(k) + a_0 e(k-2) + b_1 u(k-1) + b_2 u(k-2) \tag{6.23}$$

The same mathematical procedures have been carried out to obtain qv'_α signal of equation (6.19) in the discrete form, the result can be found in (6.24)

$$C_{cl-q}(z) = \frac{a_0 + a_1 z^{-1} + a_2 z^{-2}}{1 - b_1 z^{-1} - b_2 z^{-2}} \tag{6.24}$$

where:

$$a_0 = a_2 = \frac{B}{A+B+4}$$

$$a_1 = \frac{2B}{A+B+4}$$

$$b_1 = \frac{2(4-B)}{A+B+4}$$

$$b_2 = \frac{A-B-4}{A+B+4}$$

Hence, the differential equation of the qv'_α signal implemented in DSP can be given by:

$$u(k) = a_0 e(k) + a_1 e(k-1) + a_2 e(k-2) + b_1 u(k-1) + b_2 u(k-2) \tag{6.25}$$

6.5 Three-Dimensional SVM Assessment

To verify the performance of the 3- dimensional SVPWM algorithm, two open-loop tests have been carried out and the outcomes are compared to the simulation results. For the first test, the balanced reference voltages $v_i^*, i \in a, b, c$ have been considered, while the unbalanced reference voltages have been used for the second test. As stated in Chapter 4, a symmetrical sequence pattern with two zero vectors has been considered as the switching sequence scheme due to its low harmonic distortion and the switching losses. The balanced reference voltages can be given by:

$$\begin{cases} v_a^* = \dfrac{V_{DC}}{\sqrt{2}.\sqrt{3}} \sin(100\pi t) \\ v_b^* = \dfrac{V_{DC}}{\sqrt{2}.\sqrt{3}} \sin\left(100\pi t - \dfrac{2\pi}{3}\right) \\ v_c^* = \dfrac{V_{DC}}{\sqrt{2}.\sqrt{3}} \sin\left(100\pi t + \dfrac{2\pi}{3}\right) \end{cases} \tag{6.26}$$

In the balanced condition, the reference signals are transformed to $\alpha\beta$ coordinate without considering γ axis, as $v_\gamma = 0$. Figure 6.15 (a) shows the reference waveforms obtained from equation (6.26). Figure 6.15 (b) presents the corresponded prism and tetrahedron of (6.26) captured by the HPI. As can be observed during each sinusoidal cycle ($1/f_c$ or $200T_s$) of the balanced reference voltages, there are six identical prisms every $60^\circ(1/6f_c)$ where the space vectors are located. In this case, each prism has two active tetrahedrons, tetrahedron 1, 2 which are presented in Table 4.4. Therefore, there are twelve active tetrahedrons in each sinusoidal cycle of the reference voltages. In addition, the voltage active vectors are located in these twelve tetrahedrons, and their respective time duration can be easily calculated by referring to Appendix B. Figure 6.16 shows the close view of the output phase voltages for prisms 1, 2 and tetrahedrons1, 2 over a 1ms interval. The symmetrical alignment with three active vectors and two zero vectors has been clearly identified at each sampling period, T_s.

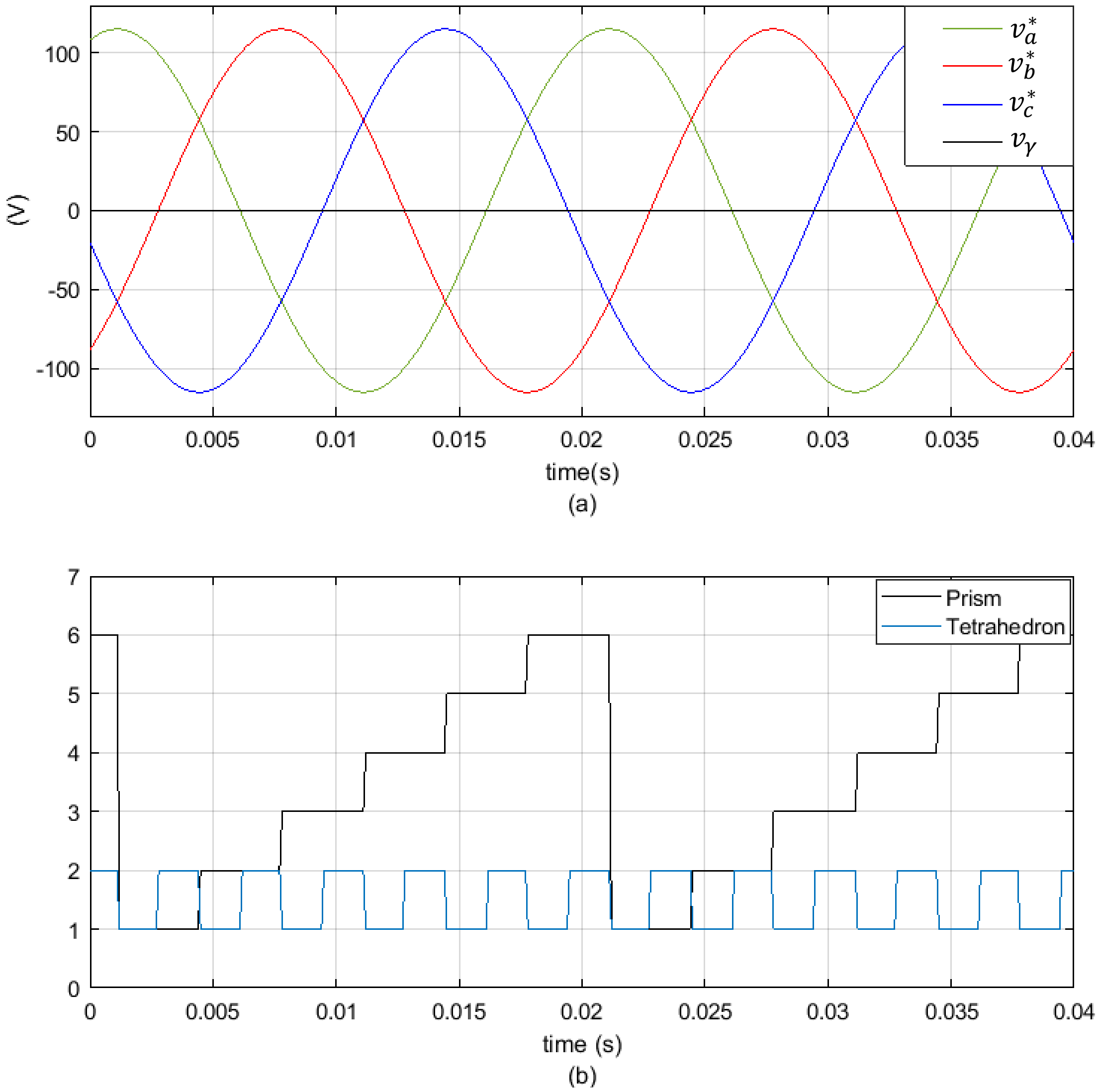

Figure 6.15: 3-D SVPWM plots of a) reference voltages, b) corresponded prisms and tetrahedron of balanced condition captured by HPI.

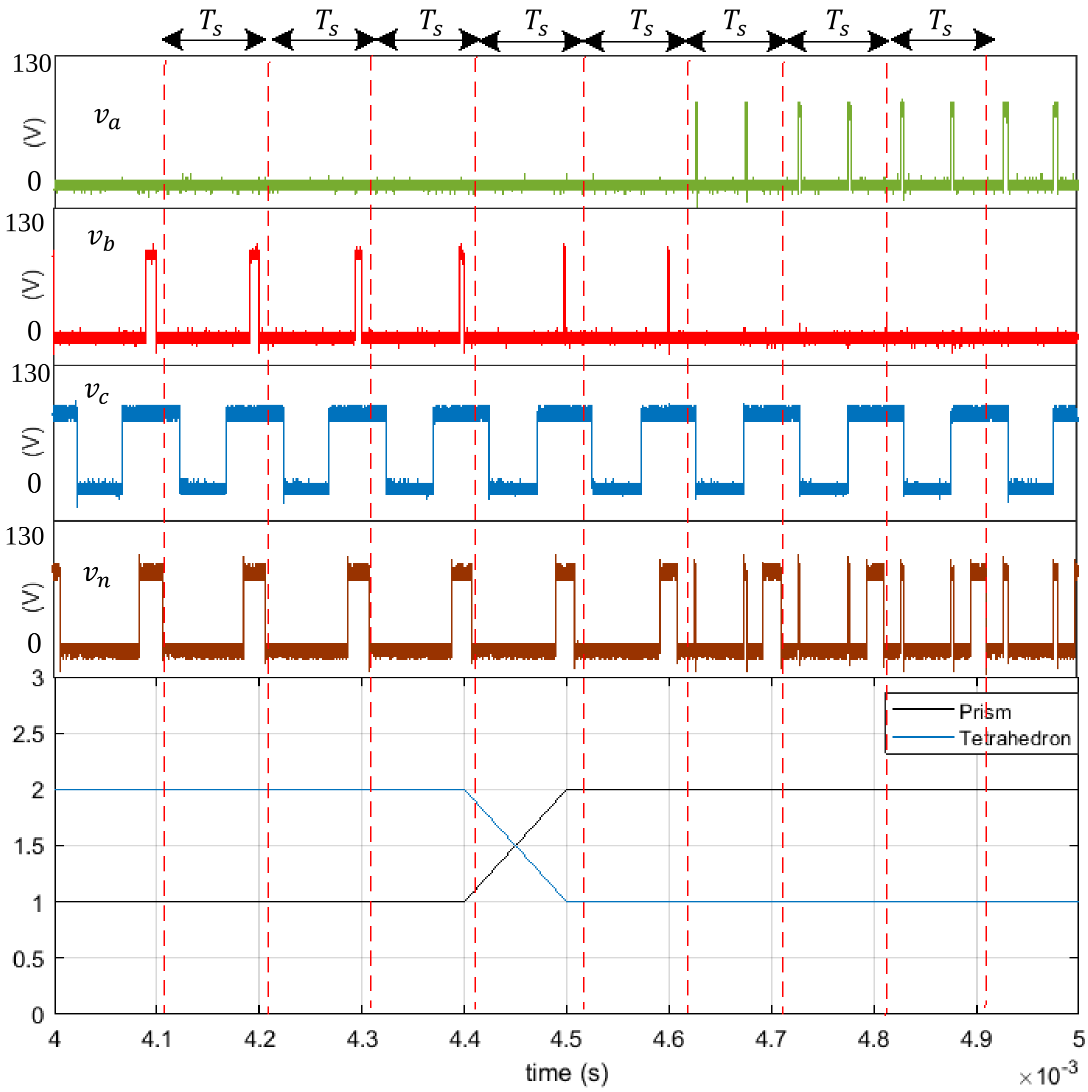

Figure 6.16: The close view of output phase voltages v_a,$v_{b,}v_{c,}v_n$ for prisms 1, 2 and tetrahedrons 1, 2. Balanced condition, sampling frequency of T_s = 10kHz and DC-link voltage of V_{DC} = 300V.

The reference voltages for the second test can be expressed by:

$$\begin{cases} v_a^* = \dfrac{-V_{DC}}{1.2\sqrt{2}.\sqrt{3}}\sin(100\pi t) \\ v_b^* = \dfrac{V_{DC}}{\sqrt{2}.\sqrt{3}}\sin\left(100\pi t - \dfrac{2\pi}{3}\right) \\ v_c^* = \dfrac{-V_{DC}}{2\sqrt{2}.\sqrt{3}}\sin\left(100\pi t + \dfrac{2\pi}{3}\right) \end{cases} \tag{6.27}$$

In this case, v_γ has a value and is obtained from equation (4.29). As the reference voltages are not balanced, the duration of each prism and the corresponding tetrahedrons are not equal, as shown in Figure 6.17 (b). Figure 6.18 shows the close view of the output phase voltages for prism 4 and tetrahedron 2 over a 1ms interval. Similar to the previous section, the symmetrical alignment with the three active vectors and the two zero vectors has been considered.

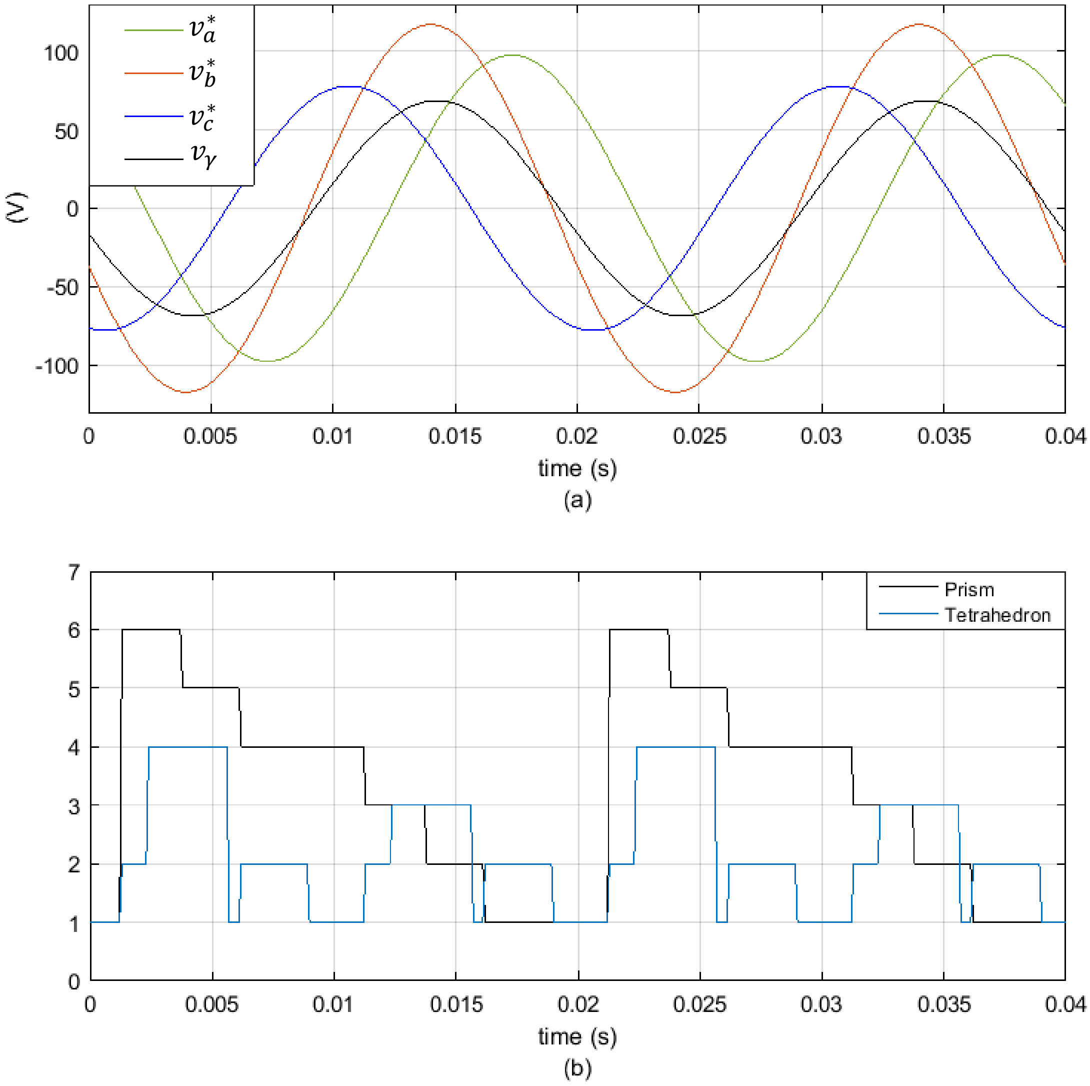

Figure 6.17: 3-D SVPWM plots of a) Reference voltages, b) Corresponded prisms and tetrahedron of unbalanced condition captured by HPI.

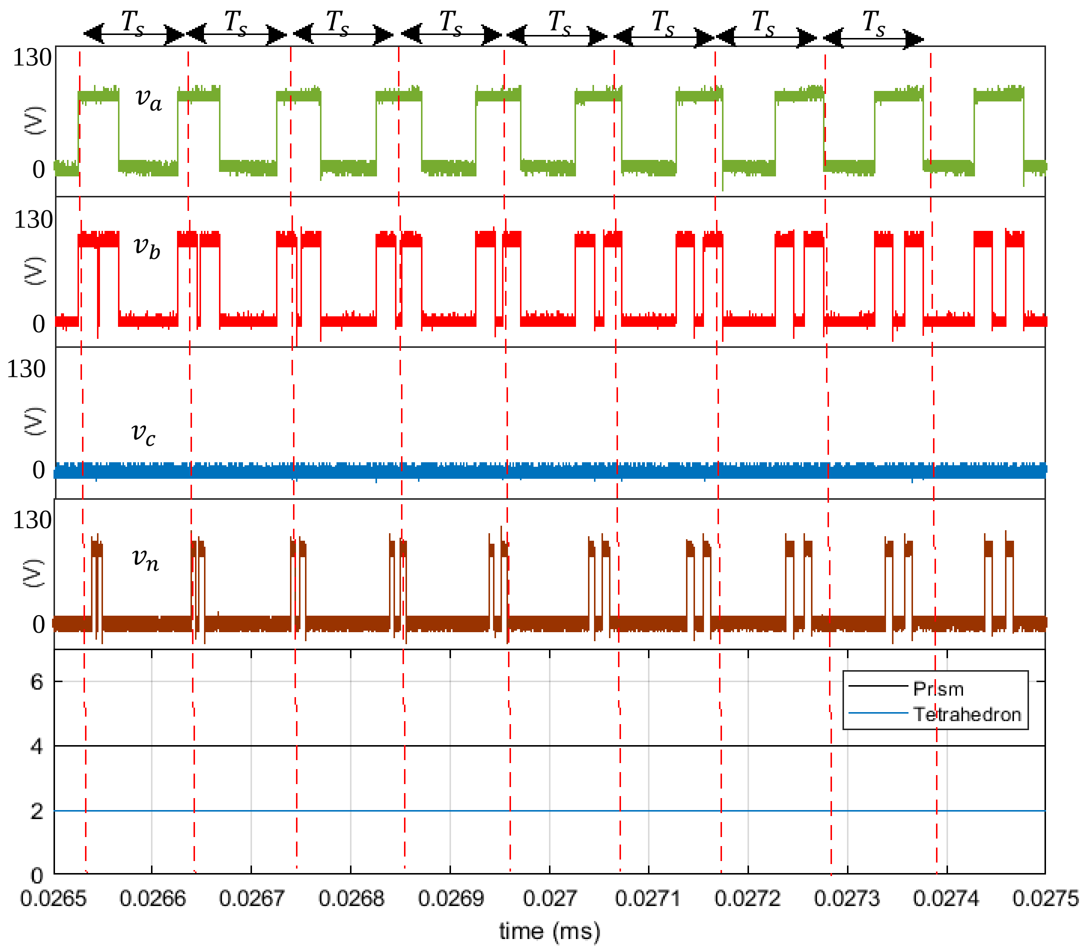

Figure 6.18: The close view of output phase voltages v_a,v_b,v_c,v_n for prism 4 and tetrahedrons 2. Unbalanced condition, sampling frequency T_s = 10kHz and DC-link voltage V_{DC} = 300V.

6.5.1 Comparison with Simulation

A simulation has been run by PLECS software with the same reference voltages used in previous section to compare and validate the 3-dimensional SVPWM that was implemented in experimental work. The results for the balanced and unbalanced conditions are shown in Figure 6.19 and 6.20, respectively. As can be observed, the simulation results are very similar to the outcomes captured by HPI, which verifies the results obtained from experimental work.

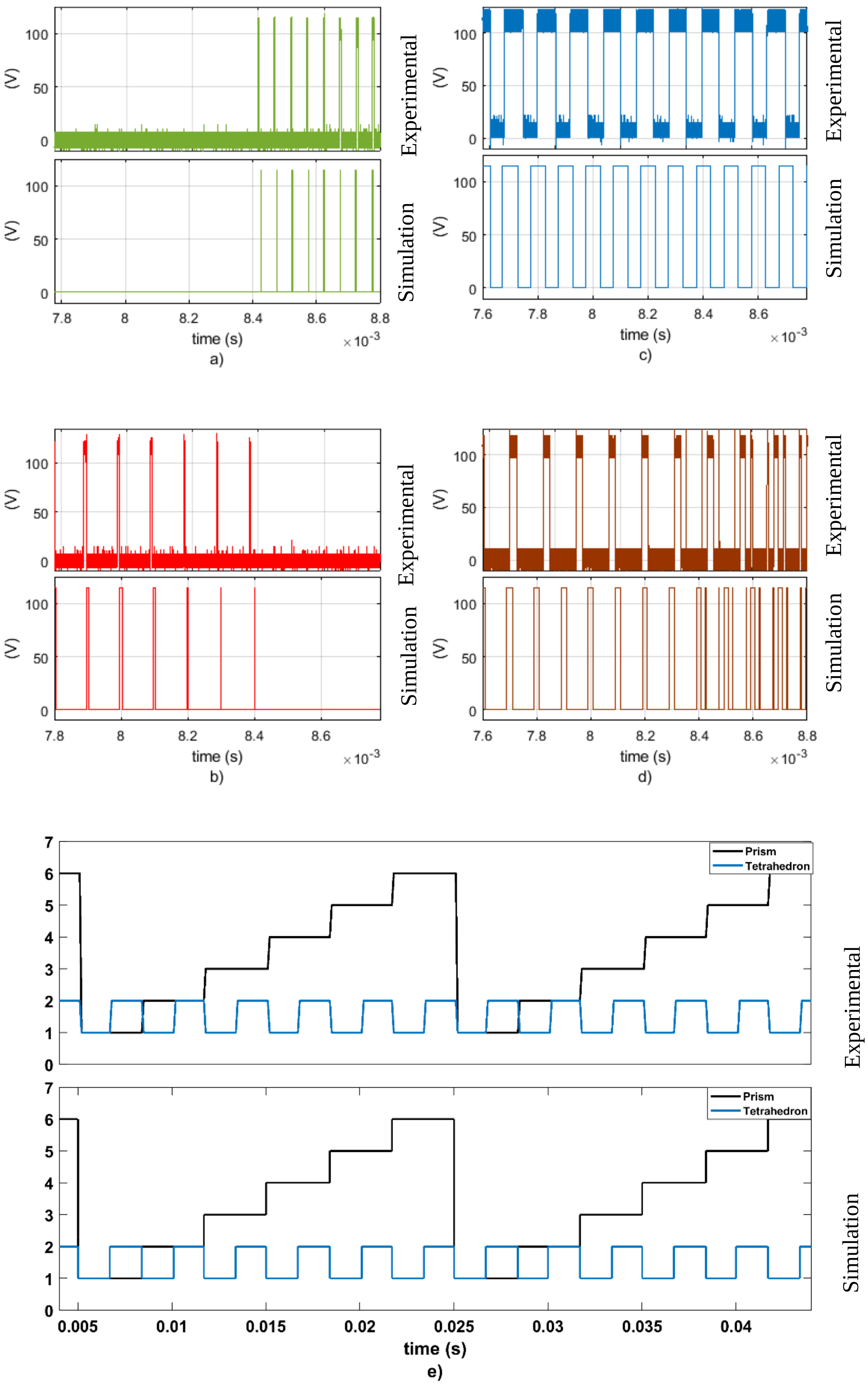

Figure 6.19: Comparison of simulated and experimental output phase voltages under balanced condition. a) v_a, b) v_b, c) v_c ,d) v_n, e) prisms and tetrahedrons

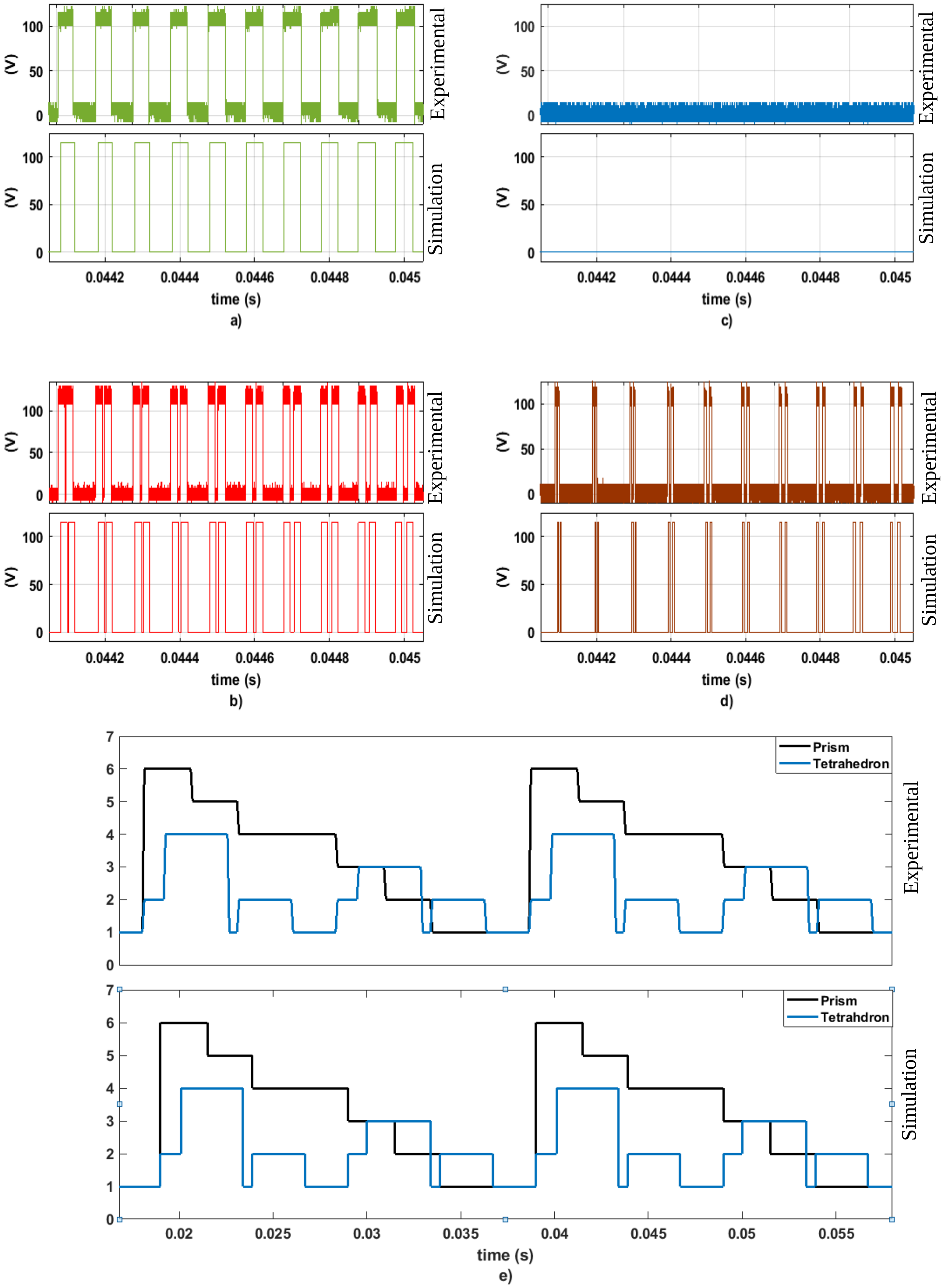

Figure 6.20 : Comparison of simulated and experimental output phase voltages under unbalanced condition. a) v_a, b) v_b, c) v_c ,d) v_n, e) Prisms and tetrahedrons

6.6 Closed-Loop Resonant Controllers' Performance

Figure 6.21 shows the experimental result of the inductor current for phase a, i_{con}^{a}, compared with the reference value under unbalanced condition. As can be seen, an acceptable reference tracking at the fundamental frequency $\omega_c = 50$Hz can be achieved for the closed-loop resonant current controller. The resonant current controller has ≈ 0Amp gain deviation with 0.1° phase shift at the main frequency.

Figure 6.22 shows the experimental results of the output capacitor voltage for phase a, v_{cap}^{a}, compared with the reference value under an unbalanced condition. As can be observed, for the proposed closed-loop multi-loop PR controllers, the output capacitor voltage (output of the multi-loop PR controllers) tracks the gain reference with ± 1V deviation and follows the phase reference with 1.2° phase shift. This results into a very good signal tracking. These verifications provide assurance that the VSC can be connected to the grid.

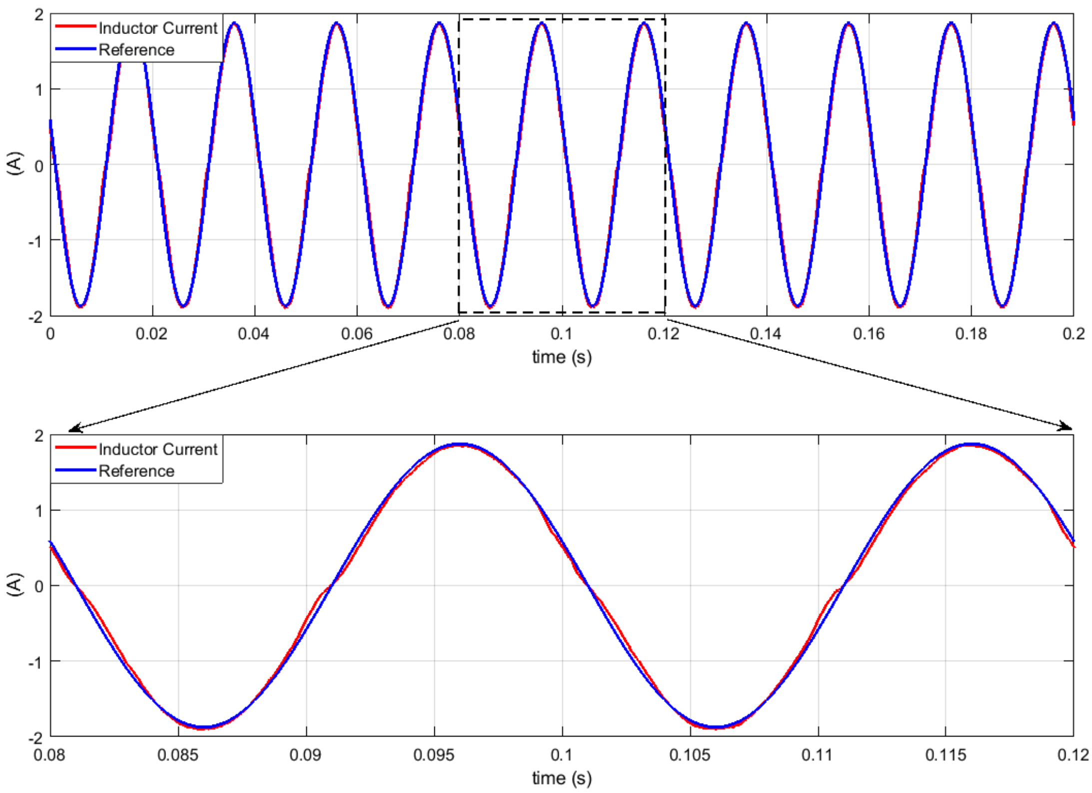

Figure 6.21: Current tracking of the PR current controller.

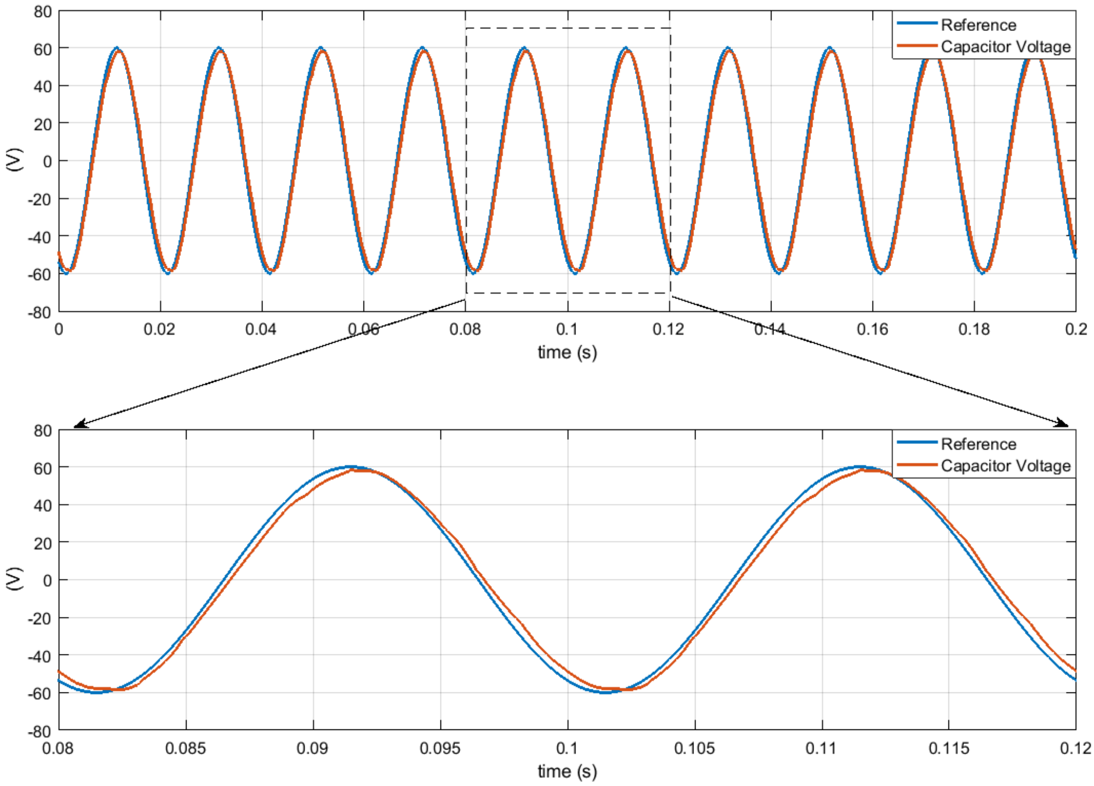

Figure 6.22: Voltage tracking of the multi-loop PR controllers.

6.7 Conclusion

A series-connected four-leg VSC has been constructed to validate the operation of the system discussed in Chapter 5. The power VSC parameters, filtering, measurement boards, protection circuit, digital control platform and controller discretisation have been described. The proposed three-dimensional SVMPWM presented in Chapter 4 is tested and the results match up with the simulated results. This proves that the equations derived for calculating the prisms, tetrahedrons, duty cycles and switching states are correct. In addition, the theory behind the PR controller design has been proved as the system has an acceptable signal tracking. The following technical issues were significantly important to have an effective experimental implementation:

- The utilisation of hardware protection circuit in addition to software overvoltage and overcurrent FPGA protection compensators
- As the proposed four-leg series-connected VSC is not a commercial prototype, it is important to design a compact circuit board with low voltage drop, losses and the noise of the system. For this purpose, a two layer PCB was designed in addition to reducing the Electromagnetic Interference (EMI). EMI was reduced by increasing the PCB's ground plane within the board total area, using decoupling capacitors and avoiding 90° traces' angles routed on PCB
- As the DC-link bus is mounted directly on the main PCB circuit board, it is vital to select the right thickness of circuit board. A two layer 1.6mm PCB board has been used to separate the positive DC voltage (top layer) and negative DC voltage (bottom layer). Distance between DC-link buses is close and hence parasitic inductance can reduce significantly. Before soldering the components, a successful 1kV flashing test was carried out to ensure that PCB board can easily tolerate the maximum experimental voltage
- Selecting cost effective, high efficient and low losses electronic devices of the power converter available in the market. This includes gate drive components, DC-link capacitors and resistors and voltage/current transducers

Next Chapter will present the experimental results, validating the designed series-connected four-leg VSC used for voltage regulation purposes.

CHAPTER 7: Experimental Studies

Summary: *This chapter presents the results taken from experimental series-connected four-leg VSC. The converter prototype has been performed under two different case studies. The effectiveness of the proposed controller has been verified and the experimental results validate the simulated outcomes.*

7.1 Introduction

This chapter presents the results obtained from the experimental system described in Chapter 6 to verify the proposed controller algorithm discussed in Chapter 5. In this chapter the experimental results for the series-connected four-leg VSC under different testing scenarios are presented and compared to the simulation results in order to confirm their validity. Due to time restrictions, the investigation has only been focused on one series-connected VSC connected to a three-phase feeder. A multi-feeder hybrid substation configuration (compromising both shunt and series VSCs) can be a potential investigation subject for the future work.

7.2 Experimental Assessment

Figure 7.1 illustrates the general diagram of the experimental set-up. To show the versatility of the proposed voltage regulation approach, the system is tested for the following case studies:

- **Case 1:** Voltage sag and swell mitigation for a three-phase feeder connected to a balanced load. This test has been done to ensure that the proposed voltage regulation approach can mitigate the unbalanced fault when it is connected to a three-phase balanced load
- **Case 2:** Voltage sag and swell mitigation for a three-phase feeder connected to a phase unbalanced supply voltage and an unbalanced load. This test has been carried out to verify the effectiveness of the proposed controller algorithm to achieve voltage regulation in an unbalanced three-phase load and grid

The maximum grid supply voltage is 170V RMS and is taken from a Chroma programmable AC source 61511 [158], which is connected to the experimental rig. The Chroma power supply can generate a very good sinusoidal waveform voltage with low THD. As mentioned in Chapter 5, the objective of the series-connected VSC is to balance and regulate load voltages by maintaining the positive sequence component at a pre-determined value. In this experimental work the reference load voltages are set to 160V RMS balanced three-phase. The experimental set-up parameters are summarised in Table 7.1.

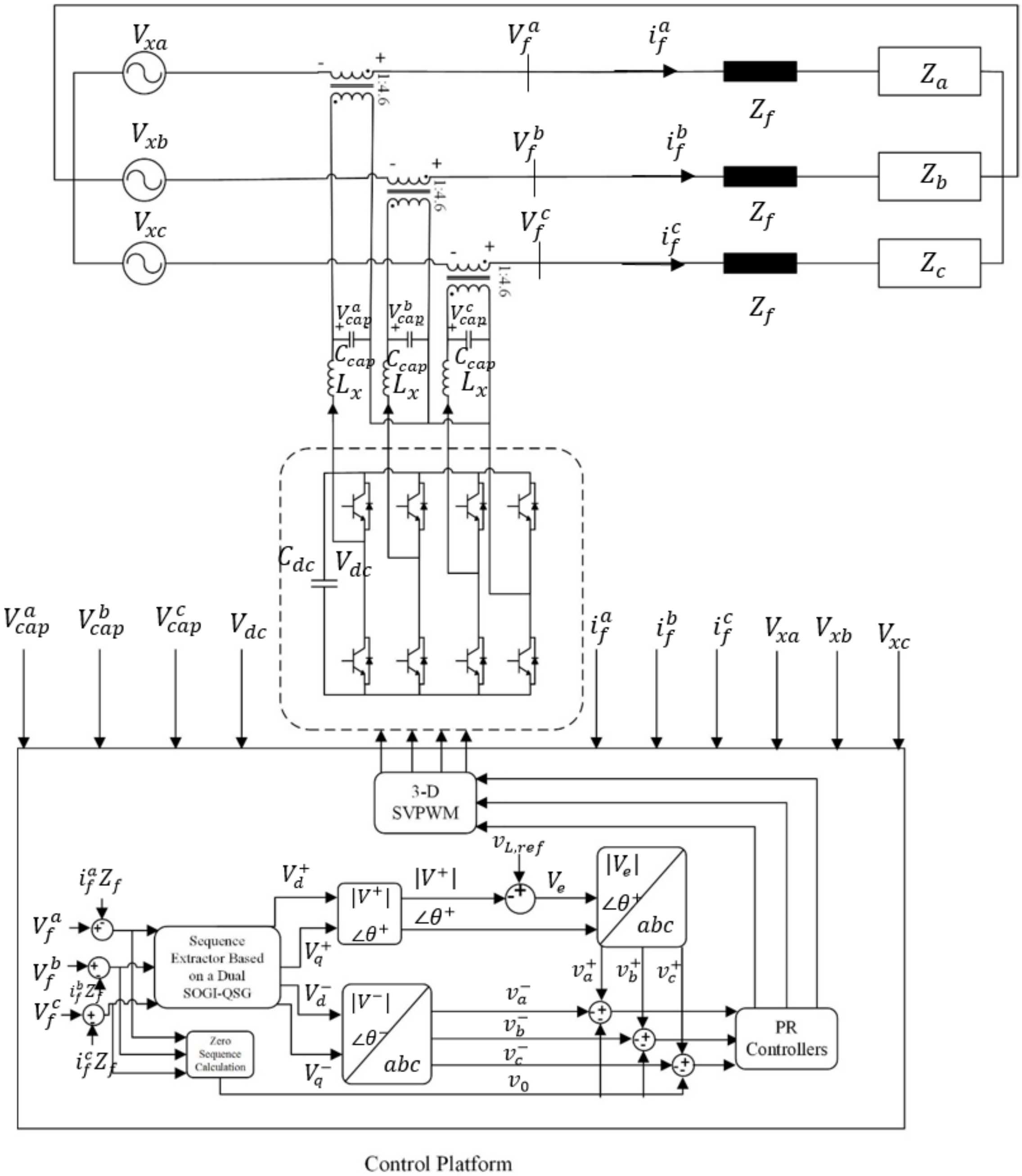

Figure 7.1: General diagram of experimental set-up.

Table 7.1: Experimental setup parameters.

System	
Supply Voltage	$V_{xa} = 170\sqrt{2}\sin(100\pi t)$ $V_{xb} = 170\sqrt{2}\sin\left(100\pi t - \frac{2\pi}{3}\right)$ $V_{xc} = 170\sqrt{2}\sin\left(100\pi t + \frac{2\pi}{3}\right)$
Line Impedance	$Z_f = 0.5\Omega$
Balanced Load Parameters	$Z_a = Z_b = Z_c = (10 + j0.3)\Omega$
Unbalanced Load Parameters	$Z_a = (10 + j0.3)\Omega$ $Z_b = (12 + j0.3)\Omega$ $Z_c = (8 + j0.3)\Omega$
Switching Frequency	$f_{sw} = 10\ kHz$
System Fundamental Frequency	$50Hz$
Filtering	
Capacitor	$C_{cap} = 5\ \mu F$
Inductor	$L_x = 10\ mH$
Injection Transformer	
Injection Transformer Turns Ratio	1:4.6
Power Rating	500VA
DC-Link	
Capacitor	$C_{dc} = 1000\ \mu F, 400V$
Voltage	$300\ V$

7.3 Experimental Tests

7.3.1 Case 1: Asymmetric Voltage Dip and Swell for Balanced Load

In this case a balanced three-phase linear load has been considered. Similar to the simulation section, phase a , phase b and phase c voltages are presented in green, red and blue colours, respectively. As shown in Figure 7.2 (a), the supply voltages are balanced up to $t = 0.1$s. At $t = 0.1$s, a 10% voltage swell and a 10% voltage dip are observed for the grid phase a and phase b , respectively. Meanwhile, the grid voltage at phase c is kept constant. The control algorithm detects the voltage sag/swell and compensates the desired voltages. The reference injection voltages can be calculated using algorithm explained in Chapter 5. Figure 7.2 (b) presents the required voltage for each capacitor to inject the desired voltage into the system (injection voltage at the converter side). As can be observed from Figure 7.2 (c), the load voltages are kept balanced at the reference value of 160V RMS at all times. Figure 7.2 (d) illustrates the Fast Fourier Transformation (FFT) spectrum of the load voltage. As can be observed, the load voltages have a peak value of 160V at fundamental frequency (50Hz) with a very low THD value of 0.2%. The proposed control approach boosts the positive sequence to the nominal load voltage (160V) without having a considerable negative sequence (2^{nd}, 5^{th}, 8^{th}, 11^{th} harmonics) or zero sequence (3^{rd} ,6^{th}, 9^{th} , 12^{th} harmonics) components.

Figure 7.3 shows the internal performance of the proposed controller captured by HPI. As shown in Figure 7.3 (a), the control algorithm has a very quick response to the fault and regulates the voltages in less than 20ms. As the system is balanced until 0.1s, the negative voltage magnitude $|V^{-}|$ and its phase angle θ^{-} are close to zero. As soon as the system becomes unbalanced, the voltage magnitude and its phase angle have a non-zero values. The corresponding negative and positive phase angles of the magnitude voltage sequences ($|V^{-}|$,$|V^{+}|$) of the controller are shown in Figure 7.3 (b). Selecting the right phase angle can minimise the injection voltage amount. The oscillations of the positive angle is due to the averaging method performance. Figure 7.3 (c) depicts the instantaneous zero voltage sequence. Similar to negative sequence component, during balanced condition, zero voltage sequence has a value close to zero. When the supply voltages become unbalanced, the instantaneous zero voltage sequence has a non-zero value. Table 7.2 summarises the sequence components of the proposed control algorithm for case 1.

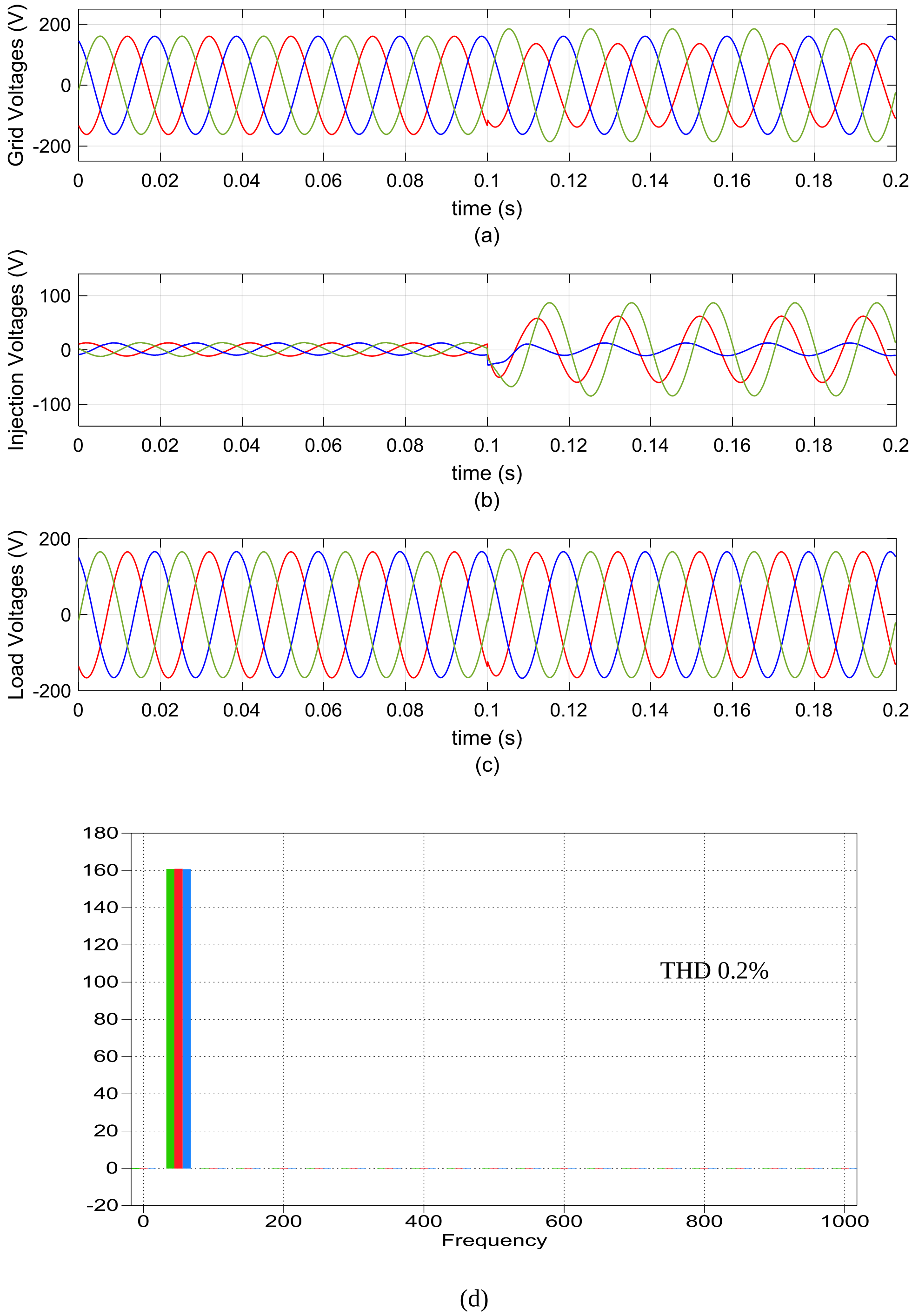

Figure 7.2: Experimental results for Case 1. a) supply voltages, b) injection voltages at converter side (capacitor voltage), c) load voltages, d) FFT spectrum of load voltages.

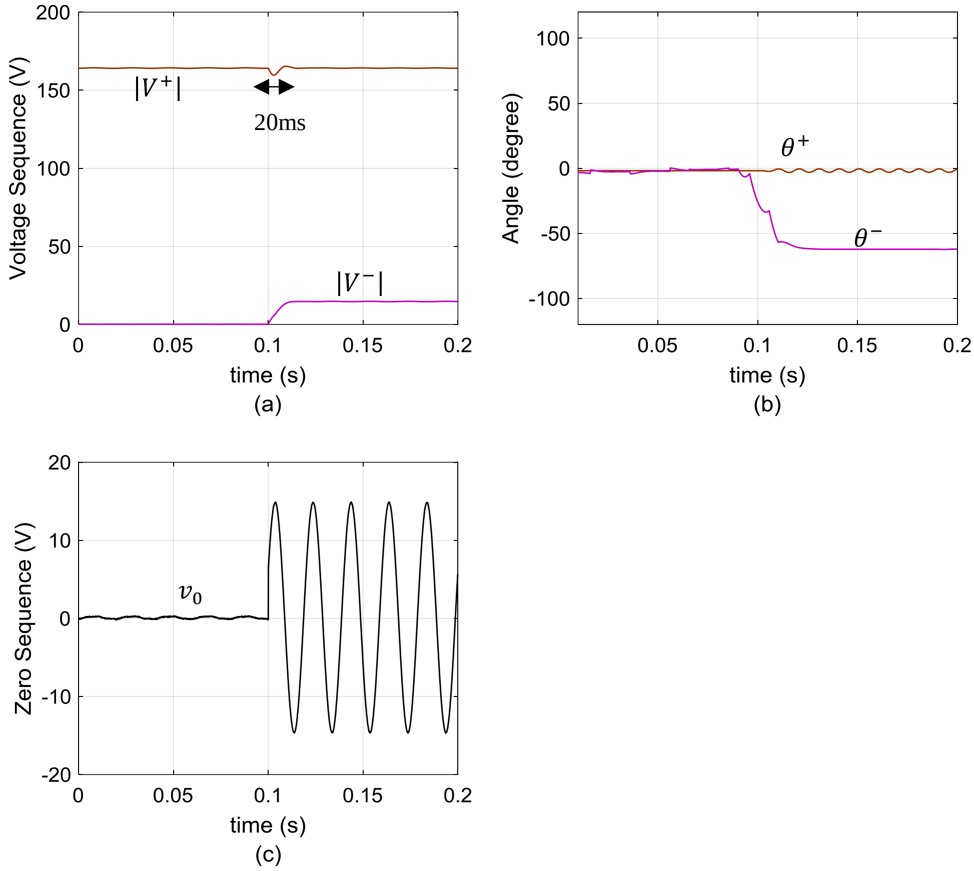

Figure 7.3: Experimental results for Case 1. a) positive/negative magnitude of the voltage sequences , b) positive/negative phase angle, c) instantaneous zero voltage sequence.

Table 7.2: Sequence components for case 1.

	V_{xa}(V)	V_{xb}(V)	V_{xc}(V)	$\|V^+\|$(V)	θ^+	$\|V^-\|$(V)	θ^-	v_0(V) (peak)
$0 < t < 0.1$	$170\angle 0^{\circ}$	$170\angle -120^{\circ}$	$170\angle 120^{\circ}$	164	-1.8°	0.2	-0.8°	0.2
$0.1 < t < 0.2$	$187\angle 0^{\circ}$	$153\angle -120^{\circ}$	$170\angle 120^{\circ}$	164.2	-1.7°	15	-62.2°	14.4

7.3.1.1 Comparison with Simulation

A comparison of experimental work with the simulation of the proposed voltage regulation approach is shown in Figure 7.4 and Table 7.3. Figure 7.4 shows the comparison of the simulated (left) and experimental (right) results obtained for case 1. It can be observed that figures from simulation results are very similar to the experimental results which verifies the practical work. Figure 7.4 (a) and (b) shows the required injection voltage for each capacitors. Both plots have a very similar waveforms, however the injection voltage in practical work has some more distortions in comparison to simulated result. The injection voltage distortion due to switching is negligible in the simulation results, whereas it is apparent in the practical results with a pre-fault THD of 2.6% and a post-fault THD of 0.8% (Figure 7.6). In the practical work, the modulation value, IGBT conduction voltage drop and deadtime can affect the converter performance and can increase the THD of the injection voltage. Figure 7.6 shows the FFT spectrum of the injection voltages of the experimental work. As can be seen, the injection voltage has positive sequence components (fundamental, 4th, 7th, 10th, 13th harmonics), negative sequence components (2nd, 5th, 8th, 11th harmonics) and zero sequence components (3rd ,6th, 9th, 12th harmonics).

It is clear from Figure 7.4 (c)-(f) that the positive, negative sequence components for the simulated and experimental results are very similar and respond to the fault at $t = 0.1$s. As can be seen from Table 7.3, there is a minor difference between simulation and practical results. In the simulation, the characteristics voltage until 0.1s has the positive voltage of $V^+ = 162\angle 0^\circ$ and negative voltage of $V^- = 0\angle 0^\circ$. While in the experimental work, the positive voltage has a value of $164\angle{-1.8}^\circ$and has a negative voltage value of $V^- = 0.2\angle{-0.8}^\circ$. In the practical work, during the balanced condition (before the fault occurs), negative and zero sequence components have a slight value, as a result there is a minor unbalanced system. This slight difference is likely due to the fact that in the simulation, the components of each phase, such as filtering inductors, capacitors and injection transformers are identical, whereas in the practical work they are not. To support the previous statement, the simulation results during balanced condition are shown in Figure 7.5. As can be seen, when the passive components are identical, the negative sequence value and its angle is equal to zero. However, when the non-identical components are used, the negative sequence components have non-zero values.

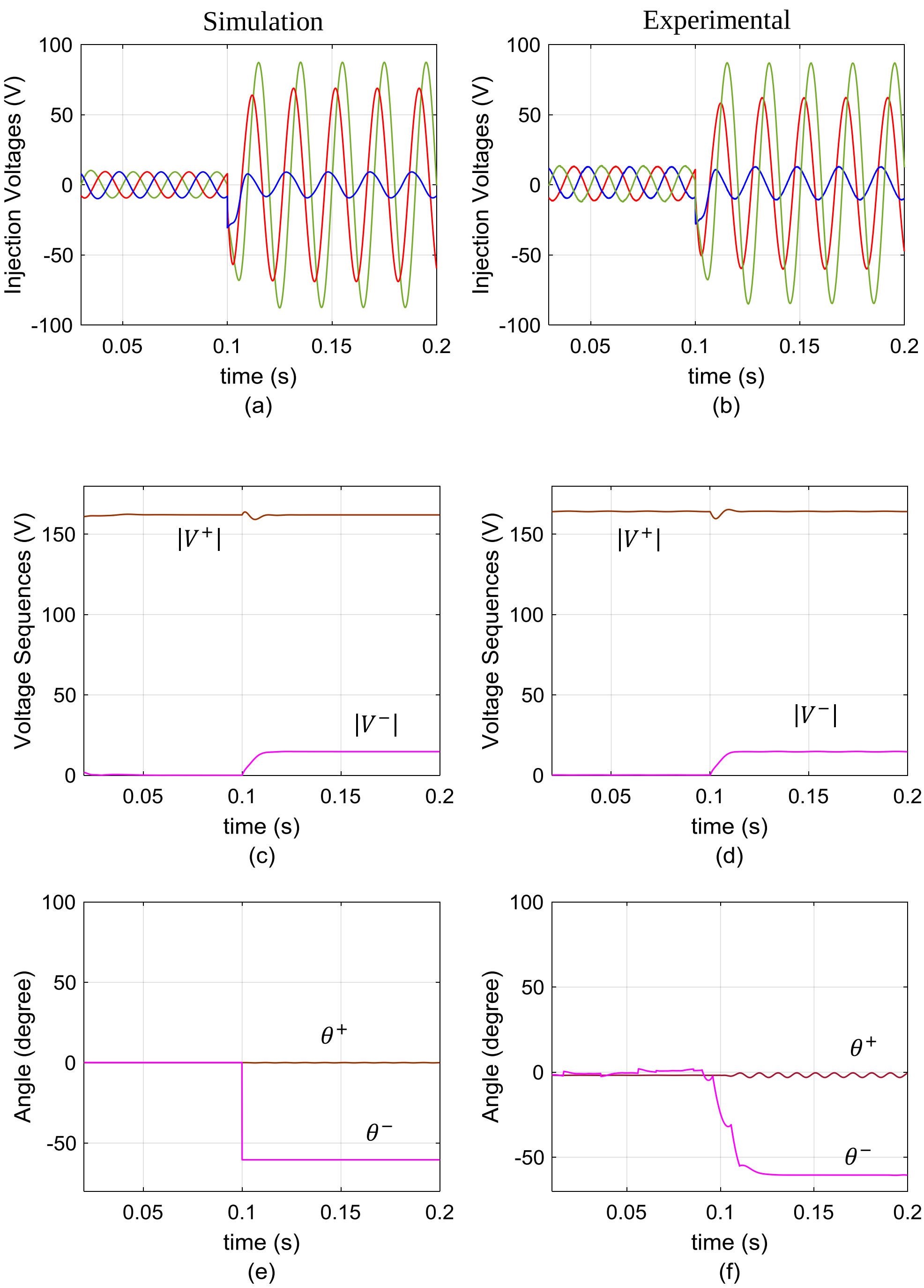

Figure 7.4: Comparison of simulated (left) and experimental (right) results for case 1.

Table 7.3: Comparison of simulated and experimental results for case 1.

	Simulation $0 < t < 0.1$	Experimental $0 < t < 0.1$	Simulation $0.1 < t < 0.2$	Experimental $0.1 < t < 0.2$
$\lvert V^{+}\rvert$(V)	162	164	162.4	164.2
θ^{+}	0°	-1.8°	0.5°	-1.7°
$\lvert V^{-}\rvert$(V)	0	0.2	13	15
θ^{-}	0°	-0.8°	-60°	-62.2°
v_0(V) (peak)	0	0.2	13	14.4
THD of injection voltages	$\cong 0\%$	2.6%	$\cong 0\%$	0.8%
THD of load voltages	$\cong 0\%$	0.2%	$\cong 0\%$	0.2%

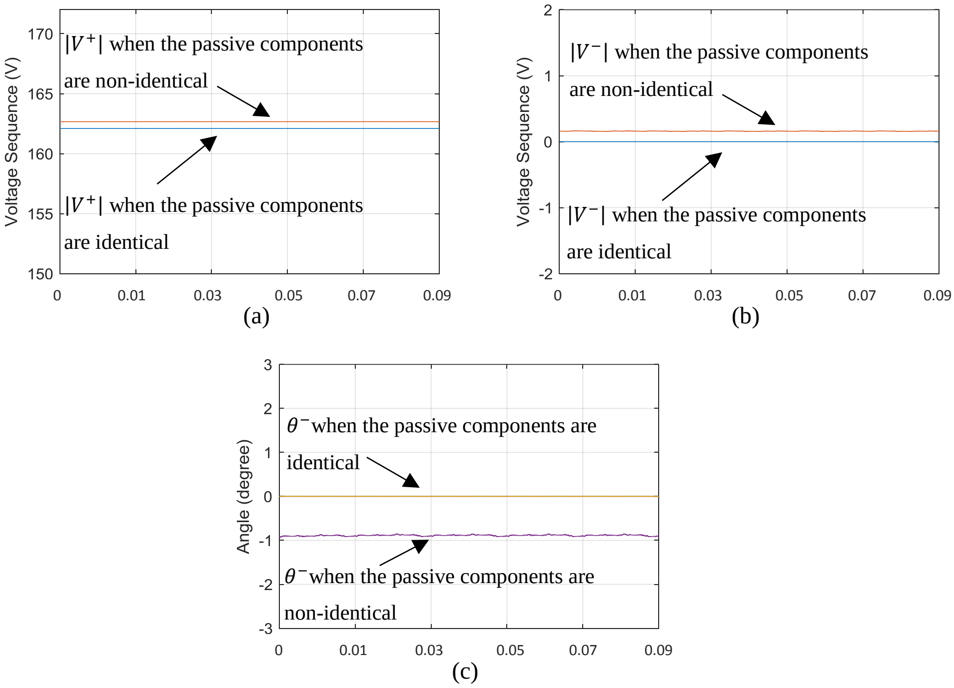

Figure 7.5: Simulation results comparison during balanced condition, a) positive sequence voltage, b) negative sequence voltage, c) negative angle

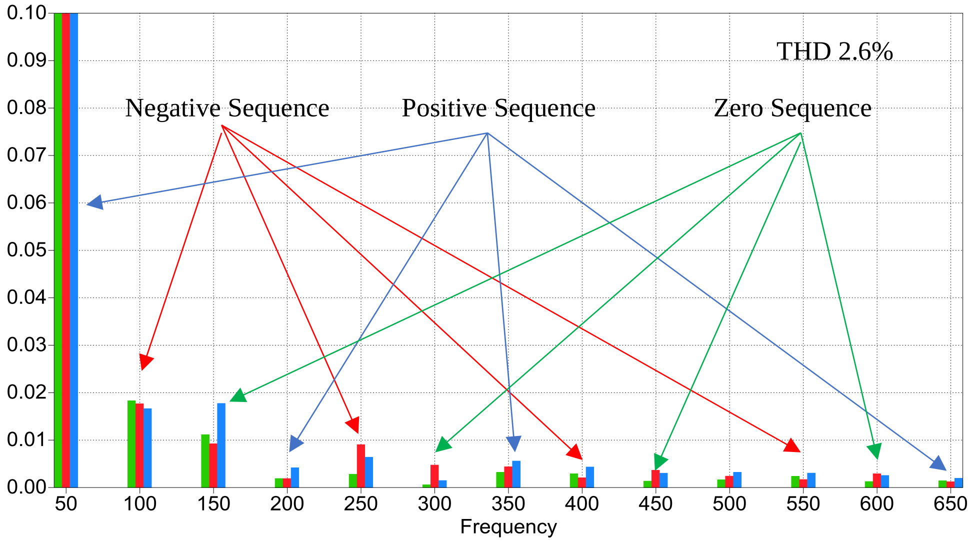

(a)

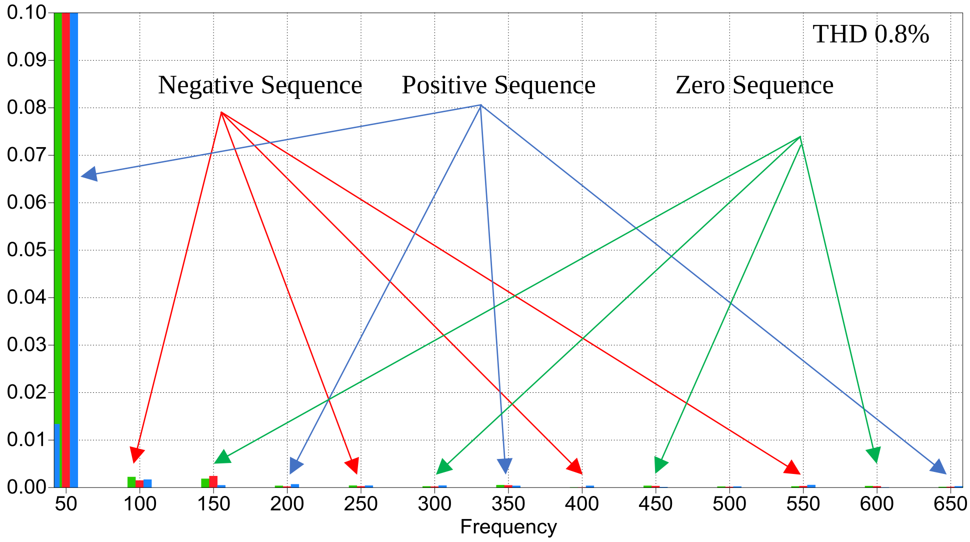

(b)

Figure 7.6: Fast Fourier Transformation (FFT) of injection voltage obtained from experimental work. a) pre-fault injection $0.02 < t < 0.04$, b) post-fault injection $0.12 < t < 0.14$. The amplitude is normalised.

7.3.2 Case 2: Phase Unbalanced Grid Voltage for Unbalanced Load

As stated in Chapter 2, phase unbalanced grid voltage normally happen when a large source of generation goes offline or a large block of loads is suddenly disconnected. The Chroma programmable AC source has the capability to generate the phase unbalanced supply voltage. In this case, the power converter is connected to an unbalanced load with initially phase unbalanced grid supply voltages. The schematic diagram of the grid voltages for this case is depicted in Figure 7.7. The sequence components of the proposed control algorithm for this case are summarised in Table 7.4.

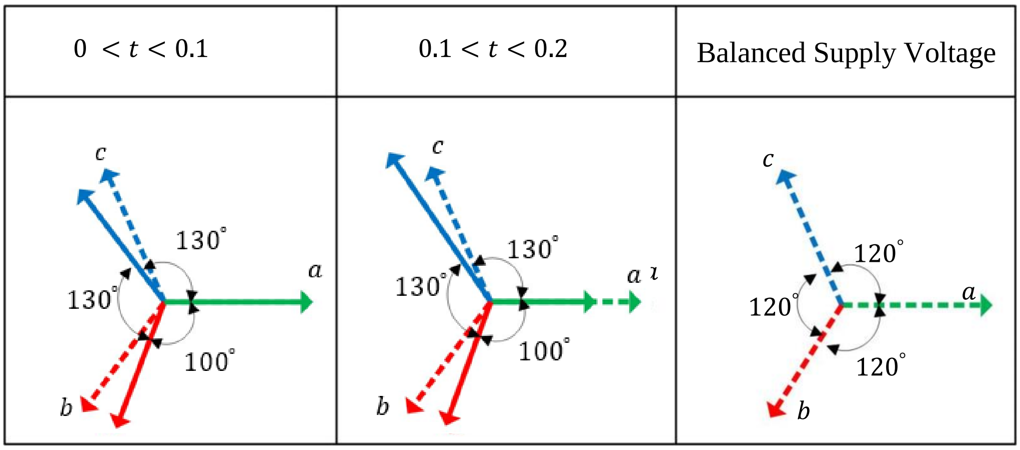

Figure 7.7: Schematic diagram of supply voltages for Case 2.

Table 7.4: Sequence components for case 2.

	V_{xa}(V)	V_{xb}(V)	V_{xc}(V)	$\|V^+\|$(V)	θ^+	$\|V^-\|$(V)	θ^-	v_0(V) (peak)
$0 < t < 0.1$	$170\angle0^\circ$	$170\angle-100^\circ$	$170\angle130^\circ$	162.5	-0.5°	17.75	-32.2°	15.5
$0.1 < t < 0.2$	$153\angle0^\circ$	$170\angle-100^\circ$	$187\angle130^\circ$	163	-1.2°	30.2	-47.5°	6

Figure 7.8 (a) shows the phase unbalanced supply voltages with a sudden step reference change at $t = 0.1$s. Similar to the previous section, phase a , phase b and phase c voltages are shown in green, red and blue colours, respectively. As can be seen, the phase unbalanced grid voltages have the same magnitude up to $t = 0.1$s. In this case, phase b is kept constant while a 10% voltage dip and a 10% voltage swell are observed for the grid phase a and phase c at $t = 0.1$s, respectively.

In this case the VSC injects the required voltage (Figure 7.8 (b)) to restore and keep the load voltage balanced at a pre-determined value (160V), while there is an unbalanced feeder drop. In addition, during the compensation, the feeder current (load current) is almost unchanged (Figure 7.8 (c)) as the load voltage is kept balanced and constant at 160V all the time (Figure 7.8 (d)). As can be seen from Figure 7.8 (e), the load voltages have only positive voltage sequence at the nominal value (160V) without having considerable zero or negative sequence components which verifies the effectiveness of the proposed control algorithm.

As can be observed from Table 7.4, the characteristics voltage until 0.1s has the negative voltage of $V^{-} = 17.75\angle{-32.2}^{\circ}$ and positive voltage of $V^{+} = 162.5\angle{-0.5}^{\circ}$. When the phase unbalanced grid voltage suddenly changes, the negative voltage gets the new value of $V^{-} = 30.2\angle{-47.5}^{\circ}$quickly, while the positive voltage is $V^{+} = 163\angle{-1.2}^{\circ}$. Figure 7.9 shows the symmetrical components' estimations captured by HPI. Figure 7.9 (a)-(c) illustrates the corresponding positive, negative and zero sequence components in order to generate the reference voltage ($v_{ref}^{a,b,c}$) using the control algorithm depicted in Figure 5.2 (or Figure 7.1). The reference voltage is the input of the multi-loop PR controllers.

The results show a high-performance controller algorithm which allows a fast and precise characterisation of the injection voltage under the phase unbalanced grid and the unbalanced load conditions.

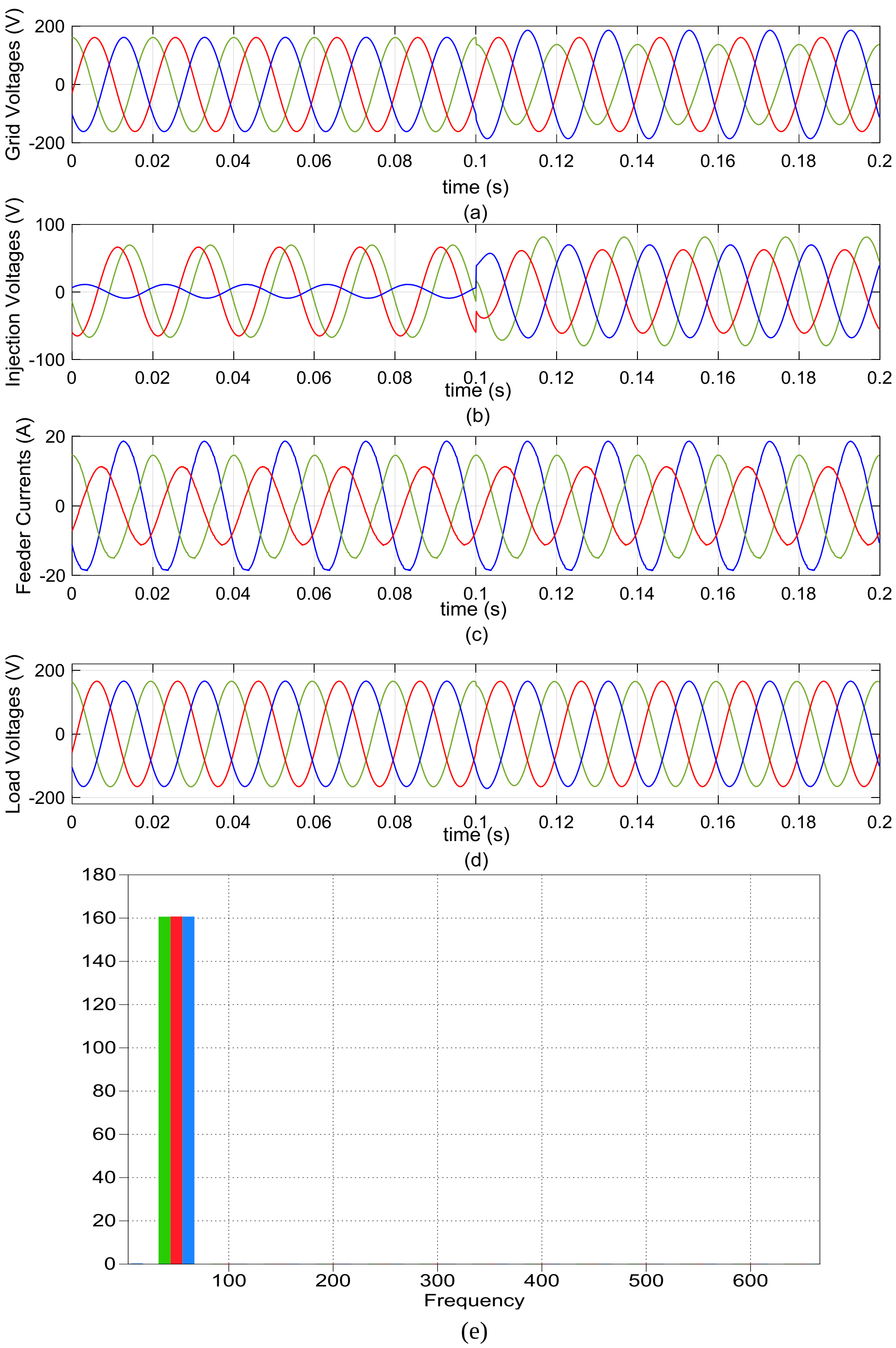

Figure 7.8: Experimental results for Case 2. a) phase unbalanced supply voltages, b) injection voltages at converter side (capacitor voltage), c) feeder currents, d) load voltages, e) FFT spectrum of load voltages..

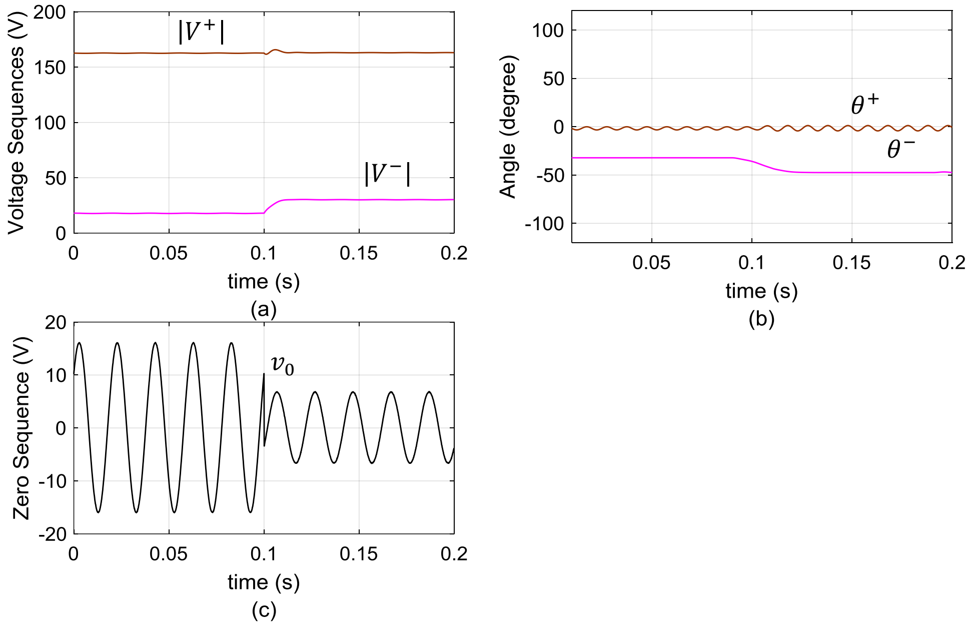

Figure 7.9: Experimental results for Case 2. a) positive/negative magnitude of the voltage sequences , b) positive/negative phase angle, c) instantaneous zero voltage sequence

7.3.2.1 Comparison with Simulation

A comparison of experimental work with the simulation of the proposed voltage regulation approach is shown in Table 7.5 and Figure 7.10. Figure 7.10 shows the comparison results of simulated (left) and experimental (right) of the injection voltages, positive and negative sequence components. As can be seen, the results show similarity in behaviour between waveforms as they are almost equal. However, by referring to Table 7.5, slight differences between experimental work and simulation can be observed. The amplitude of voltage sequences of simulation is slightly ($\approx 0.5 - 3$ V) less than experimental work and that can be due to the conduction losses, deadtime and current/voltage measurement circuits of the VSC in the practical work. This leads to the existence of harmonics in the practical work in comparison to the simulated model. Similar to previous section, the slight difference between phase angles is due to the performance of the average filter.

The experimental results are found to be satisfactory to validate the proposed sequence component based control algorithm.

Table 7.5: Comparison of simulated and experimental results for case 2.

	Simulation $0 < t < 0.1$	Experimental $0 < t < 0.1$	Simulation $0.1 < t < 0.2$	Experimental $0.1 < t < 0.2$
$\lvert V^+\rvert$(V)	160	162.5	160.2	163
θ^+	0°	-0.5°	0.5°	-1.2°
$\lvert V^-\rvert$(V)	18.5	17.75	28	30.2
θ^-	-30°	-32.2°	-46°	-47.5°
v_0(V) (peak)	16	15.5	10.5	9.5
THD of injection voltages	0.4%	0.8%	1.5%	2.5%
THD of load voltages	$\cong$ 0%	0.5%	0.2%	0.9%

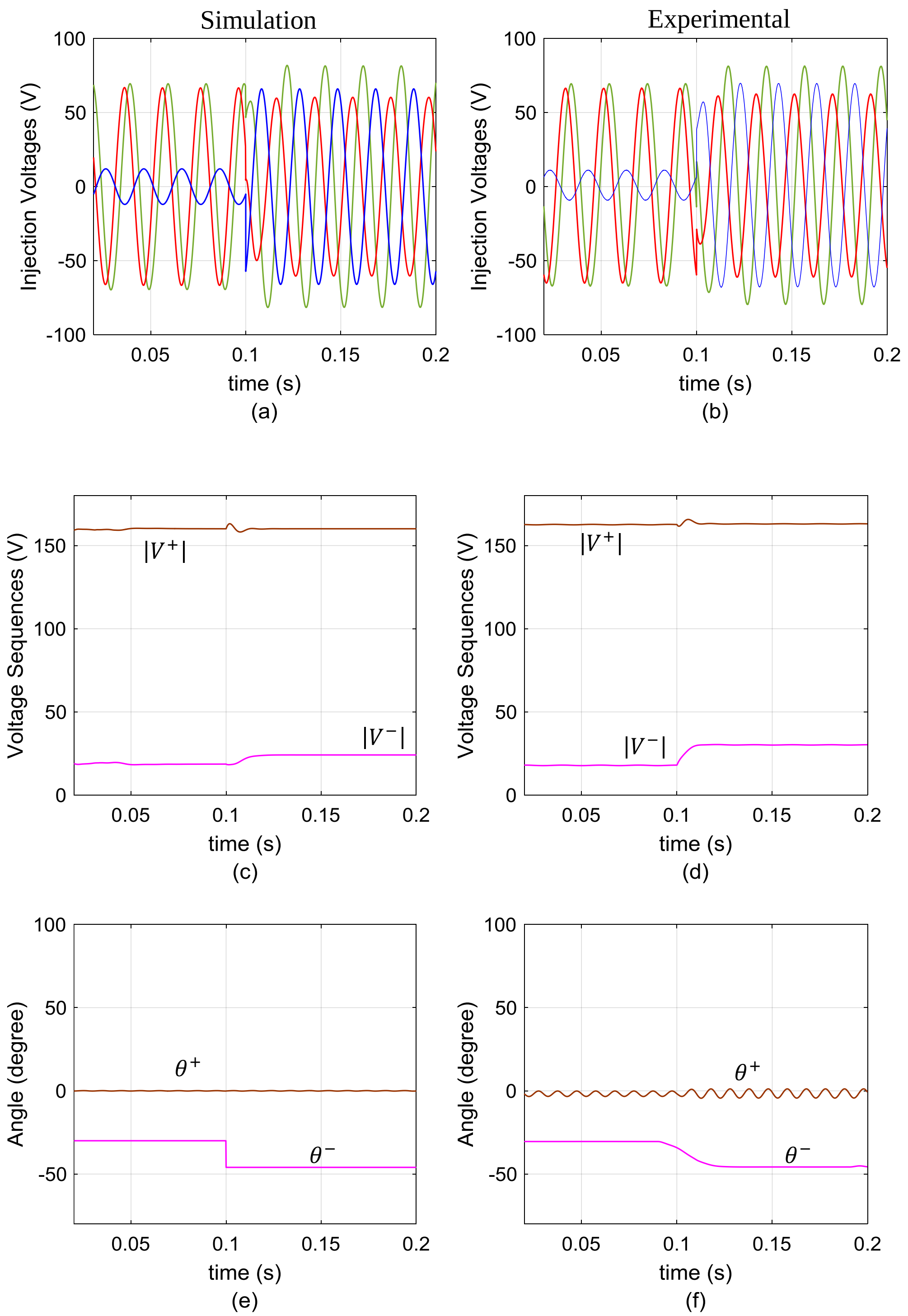

Figure 7.10: Comparison of simulated (left) and experimental (right) results for case 2.

7.4 Conclusion

This chapter presented the experimental results for the proposed voltage compensation approach to validate the controller algorithm under different case studies. The following remark summarises the outcomes of this chapter:

- An evaluation of the system performance under two different case studies has been performed. Asymmetric voltage dip and swell for the balanced/unbalanced system has been implemented and the power converter can compensate the voltage and keep the load voltages balanced at a pre-determined value. The experimental results have matched up with the simulated outcomes.

The proposed power converter operation is limited as it is not capable to compensate the voltage for the highly demanded voltage system as the voltage regulation is limited to $\pm$10% of the rated voltage. However, the experimental power converter can compensate for the voltage sag and swell for the balanced/unbalanced system quickly with a fast response, as such it meets the main objective that has been set for this work.

CHAPTER 8: Conclusions

This thesis has presented an extensive analysis and discussion of optimised power electronic-based solutions for voltage regulation purposes in LV networks. It has been demonstrated that Expectation Maximisation (EM) algorithm can compute the maximum likelihood estimates from load data to find general load model, optimal substation voltage and ideal converter kVA rating through the Gaussian Mixture Models (GMMs). The proposed GMM using EM algorithm provides several advantages as follows:

- Finding the characterisation of the probability distributions of any type of end-user customers for any time duration supplied from a feeder or substation. The characterisation of the load pattern is a primary aspect in studies regarding design consideration of distribution substations. The data on the load probability can be effectively used for addressing the distribution system planning, distribution automation, load forecasting, substation site selection, feeder route selection, substation/feeder expansion, power losses, energy management and total cost in LV distribution system
- Finding the optimised substation voltage for any number of feeders based on probability. The substation is required to guarantee normal energy supply to

end-user customers. The proposed likelihood method leads to the conclusion that for a system with a series set up VSCs, keeping the transformer substations' voltage at an optimal results in the lowest amount of the injected power of the power electronics

- Finding the optimised kVA power rating of power electronics used in LV networks for voltage regulation purposes. The proposed statistics and probability technique benefits to optimise the power electronic components size and rating such as: IGBTs, DC-link capacitors, filtering inductors, capacitors and injection transformers. This finding points to the conclusion that choosing the optimised kVA power rating can bring advantages such as: smaller overall size, less losses and less total cost of the power converter

A power electronic solution for voltage regulation purposes named as hybrid substation has been introduced. The hybrid substation comprises a three-phase four-leg shunt-connected VSC and multiple three-phase four-leg series-connected VSCs. The hybrid substation is a power electronic solution that could be retrofitted into the existing distribution substations transformers. The hybrid substation is a promising solution for instantaneous voltage compensation.

The main power electronic element of hybrid substation is a four-leg VSC which is considered to be the best candidate to provide neutral connection to single-phase or three-phase balanced, unbalanced, linear and nonlinear loads. The fourth-leg (extra leg) of VSC gives more control flexibility, at the same time, it increases the complexity of the control algorithm for the modulation of the output voltages. Among the available modulation control algorithms, three-dimensional SVM technique in $\alpha\beta\gamma$ coordinate frames is dominant due to its reliability and flexibility. This modulation technique has been implemented in both simulation and practical work and a satisfactory results have been obtained.

A method based on symmetrical components has been presented. This method separates positive, negative and zero sequence components based on SOGI-QSG in order to minimise the amount of the injection voltages generated by VSC. Possessing the information on sequence components is important for the purpose of grid monitoring which indicates the feeder power behaviour. The simulation results prove that the method can rapidly and accurately estimates the symmetrical components and keep the load balanced at a pre-determined value. The simulation results show a fast response, accurate tracking and robustness of the proposed control algorithm.

In order to validate the performance of the VSC proposed controllers' voltage injection capabilities, a three-phase four-leg series-connected VSC were constructed and tested in the PEMC lab. The converter was controlled using an FPGA and DSP-based control platform. From the study and experimental results presented in Chapter 7, it can be concluded that the proposed controller algorithm provides an effective performance of power converter under grid faulty condition. The experimental results have matched up with the simulated outcomes. However, in the experimental work, the power converter operation has been limited to the injection voltage range ($\pm$10% of the rated voltage) and the injection transformers' current/voltage restrictions. As a result, the proposed power converter is not able to compensate power quality problem such as interruption and fundamental frequency variations as the system requires a higher voltage range controllability and DC-link bus. To overcome this problem, a larger injection transformer with an appropriate turn ratio or connecting multiple winding transformers in series can be used. This solution might increase the overall size and cost of the system. Furthermore, in this practical work, only four-leg series-connected VSC has been constructed. In order to compensate the voltage for highly distorted current system, a four-leg shunt-connected VSC with an appropriate kVA power rating is required to clean the current harmonics in the system. Nevertheless, the proposed experimental power converter can compensate unbalanced voltage sag and swell for unbalanced system quickly and effectively which meets the main objective for the experimental part of this PhD thesis.

8.1 Summary of Main Contributions

The contributions of the work presented are summarised as follows:

- A comprehensive novel study has been introduced to evaluate the probabilistic data concerning the time-evaluation that can be utilised in power system analysis
- A new method has been introduced to find an optimal substation voltage and kVA rating of the series set up power converter used for voltage regulation purposes

- Research the current trend and technology advances for voltage regulation at LV networks
- Developing aspects, features and advantages of hybrid substation
- A sequence analysis based control algorithm for hybrid substation has been presented
- Simulating and modelling the hybrid substation to verify the effectiveness of the proposed controller
- An experimental three-phase four-leg series-connected VSC has been constructed to validate the operation and control of the proposed power converter

8.2 Future Work

The interesting topics for the future research of the work presented in this thesis include:

- Considering other maximum likelihood estimation methods such as Bayesian techniques to compare the results with explained method

- Modelling the hybrid substation and evaluate its performance using four-leg multilevel converters. Multilevel converters can produce better voltage waveform (lower harmonics). Hybrid substation with multilevel converters could be a potential candidate for high/medium voltage distribution applications

- The voltage compensation method has been verified for linear loads. Testing other types of loads such as, non-linear loads and motor loads to investigate the voltage compensation control performance

- Constructing the hybrid substation connecting to multi-feeder system with diverse load demand (similar to simulation section, case 3)

Appendix A

Derivation of EM for GMM Fitting

Samples $\mathcal{X}_1, \mathcal{X}_2, \dots, \mathcal{X}_j \in R^d$ from a GMM with $\mathcal{N}$ components, consider the problem of estimating parameter set $\mho_i = \{(w_i, \sum_i, \mu_i)\}_{i=1}^{\mathcal{N}}$. Let:

$$\phi(\mathcal{X}|\mu, \Sigma) \triangleq \frac{1}{(2\pi)^{d/2}|\Sigma|^{1/2}} e^{\left(-\frac{1}{2}(\mathcal{X}-\mu)^T\Sigma^{-1}(\mathcal{X}-\mu)\right)}$$

Defining $\gamma_{ij}^{(m)}$ which is the guess at the m^{th} iteration of the probability that the j^{th} sample belongs to the i^{th} Gaussian component:

$$\gamma_{ij}^{(m)} \triangleq P\left(\mathcal{Z}_j = i \middle| x_j = \mathcal{X}_j, \mho^{(m)}\right) = \frac{w_i^{(m)} P\left(x_j \middle| \mu_i^{(m)}, \Sigma_i^{(m)}\right)}{\sum_{l=1}^{\mathcal{N}} w_l^{(m)} P\left(x_j \middle| \mu_l^{(m)}, \Sigma_l^{(m)}\right)}$$

which satisfies $\sum_{i=1}^{\mathcal{N}} \gamma_{j\,i}^{(m)} = 1$. First we have:

$$Q_j\left(\mho \middle| \mho^{(m)}\right) = E_{\mathcal{Z}_j|\mathcal{X}_j,\mho^{(m)}}\left[\log P(\mathcal{X}_j, \mathcal{Z}_j|\mho\right]$$

$$= \sum_{i=1}^{\mathcal{N}} \gamma_{j\,i}^{(m)} \log P(\mathcal{X}_j, i|\mho)$$

$$= \sum_{i=1}^{\mathcal{N}} \gamma_{j\,i}^{(m)} \log w_i\, \phi\left(\mathcal{X}_j \middle| \mu_i, \Sigma_i\right) + \text{constant}$$

$$= \sum_{j=1}^{n} \sum_{i=1}^{\mathcal{N}} \gamma_{j\,i}^{(m)} \left(\log w_i - \frac{1}{2}\log|\Sigma_i| - \frac{1}{2}\left(\mathcal{X}_j - \mu_i\right)^T \Sigma_i^{-1}(\mathcal{X}_j - \mu_i)\right)$$

Which completes the E step. Let us consider:

$$n_i^{(m)} = \sum_{j=1}^{n} \gamma_{j\,i}^{(m)}$$

Then we can re-write $Q_j(\mho|\, \mho^{(m)})$ as:

$$Q_j(\mho|\, \mho^{(m)}) = \sum_{i=1}^{\mathcal{N}} n_i^{(m)} \left(\log w_i - \frac{1}{2} \log|\Sigma_i| \right) - \frac{1}{2} \sum_{j=1}^{n} \sum_{i=1}^{\mathcal{N}} \gamma_{j\,i}^{(m)} \left((\mathcal{X}_j - \mu_i)^T \Sigma_i^{-1} (\mathcal{X}_j - \mu_i) \right)$$

The M step is to solve maximize of $Q_j(\mho|\, \mho^{(m)})$. In order to maximize $Q_j(\mho|\, \mho^{(m)})$, the following log-likelihood function can be used:

$$\mathrm{L}(\mho) = \sum_{j=1}^{n} \log \left(\sum_{i=1}^{\mathcal{N}} w_i \phi(\mathcal{X}_j | \mu_i, \Sigma_i) \right)$$

Lagrange multipliers are used in multivariable calculus to find maxima and minima of a function subject to constraints (like "find the highest elevation along the given path), thus, Lagrangian multipliers theorem can calculate the weight values:

$$J(w, \lambda) = \sum_{i=1}^{\mathcal{N}} n_i^{(m)} \log w_i + \lambda \left(\sum_{i=1}^{\mathcal{N}} w_i - 1 \right)$$

From Lagrange method:

$$\frac{\partial J}{\partial w_i} = \frac{n_i^{(m)}}{w_i} + \lambda = 0, \qquad i = 1, \ldots, \mathcal{N}$$

And by referring to above equation and $\sum_{i=1}^{\mathcal{N}} w_i = 1$:

$$w_i^{(m+1)} = \frac{n_i^{(m)}}{n}$$

To solve for the means we have

$$\frac{\partial Q_j\left(\mho \middle| \mho^{(m)}\right)}{\partial \mu_i} = \Sigma_i^{-1}\left(\sum_{j=1}^{n} \gamma_{j\,i}^{(m)}\, \mathcal{X}_j - n_i^{(m)} \mu_i\right)$$

Therefore:

$$\mu_i^{(m+1)} = \frac{1}{n_i^{(m)}} \sum_{j=1}^{n} \gamma_{j\,i}^{(m)}\, \mathcal{X}_j$$

And for covariance:

$$\frac{\partial Q_j\left(\mho \middle| \mho^{(m)}\right)}{\partial \Sigma_i} = -\frac{1}{2} n_i^{(m)} \frac{\partial}{\partial \Sigma_i} \log|\Sigma_i| - \frac{1}{2} \gamma_{j\,i}^{(m)} \frac{\partial}{\partial \Sigma_i} \left(\mathcal{X}_j - \mu_i\right)^T \Sigma_i^{-1} \left(\mathcal{X}_j - \mu_i\right)$$

At the end we get:

$$\Sigma_i^{(m+1)} = \frac{1}{n_i^{(m)}} \sum_{j=1}^{n} \gamma_{j\,i}^{(m)} \left(\mathcal{X}_j - \mu_i{}^{(m+1)}\right)^T \left(\mathcal{X}_j - \mu_i{}^{(m+1)}\right)$$

Appendix B

Matrix for Switching Vector Duty Ratio Computation of 3-D SVPWM

	Tetrahedron 1	Tetrahedron 2	Tetrahedron 3	Tetrahedron 4
Prism I	$\vec{V}_5 - \vec{V}_{13} - \vec{V}_{15}$ $\begin{bmatrix} 1 & 0 & 1 \\ 1/2 & -\sqrt{3}/2 & -1 \\ 0 & \sqrt{3} & 0 \end{bmatrix}$	$\vec{V}_5 - \vec{V}_7 - \vec{V}_{15}$ $\begin{bmatrix} 3/2 & -\sqrt{3}/2 & 0 \\ -1/2 & \sqrt{3}/2 & 1 \\ 1/2 & \sqrt{3}/2 & -1 \end{bmatrix}$	$\vec{V}_5 - \vec{V}_7 - \vec{V}_8$ $\begin{bmatrix} 3/2 & -\sqrt{3}/2 & 0 \\ 0 & \sqrt{3} & 0 \\ -1/2 & -\sqrt{3}/2 & 1 \end{bmatrix}$	$\vec{V}_{13} - \vec{V}_{15} - \vec{V}_9$ $\begin{bmatrix} 3/2 & -\sqrt{3}/2 & 0 \\ 0 & \sqrt{3} & 0 \\ -1 & 0 & -1 \end{bmatrix}$
Prism II	$\vec{V}_7 - \vec{V}_{15} - \vec{V}_3$ $\begin{bmatrix} 1 & 0 & 1 \\ 1/2 & -\sqrt{3}/2 & -1 \\ -3/2 & -\sqrt{3}/2 & 0 \end{bmatrix}$	$\vec{V}_{15} - \vec{V}_3 - \vec{V}_{11}$ $\begin{bmatrix} 3/2 & \sqrt{3}/2 & 0 \\ -1/2 & \sqrt{3}/2 & 1 \\ 1 & 0 & -1 \end{bmatrix}$	$\vec{V}_7 - \vec{V}_3 - \vec{V}_8$ $\begin{bmatrix} 3/2 & \sqrt{3}/2 & 0 \\ -3/2 & \sqrt{3}/2 & 0 \\ -1/2 & -\sqrt{3}/2 & 1 \end{bmatrix}$	$\vec{V}_{15} - \vec{V}_{11} - \vec{V}_9$ $\begin{bmatrix} 3/2 & \sqrt{3}/2 & 0 \\ -3/2 & \sqrt{3}/2 & 0 \\ 1/2 & -\sqrt{3}/2 & -1 \end{bmatrix}$
Prism III	$\vec{V}_3 - \vec{V}_{11} - \vec{V}_{12}$ $\begin{bmatrix} -1/2 & -\sqrt{3}/2 & 1 \\ 1/2 & \sqrt{3}/2 & -1 \\ -3/2 & -\sqrt{3}/2 & 0 \end{bmatrix}$	$\vec{V}_3 - \vec{V}_4 - \vec{V}_{12}$ $\begin{bmatrix} 0 & \sqrt{3} & 0 \\ -1/2 & -\sqrt{3}/2 & 1 \\ -1 & 0 & -1 \end{bmatrix}$	$\vec{V}_3 - \vec{V}_4 - \vec{V}_8$ $\begin{bmatrix} 0 & \sqrt{3} & 0 \\ -3/2 & -\sqrt{3}/2 & 0 \\ 1 & 0 & 1 \end{bmatrix}$	$\vec{V}_{11} - \vec{V}_{12} - \vec{V}_9$ $\begin{bmatrix} 0 & \sqrt{3} & 0 \\ -3/2 & -\sqrt{3}/2 & 0 \\ 1/2 & -\sqrt{3}/2 & -1 \end{bmatrix}$
Prism IV	$\vec{V}_4 - \vec{V}_{12} - \vec{V}_2$ $\begin{bmatrix} -1/2 & \sqrt{3}/2 & 1 \\ -1 & 0 & -1 \\ 0 & -\sqrt{3} & 0 \end{bmatrix}$	$\vec{V}_{12} - \vec{V}_2 - \vec{V}_{10}$ $\begin{bmatrix} -3/2 & \sqrt{3}/2 & 0 \\ -1/2 & -\sqrt{3}/2 & 1 \\ 1/2 & -\sqrt{3}/2 & -1 \end{bmatrix}$	$\vec{V}_4 - \vec{V}_2 - \vec{V}_8$ $\begin{bmatrix} -3/2 & \sqrt{3}/2 & 1 \\ 0 & -\sqrt{3} & 0 \\ 1 & 0 & 1 \end{bmatrix}$	$\vec{V}_{12} - \vec{V}_{10} - \vec{V}_9$ $\begin{bmatrix} -3/2 & \sqrt{3}/2 & 0 \\ 0 & -\sqrt{3} & 0 \\ 1/2 & \sqrt{3}/2 & -1 \end{bmatrix}$
Prism V	$\vec{V}_2 - \vec{V}_{10} - \vec{V}_{14}$ $\begin{bmatrix} -1/2 & -\sqrt{3}/2 & 1 \\ -1 & 0 & -1 \\ 3/2 & -\sqrt{3}/2 & 0 \end{bmatrix}$	$\vec{V}_2 - \vec{V}_6 - \vec{V}_{14}$ $\begin{bmatrix} -3/2 & -\sqrt{3}/2 & 0 \\ 1 & 0 & 1 \\ 1/2 & -\sqrt{3}/2 & -1 \end{bmatrix}$	$\vec{V}_2 - \vec{V}_6 - \vec{V}_8$ $\begin{bmatrix} -3/2 & -\sqrt{3}/2 & 0 \\ 3/2 & -\sqrt{3}/2 & 0 \\ -1/2 & \sqrt{3}/2 & 1 \end{bmatrix}$	$\vec{V}_{10} - \vec{V}_{14} - \vec{V}_9$ $\begin{bmatrix} -3/2 & -\sqrt{3}/2 & 0 \\ 3/2 & -\sqrt{3}/2 & 0 \\ 1/2 & \sqrt{3}/2 & -1 \end{bmatrix}$
Prism VI	$\vec{V}_{14} - \vec{V}_5 - \vec{V}_{13}$ $\begin{bmatrix} 0 & -\sqrt{3} & 0 \\ 1 & 0 & 1 \\ 1/2 & \sqrt{3}/2 & -1 \end{bmatrix}$	$\vec{V}_6 - \vec{V}_{14} - \vec{V}_5$ $\begin{bmatrix} -1/2 & -\sqrt{3}/2 & 1 \\ 1/2 & -\sqrt{3}/2 & -1 \\ 3/2 & \sqrt{3}/2 & 0 \end{bmatrix}$	$\vec{V}_6 - \vec{V}_5 - \vec{V}_8$ $\begin{bmatrix} 0 & -\sqrt{3} & 0 \\ 3/2 & \sqrt{3}/2 & 0 \\ -1/2 & \sqrt{3}/2 & 1 \end{bmatrix}$	$\vec{V}_{14} - \vec{V}_{13} - \vec{V}_9$ $\begin{bmatrix} 0 & -\sqrt{3} & 0 \\ 3/2 & \sqrt{3}/2 & 0 \\ -1 & 0 & -1 \end{bmatrix}$

Appendix C

C.1. Symmetrical Components Model

For any three-phase group of variables x_a, x_b, x_c, the symmetrical components can be given by:

$$\begin{cases} x_a = x_a^+ + x_a^- + x_a^0 \\ x_b = x_b^+ + x_b^- + x_b^0 \\ x_c = x_c^+ + x_c^- + x_c^0 \end{cases} \tag{C.1}$$

where the super indexes +,- and 0 indicates the positive, negative and zero symmetrical sequences, respectively. The equation (C.1) can be re-written as:

$$\begin{cases} x_a = X^+ \sin(\omega t + \theta^+) + X^- \sin(\omega t + \theta^-) + X^0 \sin(\omega t + \theta^0) \\ x_b = X^+ \sin\left(\omega t + \theta^+ - \frac{2\pi}{3}\right) + X^- \sin\left(\omega t + \theta^- + \frac{2\pi}{3}\right) + X^0 \sin(\omega t + \theta^0) \\ x_c = X^+ \sin\left(\omega t + \theta^+ + \frac{2\pi}{3}\right) + X^- \sin\left(\omega t + \theta^- - \frac{2\pi}{3}\right) + X^0 \sin(\omega t + \theta^0) \end{cases} \tag{C.2}$$

where X^+, θ^+, X^-, θ^-, X^0, θ^0 are the magnitude and its corresponded phase angle of the instantaneous positive sequence component, negative sequence component and zero sequence component, respectively.

Using trigonometric function of $\sin(a + b) = \sin(a)\cos(b) + \cos(a)\sin(b)$, equation (C.2) can be re-written as (C.3):

(C.3):

$$x_a = X^+ \cos(\theta^+) \sin(\omega t) + X^+ \cos(\omega t) \sin(\theta^+) + X^- \cos(\theta^-) \sin(\omega t) + X^- \cos(\omega t) \sin(\theta^-) + X^0 \cos(\theta^0) \sin(\omega t) + X^0 \cos(\omega t) \sin(\theta^0)$$

$$x_b = X^+ \cos(\theta^+) \sin(\omega t - \frac{2\pi}{3}) + X^+ \cos\left(\omega t - \frac{2\pi}{3}\right) \sin(\theta^+) + X^- \cos(\theta^-) \sin(\omega t + \frac{2\pi}{3}) + X^- \cos\left(\omega t + \frac{2\pi}{3}\right) \sin(\theta^-) + X^0 \cos(\theta^0) \sin(\omega t) + X^0 \cos(\omega t) \sin(\theta^0)$$

$$x_c = X^+ \cos(\theta^+)\sin(\omega t + \frac{2\pi}{3}) + X^+ \cos\left(\omega t + \frac{2\pi}{3}\right)\sin(\theta^+) + X^- \cos(\theta^-)\sin(\omega t - \frac{2\pi}{3}) + X^- \cos\left(\omega t - \frac{2\pi}{3}\right)\sin(\theta^-) + X^0 \cos(\theta^0)\sin(\omega t) + X^0 \cos(\omega t)\sin(\theta^0)$$

Consequently, equation (C.3) can be expressed in matrix form as follows:

$$\begin{bmatrix} x_a \\ x_b \\ x_c \end{bmatrix} = \begin{bmatrix} \sin\omega t & \cos\omega t & \sin(\omega t - \frac{2\pi}{3}) & \cos(\omega t - \frac{2\pi}{3}) & \sin(\omega t + \frac{2\pi}{3}) & \cos(\omega t + \frac{2\pi}{3}) \\ \sin\omega t & \cos\omega t & \sin(\omega t + \frac{2\pi}{3}) & \cos(\omega t + \frac{2\pi}{3}) & \sin(\omega t - \frac{2\pi}{3}) & \cos(\omega t - \frac{2\pi}{3}) \\ \sin\omega t & \cos\omega t & \sin\omega t & \cos\omega t & \sin\omega t & \cos\omega t \end{bmatrix} \cdot \begin{bmatrix} X^+ \cos\theta^+ \\ X^+ \sin\theta^+ \\ X^- \cos\theta^- \\ X^- \sin\theta^- \\ X^0 \cos\theta^0 \\ X^0 \sin\theta^0 \end{bmatrix}$$

C.1. A Comparison of Symmetrical Component Voltage Injection with PLL Voltage Injection Method (Conventional Method)

In both methods, the hybrid substation is connected to a three-phase unbalanced load and supply voltage with same parameters (same load, switching frequency, grid voltage, impedance, etc.). Both techniques keep the load voltage balanced at a pre-determined value. However, as can be seen in Figure C.1, for each phase, the maximum injection voltage (peak value) for symmetrical component control algorithm is slightly less than in a PLL technique. In addition, the lack of negative and zero sequence detection by PLL method, leads to have a distorted injection voltage and load voltage when there is an unbalanced system. Figure C.2 shows the voltage conditions at the load terminals obtained by proposed two methods. Simulation was carried out by PLECS software.

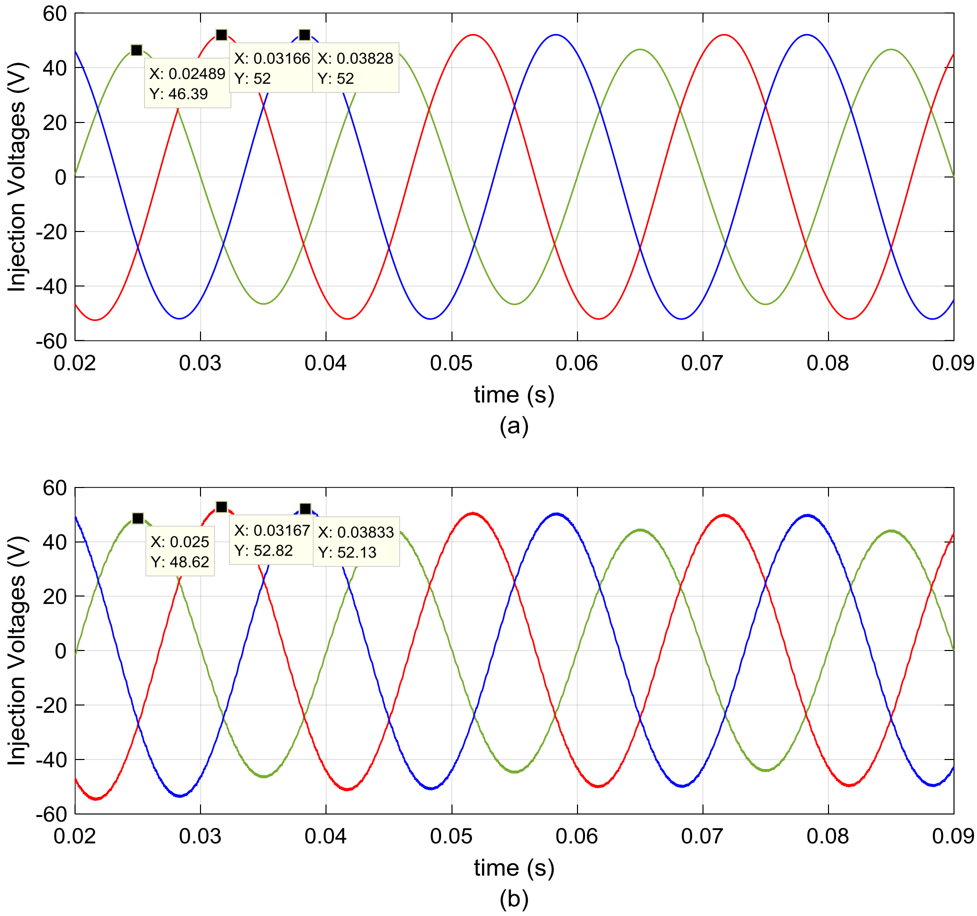

Figure C.1: Injection voltages of a) symmetrical component control algorithm, b) conventional method (PLL method).

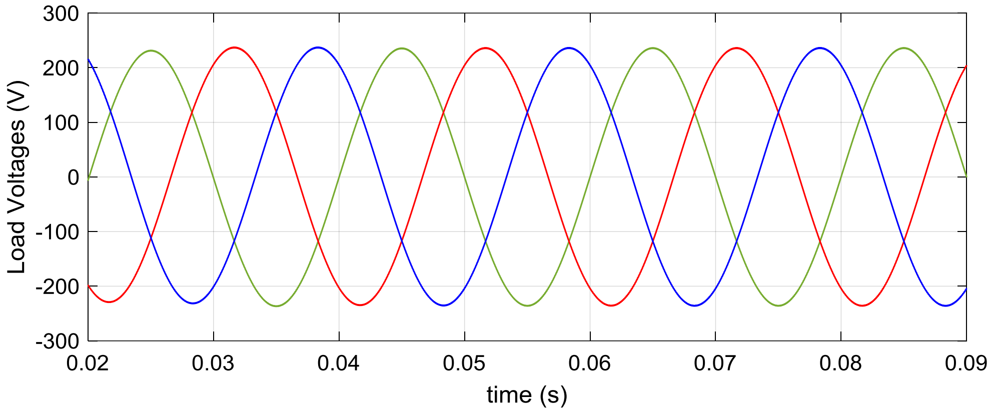

(a)

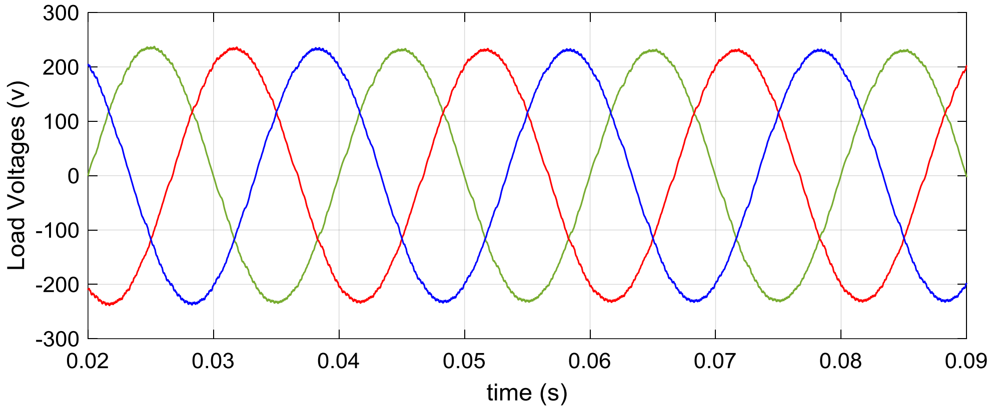

(b)

Figure C.2: Load voltages of a) symmetrical component control algorithm, b) conventional method (PLL method).

Appendix D

PCB Layout of a Four-Leg VSC

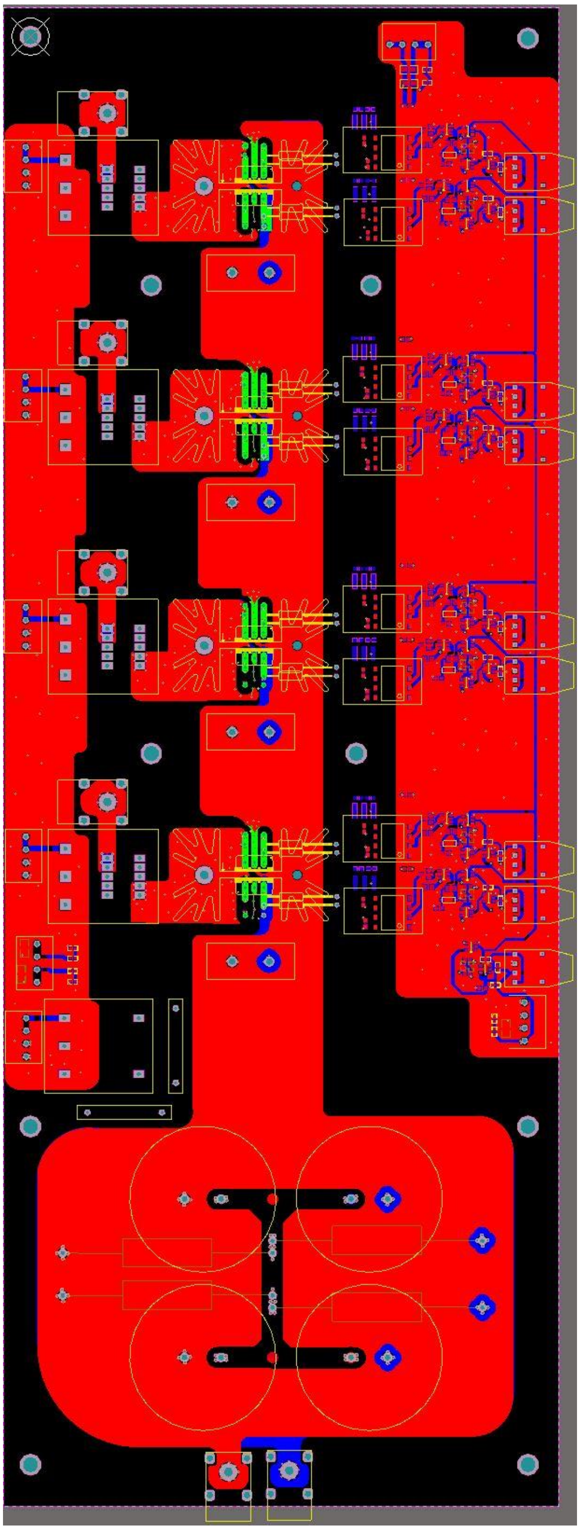

Top layer PCB layout of a 4-legVSC

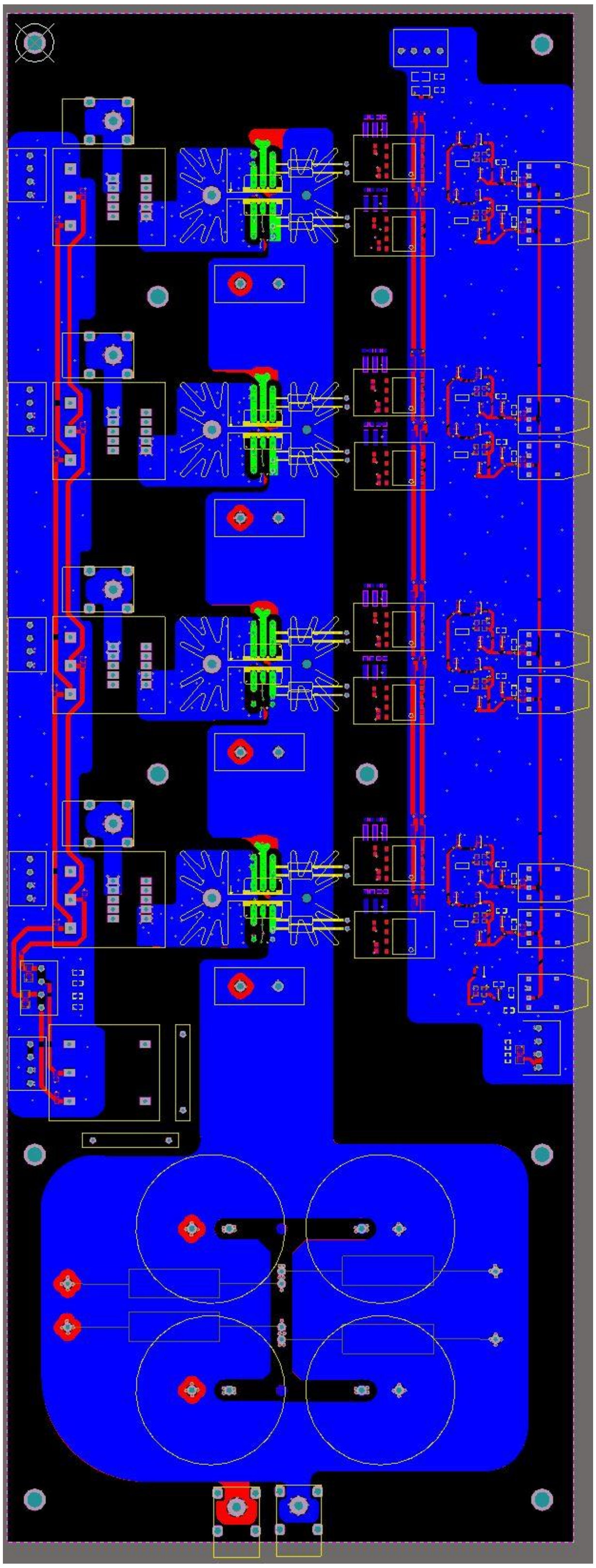

Bottom layer PCB layout of a 4-legVSC

References

[1] Gonen, T., *Electric power distribution engineering*. 2016: CRC press.

[2] Glover, J.D. , and M.S. Sarma, *Power system analysis and design: with personal computer applications*. 1994: International Thomson Publishing Company.

[3] Dugan, R.C., M.F. McGranaghan , and H.W. Beaty, *Electrical power systems quality*. New York, NY: McGraw-Hill,| c1996, 1996.

[4] Smith, J.C., G. Hensley , and L. Ray, *IEEE recommended practice for monitoring electric power quality*. IEEE Std, 1995: p. 1159-1995.

[5] Heydt, G.T., *Electric power quality: a tutorial introduction.* IEEE Computer Applications in Power, 1998. 11(1): p. 15-19.

[6] Haggis, T., *Network design manual.* E. on, 2006.

[7] Frost, T., P.D. Mitcheson , and T.C. Green. *Power electronic voltage regulation in LV distribution networks*. in *Power Electronics for Distributed Generation Systems (PEDG), 2015 IEEE 6th International Symposium on*. 2015. IEEE.

[8] Start, D., *A review of the new CENELEC standard EN 50160.* 1995.

[9] Carvalho, P.M., P.F. Correia , and L.A. Ferreira, *Distributed reactive power generation control for voltage rise mitigation in distribution networks.* IEEE transactions on Power Systems, 2008. 23(2): p. 766-772.

[10] Vlachopoulos, S. , and C. Demoulias. *Voltage regulation in low-voltage rural feeders with distributed PV systems*. in *EUROCON-International Conference on Computer as a Tool (EUROCON), 2011 IEEE*. 2011. IEEE.

[11] Sulligoi, G. , and M. Chiandone. *Voltage rise mitigation in distribution networks using generators automatic reactive power controls*. in *2012 IEEE Power and Energy Society General Meeting*. 2012. IEEE.

[12] Corsi, S., *Voltage control and protection in electrical power systems: from system components to wide-area control*. 2015: Springer.

[13] Rashid, M.H., *Power electronics: Circuits, Devices and Applications*, ed. 3rd. 2004: Pearson.

[14] Boroyevich, D., I. Cvetković, D. Dong, R. Burgos, F. Wang , and F. Lee. *Future electronic power distribution systems a contemplative view*. in *Optimization of*

Electrical and Electronic Equipment (OPTIM), 2010 12th International Conference on. 2010. IEEE.

[15] Blaabjerg, F., Z. Chen , and S.B. Kjaer, *Power electronics as efficient interface in dispersed power generation systems.* IEEE transactions on power electronics, 2004. 19(5): p. 1184-1194.

[16] Carpaneto, E. , and G. Chicco, *Probabilistic characterisation of the aggregated residential load patterns.* IET Generation, Transmission & Distribution, 2008. 2(3): p. 373-382.

[17] Aeloiza, E., P. Enjeti, L. Moran , and I. Pitel. *Next generation distribution transformer: to address power quality for critical loads*. in *Power Electronics Specialist Conference, 2003. PESC'03. 2003 IEEE 34th Annual*. 2003. IEEE.

[18] Bala, S., D. Das, E. Aeloiza, A. Maitra , and S. Rajagopalan. *Hybrid distribution transformer: Concept development and field demonstration*. in *Energy Conversion Congress and Exposition (ECCE), 2012 IEEE*. 2012. IEEE.

[19] Weedy, B.M., B.J. Cory, N. Jenkins, J.B. Ekanayake , and G. Strbac, *Electric power systems*. 2012: John Wiley & Sons.

[20] Molinas, M., J.A. Suul , and T. Undeland, *Low voltage ride through of wind farms with cage generators: STATCOM versus SVC.* IEEE Transactions on power electronics, 2008. 23(3): p. 1104-1117.

[21] Rao, P., M. Crow , and Z. Yang, *STATCOM control for power system voltage control applications.* IEEE Transactions on power delivery, 2000. 15(4): p. 1311-1317.

[22] Nielsen, J.G. , and F. Blaabjerg, *A detailed comparison of system topologies for dynamic voltage restorers.* IEEE Transactions on Industry Applications, 2005. 41(5): p. 1272-1280.

[23] Nielsen, J.G., M. Newman, H. Nielsen , and F. Blaabjerg, *Control and testing of a dynamic voltage restorer (DVR) at medium voltage level.* IEEE Transactions on power electronics, 2004. 19(3): p. 806-813.

[24] Woodley, N.H., L. Morgan , and A. Sundaram, *Experience with an inverter-based dynamic voltage restorer*. IEEE Transactions on Power Delivery, 1999. 14(3): p. 1181-1186.

[25] Fujita, H. , and H. Akagi, *The unified power quality conditioner: the integration of series-and shunt-active filters.* IEEE transactions on power electronics, 1998. 13(2): p. 315-322.

[26] Khadkikar, V., *Enhancing electric power quality using UPQC: A comprehensive overview.* IEEE transactions on Power Electronics, 2012. 27(5): p. 2284-2297.

[27] Gyugyi, L., K.K. Sen , and C.D. Schauder, *The interline power flow controller concept: a new approach to power flow management in transmission systems.* IEEE transactions on power delivery, 1999. 14(3): p. 1115-1123.

[28] Gao, C. , and M.A. Redfern. *A review of voltage control techniques of networks with distributed generations using on-load tap changer transformers*. in *Universities Power Engineering Conference (UPEC), 2010 45th International*. 2010. IEEE.

[29] Zhao, T., G. Wang, S. Bhattacharya , and A.Q. Huang, *Voltage and power balance control for a cascaded H-bridge converter-based solid-state transformer.* IEEE Transactions on Power Electronics, 2013. 28(4): p. 1523-1532.

[30] She, X., A.Q. Huang , and R. Burgos, *Review of solid-state transformer technologies and their application in power distribution systems.* IEEE Journal of Emerging and Selected Topics in Power Electronics, 2013. 1(3): p. 186-198.

[31] Haj-Maharsi, M.Y., S. Bala , and L. Tang, *Hybrid distribution transformer with an integrated voltage source converter*. 2017, Google Patents.

[32] Markiewicz, H. , and A. Klajn, *Power Quality Application Guide: Voltage Disturbances _ Standard EN50160 Voltage Characteristics in Public Distribution Systems.* Leonard Power Quality Initiative, 2004.

[33] Teodorescu, R., M. Liserre , and P. Rodriguez, *Grid converters for photovoltaic and wind power systems*. Vol. 29. 2011: John Wiley & Sons.

[34] Kaniewski, J., Z. Fedyczak , and G. Benysek, *AC voltage sag/swell compensator based on three-phase hybrid transformer with buck-boost matrix-reactance chopper*. IEEE Transactions on Industrial Electronics, 2014. 61(8): p. 3835-3846.

[35] Nijhuis, M., M. Gibescu , and J. Cobben. *Incorporation of on-load tap changer transformers in low-voltage network planning*. in *2016 IEEE PES Innovative Smart Grid Technologies Conference Europe (ISGT-Europe)*. 2016. IEEE.

[36] McMillan, B., P. Guido, O. Leitermann, V. Martinelli, A. Gonzaga , and R. McFetridge. *Application of power electronics LV power regulators in a utility distribution system*. in *Rural Electric Power Conference (REPC), 2015 IEEE*. 2015. IEEE.

[37] Song, Y.-H. , and A. Johns, *Flexible ac transmission systems (FACTS)*. 1999: IET.

[38] Sannino, A., M.G. Miller , and M.H. Bollen. *Overview of voltage sag mitigation*. in *Power Engineering Society Winter Meeting, 2000. IEEE*. 2000. IEEE.

[39] Hosseini, S., A. Nazarloo , and E. Babaei. *Application of D-STATCOM to improve distribution system performance with balanced and unbalanced fault conditions*. in *Electric Power and Energy Conference (EPEC), 2010 IEEE*. 2010. IEEE.

[40] Chen, S. , and G. Joos. *Direct power control of DSTATCOMs for voltage flicker mitigation*. in *Industry Applications Conference, 2001. Thirty-Sixth IAS Annual Meeting. Conference Record of the 2001 IEEE*. 2001. IEEE.

[41] Aggarwal, M., S. Gupta , and G. Kasal. *D-statcom control in low voltage distribution system with distributed generation*. in *Emerging Trends in Engineering and Technology (ICETET), 2010 3rd International Conference on*. 2010. IEEE.

[42] Tashackori, A., S.H. Hosseini, M. Sabahi , and T. Nouri. *A three-phase four-leg DVR using three dimensional space vector modulation*. in *Electrical Engineering (ICEE), 2013 21st Iranian Conference on*. 2013. IEEE.

[43] Gyugyi, L., C.D. Schauder , and K.K. Sen, *Static synchronous series compensator: a solid-state approach to the series compensation of transmission lines.* IEEE Transactions on power delivery, 1997. 12(1): p. 406-417.

[44] Sen, K.K., *SSSC-static synchronous series compensator: theory, modeling, and application.* IEEE Transactions on Power Delivery, 1998. 13(1): p. 241-246.

[45] Yu, Z. , and Y. Yangguang. *A three-phase four-line soft switched inverter for UPS applications*. in *Industrial Electronics, 1992., Proceedings of the IEEE International Symposium on*. 1992. IEEE.

[46] She, X. , and A. Huang. *Solid state transformer in the future smart electrical system*. in *Power and Energy Society General Meeting (PES), 2013 IEEE*. 2013. IEEE.

[47] Lai, J.-S., A. Maitra, A. Mansoor , and F. Goodman. *Multilevel intelligent universal transformer for medium voltage applications*. in *Industry Applications Conference, 2005. Fourtieth IAS Annual Meeting. Conference Record of the 2005*. 2005. IEEE.

[48] She, X., A.Q. Huang, S. Lukic , and M.E. Baran, *On integration of solid-state transformer with zonal DC microgrid.* IEEE Transactions on Smart Grid, 2012. 3(2): p. 975-985.

[49] Kang, M., P.N. Enjeti , and I.J. Pitel, *Analysis and design of electronic transformers for electric power distribution system.* IEEE Transactions on Power Electronics, 1999. 14(6): p. 1133-1141.

[50] Ganjavi, A., E. Christopher, C.M. Johnson , and J. Clare. *A study on probability of distribution loads based on expectation maximization algorithm*. in *Power & Energy Society Innovative Smart Grid Technologies Conference (ISGT), 2017 IEEE*. 2017. IEEE.

[51] Ganjavi, A., E. Christopher, C.M. Johnson , and J.C. Clare, *A new analysis for finding the optimum power rating of low voltage distribution power electronics based on statistics and probabilities.* 2017.

[52] Casanellas, F., *Losses in PWM inverters using IGBTs.* IEE Proceedings-Electric Power Applications, 1994. 141(5): p. 235-239.

[53] Graovac, D. , and M. Purschel, *IGBT Power Losses Calculation Using the Data-Sheet Parameters.* Application Note V 1.1, 2009.

[54] Cagni, A., E. Carpaneto, G. Chicco , and R. Napoli. *Characterisation of the aggregated load patterns for extraurban residential customer groups*. in *Electrotechnical Conference, 2004. MELECON 2004. Proceedings of the 12th IEEE Mediterranean*. 2004. IEEE.

[55] Carpaneto, E. , and G. Chicco. *Probability distributions of the aggregated residential load*. in *Probabilistic Methods Applied to Power Systems, 2006. PMAPS 2006. International Conference on*. 2006. IEEE.

[56] Walker, C.F. , and J.L. Pokoski, *Residential load shape modelling based on customer behavior.* IEEE Transactions on Power Apparatus and Systems, 1985(7): p. 1703-1711.

[57] Seppãlã, A. *Statistical distribution of customer load profiles*. in *Energy Management and Power Delivery, 1995. Proceedings of EMPD'95., 1995 International Conference on*. 1995. IEEE.

[58] Singh, R., B.C. Pal , and R.A. Jabr, *Statistical representation of distribution system loads using Gaussian mixture model.* IEEE Transactions on Power Systems, 2010. 25(1): p. 29-37.

[59] McQueen, D.H., P.R. Hyland , and S.J. Watson, *Monte Carlo simulation of residential electricity demand for forecasting maximum demand on distribution networks.* IEEE Transactions on power systems, 2004. 19(3): p. 1685-1689.

[60] Su, C.-L., *Probabilistic load-flow computation using point estimate method.* IEEE Transactions on Power Systems, 2005. 20(4): p. 1843-1851.

[61] Heunis, S.W. , and R. Herman, *A probabilistic model for residential consumer loads.* IEEE Transactions on Power Systems, 2002. 17(3): p. 621-625.

[62] Bhuvaneswari, M., *Gaussian mixture model: An application to parameter estimation and medical image classification.* Journal of Scientific and Innovative Research, 2016. 5(3): p. 100-105.

[63] Huang, Y., K.B. Englehart, B. Hudgins , and A.D. Chan, *A Gaussian mixture model based classification scheme for myoelectric control of powered upper limb prostheses.* IEEE Transactions on Biomedical Engineering, 2005. 52(11): p. 1801-1811.

[64] Crouse, D.F., P. Willett, K. Pattipati , and L. Svensson. *A look at Gaussian mixture reduction algorithms*. in *Information Fusion (FUSION), 2011 Proceedings of the 14th International Conference on*. 2011. IEEE.

[65] Chen, Y. , and M.R. Gupta. *Em demystified: An expectation-maximization tutorial*. in *Electrical Engineering*. 2010. Citeseer.

[66] Peel, D. , and G.J. McLachlan, *Robust mixture modelling using the t distribution.* Statistics and computing, 2000. 10(4): p. 339-348.

[67] Moon, T.K., *The expectation-maximization algorithm.* IEEE Signal processing magazine, 1996. 13(6): p. 47-60.

[68] Richardson, I. , and M. Thomson, *Domestic electricity demand model-simulation example.* 2010.

[69] Covões, T.F., E.R. Hruschka , and J. Ghosh, *Evolving gaussian mixture models with splitting and merging mutation operators.* Evolutionary computation, 2016. 24(2): p. 293-317.

[70] Li, Y. , and L. Li. *A novel split and merge em algorithm for gaussian mixture model*. in *Natural Computation, 2009. ICNC'09. Fifth International Conference on*. 2009. IEEE.

[71] Bilmes, J.A., *A gentle tutorial of the EM algorithm and its application to parameter estimation for Gaussian mixture and hidden Markov models.* International Computer Science Institute, 1998. 4(510): p. 126.

[72] Neal, R.M. , and G.E. Hinton, *A view of the EM algorithm that justifies incremental, sparse, and other variants,* in *Learning in graphical models*. 1998, Springer. p. 355-368.

[73] Jiang, C., X. Pan , and M. Gu, *The use of mixture models to detect effects of major genes on quantitative characters in a plant breeding experiment.* Genetics, 1994. 136(1): p. 383-394.

[74] Nielsen, S.F., *On simulated EM algorithms.* Journal of Econometrics, 2000. 96(2): p. 267-292.

[75] Zhang, Y., M. Brady , and S. Smith, *Segmentation of brain MR images through a hidden Markov random field model and the expectation-maximization algorithm.* IEEE transactions on medical imaging, 2001. 20(1): p. 45-57.

[76] Zheng, C., X. Meng, S. Guo , and Z. Liu, *Expectation-Maximization-Maximization: A Feasible MLE Algorithm for the Three-Parameter Logistic Model Based on a Mixture Modeling Reformulation.* Frontiers in psychology, 2018. 8: p. 2302.

[77] Dempster, A.P., N.M. Laird , and D.B. Rubin, *Maximum likelihood from incomplete data via the EM algorithm.* Journal of the royal statistical society. Series B (methodological), 1977: p. 1-38.

[78] Wu, C.J., *On the convergence properties of the EM algorithm.* The Annals of statistics, 1983: p. 95-103.

[79] Dizdarevic, N., S. Tesnjak , and G. Andersson. *Converter rating powers of unified power flow controller*. in *2002 IEEE PES Summer meeting, Chicago, USA*. 2002.

[80] Moradlou, M. , and H.R. Karshenas, *Design strategy for optimum rating selection of interline DVR.* IEEE Transactions on Power Delivery, 2011. 26(1): p. 242-249.

[81] Yazdani, A. , and R. Iravani, *Voltage-sourced converters in power systems: modeling, control, and applications*. 2010: John Wiley & Sons.

[82] Steigerwald, R.L., *Characteristics of a current-fed inverter with commutation applied through load neutral point.* IEEE Transactions on Industry Applications, 1979(5): p. 538-553.

[83] Aredes, M., J. Hafner , and K. Heumann, *Three-phase four-wire shunt active filter control strategies.* IEEE Transactions on Power Electronics, 1997. 12(2): p. 311-318.

[84] Aredes, M. , and E.H. Watanabe, *New control algorithms for series and shunt three-phase four-wire active power filters.* IEEE Transactions on Power Delivery, 1995. 10(3): p. 1649-1656.

[85] Bouscayrol, A., S. Siala , and M. Pietrzak-David. *Four-legged PWM inverters feeding two induction motors for a vehicle drive application*. in *Power Electronics and Variable-Speed Drives, 1994. Fifth International Conference on*. 1994. IET.

[86] Cárdenas, R., C. Juri, R. Peña, P. Wheeler , and J. Clare, *The application of resonant controllers to four-leg matrix converters feeding unbalanced or nonlinear loads.* IEEE Transactions on Power Electronics, 2012. 27(3): p. 1120-1129.

[87] Dai, N.-Y., M.-C. Wong , and Y.-D. Han. *Three leg center-split inverter controlled by 3D SVM under DC variation*. in *Power Electronics and Motion Control Conference, 2004. IPEMC 2004. The 4th International*. 2004. IEEE.

[88] Liang, J., T.C. Green, C. Feng , and G. Weiss, *Increasing voltage utilization in split-link, four-wire inverters.* IEEE Transactions on Power Electronics, 2009. 24(6): p. 1562-1569.

[89] Yao, J. , and T. Green. *Three-dimensional space vector modulation for a four-leg three-level inverter*. in *Power Electronics and Applications, 2005 European Conference on*. 2005. IEEE.

[90] Lobos, F.E.R., *A High Performance Power Supply based on a Four-Leg Three-Level Neutral-Point-Clamped Converter for Non-linear and Unbalanced Systems*. 2015, Technischen Universität München.

[91] Zhan, C., A. Arulampalam , and N. Jenkins, *Four-wire dynamic voltage restorer based on a three-dimensional voltage space vector PWM algorithm.* IEEE Transactions on Power Electronics, 2003. 18(4): p. 1093-1102.

[92] Naidu, S. , and D. Fernandes. *Generation of unbalanced 3-phase voltages for dynamic voltage restoration using the 4-leg voltage source converter*. in *Power Electronics Specialists Conference, 2007. PESC 2007. IEEE*. 2007. IEEE.

[93] Yaramasu, V., M. Rivera, B. Wu , and J. Rodriguez, *Model predictive current control of two-level four-leg inverters—Part I: Concept, algorithm, and simulation analysis.* IEEE Transactions on Power Electronics, 2013. 28(7): p. 3459-3468.

[94] Sawant, R.R. , and M.C. Chandorkar, *A multifunctional four-leg grid-connected compensator.* IEEE Transactions on Industry Applications, 2009. 45(1): p. 249-259.

[95] Li, Y., D.M. Vilathgamuwa , and P.C. Loh, *Microgrid power quality enhancement using a three-phase four-wire grid-interfacing compensator.* IEEE Transactions on Industry Applications, 2005. 41(6): p. 1707-1719.

[96] Demirkutlu, E., S. Cetinkaya , and A.M. Hava. *Output voltage control of a four-leg inverter based three-phase UPS by means of stationary frame resonant filter banks*. in *Electric Machines & Drives Conference, 2007. IEMDC'07. IEEE International*. 2007. IEEE.

[97] Wheeler, P., P. Zanchetta, J. Clare, L. Empringham, M. Bland , and D. Katsis, *A utility power supply based on a four-output leg matrix converter.* IEEE Transactions on Industry Applications, 2008. 44(1): p. 174-186.

[98] Khwan-on, S., L. de Lillo, P. Wheeler , and L. Empringham. *Fault tolerant four-leg matrix converter drive topologies for aerospace applications*. in *Industrial Electronics (ISIE), 2010 IEEE International Symposium on*. 2010. IEEE.

[99] Sedlak, M., S. Stynski, M.P. Kazmierkowski , and M. Malinowski. *Operation of four-leg three-level flying capacitor grid-connected converter for RES*. in *Industrial Electronics Society, IECON 2013-39th Annual Conference of the IEEE*. 2013. IEEE.

[100] Quinn, C.A. , and N. Mohan. *Active filtering of harmonic currents in three-phase, four-wire systems with three-phase and single-phase nonlinear loads*. in *Applied Power Electronics Conference and Exposition, 1992. APEC'92. Conference Proceedings 1992., Seventh Annual*. 1992. IEEE.

[101] Shen, D. , and P. Lehn, *Fixed-frequency space-vector-modulation control for three-phase four-leg active power filters.* IEE Proceedings-Electric Power Applications, 2002. 149(4): p. 268-274.

[102] Ye, Z., D. Boroyevich, K. Xing, F.C. Lee , and C. Liu. *Active common-mode filter for inverter power supplies with unbalanced and nonlinear load*. in *Industry Applications Conference, 1999. Thirty-Fourth IAS Annual Meeting. Conference Record of the 1999 IEEE*. 1999. IEEE.

[103] Prabhakar, N. , and M.K. Mishra, *Dynamic hysteresis current control to minimize switching for three-phase four-leg VSI topology to compensate nonlinear load.* IEEE Transactions on Power Electronics, 2010. 25(8): p. 1935-1942.

[104] Nasiri, R. , and A. Radan. *Pole-placement control strategy for 4-leg voltage-source inverters*. in *Power Electronic & Drive Systems & Technologies Conference (PEDSTC), 2010 1st*. 2010. IEEE.

[105] Verdelho, P. , and G. Marques. *A current control system based in/spl alpha//spl beta/0 variables for a four-leg PWM voltage converter*. in *Industrial Electronics Society, 1998. IECON'98. Proceedings of the 24th Annual Conference of the IEEE*. 1998. IEEE.

[106] Verdelho, P. , and G.D. Marques, *Four-wire current-regulated PWM voltage converter.* IEEE Transactions on Industrial Electronics, 1998. 45(5): p. 761-770.

[107] Wong, M.-C., N.-Y. Dai, J. Tang , and Y.-D. Han. *Theoretical study of 3 dimensional hysteresis PWM techniques*. in *Power Electronics and Motion Control Conference, 2004. IPEMC 2004. The 4th International*. 2004. IEEE.

[108] Prasad, V.H., D. Borojevic , and R. Zhang. *Analysis and comparison of space vector modulation schemes for a four-leg voltage source inverter*. in *Applied Power Electronics Conference and Exposition, 1997. APEC'97 Conference Proceedings 1997., Twelfth Annual*. 1997. IEEE.

[109] Perales, M.A., M. Prats, R. Portillo, J.L. Mora, J.I. León , and L.G. Franquelo, *Three-dimensional space vector modulation in abc coordinates for four-leg voltage source converters.* IEEE Power Electronics Letters, 2003. 99(4): p. 104-109.

[110] Kim, J.-H. , and S.-K. Sul, *A carrier-based PWM method for three-phase four-leg voltage source converters.* IEEE transactions on power electronics, 2004. 19(1): p. 66-75.

[111] Dai, N.-Y., M.-C. Wong, F. Ng , and Y.-D. Han, *A FPGA-based generalized pulse width modulator for three-leg center-split and four-leg voltage source inverters.* IEEE Transactions on Power Electronics, 2008. 23(3): p. 1472-1484.

[112] Zhang, R., V.H. Prasad, D. Boroyevich , and F.C. Lee, *Three-dimensional space vector modulation for four-leg voltage-source converters.* IEEE Transactions on power electronics, 2002. 17(3): p. 314-326.

[113] Li, X., Z. Deng, Z. Chen , and Q. Fei, *Analysis and simplification of three-dimensional space vector PWM for three-phase four-leg inverters.* IEEE transactions on Industrial Electronics, 2011. 58(2): p. 450-464.

[114] Zhang, M., D.J. Atkinson, B. Ji, M. Armstrong , and M. Ma, *A near-state three-dimensional space vector modulation for a three-phase four-leg voltage source inverter.* IEEE Transactions on Power Electronics, 2014. 29(11): p. 5715-5726.

[115] Blaabjerg, F., R. Teodorescu, M. Liserre , and A.V. Timbus, *Overview of control and grid synchronization for distributed power generation systems.* IEEE Transactions on industrial electronics, 2006. 53(5): p. 1398-1409.

[116] Fukuda, S. , and T. Yoda, *A novel current-tracking method for active filters based on a sinusoidal internal model [for PWM invertors]*. IEEE Transactions on Industry Applications, 2001. 37(3): p. 888-895.

[117] Sato, Y., T. Ishizuka, K. Nezu , and T. Kataoka, *A new control strategy for voltage-type PWM rectifiers to realize zero steady-state control error in input current.* IEEE Transactions on Industry Applications, 1998. 34(3): p. 480-486.

[118] Teodorescu, R., F. Blaabjerg, M. Liserre , and P.C. Loh, *Proportional-resonant controllers and filters for grid-connected voltage-source converters.* IEE Proceedings-Electric Power Applications, 2006. 153(5): p. 750-762.

[119] Timbus, A., M. Liserre, R. Teodorescu , and F. Blaabjerg. *Synchronization methods for three phase distributed power generation systems-An overview and evaluation*. in *Power Electronics Specialists Conference, 2005. PESC'05. IEEE 36th*. 2005. IEEE.

[120] Salomonsson, D. , and A. Sannino. *Comparative design and analysis of DC-Link-voltage controllers for grid-connected voltage-source converter*. in *Industry Applications Conference, 2007. 42nd IAS Annual Meeting. Conference Record of the 2007 IEEE*. 2007. IEEE.

[121] Hsieh, G.-C. , and J.C. Hung, *Phase-locked loop techniques. A survey.* IEEE Transactions on industrial electronics, 1996. 43(6): p. 609-615.

[122] Gardner, F.M., *Phaselock techniques*. 2005: John Wiley & Sons.

[123] Chung, S.-K., *A phase tracking system for three phase utility interface inverters.* IEEE Transactions on Power electronics, 2000. 15(3): p. 431-438.

[124] Bongiorno, M., *On Control of Grid-Connected Voltage Source Converters (Doctor of Philosophy)*, in *Energy and Environment* 2007, Chalmers University of Technology.

[125] Lezana, P., C.A. Silva, J. Rodriguez , and M.A. Pérez, *Zero-steady-state-error input-current controller for regenerative multilevel converters based on single-phase cells.* IEEE Transactions on Industrial Electronics, 2007. 54(2): p. 733-740.

[126] Hasan, M., A.Q. Ansari , and B. Singh. *Parameters estimation of a series VSC and shunt VSC to design a unified power quality conditioner (UPQC)*. in *Systems Conference (NSC), 2015 39th National*. 2015. IEEE.

[127] Zhou, K. , and D. Wang, *Relationship between space-vector modulation and three-phase carrier-based PWM: a comprehensive analysis [three-phase inverters]*. IEEE transactions on industrial electronics, 2002. 49(1): p. 186-196.

[128] Nguyen, T.D., J. Hobraiche, N. Patin, G. Friedrich , and J.-P. Vilain, *A direct digital technique implementation of general discontinuous pulse width modulation strategy*. IEEE Transactions on Industrial Electronics, 2011. 58(9): p. 4445-4454.

[129] Hava, A.M., R.J. Kerkman , and T.A. Lipo, *Simple analytical and graphical methods for carrier-based PWM-VSI drives*. IEEE transactions on power electronics, 1999. 14(1): p. 49-61.

[130] Holtz, J., *Pulsewidth modulation-a survey*. IEEE transactions on Industrial Electronics, 1992. 39(5): p. 410-420.

[131] Stefanovic, V.R. , and S.N. Vukosavic. *Space-vector PWM voltage control with optimized switching strategy*. in *Industry Applications Society Annual Meeting, 1992., Conference Record of the 1992 IEEE*. 1992. IEEE.

[132] Van Der Broeck, H.W., H.-C. Skudelny , and G.V. Stanke, *Analysis and realization of a pulsewidth modulator based on voltage space vectors*. IEEE transactions on industry applications, 1988. 24(1): p. 142-150.

[133] Zhan, C., V.K. Ramachandaramurthy, A. Arulampalam, C. Fitzer, S. Kromlidis, M. Bames , and N. Jenkins, *Dynamic voltage restorer based on voltage-space-vector PWM control*. IEEE transactions on Industry applications, 2001. 37(6): p. 1855-1863.

[134] Fitzer, C., M. Barnes , and P. Green, *Voltage sag detection technique for a dynamic voltage restorer*. IEEE Transactions on industry applications, 2004. 40(1): p. 203-212.

[135] Marei, M.I., E.F. El-Saadany , and M.M. Salama, *A new approach to control DVR based on symmetrical components estimation*. IEEE Transactions on Power Delivery, 2007. 22(4): p. 2017-2024.

[136] Garcia-Vite, P., J.M. Ramirez , and J.C. Rosas-Caro. *Efficient implementation of DVR's control*. in *Power & Energy Society General Meeting, 2009. PES'09. IEEE*. 2009. IEEE.

[137] Kasyap, M.S., A. Karthikeyan, B.V. Perumal , and C. Nagamani. *DSC filter based unit vector estimator for reference generation and control of dynamic voltage*

restorer. in *Power India International Conference (PIICON), 2016 IEEE 7th*. 2016. IEEE.

[138] Zhang, R.S., *High performance power converter systems for nonlinear and unbalanced load/source (Doctoral dissertation).* 1998, Virginia Tech.

[139] Jayanti, N., M. Basu, I. Axente, K. Gaughan , and M.F. Conlon. *Sequence analysis based DSP controller for Dynamic Voltage Restorer (DVR)*. in *Conference papers*. 2008.

[140] Golestan, S., M. Ramezani, J.M. Guerrero, F.D. Freijedo , and M. Monfared, *Moving average filter based phase-locked loops: Performance analysis and design guidelines.* IEEE Transactions on Power Electronics, 2014. 29(6): p. 2750-2763.

[141] Seshasayee, N., *Understanding thermal dissipation and design of a heatsink.* Texas Instruments, Dallas, 2011.

[142] *LEM, Current Transducer LA 25-NP. LA 25-NP datasheet* , . Available from: http://www.lem.com.

[143] *LEM, Voltage Transducer LV 25-P. LV 25-P datasheet* ,. Available from: http://www.lem.com.

[144] Winder, S., *Analog and digital filter design*. 2002: Elsevier.

[145] Wang, T.C., Z. Ye, G. Sinha , and X. Yuan. *Output filter design for a grid-interconnected three-phase inverter*. in *Power Electronics Specialist Conference, 2003. PESC'03. 2003 IEEE 34th Annual*. 2003. IEEE.

[146] Habetler, T.G., R. Naik , and T.A. Nondahl, *Design and implementation of an inverter output LC filter used for dv/dt reduction.* IEEE Transactions on Power Electronics, 2002. 17(3): p. 327-331.

[147] Kukrer, O., *Deadbeat control of a three-phase inverter with an output LC filter.* IEEE Transactions on power electronics, 1996. 11(1): p. 16-23.

[148] *JMS Transformers Ltd*. Available from: http://www.jmstransformers.co.uk/.

[149] Rodriguez, J., B. Wu, S. Bernet, N. Zargari, J. Rebolledo, J. Pontt , and P. Steimer. *Design and evaluation criteria for high power drives*. in *Industry Applications Society Annual Meeting, 2008. IAS'08. IEEE*. 2008. IEEE.

[150] De León, F., S. Purushothaman , and L. Qaseer, *Leakage inductance design of toroidal transformers by sector winding.* IEEE Transactions on Power Electronics, 2014. 29(1): p. 473-480.

[151] de Lillo, L., L. Empringham, P.W. Wheeler, S. Khwan-On, C. Gerada, M.N. Othman , and X. Huang, *Multiphase power converter drive for fault-tolerant machine development in aerospace applications.* IEEE Transactions on Industrial Electronics, 2010. 57(2): p. 575-583.

[152] Timbus, A.V., M. Ciobotaru, R. Teodorescu , and F. Blaabjerg. *Adaptive resonant controller for grid-connected converters in distributed power generation systems*. in *Applied Power Electronics Conference and Exposition, 2006. APEC'06. Twenty-First Annual IEEE*. 2006. IEEE.

[153] Yepes, A.G., F.D. Freijedo, J. Doval-Gandoy, O. López, J. Malvar , and P. Fernandez-Comesana, *Effects of discretization methods on the performance of resonant controllers.* IEEE Transactions on Power Electronics, 2010. 25(7): p. 1692-1712.

[154] Yepes, A.G., F.D. Freijedo, J. Doval-Gandoy, O. Lopez, J. Malvar , and P. Fernandez-Comesana. *On the discrete-time implementation of resonant controllers for active power filters*. in *Industrial Electronics, 2009. IECON'09. 35th Annual Conference of IEEE*. 2009. IEEE.

[155] Harnefors, L., *Implementation of resonant controllers and filters in fixed-point arithmetic.* IEEE Transactions on Industrial Electronics, 2009. 56(4): p. 1273-1281.

[156] Yepes, A.G., *Digital resonant current controllers for voltage source converters.* University of Vigo, Spain, 2011.

[157] Ciobotaru, M., R. Teodorescu , and F. Blaabjerg. *A new single-phase PLL structure based on second order generalized integrator*. in *Power Electronics Specialists Conference, 2006. PESC'06. 37th IEEE*. 2006. IEEE.

[158] *High Performance AC Power Source Model 61500 series*. Available from: http://www.chromaate.com/product/61500_series_Programmable_AC_Source.htm.